Synthesis, Characterization and Structure-Property Relationships of Polymer-Stabilized Nanoparticles Containing Imaging and Therapeutic Agents

Sharavanan Balasubramaniam

Dissertation submitted to the faculty of the Virginia Polytechnic Institute and State University in partial fulfillment of the requirements for the degree of

Doctor of Philosophy
In
Macromolecular Science and Engineering

Richey M. Davis, Chair

Judy S. Riffle

Nammalwar Sriranganathan

S. Richard Turner

Louis A. Madsen

11 December 2013
Blacksburg, Virginia

Keywords: magnetic nanoparticle, controlled clusters, relaxivity, MRI contrast, polylactide, poly(ethylene oxide), poly(butylene oxide), poly(*N*-isopropylacrylamide), block copolymers, ritonavir, drug delivery

Synthesis, Characterization and Structure-Property Relationships of Polymer-Stabilized Nanoparticles Containing Imaging and Therapeutic Agents

Sharavanan Balasubramaniam

ABSTRACT

The controllable design of magnetic nanocarriers is essential for advanced *in vivo* applications such as magnetic resonance image-guided therapeutic delivery and alternating magnetic field-induced remote release of drugs. This work describes the fabrication of polymer-stabilized nanoparticles encapsulating imaging and therapeutic agents and delineates relationships among materials parameters and response. The effect of aggregation of magnetic iron oxide nanoparticles in aqueous suspension was characterized using a well-defined core-corona complex comprised of a superparamagnetic magnetite nanoparticle stabilized by terminally-anchored poly(*N*-isopropylacrylamide) (PNIPAM) corona. The modified Vagberg density distribution model was employed to verify that the complexes were individually dispersed prior to aggregation and was found to accurately predict the intensity-weighted hydrodynamic diameter in water. Aggregation of the complexes was systematically induced by heating the suspension above the lower critical solution temperature (LCST) of the polymer, and substantial increase in the NMR transverse relaxation rates was noted. Controlled clusters of primary iron oxide nanoparticles stabilized by the biodegradable block copolymer, poly(ethylene oxide-*b*-D,L-lactide) were fabricated by a scalable, rapid precipitation technique using a multi-inlet vortex mixer. Quantitative control over iron oxide loading, up to 40 wt%, was achieved. Correlations between particle parameters and transverse relaxivities were studied within the framework of the analytical models of transverse relaxivity. The experimental relaxivities typically agreed to within 15% with the values predicted using the analytical models and cluster size distributions derived from cryo-

transmission electron microscopy. Hydrophilic-core particles assembled using the poly(ethylene oxide-*b*-acrylate) copolymer and at similar primary nanoparticle sizes and loadings had considerably higher transverse (r_2) and longitudinal (r_1) relaxivities, with r_2s approaching the theoretical limit for ~ 8 nm magnetite. Block copolymer nanoparticles comprised of poly(D,L-lactide) and poly(butylene oxide) cores were utilized to encapsulate the poorly water-soluble antiretroviral drug, ritonavir, at therapeutically-useful loadings. Controlled size distributions were achieved by incorporation of homopolymer additives, poly(L-lactide) or poly(butylene oxide) during the nanoparticle preparation process. Nanoparticles either co-encapsulating a highly hydrophobic polyester poly(oxy-2,2,4,4-tetramethyl-1,3-cyclobutanediyloxy-1,4-cyclohexanedicarbonyl) within the core or possessing crosslinkable groups around the core were also successfully fabricated for potential sustained release of ritonavir from block copolymer carriers.

For my mother

Radha Balasubramaniam

who would have been very proud to see this day

ACKNOWLEDGEMENTS

It is my pleasure to take this opportunity to thank all the people who have contributed to the completion of this dissertation. First, I wish to thank my advisor, Dr. Richey Davis, for his enthusiastic support and guidance throughout my work. His wisdom, helpful nature, and constant encouragement have made the whole experience pleasurable. I am indebted to him for the extraordinary kindness and understanding he showed me at a time of personal crisis. I am also thankful to Dr. Judy Riffle whose advice and inputs I greatly value. I have benefitted a great deal from interacting and working closely with several members of her group. I particularly admire her ability to bring together people from diverse backgrounds to work in a richly interdisciplinary environment.

It is a privilege to have Dr. Nammalwar Sriranganathan and Dr. Richard Turner as members of my dissertation committee, and I thank them for their helpful comments and suggestions. Thanks are also due to Dr. Lou Madsen for serving on my committee, for teaching me NMR, and for often providing me with critical remarks, questions and suggestions. Dr. Deborah Kelly has been a pleasure to work with. Her timely help with the cryo-TEM analysis was critical in the completion of this work. I have also had the privilege of knowing and working with Dr. Timothy St. Pierre, Dr. Robert Woodward, and Dr. Michael House at the University of Western Australia. They have played an important role by teaching and exciting me about the physics of magnetic nanoparticles, and have critically evaluated my work.

I thank Dr. Bruce Orler for help with DSC analyses, Dr. Gordon Yee for help with SQuID magnetization measurements, Dr. Christopher Winkler and Jay Tuggle at the Nanoscale Characterization and Fabrication Laboratory for training on the TEM, and Junia Pereira and Cigdem Arca for help with HPLC. I would also like to thank the following for financial support of this work – National Science Foundation, the Institute for Critical Technologies and Applied Science, the Macromolecules and Interfaces Institute Graduate Fellowship, and the Chevron Philips Chemical Professional Excellence Travel Award.

I wish to acknowledge all my colleagues in Prof Riffle's group – Nikorn Pothayee, Nipon Pothayee, Sanem Kayandan, and Jue Liang – without whom this dissertation would not have been

possible. I also want to thank Oguzhan Celebi, Nan Hu, Suzanne Barnes, and Hossein Abtahi with whom I have shared a warm rapport. Special thanks are due to Raquel Mejia-Ariza for her friendship, for putting up with me and helping me in several ways when I was starting out. I cherish my association with Sonal Mazumder. She has been a friend and confidant, and my experience at Virginia Tech would not be complete without her friendship.

Last but not the least, I wish to thank my family for their unwavering support, and for giving me the freedom to make my own decisions. They have stood by me no matter what and continue to do so. This would not be possible without them.

ATTRIBUTION

Dr. Yinnian Lin at Virginia Tech synthesized the Nile red acrylate discussed under section 3.3.3.

Dr. Nikorn Pothayee at Virginia Tech synthesized the ammonium bis(phosphonate)-functional PNIPAM and bis(phosphonate)-functional poly(NIPAM-*co*-Nile Red acrylate) discussed under section 3.3.4.

Dr. Robert Woodward at the University of Western Australia measured the magnetic properties of the iron oxide-PNIPAM complexes discussed under section 3.4.3.

Ms. Sanem Kayandan at Virginia Tech synthesized the polylactide block and homopolymers discussed in Chapters 4 and 5 under sections 4.3.3, 5.3.2, 5.3.3. She also synthesized the amorphous copolyester, poly(TMCBD-CHDC) discussed under section 5.4.5.

Prof. Deborah Kelly at the Virginia Tech Carilion Research Institute performed the cryo-transmission electron microscopy discussed under section 4.4.1.

Dr. Nipon Pothayee at Virginia Tech synthesized the iron oxide-poly(ethylene oxide-*b*-acrylate) complexes (hydrophilic particles) discussed under section 4.4.4.

Dr. Jue Liang at Virginia Tech synthesized the polybutylene oxide block and homopolymers discussed in Chapter 5 under sections 5.3.4 and 5.3.5.

Dr. Bruce Orler at Virginia Tech performed the DSC analyses presented in Chapter 5 under section 5.4.3.

TABLE OF CONTENTS

LIST OF FIGURES

LIST OF TABLES

1 Dissertation Overview and Motivation

The two major challenges in biomedicine are the early diagnosis of disease and the delivery of treatment in a site-specific fashion. One of the goals in nanomedicine is to enable clinically useful formulations that integrate diagnostic and therapeutic functions in one system. The nature of the problem has necessitated an interdisciplinary approach bringing together chemists, engineers, materials scientists, and biologists. The main motivation behind this dissertation is the rational design of polymer-stabilized nanoparticles for magnetic resonance imaging (MRI) contrast and antiretroviral therapy. The synthesis of nanoparticles with control over compositions and size distributions is essential for the elucidation of structure-property relationships of these materials. The overall objective of this research is to develop controlled nanoparticle systems to guide the future design of 'theranostic' carriers for the treatment of human immunodeficiency virus infections.

Magnetic nanoparticles have existing and further potential for applications in biomedicine including MRI for diagnostics and assessing biodistribution, and their capacity to generate heat in response to alternating magnetic fields to elicit biological responses. Nanoparticulate iron oxides are biocompatible, have high magnetic susceptibilities, and exhibit superparamagnetic characteristics making them suitable for bioimaging applications. The relevant magnetic and NMR relaxation properties, synthesis and surface-functionalization of iron oxide nanoparticles are described in a literature review in Chapter 2. The effect of controlled clustering of primary iron oxide nanoparticles, their integration with poorly water-soluble therapeutics, and the fabrication routes for multifunctional magnetic nanocarriers are discussed.

The synthesis of well-defined, individually dispersed polymer-stabilized iron oxide nanoparticles is a challenge. This is especially important to elucidate the effects of aggregation on the NMR T_2 relaxation times of aqueous suspensions in which the magnetic nanoparticles are suspended. Chapter 3 describes a well-defined iron oxide nanoparticle-polymer complex comprised of a superparamagnetic iron oxide core surrounded by a poly(*N*-isopropylacrylamide) corona. Conformational changes in the PNIPAM corona driven by the lower critical solution temperature (LCST) afforded thermoresponsive properties to the complexes. This system was utilized to characterize the effect of clustering on the NMR relaxation times by inducing systematic aggregation of discrete magnetic nanoparticles in aqueous suspension. The modified Vagberg density distribution model to predict the hydrodynamic diameter and brush thickness of core-corona nanostructures was successfully implemented with these complexes.

Several researchers have reported the fabrication of controlled clusters of iron oxide nanoparticles stabilized with amphiphilic block copolymers. Core-shell particles wherein the clustered magnetic nanoparticles and hydrophobic drugs are co-encapsulated in a biodegradable, hydrophobic block comprised of poly(D,L-lactide) or poly(caprolactone) are well-known in the literature. Although high transverse relaxivities for T_2-weighted MRI contrast have been demonstrated with these systems, their design is empirical and correlations between particle characteristics (size, magnetization, iron oxide loading) and observed transverse relaxivities are semi-quantitative at best. In Chapter 4, the analytical models of transverse relaxivity are revisited with an aim to predict the MRI contrast efficiencies of hybrid, polydisperse particle systems. To this end, iron oxide-amphiphilic block copolymer particles with variable size distributions and iron oxide loadings were fabricated. Quantitative agreement between the experimental transverse relaxivities and the analytical model predictions is demonstrated for the first time with particles of this chemical

composition and morphology. The goal of this study is to design theranostic magnetic carriers for poorly water-soluble drugs in a predictive, quantitative fashion.

Chapter 5 describes the synthesis and characterization of nanoparticles of the antiretroviral drug, ritonavir, for the treatment of human immunodeficiency virus type one (HIV-1) infection. Antiretroviral nanoparticles with controlled sizes and drug loadings have not been demonstrated so far. In this study, ritonavir nanoparticles stabilized with poly(lactide) and poly(butylene oxide) copolymers were prepared using a scalable rapid precipitation technique. The use of hydrophobic homopolymer additives for fabricating block copolymer nanoparticles with narrow size distributions is demonstrated. This chapter further describes approaches for potentially tailoring the release kinetics of antiretroviral drugs from well-defined block copolymer nanoparticles. For ritonavir nanoparticles stabilized with poly(ethylene oxide-*b*-D,L-lactide), an amorphous polyester with high hydrophobicity and glass transition temperature was utilized as the homopolymer additive. A novel polyether triblock copolymer with a crosslinkable center block was also used to form ritonavir nanoparticles. Varying the T_g of the nanoparticle core or introducing a crosslinked 'fence' around the core with variable crosslinking densities are potential ways to tune release rates.

Chapter 6 describes fluorescent nanoparticles based on the poly(ethylene oxide-*b*-D,L-lactide) copolymer with potential applications for intracellular tracking of nanomedicine. An organic dye and semiconductor quantum dots were utilized as model fluorophores in this study. Macrophage cells are known to be reservoirs for viruses, and therefore macrophage-targeting of nanoparticles has been demonstrated as an effective approach in antiretroviral therapy. However, characterizing the intracellular dynamics of drug-loaded nanoparticles and monitoring of drug release are much needed. The uptake and intracellular trafficking of block copolymer nanoparticles can be investigated with laser-induced fluorescence microscopy with single particle tracking analysis.

Chapter 7 describes the synthesis of 25 nm iron oxide nanoparticles coated with oleic acid, and their assembly into water-dispersible clusters using the rapid precipitation method. These particles have potential applications for alternating magnetic field-induced release of hydrophobic drugs at specific sites *in vivo*. The major conclusions drawn from the above studies and recommendations for future work are described in Chapter 8.

2 Literature Review

2.1 Biological applications of nanoparticles – Overview

The last two decades have seen an explosive interest in nanoparticles owing to their unique, size-dependent properties. The convergence of nanotechnology and biomedicine has been driven by the need for early diagnosis of diseases, and the selective delivery of drugs to specific sites in the body so as to maximize therapeutic action and minimize side effects. Advances in size-controlled chemical synthesis, stabilization, and targeting strategies have made nanoparticles a promising platform for a range of biological applications. These applications can be broadly categorized as (i) therapeutic delivery, (ii) biological sensing, and (iii) bioimaging.[1] The utilization of nanoparticles that integrate more than one of these functions in one system is an area of intense interest. For example, multifunctional magnetic nanoparticles attract considerable attention as 'theranostic' materials for the real-time monitoring of therapeutic delivery through magnetic resonance imaging (MRI).

There are already over 240 FDA-approved nanomedicine products on the market and more under clinical trials currently.[2] The full realization of the potential of nanoparticles, however, relies on understanding and manipulating how they function in the complex biological environment. One of the challenges associated with the use of nanoparticles *in vivo* is to circumvent various biological barriers, such as binding of serum proteins, and recognition and clearance by the reticuloendothelial system (RES). The nanoparticle size, shape, charge, and surface chemistry play a crucial role in determining the fate of these materials inside the body.[3] Nevertheless, considerable

progress has been made in both the design of novel nanomaterials and the understanding of their biological interactions, offering exciting possibilities for the future of nanomedicine.

2.1.1 Magnetic iron oxide nanoparticles in biomedicine

The concept of using magnetic nanoparticles as MRI contrast agents or for the site-specific delivery of chemotherapeutic drugs dates back to the 1970s.[4,5] Today, multifunctional magnetic nanoparticles are being explored as versatile materials for several applications such as diagnostic imaging, hyperthermia treatment of cancer, retinal detachment therapy, and targeted drug delivery. The useful biomedical applications of nanoparticulate iron oxides are attributed to their excellent biocompatibility, superparamagnetic characteristics, high magnetic susceptibility, and the ability to be synthesized in a size-controlled fashion.

The ability of iron oxide nanoparticles to influence the relaxation of water molecules in their vicinity by reducing their transverse (T_2) relaxation times gives rise to their most promising application – as contrast enhancement agents in MRI. In fact, superparamagnetic iron oxide nanoparticles are approved by the Food and Drug Administration (FDA) and have found clinical use as MRI contrast agents for almost two decades.[6] Besides, magnetic nanocarriers have the potential for guided transport of therapeutics using external magnetic fields and can respond to alternating magnetic fields to generate localized heat for hyperthermia.[7,8] However, these applications demand well-defined nanostructures with controlled sizes and compositions. The size-controlled synthesis of magnetic iron oxide nanoparticles and their stabilization with suitable macromolecules is crucial to render them hydrophilic, stable, non-toxic and non-immunogenic for *in vivo* applications.

2.2 Magnetic properties - Superparamagnetism

A bulk ferromagnetic material is comprised of domains such that all magnetic moments of constituent atoms in a domain are aligned in the same direction. The magnetostatic energy of the material is lowered as a result of the formation of domains. However, the creation of new domains entails an energetic cost of the formation of domain boundaries. Consequently, a critical size exists, below which the energy required for the formation of a smaller domain is greater than the energy gained from the reduction in magnetostatic energy. This means that a magnetic nanoparticle smaller than this critical size exists as a single domain. For magnetite, the critical domain size is 128 nm,[9] and therefore a typical 10-100 nm magnetite (Fe_3O_4) or maghemite (γ-Fe_2O_3) nanoparticle used for biomedical applications is a single-domain particle with a unique magnetic moment orientation.

A single-domain nanoparticle has an anisotropy energy barrier which prevents the magnetic moment flipping from one direction to the opposite. The anisotropy energy is given by K_aV, where K_a is the anisotropy constant and V is the particle volume. When the particle size decreases sufficiently such that K_aV is equal to or lower than thermal energy (= k_BT), the magnetic moments are able to flip directions with a characteristic time known as the Néel relaxation time. This critical particle size is termed as the superparamagnetic limit. Using K_a = 13,500 J m^{-3} for magnetite,[10] an Fe_3O_4 particle of diameter 18 nm or lower would be superparamagnetic at ambient temperatures. It follows that for particle sizes above the superparamagnetic limit and below the critical domain size, the material is ferromagnetic and single-domain.

A superparamagnetic material is characterized by the build-up of a huge magnetic moment in the presence of an external magnetic field due to the alignment of the individual spins with the field direction. When the field is removed, the moments return to zero without remanence (Figure 2.1).

This behavior is similar to that of paramagnetic materials. However, compared to a paramagnetic ion, each magnetite or maghemite nanoparticle bears a huge magnetic moment arising from the individual magnetic atoms, and hence the term 'superparamagnetic'.

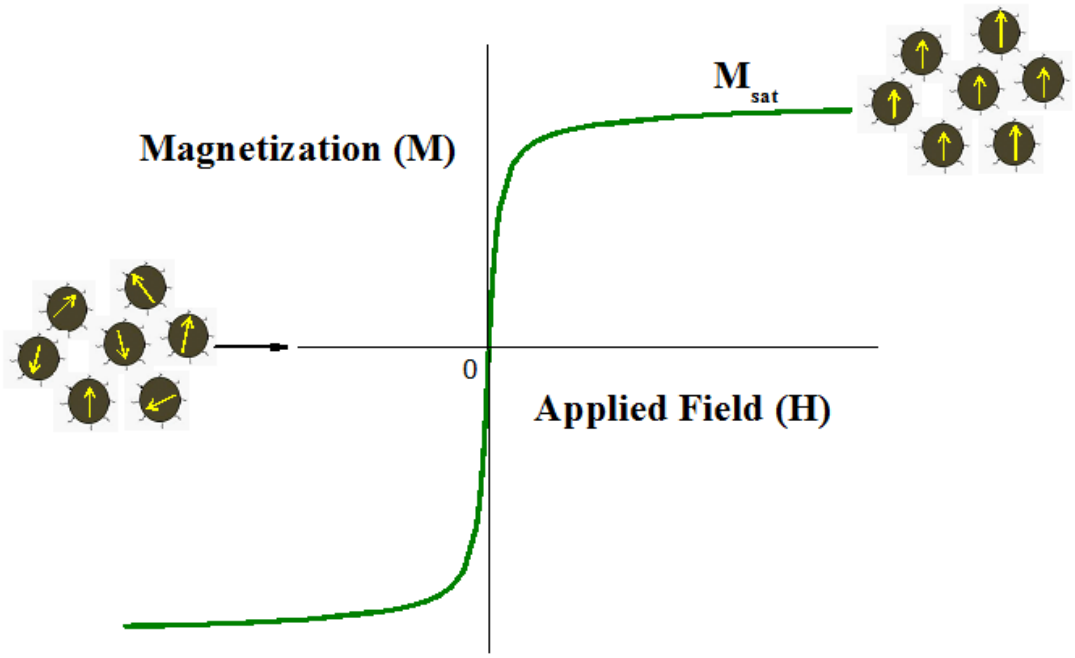

Figure 2.1. Hysteresis curve of superparamagnetic nanoparticles.

The magnetization behavior of a superparamagnetic particle, as depicted in Figure 2.1, can be represented by the Langevin function, whose shape depends on the saturation magnetization (M_{sat}) and the size of the magnetic particle:[10]

$$M(H) = M_{sat}L(x) = M_{sat}\left[\coth(x) - \frac{1}{x}\right] \tag{2.1}$$

where $$x = \frac{\mu_{sat}H}{k_BT}$$

For a superparamagnetic particle of a given size, there also exists a characteristic temperature, known as the blocking temperature (T_B), which marks the superparamagnetic-to-ferromagnetic

transition. Below T_B, a finite hysteresis would be observed on the *M-H* curve. The blocking temperature can also be defined as the temperature at which the relaxation time equals the measurement time.

The blocking temperature of a magnetic nanoparticle can be experimentally determined by measuring the magnetization as a function of temperature in the presence of an external magnetic field. This is called a zero-field-cooled/field-cooled (ZFC/FC) experiment, where the sample is first cooled down to a very low temperature (usually 5 K), much below the expected blocking temperature. Then, a small magnetic field (~ 100 Oe) is turned on, and the sample is heated while measuring its magnetization. This is the ZFC curve. In the next stage, the sample is cooled again without removing the magnetic field and the magnetization is measured, producing the FC curve. A typical ZFC/FC curve is shown in Figure 2.2. As the temperature increases, the 'blocked' magnetic moments begin to align with the external magnetic field leading to an increase in the magnetization. When the thermal fluctuations push the magnetic moments above the anisotropy barrier (corresponding to the onset of superparamagnetic behavior), the magnetization begins to decrease. Thus, the peak on the ZFC curve corresponds to the blocking temperature. Above T_B, the ZFC and FC curves coincide indicating that the system is in thermal equilibrium and the heating/cooling processes are reversible.[11]

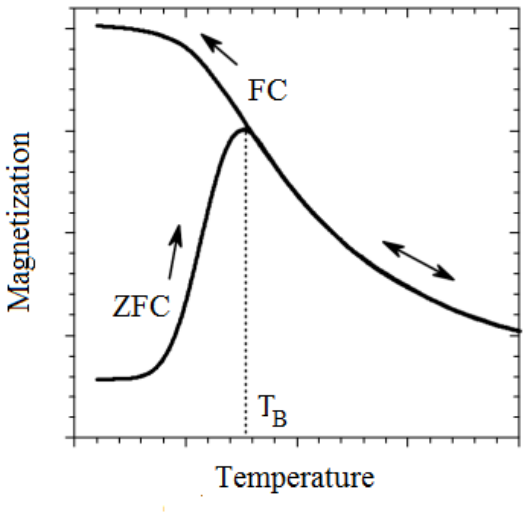

Figure 2.2. Typical zero-field-cooled/field-cooled (ZFC/FC) magnetization curves for the determination of blocking temperature (T_B). Adapted from reference [11].

2.3 Magnetite

Magnetite (Fe_3O_4) is a black, ferrimagnetic mineral which is abundant in natural rocks.[10] It consists of Fe^{2+} and Fe^{3+} ions in an inverse spinel structure. Thirty-two oxygen anions form a face-centered cubic unit cell with an edge length of 0.839 nm, where the iron ions are located on eight tetrahedral sites and sixteen octahedral sites.[12] The tetrahedral sites are exclusively occupied by the Fe^{3+} ions, whereas Fe^{2+} and Fe^{3+} alternately occupy the octahedral sites. The magnetic moments of the tetrahedral iron ions are aligned in a specific direction, whereas the octahedral iron magnetic moments are aligned in the opposite direction. Since there is the same number of octahedral and tetrahedral Fe^{3+} ions, they compensate for each other, and the resulting moment of a magnetite crystal arises only from the uncompensated octahedral Fe^{2+} ions.[10] Magnetite is susceptible to oxidation to maghemite (γ-Fe_2O_3), which is a red-brown, ferrimagnetic iron oxide isostructural with magnetite but with cation deficient sites. The magnetic properties of maghemite are due to the uncompensated octahedral Fe^{3+} ions.[12] The density and magnetization of maghemite are

slightly lower than that of magnetite. It should be noted that a pure magnetite sample hardly exists, and some amount of maghemite is always present in the magnetite sample.

2.4 Synthesis of iron oxide nanoparticles

The most common method for synthesizing iron oxide nanoparticles is by the chemical co-precipitation of iron salts (Fe^{2+} and Fe^{3+}) in an aqueous solution under alkaline conditions:[13-15]

$$Fe^{2+} + 2Fe^{3+} + 8OH^- \longrightarrow Fe_3O_4 + 4H_2O$$

This reaction has the advantage of providing a simple and efficient way of synthesizing large quantities of magnetite nanoparticles. However, careful control of pH, poor size control (Figure 2.4a), broad size distributions and poor crystallinity are drawbacks of this method.

Highly monodisperse nanoparticles with good crystallinity and size control (Figure 2.4b) can be synthesized by high temperature decomposition reactions in organic solvents using organic iron precursors and surfactants.[16-18] Size-controlled synthesis of magnetic particles is particularly useful for magnetic recording and biomedical applications. According to La Mer and Dinegar,[19] the synthesis of monodisperse, colloidal nanocrystals can be achieved through a single, temporally discrete nucleation event, followed by slower, controlled growth of the existing nuclei. This is illustrated in Figure 2.3.[20] Surfactants are required in these syntheses to prevent agglomeration of the nanoparticles owing to their extremely high surface area-to-volume ratios.

Sun et al. have described the high-temperature reaction of iron (III) acetyacetonate, $Fe(acac)_3$, with 1,2-hexadecanediol in the presence of oleic acid and oleylamine leading to monodisperse Fe_3O_4 nanoparticles.[21] The choice of solvent determined the nanoparticle size. While phenyl ether (b.p. 259°C) gave 4 nm particles, benzyl ether (b.p. 298°C) led to 6 nm particles. It was found that holding the reaction mixture at 200°C for 30 min. in the case of the 4 nm particles, and for 2 h in

the case of the 6 nm particles, was key to the formation of monodisperse nanoparticles. Nanoparticles with larger diameters (8-20 nm) were further synthesized by using the 4 nm or 6 nm particles as seeds.

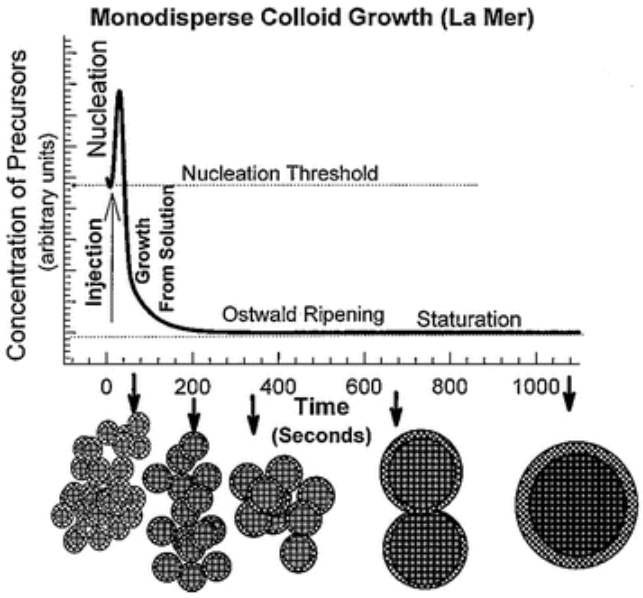

Figure 2.3 Schematic illustration of the La Mer model for the synthesis of monodisperse nanoparticles. Reproduced from reference [20], Copyright 2000, with permission from Annual Reviews, Inc. Murray, C. B.; Kagan, C. R.; Bawendi, M. G.: Synthesis and characterization of monodisperse nanocrystals and close-packed nanocrystal assemblies. *Annu. Rev. Mater. Sci.* **2000**, *30*, 545-610. Used with permission from Annual Reviews, Inc. 2013.

Hyeon et al. reported the synthesis of highly crystalline and monodisperse γ-Fe_2O_3 nanoparticles by the controlled oxidation of iron nanoparticles formed as a result of the high-temperature aging of an iron-oleic acid metal complex.[17] The metal complex was formed by the thermal decomposition of iron pentacarbonyl in the presence of oleic acid at 100°C. A modified, large-scale synthesis of monodisperse iron oxide nanoparticles was later described where the iron oleate complex was synthesized by the reaction of inexpensive and environmentally friendly compounds, namely iron chloride ($FeCl_3.6H_2O$) and sodium oleate.[22] The iron oleate complex was then slowly

heated to 320°C in 1-octadecene, and aged at that temperature to generate 12 nm iron oxide nanocrystals. Similar to Sun et al., nanoparticle sizes could be varied by using different solvents – 1-hexadecene (b.p. 274°C) for 5 nm, octyl ether (b.p. 287°C) for 9 nm, 1-eicosine (b.p. 330°C) for 16 nm, and trioctylamine (b.p. 365°C) for 22 nm nanoparticles. It was reasoned that the increase in reactivity of the iron oleate complex with the solvent boiling point led to nanoparticles with increased sizes. Pinna et al. have synthesized 12-25 nm monocrystalline magnetite nanoparticles by the reaction of $Fe(acac)_3$ and benzyl alcohol, without the use of ligands/surfactants, in an autoclave between 175-200°C.[23] In this reaction, benzyl alcohol acts as both solvent and ligand. The nanoparticles were made dispersible in polar and non-polar solvents by coating them with dopamine or undecanoic acid, respectively, after synthesis.

(a) (b)

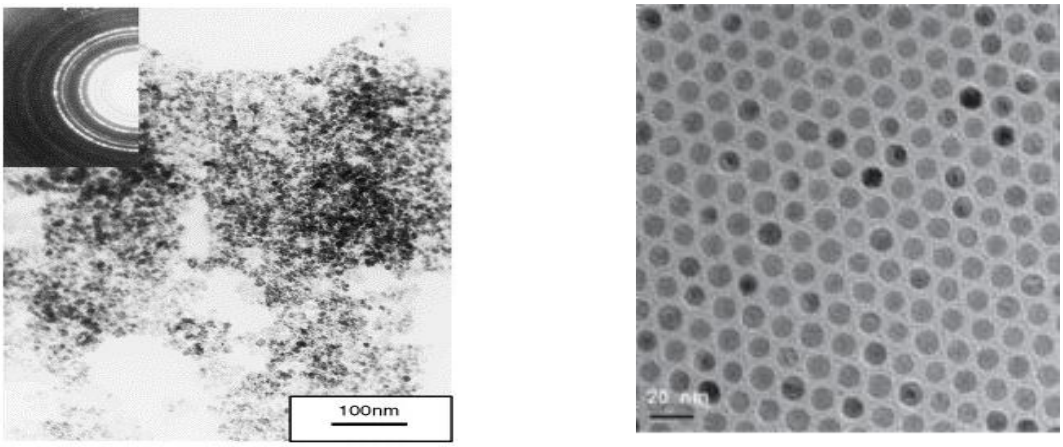

Figure 2.4 (a) Synthesis of magnetite nanoparticles by coprecipitation. Reproduced from reference [13], Copyright 2004, with permission from Elsevier. Sun, Y.-k.; Ma, M.; Zhang, Y.; Gu, N.: Synthesis of nanometer-size maghemite particles from magnetite. *Coll. Surf. A: Physicochem. Eng. Aspects* **2004**, *245*, 15-19. Used with permission from Elsevier 2013. (b) Synthesis of magnetite nanoparticles by thermal decomposition. Reproduced from reference [22], Copyright 2004, with permission from Nature Publishing Group. Park, J.; An, K.; Hwang, Y.; Park, J.-G.; Noh, H.-J.; Kim, J.-Y.; Park, J.-H.; Hwang, N.-M.; Hyeon, T.: Ultra-large-scale syntheses of monodisperse nanocrystals. *Nat. Mater.* **2004**, *3*, 891-895. Used with permission from Nature Publishing Group 2013.

In addition to coprecipitation and thermal decomposition, numerous other methods have been used to synthesize magnetic nanoparticles including, but not limited to, sonochemical reactions,[24] sol-gel syntheses,[25] hydrothermal reactions,[26] flow injection syntheses[27] and spray/laser pyrolysis.[28,29] These techniques have been reviewed in detail by Laurent et al.[30]

2.5 Surface functionalization of iron oxide nanoparticles

A crucial step in the design of iron oxide nanoparticles for *in vivo* applications is their dispersion and colloidal stability in physiological media, which obviously requires a hydrophilic surface coating around the magnetic particle core. The size-controlled syntheses of discrete iron oxide nanoparticles mostly result in a hydrophobic coating comprised of oleic acid/oleylamine. The nanoparticles must be endowed with hydrophilic character through ligand-exchange reactions to make them suitable for biological applications. Furthermore, the surface coverage of the hydrophilic coatings must be sufficient because the agglomeration of iron oxide nanoparticles can also be driven by magnetic attraction in addition to the van der Waals forces of attraction. Coating strategies for iron oxide nanoparticles must also ensure biocompatibility, low toxicity, colloidal stability over a broad pH range and in high ionic strengths, and the possibility of further derivatization to incorporate antibodies, targeting ligands and other biomolecules.

Various inorganic and organic (low molecular weight and polymeric) coating materials have been used for iron oxide nanoparticles which will be discussed below. A relatively straightforward approach to rendering the as-synthesized hydrophobic nanoparticles water-dispersible is through the addition of a secondary surfactant which forms a bilayer structure with the primary surfactant layers around the magnetic particle. Aqueous dispersions of magnetite nanoparticles coated with a self-organized bilayer structure of *n*-alkanoic acids (9-13 carbon atoms) have been reported.[31] The long alkyl chains of the secondary surfactant were integrated between those of the primary

surfactant through attractive van der Waals interactions, whereas the polar head group (carboxylic acid in this example) was on the outer surface providing electrostatic stabilization. Qin et al. reported an amphiphilic poly(maleic anhydride-*alt*-1-octadecene)-*graft*-poly(N-isopropylacrylamide) copolymer to encapsulate oleic acid-coated magnetite nanoparticles.[32] Again, the alkyl chains on the copolymer associated with the hydrophobic tails of oleic acid around the Fe_3O_4. Similarly, amphiphilic PEG-phospholipids have also been employed to coated hydrophobic iron oxide nanoparticles.[33]

Ligand exchange reactions to replace the hydrophobic layer with a suitable hydrophilic ligand are more common (Figure 2.5).[34] The hydrophilic molecule bears anchor groups such as carboxylates,[35-37] phosphonates[38,39] or catechols[40] for attachment on the surface of the iron oxide nanoparticle and may additionally be functionalized on the other end for further chemical modification. Both low molecular weight and polymeric molecules have been employed for this purpose. Citric acid and dopamine are examples of "monomeric" stabilizers for iron oxide nanoparticles.[40,41] Recently, a zwitterionic dopamine sulfonate molecule was described where the vicinal diol groups of the dopamine coordinate with the iron oxide surface and the sulfonate groups afford good dispersibility in water.[42]

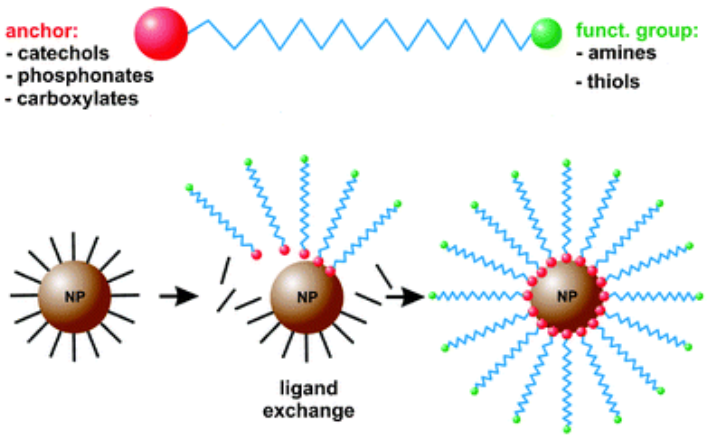

Figure 2.5 Ligand exchange for the surface modification of iron oxide nanoparticles with a hydrophilic polymer. Reproduced from reference [34], Copyright 2011, with permission from The Royal Society of Chemistry. Schladt, T. D.; Schneider, K.; Schild, H.; Tremel, W.: Synthesis and bio-functionalization of magnetic nanoparticles for medical diagnosis and treatment. *Dalton Trans.* **2011**, *40*, 6315-6343. Used with permission from The Royal Society of Chemistry 2013.

Non-ionic, polymeric stabilizers are most commonly used to provide long-term colloidal stability to iron oxide nanoparticles which is much-needed for biomedical applications. Poly(ethylene oxide) is perhaps the most widely used hydrophilic stabilizer owing to its high solubility, excellent biocompatibility, and the ability to prevent adsorption of plasma proteins and non-specific uptake by the RES.[43,44] Dextran, a polysaccharide, has also been widely used owing to its biocompatibility. Most commercial MRI contrast agents, such as Feridex, Resovist and Combidex, are comprised of dextran-coated iron oxide nanoparticles wherein the dextran is incorporated as a stabilizer during the alkaline coprecipitation process.[45,46] However, these materials are aggregates containing multiple iron oxide cores within a dextran shell, where the degree of aggregation and thickness of the shell are variable and disperse. Other polymers used to stabilize iron oxide nanoparticles include poly(vinyl alcohol), chitosan, alginate, poly(vinylpyrrolidone), poly(acrylic acid), poly(ethyleneimine), poly(lactic acid), and their copolymers.[47-52]

Inorganic coatings such as silica and gold around the iron oxide nanoparticles have also been described. The coating of iron oxide nanoparticles with an overlayer of gold is aimed at applications such as multimodal imaging agents or the magnetic field-driven separation of proteins by the immobilization of antibodies on the gold-coated magnetic nanoparticles.[53,54] A silica coating improves the chemical and colloidal stability of the magnetic nanoparticles. Among the different approaches available for the fabrication of silica coatings, the water-in-oil microemulsion method is directly applicable to hydrophobically-modified iron oxide nanoparticles. In a typical synthesis, the hydrophobic nanoparticles and a surfactant are dispersed in a non-polar solvent. Aqueous NH_4OH solution is added to form inverse micelles with the entrapment of nanoparticles, and subsequently the condensation of tetraethyl orthosilicate (TEOS) leads to the formation of SiO_2 on the nanoparticle surface.[55]

2.6 Magnetic Resonance Imaging

MRI is currently one of the most powerful tools in biomedical imaging and diagnostics because of its non-invasive nature, and the ability to provide anatomical information with good spatial and temporal resolution.[56] It provides resolutions varying from ~1 mm at clinical field strengths, down to ~50 μm at higher field strengths that are accessible in a research setting. It has been used to image the brain and the central nervous system (CNS), to assess cardiac functions and to detect tumors.[57]

2.6.1 Basic principles of MRI

MRI is based on the excitation and relaxation of hydrogen nuclei which are abundant in water and lipids in the body. In the absence of an external magnetic field, the magnetic moments of the hydrogen nuclei are randomly oriented. This results in zero net magnetization which is given by the vector sum of the individual nuclear magnetic moments. In the presence of an external static

magnetic field, the nuclear magnetic moments undergo a rotational motion known as 'precession', analogous to a spinning top, about the magnetic field. This precessional motion has a characteristic frequency known as the Larmor frequency (ω) which is proportional to the strength of the static magnetic field (B^0):

$$\omega = \gamma B^0 \tag{2.2}$$

where $\boldsymbol{\gamma}$ is the proton gyromagnetic ratio.

For protons with spin = ½ placed in a magnetic field, the Zeeman effect produces two energy states corresponding to "spin up" and "spin down". At equilibrium, there is a slightly higher population of spins in the lower energy "spin up" state, giving rise to a small net longitudinal magnetization (Figure 2.6) along the magnetic field direction.[58] In an MRI procedure, this magnetization must be perturbed from the equilibrium state in order to obtain a measurable signal.

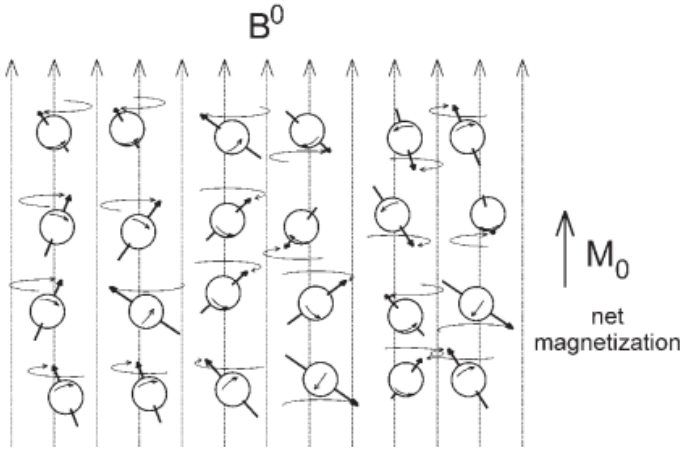

Figure 2.6 Equilibrium precession of hydrogen nuclei about an external static magnetic field ($\mathbf{B^0}$).[58]

By applying a transverse oscillating magnetic field (90° RF pulse) exactly at the Larmor frequency, the nuclear magnetization can be tipped away from the longitudinal axis, creating a transverse component of the magnetization. At the instant the oscillating field is turned off, the magnetic

moments precess with the same phase (same projection in the transverse plane). However, internuclear interactions and inhomogeneities in the static magnetic field will cause the moments to dephase leading to an attenuation in the transverse magnetization signal. The relaxation time constant for this signal decay is T_2^*. Using the Carr-Purcell-Meiboom-Gill pulse sequence (Figure 2.7),[59] the dephasing due to field inhomogeneities can be largely reversed by the application of a train of 180° RF pulses applied along a direction in the transverse plane. Each 180° pulse causes the magnetic moments to rephase by rotation in the transverse plane leading to the formation of spin echoes. The first spin echo is formed at a time TE following the initial 90° pulse. The time between subsequent echoes, which is the same as the time between subsequent 180° pulses, is called the echo spacing (ES). The magnitude of the signal decreases at each successive echo which is attributed to signal decay solely due to interactions between magnetic moments. The signal amplitude corresponding to each echo time is used to calculate the spin-spin relaxation time constant T_2:

$$M_{xy}(t) = M_0 exp(\frac{-t}{T_2}) \tag{2.3}$$

where $M_{xy}(t)$ is the transverse magnetization at time t after the 90° pulse, M_0 is the maximum magnetization immediately after the application of the 90° pulse.

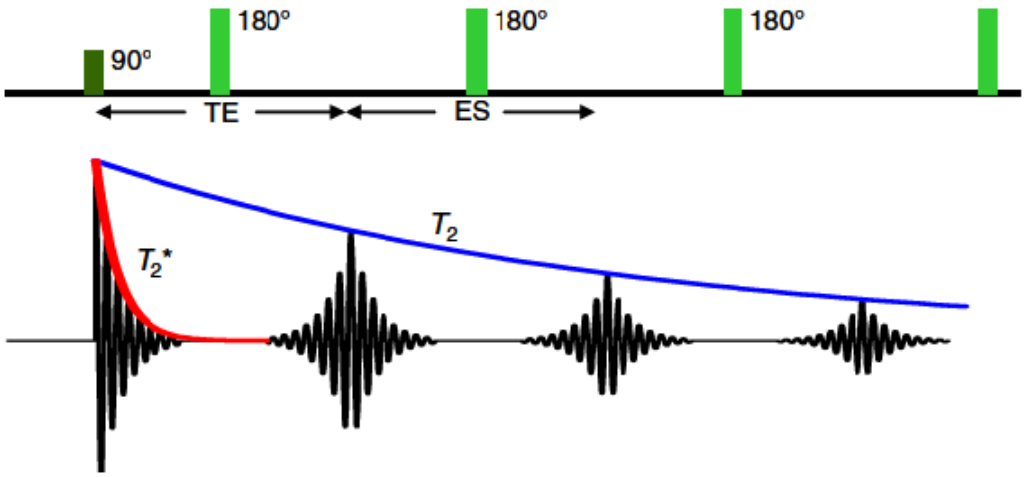

Figure 2.7 Schematic representation of the Carr-Purcell-Meiboom-Gill (CPMG) pulse sequence to measure the T_2 relaxation time.[59]

2.7 Contrast effect of iron oxide nanoparticles

The intrinsic transverse relaxation time differences of different parts of the tissues bring about changes in the MR signal intensity, which in turn results in an image contrast.[60] For diagnostic imaging, however, normal tissues and lesions may not have sufficient differences in relaxation times, thereby necessitating a contrast agent. The relaxation times can be manipulated by the use of nanoparticulate iron oxide contrast agents, which produce darker regions where they are accumulated. In fact, iron oxide nanoparticle contrast agents have been shown to be very effective and have been widely used in T_2-weighted magnetic resonance imaging applications. For example, high-resolution MRI in the presence of magnetic iron oxide nanoparticles allowed for the detection of small (~ 2 mm) and otherwise undetectable lymph-node metastases in patients with prostate cancer (Figure 2.8).[61]

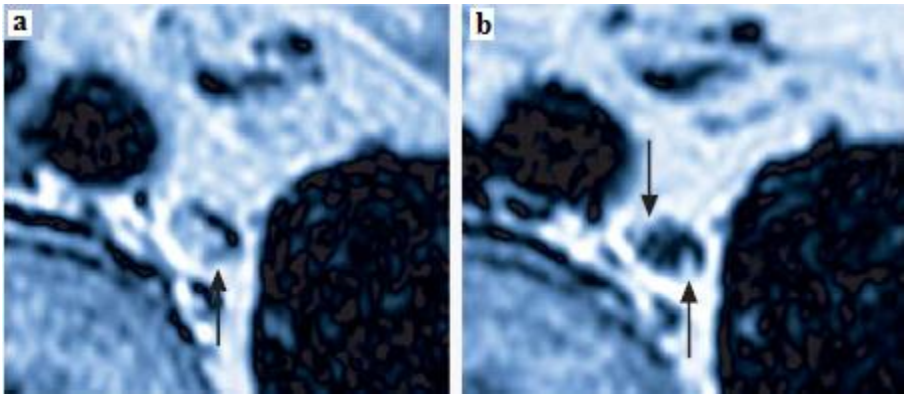

Figure 2.8 Magnetic resonance images of a metastatic lymph node (a) before, and (b) after administration of superparamagnetic nanoparticles. Reproduced from reference [61], Copyright Massachusetts Medical Society. Harisinghani, M. G.; Barentsz, J.; Hahn, P. F.; Deserno, W. M.; Tabatabaei, S.; van de Kaa, C. H.; de la Rosette, J.; Weissleder, R.: Noninvasive detection of clinically occult lymph-node metastases in prostate cancer. *New Engl. J. Med.* **2003**, *348*, 2491-2499. Used with permission from the Massachusetts Medical Society 2013.

The contrast effect of iron oxide arises from its ability to perturb the transverse relaxation (or T_2 relaxation) of the neighboring water protons. As previously described in Section 2.6.1, the proton magnetic moments of water and fat in the body, when subjected to an external static magnetic field, precess at a characteristic frequency proportional to the magnetic field strength. When an iron oxide nanoparticle is introduced in the system, it leads to a reduction in the transverse relaxation time of the protons. This effect is due to the local field inhomogeneities created by the induced magnetic moment in the nanoparticle which cause the nearby proton magnetic moments to precess at slightly different rates and lose phase coherence at a faster rate (Figure 2.9a).[62] The accelerated dephasing of the proton magnetic moments leads to a loss of signal in T_2–weighted MR images giving final image contrast (Figure 2.9c).[62]

It is common to express the effectiveness of the contrast agent in terms of the transverse relaxivity, r_2, which is the slope of the straight line on a graph of the transverse relaxation rate ($R_2 = 1/T_2$)

versus the concentration of magnetic material (mM Fe) (Figure 2.9b). Thus, r_2 can be defined as the relaxation rate enhancement per millimolar iron.

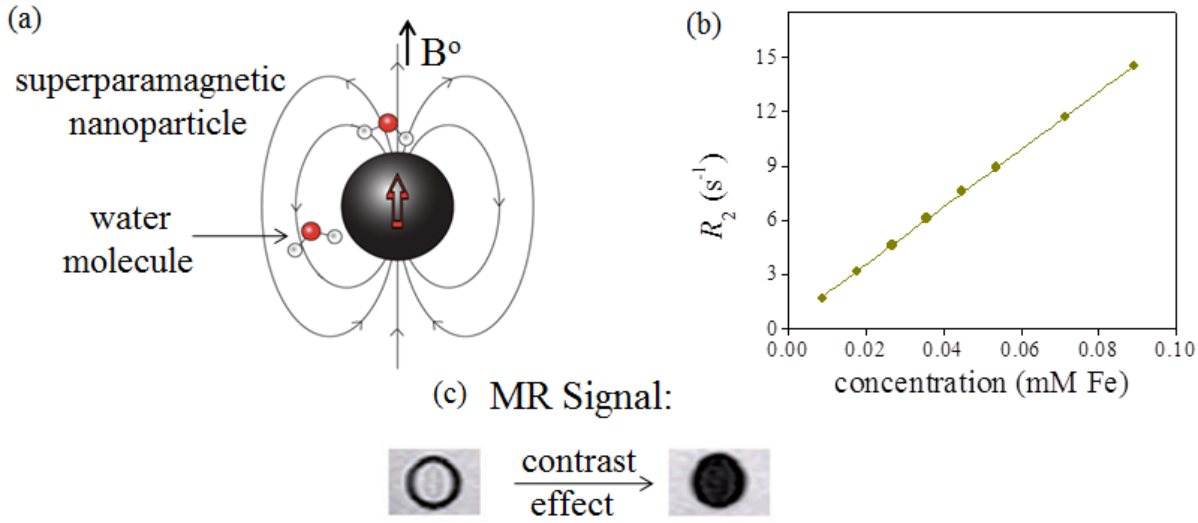

Figure 2.9 (a) The contrast effect of iron oxide arises from its ability to perturb the transverse relaxation of the neighboring water protons. (b) It is common to express the effectiveness of the contrast agent in terms of the transverse relaxivity, r_2, which is the slope of the straight line on a graph of the transverse relaxation rate ($R_2 = 1/T_2$) versus the concentration of magnetic material (mM Fe). (c) The accelerated dephasing of the proton magnetic moments leads to a loss of signal in T_2–weighted MR images giving final image contrast. Adapted from reference [62], Copyright 2008, with permission from John Wiley & Sons. Cheon, J.: Chemical design of nanoparticle probes for high-performance magnetic resonance imaging. *Angew. Chem. Int. Ed.* **2008**, *47*, 5122-5135. Used with permission from with permission from John Wiley & Sons 2013.

2.7.1 Theoretical models of transverse relaxivity

The effect of magnetic nanoparticles on proton transverse relaxation rates has been modeled by several researchers.[63-66] These models are generally categorized into the motional averaging regime, the static dephasing regime and the echo limited regime. Each regime is based on the characteristic time, τ_D, for a water molecule to diffuse a distance of the order of the radius of the magnetic nanoparticles given by:

$$\tau_D = \frac{r^2}{D} \tag{2.4}$$

where *r* is the radius of the field-creating magnetic particle and *D* is the self-diffusion coefficient of water.[67]

2.7.1.1 *Motional averaging regime*

The motional averaging regime dominates when $\tau_D << 1/\Delta\omega$, where $\Delta\omega$ is the spread of Larmor frequencies at the surface of the particle given by:

$$\Delta\omega = \frac{\mu_0 \gamma M}{3} \tag{2.5}$$

where μ_0 is the permeability of free space, γ is the proton gyromagnetic ratio, and M is the magnetic moment per unit volume of the particle. In this regime, protons rapidly diffuse in the inhomogeneous fields created by the magnetic particles and thus experience a wide range of local precession frequencies which are time averaged. The transverse relaxation rate, $(R_2)_{ma}$, is given by:

$$(R_2)_{ma} = \frac{16 f (\Delta\omega)^2 r^2}{45 D} \tag{2.6}$$

where f is the volume fraction of magnetic material.[63]

2.7.1.2 *Static dephasing regime*

The system can be described by the static dephasing regime when $\tau_D > \pi\sqrt{3}/(2\,\Delta\omega)$.[67] In this regime, the NMR signal decay due to the magnetic moment dephasing occurs faster than diffusion phenomena manage to average out the phases of the different protons.[66] Sometimes, this regime is

also known as the slow motion regime or the inhomogeneous broadening regime.[68,69] The transverse relaxation rate, $(R_2)_{sd}$, is then given by:

$$(R_2)_{sd} = \frac{2\pi f \Delta\omega}{\sqrt{27}} \tag{2.7}$$

The relaxation rate in this regime is independent of particle size. $(R_2)_{sd}$ represents the absolute upper limit on R_2 and is proposed to be a good approximation of R_2 when $1/\Delta\omega < \tau_D < 2\tau_{CP}$,[63] where τ_{CP} is half the echo time (τ_{CP} = TE/2).

2.7.1.3 *Echo-limited regime*

When $\tau_D < 2\tau_{CP}$ the refocussing of proton magnetic moments is not efficient (relaxation is not interrupted by refocusing pulses), and R_2 and R_2^* are equivalent. However, when $\tau_D > 2\tau_{CP}$, partial refocusing of the transverse magnetization leads to a decrease in R_2 compared to R_2^*. This regime is known as the echo-limited regime. The transverse relaxation rate in the echo-limited regime, $(R_2)_{el}$, given by:

$$(R_2)_{el} = \frac{7.2 f D x^{\frac{1}{3}} (1.52 + fx)^{\frac{5}{3}}}{d^2} \tag{2.8}$$

where $x = \Delta\omega . \tau_{CP}$.[63]

2.7.2 Effect of structural parameters on transverse relaxivity

Transverse relaxivities of individually-dispersed iron oxide nanoparticles as well as hybrid nanostructures such as block copolymer-stabilized clusters depend on a combination of structural and experimental parameters. These include particle/cluster diameter, magnetization, volume fraction of magnetic material in the particle/cluster, magnetic field strength, and echo time of the pulse sequence. Field strength dependence is not significant for the transverse relaxivity of

susceptibility-based contrast agents if the induced magnetization of the magnetic particle saturates at magnetic fields below ~ 1 T (in accordance with the Langevin function). This is often the case for superparamagnetic magnetite and maghemite nanoparticles, for which r_2 is almost independent of the field strength around clinically relevant magnetic fields. This effect was studied by Bulte et al. for commercially-available contrast agents AMI-25 (Endorem)[70] and MION-46L.[71] On the other hand, r_2 relaxivity is very sensitive to the aforementioned structural parameters. The delineation of structure-relaxivity relationships of T_2 contrast agents therefore requires precise control of these structural parameters, which will be discussed below.

2.7.2.1 *Effect of particle size and magnetization*

The magnetization at saturation of iron oxide nanoparticles increases with increasing particle size. The lower magnetization at smaller particle sizes is attributed to higher fractions of disordered surface spins.[72] As a result, the transverse relaxivity also increases with particle size. Cheon et al. systematically studied the effect of size and magnetization on the T_2 relaxation time by synthesizing monodisperse magnetite nanocrystals in the size range of 4-12 nm.[73] A 3.5-fold reduction in the T_2 relaxation times was observed as the particle size increased from 4 to 12 nm (Figure 2.10).

Fe_3O_4 nanocrystal size (nm)	Magnetization at 1.5 T (emu/g Fe)
4	25
6	43
9	80
12	102

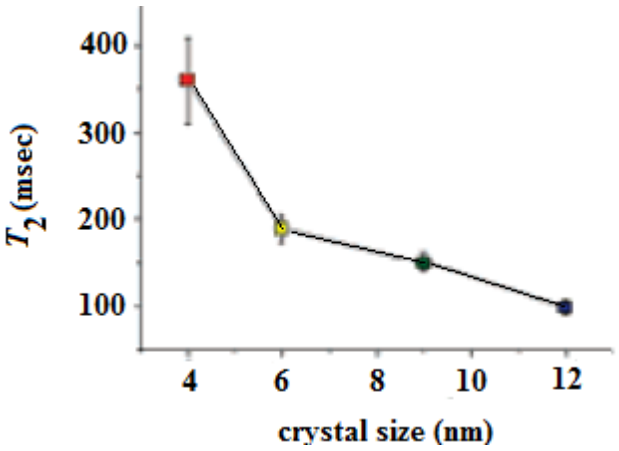

Figure 2.10 The magnetization at saturation of iron oxide nanoparticles increases with increasing particle size. Figure reproduced from reference [73], Copyright 2005, with permission from American Chemical Society. Jun, Y. W.; Huh, Y. M.; Choi, J. S.; Lee, J. H.; Song, H. T.; Kim, S.; Yoon, S.; Kim, K. S.; Shin, J. S.; Suh, J. S.; Cheon, J.: Nanoscale size effect of magnetic nanocrystals and their utilization for cancer diagnosis via magnetic resonance imaging. *J. Am. Chem. Soc.* **2005**, *127*, 5732-5733. Used with permission from American Chemical Society 2013.

In another study, the magnetization of maghemite nanoparticles of mean diameters 6, 8, 10, 11 and 13 nm at 1.4 T were 13, 23, 33, 42 and 63 emu g^{-1}, respectively. The transverse relaxivities increased from 13 s^{-1} mM Fe^{-1} for the 6 nm particles to 254 s^{-1} mM Fe^{-1} for the 13 nm particles.[74]

2.7.2.2 *Effect of particle aggregation*

Aggregates of magnetic nanoparticles in suspension cause a greater reduction in T_2 than the primary nanoparticles. This decrease in T_2 on aggregation can be related to either an increase in average particle size within the motional averaging regime (MAR), where T_2 is proportional to $1/r^2$ or with a larger fraction of the particle size distribution located within the static dephasing regime (SDR), where R_2 has its maximum value and is independent of r (Figure 2.11).

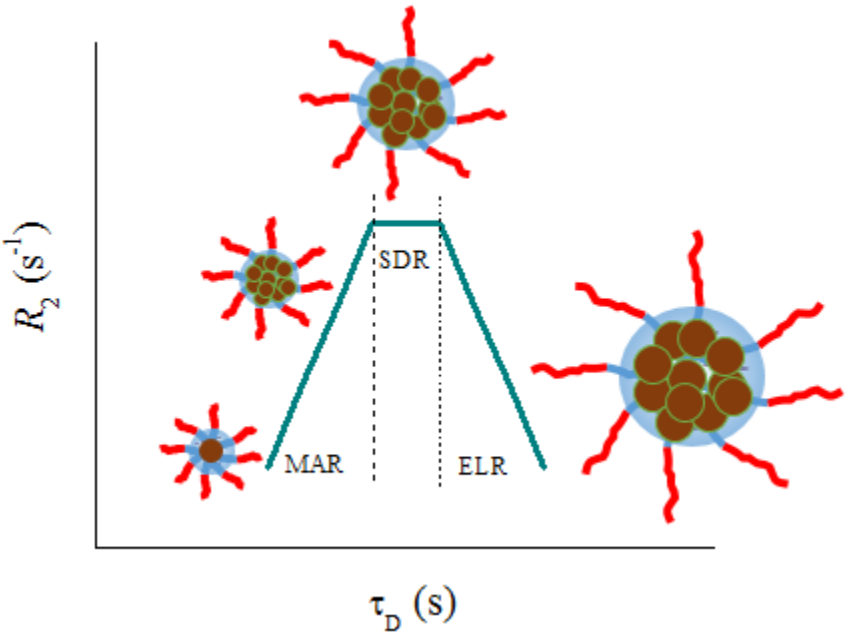

Figure 2.11. Aggregates of magnetic nanoparticles in suspension cause a greater reduction in T_2 than the primary nanoparticles. [τ_D : proton diffusion time = (particle diameter)^2/4D].

The design of well-defined aggregates with control over size distributions and compositions is important. Most hybrid magnetic nanoparticle-polymer systems designed for T_2 MRI contrast applications are comprised of broad particle size distributions. Both the motional averaging and echo-limited regimes reduce the maximum achievable r_2 for a particle system. For iron oxide nanoparticles of a certain size and magnetization, the transverse relaxivity of controlled clusters can be maximized when the size distributions are tailored to be narrow and located entirely within the static dephasing regime.

Besides sensitive imaging, increase in transverse relaxation rates due to aggregation of magnetic nanoparticles has also been exploited for monitoring of biological activity and to report on biochemical processes. Osborne et al. have reported "smart" T_2 contrast agents based on dextran sulfate-coated iron oxide nanoparticles derivatized with a light-sensitive molecule (spiropyran).[75]

Conformational switching of the spiropyran between hydrophilic and hydrophobic isomers, in response to light irradiation, resulted in reversible aggregation of the nanoparticles with ~33% difference in the T_2 relaxation times of the dispersed nanoparticles and the aggregates. Weissleder and co-workers developed an *in vitro* MRI probe that employs cross-linked iron oxide nanoparticles functionalized with DNA sequences. Upon recognition of a complementary oligonucleotide, the nanoparticles aggregate into clusters leading to reduced T_2 relaxation times. The process was reversible through the action of a DNA-cleaving enzyme that separated the clusters into the constituent nanoparticles.[76] Schellenberger et al. have described protease-specific T_2 contrast agents comprised of peptide-poly(ethylene oxide) copolymers adsorbed on citrate-coated iron oxide nanoparticles.[77] The action of matrix metalloproteinase 9 led to cleavage of the peptide-poly(ethylene oxide) copolymer, resulting in irreversible aggregation and higher r_2. Recently, an aptamer-based biosensor for protein detection has been demonstrated that utilizes changes in T_2 upon recognition of the analyte (lysozyme).[78] In this example, clusters with short T_2 were initially formed by magnetic nanoparticles conjugated with either a lysozyme aptamer or a DNA linker. Exposure to the lysozyme caused disassembly of the clusters due to preferential binding and longer T_2.

2.7.3 Experimental validation of theoretical models of transverse relaxivity

The theoretical relaxation regimes, namely the motional averaging, static dephasing and the echo-limited regimes, have been experimentally verified by some researchers. In the first such experimental confirmation, Roch et al. induced agglomeration of dextran-coated magnetite particles by progressively destroying the polymer coating with acid.[67] They observed a gradual increase in transverse relaxivity due to clustering, followed by a plateau and subsequent decrease, consistent with the motional averaging, static dephasing and echo-limited regimes, respectively.

Recent works have provided further confirmation of the theoretical models through the synthesis of controlled magnetite clusters. Poselt et al. described controlled clusters in the size range of 30-200 nm using primary magnetite nanocrystals 4-13 nm in diameter. They showed that the maximum achievable relaxivity increased as the size of the individual magnetite nanocrystal increased. Furthermore, the cluster relaxivities showed evidence of all the three relaxation regimes. A similar trend was observed in the work of Xu et al. who also synthesized controlled clusters in the hydrodynamic size range of 30-200 nm.[79] They observed that the r_2 initially increased with cluster size, reached a maximum value of 650 s^{-1} mM Fe^{-1} at a size of 97 nm, and gradually decreased at higher sizes. It should be noted that these clusters were only stabilized with polyacrylic acid, and are therefore hydrophilic.

Although the above observations provide some insights into the design of controlled clusters with tailored sizes, quantitative agreement between the experimental relaxivities and the theoretical model predictions has remained a challenge. This can be attributed to the considerable size polydispersities characteristic of most particle systems, resulting in a distribution of particles across the relaxation regimes. In one study, a comparison between experimental r_2 and analytical model predictions was made for nanoparticles comprised of polymethacrylate-based microgels that contained iron oxide.[80] The predictions were based on the average particle sizes measured by dynamic light scattering and only semi-quantitative agreement was found. Carroll et al. showed that the theoretical models can be used to quantitatively predict the transverse relaxivities of predominantly individual maghemite nanoparticles in the size range of 6-13 nm.[74] They determined the theoretical transverse relaxivities by integrating over a lognormal distribution of sizes that included the relaxation rates for the three R_2 regimes. The size distribution derived from small-angle X-ray scattering (SAXS) was found to be a good predictor of relaxivities as it

accounted for the presence of aggregates in suspension. This study demonstrates the importance of characterizing the entire size distribution of the particle system and factoring it in the calculation of theoretical relaxivities.

Vuong et al. have recently developed an empirical model to predict the transverse relaxivities of single and clustered magnetic nanoparticles based on the motional averaging model.[81] They based their findings on data derived from the literature for magnetic particles and clusters in a range of morphologies – individually dispersed maghemite nanoparticles, maghemite core-silica shell nanoparticles, clusters of magnetite and maghemite nanoparticles stabilized by hydrophilic and amphiphilic polymers, and nanoparticles embedded within the membrane of lipid or polymer vesicles.[81] For hybrid nanostructures such as iron oxide-block copolymer clusters, they incorporated the intra-aggregate volume fraction of iron oxide (φ_{intra}) into the empirical equation and found the following relationship between the particles parameters and the r_2 relaxivity:

$$\frac{r_2 \times \varphi_{intra}}{{M_v}^2} = 11.6 \times 10^{-12} d^2 \qquad (2.9)$$

where M_v is the magnetization of the particle/aggregate, and d is the hydrodynamic diameter of the particle/aggregate. This prediction, however, is only valid for individual nanoparticles and clusters obeying the motional averaging condition of $\Delta\omega . \tau_D < 1$.

2.8 Controlled clusters of iron oxide nanoparticles

The synthesis of controlled clusters of iron oxide nanoparticles is a better strategy for the design of sensitive T_2 contrast agents than increasing the size of the primary nanoparticles, as the latter would result in the loss of superparamagnetic characteristics when the particle size exceeds ~ 20 nm. Higher MRI contrast efficiency through controlled clustering can be attributed to either an

increase in average size, via clustering, that leads to higher r_2 values within the motional averaging regime, or due to a larger fraction of the cluster size distribution being within the static dephasing regime, where r_2 reaches its maximum value.

Several groups have reported the fabrication of controlled magnetic nanoparticle clusters. The common design feature in all these works has been the stabilization of the clusters with block copolymers – mostly amphiphilic block copolymers, and, in a few cases, doubly hydrophilic block copolymers. Berret et al. first reported block copolymer-stabilized maghemite nanoparticle clusters.[82] They used a poly(trimethylammonium ethylacrylate)-poly(acrylamide) (PTEA-*b*-PAM) cationic-neutral block copolymer to complex citrate-coated maghemite nanoparticles synthesized by the alkaline coprecipitation of iron salts. An r_2 increase from 39 s^{-1} mM Fe^{-1} for the citrate-coated γ-Fe_2O_3 nanoparticles to 162 s^{-1} mM Fe^{-1} for the PTEA(11k)-*b*-PAM(30k)-stabilized clusters was noted.

Several works employed amphiphilic block copolymers comprised of poly(ethylene oxide) and biodegradable poly(D,L-lactide),[83] poly(lactide-*co*-glycolide),[84] or poly(caprolactone)[85] to load hydrophobically-modified Fe_3O_4 nanoparticles synthesized using the thermal decomposition method. In these systems, the iron oxide nanoparticles were clustered within the hydrophobic block through hydrophobic interactions. For example, Ai et al. loaded 4 nm, 8 nm, and 16 nm hydrophobic Fe_3O_4 nanoparticles into 5k-poly(caprolactone)-5k-poly(ethylene oxide) block copolymer micelles using the solvent evaporation method (described in section 2.9.4.3). They achieved size and composition control for the clusters by varying the size of the primary nanoparticles, and noted an increase in the r_2 relaxivities with increasing cluster size and magnetite loading.[85] The hydrodynamic sizes, iron oxide loadings and transverse relaxivities obtained for these systems are tabulated in Table 2.1 below. Poselt et al. have reported the controlled clustering

of Fe_3O_4/γ-Fe_2O_3 nanocrystals in the size range of 4-13 nm within 0.7k-poly(ethyleneimine)-0.9k-poly(caprolactone)-2k-poly(ethylene oxide) triblock copolymer micelles.[86] They showed that the maximum achievable relaxivity at 1.41 T increased in the range of 200-500 s^{-1} mM Fe^{-1} with increasing primary nanocrystal diameter.

Table 2.1 Controlled iron oxide-block copolymer nanoparticle clusters

Reference Copolymer stabilizer	Magnetic material	φ_{IO}*	Size (nm)	Method	Transverse Relaxivity, (s^{-1} mM Fe^{-1})	
Berret et al. PTEA(11k)-*b*-PAM(30k)	6.3 nm γ-Fe_2O_3	0.38	170	DLS	162	(0.47 T)
Yang et al. PLGA(5k)-*b*-PEG(3.4k)	8 nm Fe_3O_4	0.12	73	TEM	333	(1.5 T)
Ai et al.	4 nm Fe_3O_4	0.05	75	DLS	169	(1.5 T)
PCL(5k)-*b*-PEG(5k)	8 nm Fe_3O_4	0.11	97		318	
	16 nm Fe_3O_4	0.19	110		471	
Xie et al.	6 nm Fe_3O_4	0.12	58	DLS	117	(1.41 T)
PLA(2.5k)-*b*-PEG(5k)		0.20	73		234	
			95		363	
			97		413	
			144		458	
			199		512	

*Volume fraction of magnetic material (iron oxide) in the cluster

Xu et al. have described the size-controlled synthesis of carboxyl-functionalized magnetite nanocrystal clusters using a one-pot polyol process.[79,87] In this method, an iron precursor

($FeCl_3.6H_2O$) is heated in diethylene glycol in the presence of urea and polyacrylic acid at 200°C in an autoclave. The reaction produces magnetite nanoparticle clusters stabilized by polyacrylic acid, wherein some of the carboxylate groups of the polymer are adsorbed on the iron oxide surface, and the remaining provide stabilization to the clusters in suspension.[88] They reported r_2 relaxivities (at 1.41 T) of 240, 540, 650, 495, 455, and 305 s^{-1} mM Fe^{-1} at clusters sizes (by DLS) of 29, 59, 97, 133, 157, and 206 nm, respectively. The r_2 value of 650 s^{-1} mM Fe^{-1} is the highest reported relaxivity at 1.41 T so far.

Clusters with high r_2 relaxivities encased within hydrogel coatings have also been reported.[89] The hydrogel was comprised of a random copolymer of *N*-isopropylacrylamide, *N*,*N*'-methylene-bis-acrylamide and acrylic acid, affording pH responsivity to the clusters. The thickness of the hydrogel coating was varied by controlling the ratio of iron oxide nanoparticles to monomers. It was shown that the r_2 relaxivities correlated with the thickness of the coating, with r_2 increasing with the hydrogel coating thickness. A maximum r_2 value of 505 s^{-1} mM Fe^{-1} was obtained at neutral pH and 3 T at a coating thickness of 54 nm. Notably, the iron oxide loading was only 8 wt%. The high relaxivities in the presence of the hydrogel coating were attributed to the slower diffusion (and higher residence time) of water molecules near the magnetic cluster cores. This enhancement should, however, only be attributed to clusters within the motional averaging regime where the transverse relaxation rate is directly proportional to the diffusion time of protons around the magnetic particle (2.7.1.1). For clusters within the echo-limited regime, the coating would reduce the relaxation rate, whereas in the static dephasing regime, the relaxation rate would be unaffected by the coating.[90]

The above examples are for predominantly spherical clusters of iron oxide nanoparticles. Elongated clusters with a wormlike architecture have also been described. Park et al. have reported

'nanoworms' synthesized by a method similar to that used for conventional dextran-coated iron oxide nanoparticles.[91] The wormlike morphology was apparently the result of higher concentrations of iron salts and higher molecular weight of the dextran polymer during synthesis. The 50-80 nm linear aggregates consisted of 5-10 iron oxide cores and had higher transverse relaxivities (116 s^{-1} mM Fe^{-1}) than the 30 nm dextran-coated nanospheres (70 s^{-1} mM Fe^{-1}) at 4.7 T. Recently, Gossuin et al. have reported the NMR relaxation and magnetic properties of maghemite nanoworms.[92] It is noteworthy that elongated aggregates of iron oxide nanoparticles functionalized with targeting peptides can be internalized better by tumor cells than the spherical aggregates. Furthermore, such elongated clusters have been shown to exhibit lower uptake by the mononuclear phagocytic system (MPS) and as a result, prolonged blood half-life relative to spherical shapes.[91]

The formulation of controlled clusters with high transverse relaxivities is aimed at maximizing the MRI sensitivity. Gao and co-workers have defined sensitivity as the lowest concentration of the clusters (iron oxide + block copolymer) in aqueous suspension that produce a 50% decrease in the MRI signal intensity of pure water on a T_2-weighted MR image.[85] In their study, clusters of 16 nm magnetite nanoparticles encapsulated within 5k-PCL-*b*-5k-PEO micelles had a sensitivity of 5.2 μg mL^{-1} corresponding to an r_2 value of 471 s^{-1} mM Fe^{-1}. When r_2 decreased to 318, 169, and 25 s^{-1} mM Fe^{-1}, the minimum concentration increased to 6.9, 21, and 450 μg mL^{-1}, respectively.

2.9 Multifunctional magnetic nanoparticles

The integration of magnetic nanoparticle clusters and therapeutic molecules by their co-encapsulation into polymeric nanocarriers paves the way for 'theranostic' nanoparticles with high relaxivities for sensitive MRI and therapeutically-useful drug loadings. The rational design of such multifunctional nanoparticles is important for the delivery of drugs and for the simultaneous

monitoring of their biodistribution *in vivo*. To this end, various macromolecular architectures have been utilized, among which amphiphilic block copolymers are noteworthy owing to their unique nanoscopic characteristics. The core-shell structure of block copolymer micelles provides a viable means for the solubilization of poorly water-soluble drugs and hydrophobically-modified imaging agents (Figure 2.12). While the hydrophilic shell imparts steric stability and may possess targeting ligands, the core-forming polymer allows for drug incorporation through physical entrapment.

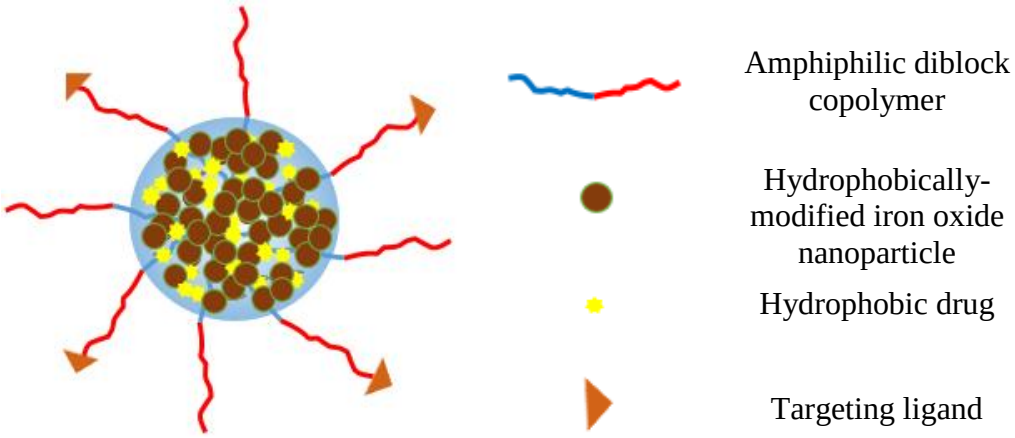

Figure 2.12 Schematic of a multifunctional magnetic nanoparticle.

2.9.1 Core-forming hydrophobic polymers

A variety of hydrophobic polymers have been explored for the encapsulation of hydrophobic drugs and imaging agents through physical entrapment. The compatibility between the hydrophobic ingredients and the polymer, and the hydrophobicity of the polymer are important design considerations. The greater the polymer hydrophobicity, the lower is the critical micelle concentration (*cmc*), and higher the micelle stability. This is important in view of the extreme dilutions encountered under *in vivo* conditions. The most commonly used polymers for drug/imaging agent encapsulation and controlled release applications include biocompatible and biodegradable polymers such as poly(lactide), poly(lactide-*co*-glycolide), poly(caprolactone), N-

(2-hydroxypropyl)-methacrylate copolymers (HPMA) and poly(amino acids). Figure 2.13 shows the chemical structures of some of these polymers.

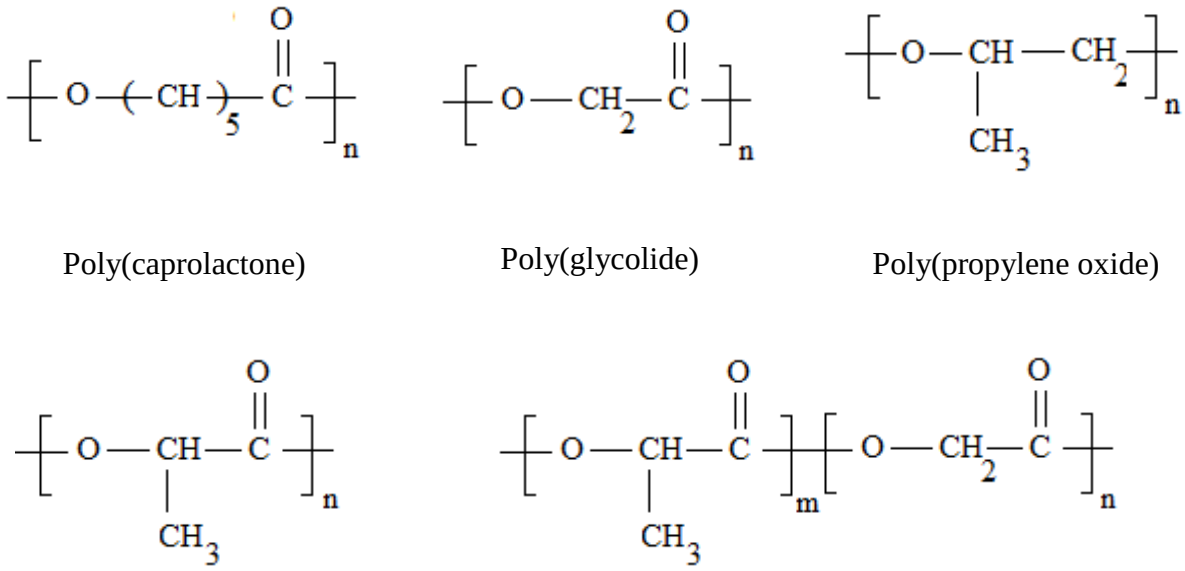

Poly(caprolactone) Poly(glycolide) Poly(propylene oxide)

Poly(lactide) Poly(lactide-*co*-glycolide)

Figure 2.13 Chemical structures of commonly used hydrophobic polymers for encapsulation of hydrophobic drugs and imaging agents.

Amphiphilic copolymers based on poly(propylene oxide) (PPO), such as the commercially-available Pluronic® copolymers, are one of the most widely investigated materials for drug delivery.[93] Although PPO is non-biodegradable, copolymer chains in the molecular weight range of 10-15 kg mol^{-1} have been shown to be eliminated from the bloodstream through renal filtration.[94] However, susceptibility to micelle dissociation due to the relatively higher *cmc*s of PPO is a cause for concern.[95] Biodegradable, aliphatic polyesters such as poly(lactide) (PLA) and poly(caprolactone) (PCL) overcome the limitations of poly(propylene oxide). PCL is a semi-crystalline polymer that has been shown to have higher stability and drug-loading capacity than PPO.[96] Poly(lactide) was first investigated as a hydrophobic drug carrier by Gref et al.[97] The lactide

monomer exists in the form of two stereoisomers – D-lactide and L-lactide. The form of poly(lactide) most widely used for encapsulation of hydrophobic actives is the racemic mixture of the D- and L-stereoisomers – poly(D,L-lactide) (PDLLA).

2.9.2 Poly(ethylene oxide)

The nearly universal use of poly(ethylene oxide) as the hydrophilic polymer to stabilize the nanoparticles is in contrast to the variety of hydrophobic polymers used to encapsulate the active ingredients. It has been demonstrated that the circulation half-lives of polymeric nanoparticles can be dramatically increased by copolymerizing many of the hydrophobic polymers in Figure 2.13 with poly(ethylene oxide), a biocompatible polymer approved by the FDA for clinical applications.[44,97-99] Diblock copolymers with PEO have been studied in terms of nanoparticle formation,[100-102] drug loading,[103,104] and biocompatibility.[105]

The length and conformation of the PEO chains forming the corona are important considerations for nanoparticle design. The PEO conformation can be described in terms of the Flory radius which depends on the number of ethylene oxide repeat units and the length of one repeat unit (3.5 Å for PEO).[44] When the distance between adjacent polymer attachment points on the surface of the core is less than the Flory radius (high chain density), the polymer assumes a brush conformation with thin, long bristles of PEO extending out of the nanoparticle core. Nanoparticles with a PEO brush have long circulation times as the dense coatings better shield the nanoparticles from the mononuclear phagocytic system. Gref et al. performed an elegant study of the influence of the PEO corona length and brush density on phagocytic uptake and plasma protein adsorption.[106] They found maximum reduction in protein adsorption at a PEO molecular weight of 5000 g mol^{-1} and a chain footprint of 2.1 nm^2 corresponding to a distance of 1.4 nm between two terminally-attached PEO chains in the brush.

2.9.3 'Theranostic' magnetic nanocarriers

Block copolymers comprised of biodegradable hydrophobic blocks and poly(ethylene oxide) have been employed to simultaneously encapsulate hydrophobically-modified iron oxide nanoparticles and poorly water soluble drugs. Most of these works have focused on anti-cancer chemotherapeutics, notably doxorubicin (DOX). Table 2.2 shows the hydrodynamic size, drug and magnetite loadings, and transverse relaxivities reported for block copolymer micelles co-encapsulating doxorubicin in the uncharged, freebase form and magnetite nanoparticles.

Table 2.2 Amphiphilic block copolymer micelles co-encapsulating drug and magnetite nanoparticles

Reference Copolymer stabilizer	Doxorubicin loading	MRI probe (wt %)	Size (nm)	r_2 (s^{-1} mM Fe^{-1})
Yang et al.[84] PLGA(5k)-*b*-PEG(3.4k)	3.5 wt%	Fe_3O_4 (40.9 %)	73	333 (1.5 T)
Nasongkla et al.[107] PLA(4k)-*b*-PEG(3.2k)	2.7 wt%	8 nm Fe_3O_4 (6.7 %)	46	
Guthi et al.[108] PLA(5k)-*b*-PEG(5k)	5.0 wt%	8 nm Fe_3O_4 (11.6 %)	48	407 (1.4 T)

The above works employed biodegradable poly(D,L-lactide)[107,108] or poly(D,L-lactide-*co*-glycolide)[84,109,110] for the encapsulation of the active ingredients, and end-functionalized poly(ethylene oxide) for cancer cell targeting. Jain et al. loaded 8.2 wt% doxorubicin in Pluronic® stabilized-oleic acid coated-iron oxide nanoparticles wherein the drug was held in the oleic acid shell through hydrophobic interactions.[111]

Multifunctional magnetic nanoparticles based on polymer vesicles have also been reported. A pH sensitive vesicle of 1k-poly(ethylene oxide)-*co*-12.5k-poly(2-diisopropylamino-ethyl aspartate) has been described wherein doxorubicin (5.8 wt%) and iron oxide nanoparticles (8.2 wt%) were

encapsulated in the aqueous core of the vesicle.[112] The transverse relaxivity was 214 s^{-1} mM Fe^{-1} at 1.5 T and room temperature. Gong and co-workers have described polymeric vesicles formed by heterobifunctional triblock copolymers – 5k-folate-PEG-*b*-37k-poly(glutamate)-*b*-2k-PEG acrylate[113] and 5k-folate-PEG-*b*-21k-poly(D,L-lactide)-*b*-2k-PEG acrylate[114] – where hydrophilic iron oxide nanoparticles were incorporated in the inner core formed by the PEG acrylate and doxorubicin was loaded in the hydrophobic polyglutamate or polylactide membrane. A DOX loading of 14 wt % and transverse relaxivity of 346 s^{-1} mM Fe^{-1} (4.7 T) were achieved at a loading of 46 wt% iron oxide.[113]

2.9.4 Fabrication of multifunctional magnetic nanoparticles

2.9.4.1 *Oil-in-water emulsion*

The preparation of polymeric nanoparticles co-encapsulating drugs and magnetic nanoparticle imaging agents can be achieved by the oil-in-water (single emulsion) emulsification technique. In this technique, the polymer carrier (e.g. PLGA) and the hydrophobic actives are dissolved in a volatile, water-immiscible organic solvent such as dichloromethane or chloroform. The organic phase is added to the aqueous phase containing a surfactant (e.g. poly(vinyl alcohol)) and emulsified by sonication or homogenization. This leads to the formation of nanosize droplets containing the active agents and the polymer encapsulant dispersed in the aqueous phase stabilized by the surfactant which assembles at the solvent-water interface. The organic phase is then allowed to evaporate, resulting in the formation of nanoparticles. Moderate loadings of magnetite and drug have been reported with this method. For example, Yang et al. have reported PLGA nanoparticles prepared using the single emulsion method encapsulating 23 wt % magnetite nanoparticles, and 6 wt % doxorubicin with an encapsulation efficiency of 68%.[115] Unlike solvent evaporation (described in the next section 1.9.4.3), no details were provided about whether the organic phase

was added slowly or dropwise. Even though TEM and DLS results were shown, no quantitation of the size distribution was presented either in the form of a TEM-based distribution function or PDI values calculated from DLS. The polydispersities are claimed to be low but there are no reported numerical values.

2.9.4.2 *Water-in-oil-in-water (double) emulsion*

This method is used for the encapsulation of hydrophilic drugs and/or imaging agents typically to form vesicles. The hydrophilic active agent is dissolved in a small volume of aqueous phase, added to the organic phase containing the copolymer, and emulsified. This water-in-oil emulsion is then dispersed in a large volume of aqueous phase containing a suitable surfactant, such as poly(vinyl alcohol), to form the water-in-oil-in-water double emulsion. The organic solvent is finally evaporated resulting in the formation of nanoparticles. This method leads to larger nanoparticles relative to the single emulsion method, and moderate drug loadings and encapsulation efficiencies. This method was used to form the vesicles loaded with magnetite and doxorubicin reported earlier by Gong *et al*. [113,116]

2.9.4.3 *Solvent evaporation*

In the solvent evaporation method, the copolymer and the actives are dissolved or dispersed in a water-miscible organic solvent. The solvent is usually one of high water miscibility such as tetrahydrofuran. This organic phase is added dropwise into the aqueous phase under vigorous ultrasonic agitation. The organic solvent is removed over a period of hours with concomitant copolymer self-assembly and encapsulation of the actives. This method was used to form nanoparticles loaded with hydrophobically modified magnetite and doxorubicin in the freebase form in a PEG-PLA micelle reported earlier.[107] Numerical values of polydispersity were not reported.

2.9.4.4 *Rapid precipitation*

The emulsification and solvent evaporation techniques have several limitations including low drug loadings and low encapsulation efficiencies at high drug loadings. Furthermore, they require stabilizing surfactants and several purification steps. Most of the existing reports of drug and magnetite co-encapsulation into block copolymer carriers (Table 2.2) utilize the emulsion and solvent evaporation techniques for nanoparticle formation leading to only modest drug loadings (< 10 wt %).

The limitations of the emulsion/solvent evaporation methods can be overcome by employing kinetically-controlled processes of nanoparticle preparation.[117] Prud'homme and co-workers have reported extensively on the preparation of kinetically-assembled block copolymer nanoparticles containing drugs, imaging agents, peptides, and targeting ligands.[101,118-124] They termed this method 'flash nanoprecipitation'. In this method, a water-miscible organic stream containing the active ingredients and a block copolymer stabilizer is rapidly combined with one or more streams of water in a continuous mixer to produce kinetically-trapped nanoparticles, as illustrated in Figure 2.14. The rapid mixing creates high supersaturations of the drug and/or imaging agent leading to nucleation and growth, whereby size is controlled by copolymer self-assembly. This process is scalable and has been used to produce stable nanoparticles with sizes in the range 20-500 nm and controlled size distributions.

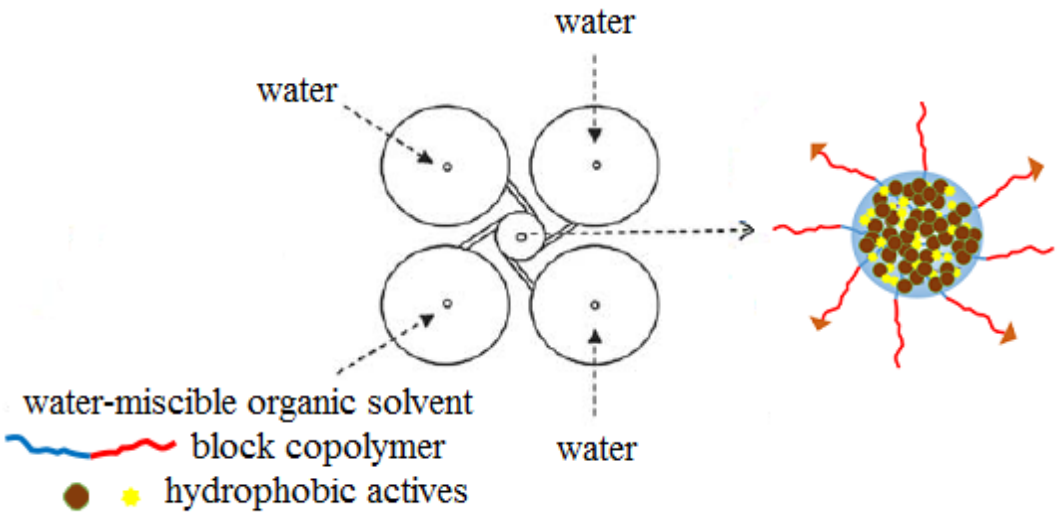

Figure 2.14 Schematic of the rapid precipitation process for the fabrication of block copolymer-stabilized multifunctional nanoparticles using a multi-inlet vortex mixer. Adapted from reference [101], Copyright 2008, with permission from American Chemical Society. Gindy, M. E.; Panagiotopoulos, A. Z.; Prud'homme, R. K.: Composite block copolymer stabilized nanoparticles: simultaneous encapsulation of organic actives and inorganic nanostructures. *Langmuir* **2008**, *24*, 83-90. Used with permission from American Chemical Society 2013.

In this process, particle size can be controlled by controlling the supersaturation. The particle size depends on the rate of nucleation, J, according to:

$$J \propto \exp\left(\frac{-16\pi\gamma^3 v^2}{3{k_B}^3 T^3 (\ln S)^2}\right) \tag{2.10}$$

where γ is the solid-liquid interfacial tension of the solute, v is the molar volume of the solute, and S is the supersaturation ratio given by:

$$S = \frac{c}{c_\infty} \tag{2.11}$$

In eq 2.11, c is the concentration of the solute in the final solvent mixture after the rapid mixing process, and c_∞ is the bulk solubility in the final solvent mixture.[125] Supersaturations as high as

1000 can be achieved on the order of milliseconds to induce rapid precipitation of all hydrophobic components with the formation of nanoparticles.[126]

The rapid precipitation technique has been employed by the Prud'homme group to develop nanoparticles of hydrophobic drugs. The key to the formation of stable nanoparticles with high drug loadings by this technique is believed to be the creation of rapid and uniform supersaturation over a timescale of milliseconds.[122] While high supersaturations are readily achieved with very hydrophobic drugs, for drugs that are not sufficiently hydrophobic, the supersaturation needs to be increased by modifying the hydrophobicity to enable the formation of nanoparticles. To effect higher drug hydrophobicities and supersaturations, ionic complexation or covalent conjugation with a hydrophobic anchor to form a "prodrug" have been proposed.[122,127] The overall stability of the nanoparticles depends on several factors such as the state of the drug (amorphous or crystalline), the interaction energy between the drug and the hydrophobic block of the copolymer, and the glass transition temperature of the hydrophobic block.[120,128]

2.10 Antiretroviral drugs for treating HIV infection

The central nervous system represents one of the major anatomical reservoirs for HIV-1, and the replication of the virus in the brain leads to a range of neurological disorders. Currently, over twenty antiretroviral drugs have been approved in the United States and are classified as nucleoside reverse transcriptase inhibitors (NRTIs), non-nucleoside reverse transcriptase inhibitors (NNRTIs), protease inhibitors (PIs), fusion inhibitors (FIs), and integrase strand transfer inhibitors (ISTIs).[129] Although highly active antiretroviral drugs are known to reduce disease severity, there is still a lack of effective treatment for HIV-associated neurocognitive disorders. This problem has been attributed, to a large extent, to the poor permeability of antiretroviral drugs across the blood-

brain barrier, which owing to its physical structure, presence of efflux pumps, and higher expression of metabolizing enzymes, acts as a major physiological barrier against drug entry.[130]

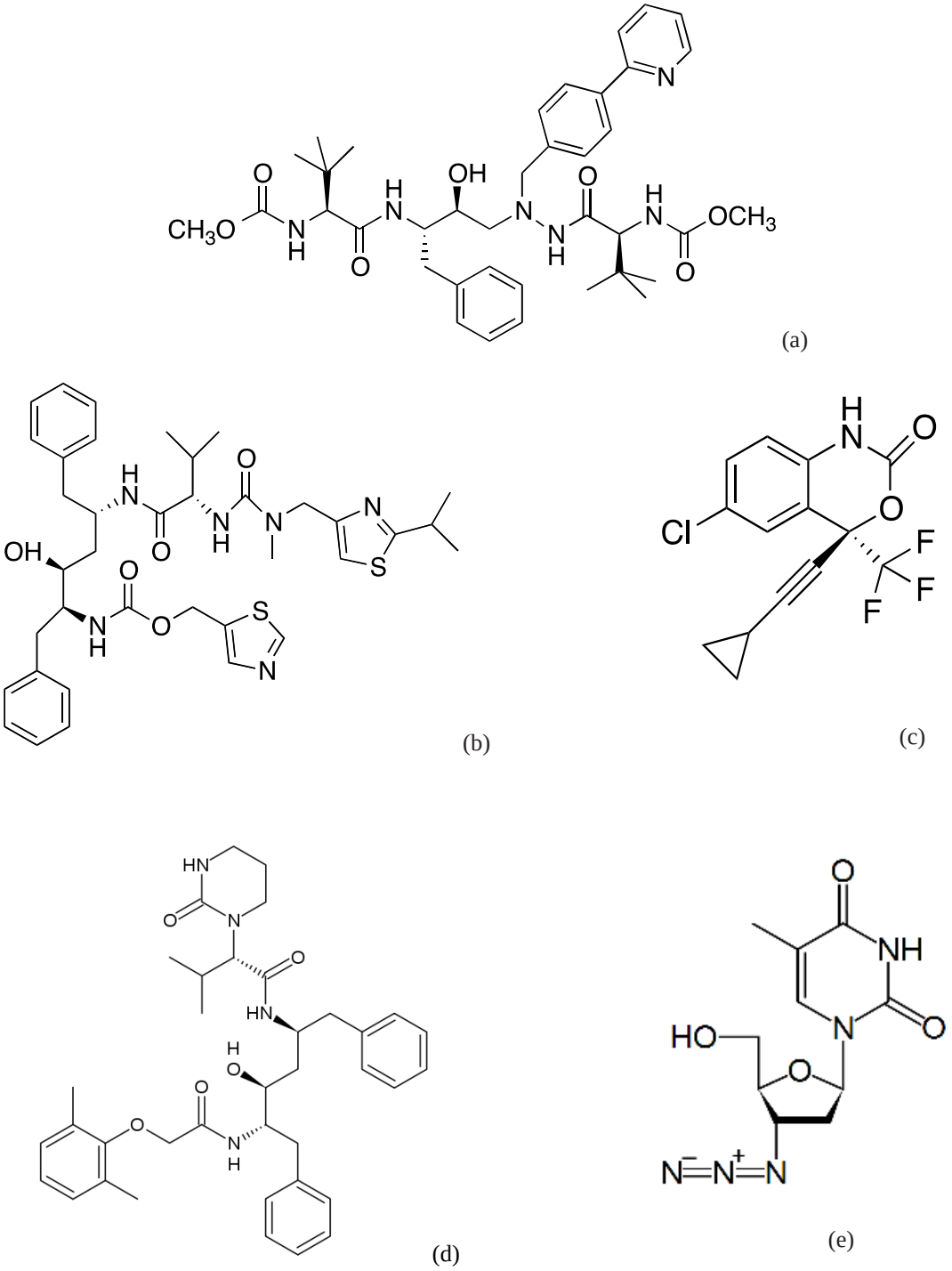

Figure 2.15 Chemical structures of common antiretroviral drugs - (a) atazanavir (ATV), (b) ritonavir (RTV), (c) efavirenz (EFV), (d) lopinavir (LPV), and (e) zidovudine (AZT).

Based on several basic and preclinical studies, it has been posited that nanoparticle-based drug delivery systems have tremendous potential for targeting antiretroviral drugs to the brain.[131] To this end, several nanoparticle formulations of antiretroviral drugs and their therapeutic efficacies have been reported. Most of these works utilized commercially-available Pluronic® copolymers, or biodegradable PLA and PLGA to encapsulate antiretroviral drugs (Table 2.3). Some of these works demonstrated the potential of the nanoformulations to deliver antiretroviral drugs across the blood-brain barrier (BBB). Kuo et al. described nanoformulations of stavudine (NRTI), delavirdine (NNRTI) and saquinavir (PI) encapsulated within poly(butylcyanoacrylate) (PBCA) and methylmethacrylate-sulfopropylmethacrylate (MMA-SPM).[132] Enhanced permeability across an *in vitro* BBB model was observed for all the drugs – by 12-16 folds with PBCA, and by 3-7 folds with MMA-SPM. Rao et al. have shown that trans-activating transcriptor (TAT)-peptide conjugated poly(lactide) nanoparticles bypass the efflux action of P-glycoprotein and enhance the transport of the encapsulated ritonavir across the BBB.[133] These are promising results for the development of antiretroviral drug nanoparticles. However, well-defined nanoparticles with controlled drug compositions and particle sizes have not been demonstrated. This could be attributed to the emulsification/solvent evaporation techniques employed for the nanoparticle preparation, which as noted earlier in Section 2.9.4, suffer from several limitations, namely, inadequate control over particle sizes and compositions.

Table 2.3 Nanoparticle formulations of antiretroviral drugs

Reference	Antiretroviral drug	Polymer stabilizer	Nanoparticle preparation technique	Particle size/PDI/drug loading (wt%)
Mainardes et al.[134]	zidovudine	PLA PLA/PEG 1:1 blend	Double emulsion/solvent evaporation	PLA: 266 nm, PDI 0.31 PLA/PEG: 374 nm, PDI 0.40
Destache et al.[135]	ritonavir + lopinavir + efavirenz	PLGA	Double emulsion/solvent evaporation	262 nm, 4.9% RTV, 5.2% LPV, 1.9% EFV
Rao et al.[133]	ritonavir	PLA	Emulsion/solvent evaporation	300 nm, PDI 0.1, 18.3% RTV
Chattopadhyay et al.[136]	atazanavir	Pluronic® F68	Emulsion	167 nm, PDI 0.16, 4.5% ATV
Nowacek et al.[137]	atazanavir ritonavir efavirenz indinavir	Poloxamer® P188	Wet-milling	ATV: 281 nm, PDI 0.29 RTV: 347 nm, PDI 0.24 EFV: 311 nm, PDI 0.27 IDV: 302 nm, PDI 0.26

The integration of magnetic nanoparticles and antiretroviral drugs in suitable polymeric carriers holds promise for site-specific delivery of these drugs, thereby improving therapeutic efficacies. Figure 2.16 shows a schematic illustration of magnetic field-activated delivery of antiretroviral drugs in the brain.[138]

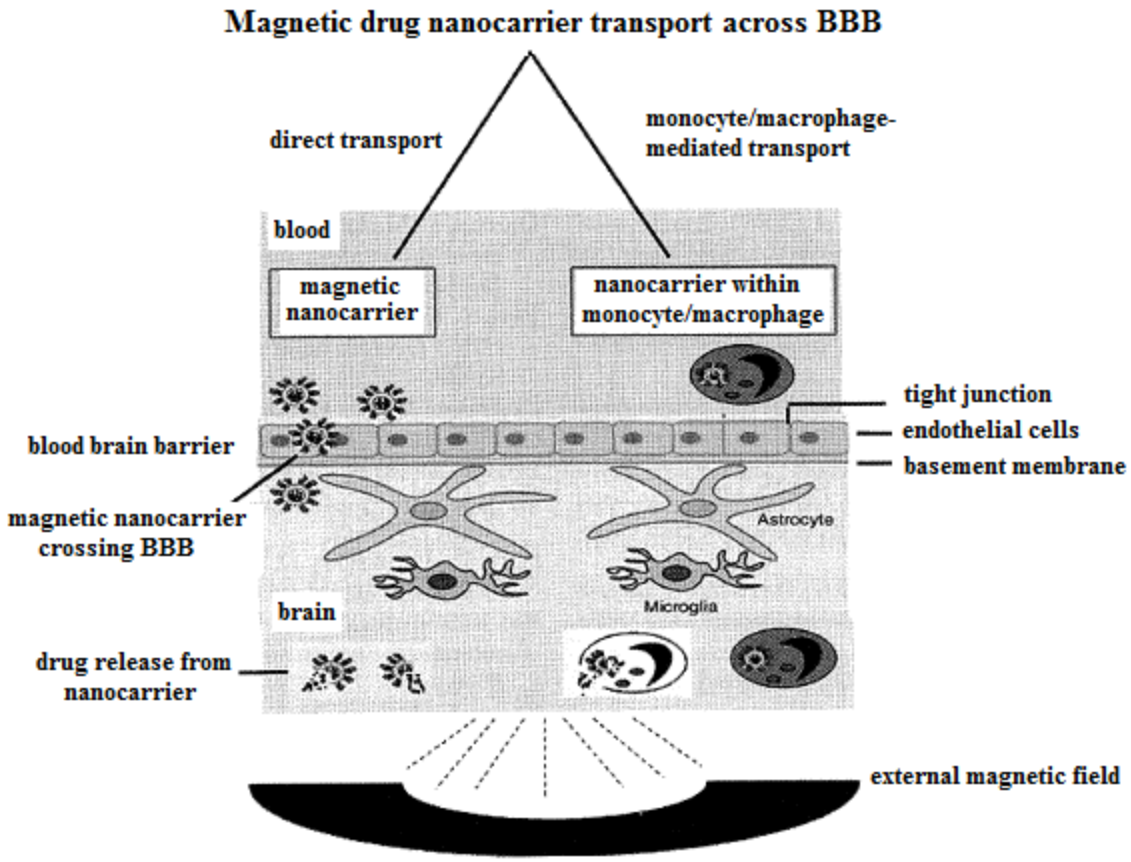

Figure 2.16 Schematic illustration of magnetic field-facilitated transport of magnetic nanocarriers containing antiretroviral drugs across the blood brain barrier.[138]

Saiyed et al. have reported a magnetic nanoformulation where zidovudine (3'-azido-3'-deoxythymidine-5'-triphosphate, AZTTP) was adsorbed onto magnetite nanoparticles through the strong interactions between the triphosphate groups of the drug and the Fe_3O_4 nanoparticles.[139] They showed that the magnetic particle-bound drug completely retained its biological activity as assessed by inhibition of HIV-1 replication in peripheral blood mononuclear cells (PBMCs). It was hypothesized that this magnetic nanoformulation can be used to target the antiretroviral drug to the brain by application of an external magnetic field. This group later loaded magnetic AZTTP into liposomes and showed that the ~ 150 nm magnetic AZTTP liposome migrates an *in vitro* BBB

model via direct and monocyte-mediated transport by application of an external magnetic field.[140] They noted a three-fold increase in the permeability of the drug in the magnetic formulation than in the free form. Furthermore, the anti-HIV activity of the magnetic liposome was comparable to that of the free AZTTP.

2.11 References

(1) De, M.; Ghosh, P. S.; Rotello, V. M.: Applications of nanoparticles in biology. *Adv. Mater.* **2008**, *20*, 4225-4241.

(2) Etheridge, M. L.; Campbell, S. A.; Erdman, A. G.; Haynes, C. L.; Wolf, S. M.; McCullough, J.: The big picture on nanomedicine: the state of investigational and approved nanomedicine products. *Nanomedicine* **2013**, *9*, 1-14.

(3) Verma, A.; Stellacci, F.: Effect of surface properties on nanoparticle–cell interactions. *Small* **2010**, *6*, 12-21.

(4) Ohgushi, M.; Nagayama, K.; Wada, A.: Dextran-magnetite: a new relaxation reagent and its application to T2 measurements in gel systems. *J. Magn. Reson.* **1978**, *29*, 599-601.

(5) Senyei, A.; Widder, K.; Czerlinski, G.: Magnetic guidance of drug-carrying microspheres. *J. Appl. Phys.* **1978**, *49*, 3578-3583.

(6) Geraldes, C.; Laurent, S.: Classification and basic properties of contrast agents for magnetic resonance imaging. *Contrast Media Mol. Imaging* **2009**, *4*, 1-23.

(7) Krishnan, K. M.: Biomedical Nanomagnetics: A spin through possibilities in imaging, diagnostics, and therapy. *IEEE Trans. Magn.* **2010**, *46*, 2523-2558.

(8) Jordan, A.; Scholz, R.; Wust, P.; Fahling, H.; Felix, R.: Magnetic fluid hyperthermia (MFH): Cancer treatment with AC magnetic field induced excitation of biocompatible superparamagnetic nanoparticles. *J. Magn. Magn. Mater.* **1999**, *201*, 413-419.

(9) Kittel, C.: Theory of the structure of ferromagnetic domains in films and small particles. *Phys. Rev.* **1946**, *70*, 965-971.

(10) Gossuin, Y.; Gillis, P.; Hocq, A.; Vuong, Q. L.; Roch, A.: Magnetic resonance relaxation properties of superparamagnetic particles. *Wiley Interdiscip. Rev.: Nanomed. Nanobiotechnol.* **2009**, *1*, 299-310.

(11) Sattler, K. D.; Editor: *Handbook Of Nanophysics: Nanoparticles And Quantum Dots*; CRC Press, **2011**.

(12) Cornell, R. M. S. U.: *The iron oxides : structure, properties, reactions, occurrences, and uses*; Wiley-VCH: Weinheim, 2003.

(13) Sun, Y.-k.; Ma, M.; Zhang, Y.; Gu, N.: Synthesis of nanometer-size maghemite particles from magnetite. *Coll. Surf. A: Physicochem. Eng. Aspects* **2004**, *245*, 15-19.

(14) Qiu, J.; Yang, R.; Li, M.; Jiang, N.: Preparation and characterization of porous ultrafine Fe2O3 particles. *Mater. Res. Bull.* **2005**, *40*, 1968-1975.

(15) Lee, S.-J.; Jeong, J.-R.; Shin, S.-C.; Kim, J.-C.; Kim, J.-D.: Synthesis and characterization of superparamagnetic maghemite nanoparticles prepared by coprecipitation technique. *J. Magn. Magn. Mater.* **2004**, *282*, 147-150.

(16) Rockenberger, J.; Scher, E. C.; Alivisatos, A. P.: A new nonhydrolytic single-precursor approach to surfactant-capped nanocrystals of transition metal oxides. *J. Am. Chem. Soc.* **1999**, *121*, 11595-11596.
(17) Hyeon, T.; Lee, S. S.; Park, J.; Chung, Y.; Na, H. B.: Synthesis of highly crystalline and monodisperse maghemite nanocrystallites without a size-selection process. *J. Am. Chem. Soc.* **2001**, *123*, 12798-12801.
(18) Li, Z.; Chen, H.; Bao, H.; Gao, M.: One-pot reaction to synthesize water-soluble magnetite nanocrystals. *Chem. Mater.* **2004**, *16*, 1391-1393.
(19) LaMer, V. K.; Dinegar, R. H.: Theory, production, and mechanism of formation of monodispersed hydrosols. *J. Am. Chem. Soc.* **1950**, *72*, 4847-54.
(20) Murray, C. B.; Kagan, C. R.; Bawendi, M. G.: Synthesis and characterization of monodisperse nanocrystals and close-packed nanocrystal assemblies. *Annu. Rev. Mater. Sci.* **2000**, *30*, 545-610.
(21) Sun, S. H.; Zeng, H.; Robinson, D. B.; Raoux, S.; Rice, P. M.; Wang, S. X.; Li, G. X.: Monodisperse MFe2O4 (M = Fe, Co, Mn) nanoparticles. *J. Am. Chem. Soc.* **2004**, *126*, 273-279.
(22) Park, J.; An, K.; Hwang, Y.; Park, J.-G.; Noh, H.-J.; Kim, J.-Y.; Park, J.-H.; Hwang, N.-M.; Hyeon, T.: Ultra-large-scale syntheses of monodisperse nanocrystals. *Nat. Mater.* **2004**, *3*, 891-895.
(23) Pinna, N.; Grancharov, S.; Beato, P.; Bonville, P.; Antonietti, M.; Niederberger, M.: Magnetite nanocrystals: Nonaqueous synthesis, characterization, and solubility. *Chem. Mater.* **2005**, *17*, 3044-3049.
(24) Hee Kim, E.; Sook Lee, H.; Kook Kwak, B.; Kim, B.-K.: Synthesis of ferrofluid with magnetic nanoparticles by sonochemical method for MRI contrast agent. *J. Magn. Magn. Mater.* **2005**, *289*, 328-330.
(25) Albornoz, C.; Jacobo, S. E.: Preparation of a biocompatible magnetic film from an aqueous ferrofluid. *J. Magn. Magn. Mater.* **2006**, *305*, 12-15.
(26) Wan, J.; Chen, X.; Wang, Z.; Yang, X.; Qian, Y.: A soft-template-assisted hydrothermal approach to single-crystal Fe3O4 nanorods. *J. Cryst. Growth* **2005**, *276*, 571-576.
(27) Salazar-Alvarez, G.; Muhammed, M.; Zagorodni, A. A.: Novel flow injection synthesis of iron oxide nanoparticles with narrow size distribution. *Chem. Eng. Sci.* **2006**, *61*, 4625-4633.
(28) González-Carreño, T.; Morales, M. P.; Gracia, M.; Serna, C. J.: Preparation of uniform γ-Fe2O3 particles with nanometer size by spray pyrolysis. *Mater. Lett.* **1993**, *18*, 151-155.
(29) Morales, M. P.; Bomati-Miguel, O.; Pérez de Alejo, R.; Ruiz-Cabello, J.; Veintemillas-Verdaguer, S.; O'Grady, K.: Contrast agents for MRI based on iron oxide nanoparticles prepared by laser pyrolysis. *J. Magn. Magn. Mater.* **2003**, *266*, 102-109.
(30) Laurent, S.; Forge, D.; Port, M.; Roch, A.; Robic, C.; Elst, L. V.; Muller, R. N.: Magnetic iron oxide nanoparticles: Synthesis, stabilization, vectorization, physicochemical characterizations, and biological applications. *Chem. Rev.* **2008**, *108*, 2064-2110.
(31) Shen, L.; Laibinis, P. E.; Hatton, T. A.: Bilayer surfactant stabilized magnetic fluids: Synthesis and interactions at interfaces. *Langmuir* **1998**, *15*, 447-453.
(32) Qin, J.; Jo, Y. S.; Muhammed, M.: Coating nanocrystals with amphiphilic thermosensitive copolymers. *Angew. Chem. Int. Ed.* **2009**, *48*, 7845-7849.
(33) Nitin, N.; LaConte, L. E. W.; Zurkiya, O.; Hu, X.; Bao, G.: Functionalization and peptide-based delivery of magnetic nanoparticles as an intracellular MRI contrast agent. *J. Biol. Inorg. Chem.* **2004**, *9*, 706-712.

(34) Schladt, T. D.; Schneider, K.; Schild, H.; Tremel, W.: Synthesis and bio-functionalization of magnetic nanoparticles for medical diagnosis and treatment. *Dalton Trans.* **2011**, *40*, 6315-6343.
(35) Harris, L. A.; Goff, J. D.; Carmichael, A. Y.; Riffle, J. S.; Harburn, J. J.; St Pierre, T. G.; Saunders, M.: Magnetite nanoparticle dispersions stabilized with triblock copolymers. *Chem. Mater.* **2003**, *15*, 1367-1377.
(36) Miles, W. C.; Goff, J. D.; Huffstetler, P. P.; Reinholz, C. M.; Pothayee, N.; Caba, B. L.; Boyd, J. S.; Davis, R. A.; Riffle, J. S.: Synthesis and colloidal properties of polyether-magnetite complexes in water and phosphate-buffered saline. *Langmuir* **2009**, *25*, 803-813.
(37) Pothayee, N.; Pothayee, N.; Jain, N.; Hu, N.; Balasubramaniam, S.; Johnson, L. M.; Davis, R. M.; Sriranganathan, N.; Riffle, J. S.: Magnetic block ionomer complexes for potential dual imaging and therapeutic agents. *Chem. Mater.* **2012**, *24*, 2056-2063.
(38) Goff, J. D.; Huffstetler, P. P.; Miles, W. C.; Pothayee, N.; Reinholz, C. M.; Ball, S.; Davis, R. M.; Riffle, J. S.: Novel phosphonate-functional poly(ethylene oxide)-magnetite nanoparticles form stable colloidal dispersions in phosphate-buffered saline. *Chem. Mater.* **2009**, *21*, 4784-4795.
(39) Pothayee, N.; Balasubramaniam, S.; Davis, R. M.; Riffle, J. S.; Carroll, M. R. J.; Woodward, R. C.; St. Pierre, T. G.: Synthesis of 'ready-to-adsorb' polymeric nanoshells for magnetic iron oxide nanoparticles via atom transfer radical polymerization. *Polymer* **2011**, *52*, 1356-1366.
(40) Xu, C.; Xu, K.; Gu, H.; Zheng, R.; Liu, H.; Zhang, X.; Guo, Z.; Xu, B.: Dopamine as a robust anchor to immobilize functional molecules on the iron oxide shell of magnetic nanoparticles. *J. Am. Chem. Soc.* **2004**, *126*, 9938-9939.
(41) Hohnholt, M. C.; Geppert, M.; Nürnberger, S.; von Byern, J.; Grunwald, I.; Dringen, R.: Advanced biomaterials accumulation of citrate-coated magnetic iron oxide nanoparticles by cultured brain astrocytes. *Adv. Eng. Mater.* **2010**, *12*, B690-B694.
(42) Wei, H.; Insin, N.; Lee, J.; Han, H.-S.; Cordero, J. M.; Liu, W.; Bawendi, M. G.: Compact zwitterion-coated iron oxide nanoparticles for biological applications. *Nano Lett.* **2011**, *12*, 22-25.
(43) Butterworth, M. D.; Illum, L.; Davis, S. S.: Preparation of ultrafine silica- and PEG-coated magnetite particles. *Coll. Surf. A: Physicochem. Eng. Aspects* **2001**, *179*, 93-102.
(44) Jokerst, J. V.; Lobovkina, T.; Zare, R. N.; Gambhir, S. S.: Nanoparticle PEGylation for imaging and therapy. *Nanomedicine* **2011**, *6*, 715-728.
(45) Jung, C. W.; Jacobs, P.: Physical and chemical properties of superparamagnetic iron oxide MR contrast agents: Ferumoxides, ferumoxtran, ferumoxsil. *Magn. Reson. Imaging* **1995**, *13*, 661-674.
(46) Wang, Y. X.; Hussain, S. M.; Krestin, G. P.: Superparamagnetic iron oxide contrast agents: physicochemical characteristics and applications in MR imaging. *Eur. Radiol.* **2001**, *11*, 2319-31.
(47) Lee, J.; Isobe, T.; Senna, M.: Preparation of ultrafine Fe3O4 particles by precipitation in the presence of PVA at high pH. *J. Coll. Interf. Sci.* **1996**, *177*, 490-494.
(48) Lee, H. S.; Hee Kim, E.; Shao, H.; Kook Kwak, B.: Synthesis of SPIO-chitosan microspheres for MRI-detectable embolotherapy. *J. Magn. Magn. Mater.* **2005**, *293*, 102-105.
(49) Nishio, Y.; Yamada, A.; Ezaki, K.; Miyashita, Y.; Furukawa, H.; Horie, K.: Preparation and magnetometric characterization of iron oxide-containing alginate/poly(vinyl alcohol) networks. *Polymer* **2004**, *45*, 7129-7136.
(50) Liu, H.-L.; Ko, S. P.; Wu, J.-H.; Jung, M.-H.; Min, J. H.; Lee, J. H.; An, B. H.; Kim, Y. K.: One-pot polyol synthesis of monosize PVP-coated sub-5 nm Fe3O4 nanoparticles for biomedical applications. *J. Magn. Magn. Mater.* **2007**, *310*, e815-e817.

(51) Iijima, M.; Yonemochi, Y.; Tsukada, M.; Kamiya, H.: Microstructure control of iron hydroxide nanoparticles using surfactants with different molecular structures. *J. Coll. Interf. Sci.* **2006**, *298*, 202-208.
(52) Gómez-Lopera, S. A.; Arias, J. L.; Gallardo, V.; Delgado, Á. V.: Colloidal stability of magnetite/poly(lactic acid) core/shell nanoparticles. *Langmuir* **2006**, *22*, 2816-2821.
(53) Ma, L. L.; Feldman, M. D.; Tam, J. M.; Paranjape, A. S.; Cheruku, K. K.; Larson, T. A.; Tam, J. O.; Ingram, D. R.; Paramita, V.; Villard, J. W.; Jenkins, J. T.; Wang, T.; Clarke, G. D.; Asmis, R.; Sokolov, K.; Chandrasekar, B.; Milner, T. E.; Johnston, K. P.: Small multifunctional nanoclusters (nanoroses) for targeted cellular imaging and therapy. *ACS Nano* **2009**, *3*, 2686-2696.
(54) Park, H.-Y.; Schadt, M. J.; Wang; Lim, I. I. S.; Njoki, P. N.; Kim, S. H.; Jang, M.-Y.; Luo, J.; Zhong, C.-J.: Fabrication of magnetic core@shell Fe oxide@Au nanoparticles for interfacial bioactivity and bio-separation. *Langmuir* **2007**, *23*, 9050-9056.
(55) Yi, D. K.; Selvan, S. T.; Lee, S. S.; Papaefthymiou, G. C.; Kundaliya, D.; Ying, J. Y.: Silica-coated nanocomposites of magnetic nanoparticles and quantum dots. *J. Am. Chem. Soc.* **2005**, *127*, 4990-4991.
(56) Richardson, J. C.; Bowtell, R. W.; Maeder, K.; Melia, C. D.: Pharmaceutical applications of magnetic resonance imaging (MRI). *Adv. Drug Deliv. Rev.* **2005**, *57*, 1191-1209.
(57) Na, H. B.; Song, I. C.; Hyeon, T.: Inorganic nanoparticles for MRI contrast agents. *Adv. Mater.* **2009**, *21*, 2133-2148.
(58) Prasad, P. V.; Editor: *Magnetic Resonance Imaging: Methods and Biologic Applications. [In: Methods Mol. Med.; 2006, 124]*; Humana Press Inc., 2006.
(59) Lepage, M.; Gore, J. C.: Contrast mechanisms in magnetic resonance imaging. *J. Phys.: Conf. Ser.* **2004**, *3*, 78-86.
(60) Qin, J.; Laurent, S.; Jo, Y. S.; Roch, A.; Mikhaylova, M.; Bhujwalla, Z. M.; Muller, R. N.; Muhammed, M.: A high-performance magnetic resonance imaging T2 contrast agent. *Adv. Mater.* **2007**, *19*, 1874-1878.
(61) Harisinghani, M. G.; Barentsz, J.; Hahn, P. F.; Deserno, W. M.; Tabatabaei, S.; van de Kaa, C. H.; de la Rosette, J.; Weissleder, R.: Noninvasive detection of clinically occult lymph-node metastases in prostate cancer. *New Engl. J. Med.* **2003**, *348*, 2491-2499.
(62) Cheon, J.: Chemical design of nanoparticle probes for high-performance magnetic resonance imaging. *Angew. Chem. Int. Ed.* **2008**, *47*, 5122-5135.
(63) Gillis, P.; Moiny, F.; Brooks, R. A.: On T-2-shortening by strongly magnetized spheres: A partial refocusing model. *Magn. Reson. Med.* **2002**, *47*, 257-263.
(64) Koenig, S. H.; Kellar, K. E.: Theory of 1/T1 and 1/T2 NMRD profiles of solutions of magnetic nanoparticles. *Magn. Reson. Med.* **1995**, *34*, 227-233.
(65) Matsumoto, Y.; Jasanoff, A.: T-2 relaxation induced by clusters of superparamagnetic nanoparticles: Monte Carlo simulations. *Magn. Reson. Imaging* **2008**, *26*, 994-998.
(66) Yablonskiy, D. A.; Haacke, E. M.: Theory of NMR signal behavior in magnetically inhomogeneous tissues - The static dephasing regime. *Magn. Reson. Med.* **1994**, *32*, 749-763.
(67) Roch, A.; Gossuin, Y.; Muller, R. N.; Gillis, P.: Superparamagnetic colloid suspensions: Water magnetic relaxation and clustering. *J. Magn. Magn. Mater.* **2005**, *293*, 532-539.
(68) Kennan, R. P.; Zhong, J.; Gore, J. C.: Intravascular susceptibility contrast mechanisms in tissues. *Magn. Reson. Med.* **1994**, *31*, 9-21.
(69) Callaghan, P.: *Principles of Nuclear Magnetic Resonance Microscopy*; Oxford Univ. Press, 1994.

(70) Bulte, J. W.; Vymazal, J.; Brooks, R. A.; Pierpaoli, C.; Frank, J. A.: Frequency dependence of MR relaxation times. II. Iron oxides. *J. Magn. Reson. Imaging* **1993**, *3*, 641-648.
(71) Bulte, J. W.; Brooks, R. A.; Moskowitz, B. M.; Bryant, L. H., Jr.; Frank, J. A.: Relaxometry and magnetometry of the MR contrast agent MION-46L. *Magn. Reson. Med.* **1999**, *42*, 379-384.
(72) Morales, M. P.; Veintemillas-Verdaguer, S.; Montero, M. I.; Serna, C. J.; Roig, A.; Casas, L.; Martinez, B.; Sandiumenge, F.: Surface and internal spin canting in gamma-Fe2O3 nanoparticles. *Chem. Mater.* **1999**, *11*, 3058-3064.
(73) Jun, Y. W.; Huh, Y. M.; Choi, J. S.; Lee, J. H.; Song, H. T.; Kim, S.; Yoon, S.; Kim, K. S.; Shin, J. S.; Suh, J. S.; Cheon, J.: Nanoscale size effect of magnetic nanocrystals and their utilization for cancer diagnosis via magnetic resonance imaging. *J. Am. Chem. Soc.* **2005**, *127*, 5732-5733.
(74) Carroll, M. R. J.; Woodward, R. C.; House, M. J.; Teoh, W. Y.; Amal, R.; Hanley, T. L.; St Pierre, T. G.: Experimental validation of proton transverse relaxivity models for superparamagnetic nanoparticle MRI contrast agents. *Nanotechnology* **2010**, *21*.
(75) Osborne, E. A.; Jarrett, B. R.; Tu, C. Q.; Louie, A. Y.: Modulation of T2 relaxation time by light-induced, reversible aggregation of magnetic nanoparticles. *J. Am. Chem. Soc.* **2010**, *132*, 5934-5935.
(76) Perez, J. M.; Josephson, L.; O'Loughlin, T.; Hogemann, D.; Weissleder, R.: Magnetic relaxation switches capable of sensing molecular interactions. *Nat. Biotechnol.* **2002**, *20*, 816-820.
(77) Schellenberger, E.; Rudloff, F.; Warmuth, C.; Taupitz, M.; Hamm, B.; Schnorr, J.: Protease-specific nanosensors for magnetic resonance imaging. *Bioconjugate Chem.* **2008**, *19*, 2440-2445.
(78) Bamrungsap, S.; Shukoor, M. I.; Chen, T.; Sefah, K.; Tan, W.: Detection of lysozyme magnetic relaxation switches based on aptamer-functionalized superparamagnetic nanoparticles. *Anal. Chem.* **2011**, *83*, 7795-7799.
(79) Xu, F.; Cheng, C.; Chen, D.-X.; Gu, H.: Magnetite nanocrystal clusters with ultra-high sensitivity in magnetic resonance imaging. *ChemPhysChem* **2012**, *13*, 336-341.
(80) Lee, E. S. M.; Shuter, B.; Chan, J.; Chong, M. S. K.; Ding, J.; Teoh, S.-H.; Beuf, O.; Briguet, A.; Tam, K. C.; Choolani, M.; Wang, S.-C.: The use of microgel iron oxide nanoparticles in studies of magnetic resonance relaxation and endothelial progenitor cell labelling. *Biomaterials* **2010**, *31*, 3296-3306.
(81) Vuong, Q. L.; Berret, J.-F.; Fresnais, J.; Gossuin, Y.; Sandre, O.: A universal scaling law to predict the efficiency of magnetic nanoparticles as MRI T2-Contrast Agents. *Adv. Healthcare Mater.* **2012**, *1*, 502-512.
(82) Berret, J. F.; Schonbeck, N.; Gazeau, F.; El Kharrat, D.; Sandre, O.; Vacher, A.; Airiau, M.: Controlled clustering of superparamagnetic nanoparticles using block copolymers: Design of new contrast agents for magnetic resonance imaging. *J. Am. Chem. Soc.* **2006**, *128*, 1755-1761.
(83) Xie, X.; Zhang, C.: Controllable assembly of hydrophobic superparamagnetic iron oxide nanoparticle with mPEG-PLA copolymer and its effect on MR transverse relaxation rate. *J. Nanomater.* **2011**, *2011*.
(84) Yang, J.; Lee, C. H.; Ko, H. J.; Suh, J. S.; Yoon, H. G.; Lee, K.; Huh, Y. M.; Haam, S.: Multifunctional magneto-polymeric nanohybrids for targeted detection and synergistic therapeutic effects on breast cancer. *Angew. Chem. Int. Ed.* **2007**, *46*, 8836-8839.
(85) Ai, H.; Flask, C.; Weinberg, B.; Shuai, X.; Pagel, M. D.; Farrell, D.; Duerk, J.; Gao, J. M.: Magnetite-loaded polymeric micelles as ultrasensitive magnetic-resonance probes. *Adv. Mater.* **2005**, *17*, 1949-1952.

(86) Poeselt, E.; Kloust, H.; Tromsdorf, U.; Janschel, M.; Hahn, C.; Masslo, C.; Weller, H.: Relaxivity optimization of a PEGylated iron-oxide-based negative magnetic resonance contrast agent for T-2-weighted spin-echo imaging. *ACS Nano* **2012**, *6*, 1619-1624.
(87) Cheng, C.; Wen, Y.; Xu, X.; Gu, H.: Tunable synthesis of carboxyl-functionalized magnetite nanocrystal clusters with uniform size. *J. Mater. Chem.* **2009**, *19*, 8782-8788.
(88) Ge, J.; Hu, Y.; Biasini, M.; Beyermann, W. P.; Yin, Y.: Superparamagnetic magnetite colloidal nanocrystal clusters. *Angew. Chem., Int. Ed.* **2007**, *46*, 4342-4345.
(89) Paquet, C.; de Haan, H. W.; Leek, D. M.; Lin, H. Y.; Xiang, B.; Tian, G. H.; Kell, A.; Simard, B.: Clusters of superparamagnetic iron oxide nanoparticles encapsulated in a hydrogel: A particle architecture generating a synergistic enhancement of the T-2 relaxation. *ACS Nano* **2011**, *5*, 3104-3112.
(90) de Haan, H. W.; Paquet, C.: Enhancement and degradation of the R2* relaxation rate resulting from the encapsulation of magnetic particles with hydrophilic coatings. *Magn. Reson. Med.* **2011**, *66*, 1759-1766.
(91) Park, J. H.; von Maltzahn, G.; Zhang, L. L.; Schwartz, M. P.; Ruoslahti, E.; Bhatia, S. N.; Sailor, M. J.: Magnetic iron oxide nanoworms for tumor targeting and imaging. *Adv. Mater.* **2008**, *20*, 1630-1635.
(92) Gossuin, Y.; Disch, S.; Quoc, L. V.; Gillis, P.; Hermann, R. P.; Park, J.-H.; Sailor, M. J.: NMR relaxation and magnetic properties of superparamagnetic nanoworms. *Contrast Media Mol. Imaging* **2010**, *5*, 318-322.
(93) Kabanov, A. V.; Batrakova, E. V.; Alakhov, V. Y.: Pluronic block copolymers as novel polymer therapeutics for drug and gene delivery. *J. Control. Rel.* **2002**, *82*, 189-212.
(94) Batrakova, E. V.; Li, S.; Li, Y.; Alakhov, V. Y.; Elmquist, W. F.; Kabanov, A. V.: Distribution kinetics of a micelle-forming block copolymer Pluronic P85. *J. Control. Rel.* **2004**, *100*, 389-397.
(95) Chiappetta, D. A.; Sosnik, A.: Poly(ethylene oxide)-poly(propylene oxide) block copolymer micelles as drug delivery agents: Improved hydrosolubility, stability and bioavailability of drugs. *Eur. J. Pharm. Biopharm.* **2007**, *66*, 303-317.
(96) Allen, C.; Yu, Y.; Maysinger, D.; Eisenberg, A.: Polycaprolactone-b-poly(ethylene oxide) block copolymer micelles as a novel drug delivery vehicle for neurotrophic agents FK506 and L-685,818. *Bioconjugate Chem.* **1998**, *9*, 564-572.
(97) Gref, R.; Minamitake, Y.; Peracchia, M.; Trubetskoy, V.; Torchilin, V.; Langer, R.: Biodegradable long-circulating polymeric nanospheres. *Science* **1994**, *263*, 1600-1603.
(98) Knop, K.; Hoogenboom, R.; Fischer, D.; Schubert, U. S.: Poly(ethylene glycol) in drug delivery: Pros and cons as well as potential alternatives. *Angew. Chem. Int. Ed.* **2010**, *49*, 6288-6308.
(99) Harris, J. M.; Chess, R. B.: Effect of PEGylation on pharmaceuticals. *Nat. Rev. Drug Discovery* **2003**, *2*, 214-221.
(100) Gindy, M. E.; Ji, S.; Hoye, T. R.; Panagiotopoulos, A. Z.; Prud'homme, R. K.: Preparation of poly(ethylene glycol) protected nanoparticles with variable bioconjugate ligand density. *Biomacromolecules* **2008**, *9*, 2705-2711.
(101) Gindy, M. E.; Panagiotopoulos, A. Z.; Prud'homme, R. K.: Composite block copolymer stabilized nanoparticles: simultaneous encapsulation of organic actives and inorganic nanostructures. *Langmuir* **2008**, *24*, 83-90.

(102) Ji, S.; Zhu, Z.; Hoye, T. R.; Macosko, C. W.: Maleimide functionalized poly(epsilon-caprolactone)-block-poly(ethylene glycol) (PCL-PEG-MAL): Synthesis, nanoparticle formation, and thiol conjugation. *Macromol. Chem. Phys.* **2009**, *210*, 823-831.
(103) Conti, B.; Pavanetto, F.; Genta, I.: Use of polylactic acid for the preparation of microparticulate drug delivery systems. *J. Microencapsulation* **1992**, *9*, 153-66.
(104) Wang, F.; Bronich, T. K.; Kabanov, A. V.; Rauh, R. D.; Roovers, J.: Synthesis and characterization of star poly(epsilon-caprolactone)-b-Poly(ethylene glycol) and Poly(L-lactide)-b-Poly(ethylene glycol) Copolymers: Evaluation as Drug Delivery Carriers. *Bioconjugate Chem.* **2008**, *19*, 1423-1429.
(105) Sahli, H.; Tapon-Bretaudiere, J.; Fischer, A.-M.; Sternberg, C.; Spenlehauer, G.; Verrecchia, T.; Labarre, D.: Interactions of poly(lactic acid) and poly(lactic acid-co-ethylene oxide) nanoparticles with the plasma factors of the coagulation system. *Biomaterials* **1997**, *18*, 281-288.
(106) Gref, R.; Lück, M.; Quellec, P.; Marchand, M.; Dellacherie, E.; Harnisch, S.; Blunk, T.; Müller, R. H.: 'Stealth' corona-core nanoparticles surface modified by polyethylene glycol (PEG): influences of the corona (PEG chain length and surface density) and of the core composition on phagocytic uptake and plasma protein adsorption. *Coll. Surf. B: Biointerf.* **2000**, *18*, 301-313.
(107) Nasongkla, N.; Bey, E.; Ren, J. M.; Ai, H.; Khemtong, C.; Guthi, J. S.; Chin, S. F.; Sherry, A. D.; Boothman, D. A.; Gao, J. M.: Multifunctional polymeric micelles as cancer-targeted, MRI-ultrasensitive drug delivery systems. *Nano Lett.* **2006**, *6*, 2427-2430.
(108) Guthi, J. S.; Yang, S.-G.; Huang, G.; Li, S.; Khemtong, C.; Kessinger, C. W.; Peyton, M.; Minna, J. D.; Brown, K. C.; Gao, J.: MRI-visible micellar nanomedicine for targeted drug delivery to lung cancer cells. *Mol. Pharm.* **2009**, *7*, 32-40.
(109) Yang, J.; Lee, C.-H.; Park, J.; Seo, S.; Lim, E.-K.; Song, Y. J.; Suh, J.-S.; Yoon, H.-G.; Huh, Y.-M.; Haam, S.: Antibody conjugated magnetic PLGA nanoparticles for diagnosis and treatment of breast cancer. *J. Mater. Chem.* **2007**, *17*, 2695-2699.
(110) Kim, J.; Lee, J. E.; Lee, S. H.; Yu, J. H.; Lee, J. H.; Park, T. G.; Hyeon, T.: Designed fabrication of a multifunctional polymer nanomedical platform for simultaneous cancer-targeted imaging and magnetically guided drug delivery. *Adv. Mater.* **2008**, *20*, 478-483.
(111) Jain, T. K.; Morales, M. A.; Sahoo, S. K.; Leslie-Pelecky, D. L.; Labhasetwar, V.: Iron oxide nanoparticles for sustained delivery of anticancer agents. *Mol. Pharm.* **2005**, *2*, 194-205.
(112) Sun, Q.; Cheng, D.; Yu, X.; Zhang, Z.; Dai, J.; Li, H.; Liang, B.; Shuai, X.: A pH-sensitive polymeric nanovesicle based on biodegradable poly(ethylene glycol)-b-poly(2-(diisopropylamino)ethyl aspartate) as a MRI-visible drug delivery system. *J. Mater. Chem.* **2011**, *21*, 15316-15326.
(113) Yang, X.; Grailer, J. J.; Rowland, I. J.; Javadi, A.; Hurley, S. A.; Matson, V. Z.; Steeber, D. A.; Gong, S.: Multifunctional stable and pH-responsive polymer vesicles formed by heterofunctional triblock copolymer for targeted anticancer drug delivery and ultrasensitive MR imaging. *ACS Nano* **2010**, *4*, 6805-6817.
(114) Yang, X.; Grailer, J. J.; Rowland, I. J.; Javadi, A.; Hurley, S. A.; Steeber, D. A.; Gong, S.: Multifunctional SPIO/DOX-loaded wormlike polymer vesicles for cancer therapy and MR imaging. *Biomaterials* **2010**, *31*, 9065-9073.
(115) Yang, J.; Lee, C. H.; Park, J.; Seo, S.; Lim, E. K.; Song, Y. J.; Suh, J. S.; Yoon, H. G.; Huh, Y. M.; Haam, S.: Antibody conjugated magnetic PLGA nanoparticles for diagnosis and treatment of breast cancer. *J. Mater. Chem.* **2007**, *17*, 2695-2699.

(116) Kamaly, N.; Xiao, Z.; Valencia, P. M.; Radovic-Moreno, A. F.; Farokhzad, O. C.: Targeted polymeric therapeutic nanoparticles: design, development and clinical translation. *Chem. Soc. Rev.* **2012**, *41*, 2971-3010.
(117) Kumar, V.; Prud'homme, R. K.: Thermodynamic limits on drug loading in nanoparticle cores. *J. Pharm. Sci.* **2008**, *97*, 4904-4914.
(118) Ungun, B.; Prud'homme, R. K.; Budijono, S. J.; Shan, J.; Lim, S. F.; Ju, Y.; Austin, R.: Nanofabricated upconversion nanoparticles for photodynamic therapy. *Opt. Express* **2009**, *17*, 80-86.
(119) Kumar, V.; Hong, S. Y.; Maciag, A. E.; Saavedra, J. E.; Adamson, D. H.; Prud'homme, R. K.; Keefer, L. K.; Chakrapani, H.: Stabilization of the nitric oxide (NO) prodrugs and anticancer leads, PABA/NO and double JS-K, through incorporation into PEG-protected nanoparticles. *Mol. Pharm.* **2010**, *7*, 291-298.
(120) Chen, T.; D'Addio, S. M.; Kennedy, M. T.; Swietlow, A.; Kevrekidis, I. G.; Panagiotopoulos, A. Z.; Prud'homme, R. K.: Protected peptide nanoparticles: Experiments and brownian dynamics simulations of the energetics of assembly. *Nano Lett.* **2009**, *9*, 2218-2222.
(121) Ansell, S. M.; Johnstone, S. A.; Tardi, P. G.; Lo, L.; Xie, S.; Shu, Y.; Harasym, T. O.; Harasym, N. L.; Williams, L.; Bermudes, D.; Liboiron, B. D.; Saad, W.; Prud'homme, R. K.; Mayer, L. D.: Modulating the therapeutic activity of nanoparticle delivered paclitaxel by manipulating the hydrophobicity of prodrug conjugates. *J. Med. Chem.* **2008**, *51*, 3288-3296.
(122) D'Addio, S. M.; Prud'homme, R. K.: Controlling drug nanoparticle formation by rapid precipitation. *Adv. Drug Deliv. Rev.* **2011**, *63*, 417-426.
(123) York, A. W.; Zablocki, K. R.; Lewis, D. R.; Gu, L.; Uhrich, K. E.; Prud'homme, R. K.; Moghe, P. V.: Kinetically assembled nanoparticles of bioactive macromolecules exhibit enhanced stability and cell-targeted biological efficacy. *Adv. Mater.* **2012**, *24*, 733-739.
(124) Zhang, C.; Pansare, V. J.; Prud'homme, R. K.; Priestley, R. D.: Flash nanoprecipitation of polystyrene nanoparticles. *Soft Matter* **2012**, *8*, 86-93.
(125) Brick, M. C.; Palmer, H. J.; Whitesides, T. H.: Formation of colloidal dispersions of organic materials in aqueous media by solvent shifting. *Langmuir* **2003**, *19*, 6367-6380.
(126) Liu, Y.; Cheng, C. Y.; Prud'homme, R. K.; Fox, R. O.: Mixing in a multi-inlet vortex mixer (MIVM) for flash nano-precipitation. *Chem. Eng. Sci.* **2008**, *63*, 2829-2842.
(127) Pinkerton, N. M.; Grandeury, A.; Fisch, A.; Brozio, J.; Riebesehl, B. U.; Prud'homme, R. K.: Formation of stable nanocarriers by in situ ion pairing during block-copolymer-directed rapid precipitation. *Mol. Pharm.* **2013**, *10*, 319-328.
(128) Kumar, V.; Wang, L.; Riebe, M.; Tung, H.-H.; Prud'homme, R. K.: Formulation and stability of itraconazole and odanacatib nanoparticles: governing physical parameters. *Mol. Pharm.* **2009**, *6*, 1118-1124.
(129) Vyas, T. K.; Shahiwala, A.; Amiji, M. M.: Improved oral bioavailability and brain transport of saquinavir upon administration in novel nanoemulsion formulations. *Int. J. Pharm.* **2008**, *347*, 93-101.
(130) Nowacek, A.; Gendelman, H. E.: NanoART, neuroAIDS and CNS drug delivery. *Nanomedicine* **2009**, *4*, 557-574.
(131) Silva, G. A.: Nanotechnology approaches for drug and small molecule delivery across the blood brain barrier. *Surg. Neurol.* **2007**, *67*, 113-116.
(132) Kuo, Y.-C.; Su, F.-L.: Transport of stavudine, delavirdine, and saquinavir across the blood-brain barrier by polybutylcyanoacrylate, methylmethacrylate-sulfopropylmethacrylate, and solid lipid nanoparticles. *Int. J. Pharm.* **2007**, *340*, 143-152.

(133) Rao, K. S.; Reddy, M. K.; Horning, J. L.; Labhasetwar, V.: TAT-conjugated nanoparticles for the CNS delivery of anti-HIV drugs. *Biomaterials* **2008**, *29*, 4429-4438.
(134) Mainardes, R. M.; Gremiao, M. P. D.; Brunetti, I. L.; Da, F. L. M.; Khalil, N. M.: Zidovudine-loaded PLA and PLA-PEG blend nanoparticles: influence of polymer type on phagocytic uptake by polymorphonuclear cells. *J. Pharm. Sci.* **2009**, *98*, 257-267.
(135) Destache, C. J.; Belgum, T.; Christensen, K.; Shibata, A.; Sharma, A.; Dash, A.: Combination antiretroviral drugs in PLGA nanoparticle for HIV-1. *BMC Infect Dis* **2009**, *9*, 198.
(136) Chattopadhyay, N.; Zastre, J.; Wong, H.-L.; Wu, X. Y.; Bendayan, R.: Solid lipid nanoparticles enhance the delivery of the HIV protease inhibitor, atazanavir, by a human brain endothelial cell line. *Pharm. Res.* **2008**, *25*, 2262-2271.
(137) Nowacek, A. S.; Balkundi, S.; McMillan, J.; Roy, U.; Martinez-Skinner, A.; Mosley, R. L.; Kanmogne, G.; Kabanov, A. V.; Bronich, T.; Gendelman, H. E.: Analyses of nanoformulated antiretroviral drug charge, size, shape and content for uptake, drug release and antiviral activities in human monocyte-derived macrophages. *J. Control. Rel.* **2011**, *150*, 204-211.
(138) Nair, M. P. N., Saiyed, Z. M.: Antiretroviral Nanotherapies. In *The Neurology of AIDS*; 3 ed.; Howard E. Gendelman, I. G., Ian Paul Everall, Howard S. Fox, Harris A. Gelbard, Stuart A. Lipton, Susan Swindells, Ed., **2011**.
(139) Saiyed, Z. M.; Gandhi, N. H.; Nair, M. P. N.: AZT 5′-triphosphate nanoformulation suppresses human immunodeficiency virus type 1 replication in peripheral blood mononuclear cells. *J. NeuroVirology* **2009**, *15*, 343-347.
(140) Saiyed, Z. M.; Gandhi, N. H.; Nair, M. P. N.: Magnetic nanoformulation of azidothymidine 5'-triphosphate for targeted delivery across the blood-brain barrier. *Int. J. Nanomed.* **2010**, *5*, 157-166.

3 Poly(*N*-isopropylacrylamide)-coated Superparamagnetic Iron Oxide Nanoparticles: Relaxometric and Fluorescence Behavior Correlate to Temperature-dependent Aggregation

Sharavanan Balasubramaniam,[†] *Nikorn Pothayee,*[†] *Yin-Nian Lin*,[†] *Michael J. House,*[‡] *Robert C. Woodward,*[‡] *Timothy G. St. Pierre,*[‡] *Richey M. Davis*,[†] *and Judy S. Riffle*[†]

[†]Macromolecules and Interfaces Institute, Virginia Tech, Blacksburg, VA 24061, U. S. A.
[‡]School of Physics, The University of Western Australia, Crawley, Western Australia 6009, Australia.

Reproduced with permission from *Chemistry of Materials* **2011**, *23*, 3348–3356.

3.1 Abstract

Magnetic nanoparticles coated with polymers have existing and further potential for applications in medicine including MRI imaging for diagnostics and assessing biodistribution, and their capacity to remotely generate heat in response to alternating current magnetic fields to elicit biological responses. Advances in such domains rely on developing better understanding of how such materials respond to magnetic fields. This chapter reports thermosensitive properties of poly(*N*-isopropylacrylamide-*co*-Nile Red)-coated magnetic nanostructures upon passing through the lower critical solution temperature (LCST) of the polymer brush, and correlation of this behavior with formation of aggregates. Discrete magnetic iron oxide nanoparticles coated with brush layers comprised of terminally-attached poly(*N*-isopropylacrylamide-*co*-Nile Red) afforded highly water-dispersible nanoparticles (intensity avg. diameter = 38 nm) with good colloidal stability in phosphate buffers. The nanoparticles displayed enhanced transverse (T_2) NMR

relaxation rates as the temperature was raised through the LCST. Moreover, incorporation of the environmentally-sensitive Nile Red dye into the copolymer leads to significant changes in fluorescence emission intensity upon aggregation that present new possibilities for remote fluorescence detection of aggregated structures.

3.2 Introduction

Superparamagnetic iron oxide nanoparticles have a range of existing and potential biomedical applications such as contrast agents for magnetic resonance imaging (MRI), hyperthermia treatment of cancer, tags for cell separations, retinal detachment therapy and targeted drug delivery.[1-9] Magnetite (Fe_3O_4) has attracted much attention because of its superior magnetic properties combined with stability, biocompatibility and low cytotoxicity.[10] The development of MRI as a versatile imaging modality has provided a major thrust to the design and optimization of colloidal iron oxide nanoparticles, which belong to the class of T_2 contrast agents. The contrast enhancing characteristics of magnetite nanoparticles have been attributed to a microscopic susceptibility effect, whereby dephasing of the diffusing water protons is accelerated by field gradients created by the induced magnetization of the particles. However, the degree of contrast enhancement, defined by the transverse relaxivity coefficient (r_2), depends on various parameters such as particle size, magnetization and aggregation, and interrelationships among chemical and physical parameters of the nanoparticles and relaxivities have not been well defined.

Recently, it has been shown that aggregates of magnetic nanoparticles in suspension can cause a greater reduction in T_2 (= $1/R_2$) than the primary nanoparticles.[11-13] This decrease in T_2 on aggregation can be related to either an increase in average particle size within the motional averaging regime where the T_2 is proportional to $1/r^2$ or with a larger fraction of the particle size

distribution being located within the static dephasing regime where R_2 has its maximum value and is independent of r. If the aggregates grow too large, then T_2 will eventually increase as the system moves into the echo limited regime where T_2 is proportional to r^2.[13-16]

The higher proton relaxation rates translate into better contrast in T_2-weighted MR images. As a result, some effort has now turned toward creating controlled clusters of magnetic nanoparticles. Berret et al. have described the controlled clustering of maghemite (γ-Fe_2O_3) nanoparticles through electrostatic complexation with cationic-nonionic block copolymers.[17] They reported enhanced transverse relaxivities for the clusters as compared to primary nanoparticles and also observed an increase in r_2 with increase in the size of the clusters. Gao et al. reported very high transverse relaxivities of clusters of oleic acid-coated magnetite nanoparticles encased in hydrophobic cores of poly(ε-caprolactone-*b*-ethylene oxide) micelles in water.[18] Previous data from our laboratories has also shown that small clusters of individually coated poly(ethylene oxide)-magnetite complexes can form in water when sufficiently low polymer loadings are utilized, and that these also correlate with enhanced r_2.[19]

Modulation of T_2 relaxation times by reversible aggregation of magnetic nanoparticles has also been demonstrated. Osborne et al. have reported "smart" T_2 contrast agents based on dextran sulfate-coated iron oxide nanoparticles derivatized with a light-sensitive molecule, spiropyran.[20] Conformational switching of the latter between hydrophilic and hydrophobic isomers in response to light irradiation resulted in reversible aggregation of the nanoparticles with a ~33% difference in the T_2 relaxation times of the dispersed nanoparticles and the aggregates. Weissleder and coworkers developed an *in vitro* MRI probe that employs crosslinked iron oxide nanoparticles functionalized with DNA sequences.[21] Upon recognition of a complementary oligonucleotide, the nanoparticles aggregate into clusters leading to reduced T_2 relaxation times. The process was

reversible through the action of a DNA-cleaving enzyme that separated the clusters into the constituent nanoparticles. Schellenberger et al. have described protease-specific T_2 contrast agents comprised of peptide-poly(ethylene oxide) copolymers adsorbed on citrate-coated iron oxide nanoparticles.[22] The action of matrix metalloproteinase 9 led to cleavage of the peptide-poly(ethylene oxide) copolymer, resulting in irreversible aggregation and higher r_2.

Poly(*N*-isopropylacrylamide) (PNIPAM) has been one of the most studied water soluble polymers ever since its lower critical solution temperature (LCST) behavior was first described by Heskins and Guillet.[23] Above the LCST (~32°C), PNIPAM chains in aqueous solution undergo a phase transition from an expanded coil to a collapsed state as a result of loss of hydration. We have recently reported the synthesis of magnetic nanostructures where a bis(phosphonate)-functional PNIPAM was terminally attached to discrete magnetite nanoparticles.[24] Herein we report thermoresponsive core-shell nanoparticles comprised of ~8-nm diameter magnetic iron oxide stabilized in water by a PNIPAM-*co*-Nile Red corona, with temperature-dependent aggregation and NMR relaxation effects. We describe the LCST-induced aggregation and the effect on T_2-shortening of highly water-dispersible PNIPAM-coated iron oxide nanoparticles (Figure 3.1). When heated above the LCST of PNIPAM in water, the nanoparticles aggregated due to a loss of steric stabilization. However, the state of dispersion could be fully restored by cooling the suspension down to ambient temperature and sonicating. The LCST-induced aggregation of the magnetite-PNIPAM nanoparticles was observed using a combination of dynamic light scattering, steady-state fluorescence spectroscopy and magnetic resonance relaxometry. Thermally-driven aggregation of magnetite-PNIPAM complexes has been studied previously,[3,25-27] but until now, the effect of this aggregation on the relaxometric properties has not been studied. For the fluorescence experiments, *N*-isopropylacrylamide was copolymerized with an acrylate monomer

containing Nile Red, and the copolymer was adsorbed onto the magnetite to render the nanoparticles fluorescent. Changes in the transverse and longitudinal relaxation times of water protons were investigated as a function of aggregation of the nanoparticles. The nature of the environment of the Nile Red comonomer in the hydrated (non-aggregated) vs. dehydrated (aggregated) state was accompanied by a significant change in fluorescence intensity, thus providing an additional means of detecting the onset of dehydration and aggregation.

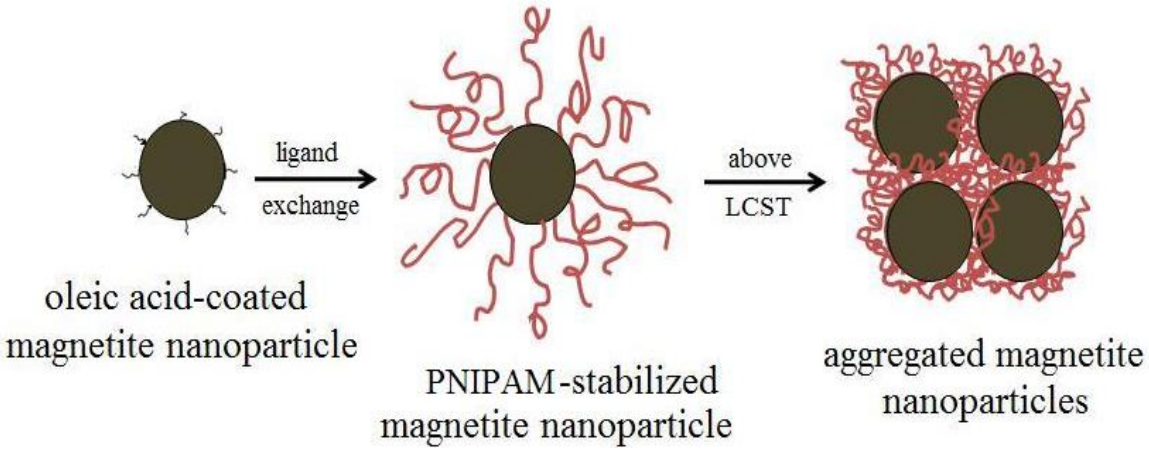

Figure 3.1 LCST-induced aggregation in water of individually coated iron oxide-PNIPAM nanoparticles.

3.3 Experimental Section

3.3.1 Materials

All materials were used as received unless otherwise noted. Benzyl alcohol (>98%), diethyl ether, diethyl vinyl phosphonate (97%), hexanes (HPLC grade), iron (III) acetylacetonate ($Fe(acac)_3$), trimethylsilyl bromide (TMSBr, 97%), oleic acid (90%, technical grade), 2-chloropropionyl chloride, 3-amino-1-propanol, diethylaminophenol (97%), sodium nitrite (>97%), 1,6-dihydroxynaphthalene (99%), thallium ethoxide (98%), and acryloyl chloride (97%) were purchased from Aldrich. *N*-isopropylacrylamide (NIPAM) was recrystallized twice from hexane. Tris[2-(dimethylamino)ethylamine] (Me_6TREN) was synthesized and purified according to a

previously-reported method.[28] Dichloromethane (anhydrous), acetone (HPLC grade), conc. HCl (ACS plus), ethyl acetate (99.9%) and isopropanol (USP) were purchased from Fisher Scientific. Ethanol (200 proof) was purchased from Decon Labs. Dialysis tubing (25,000 and 3,500 g mol^{-1} MWCO) was obtained from Spectra/Por. Phosphate buffered saline (PBS) was purchased from Mediatech. A NdFeB permanent magnet with a diameter of 11/16" and a thickness of 1/4" was obtained from K and J Magnetics. It was axially magnetized with a surface field of 3880 Gauss.

3.3.2 Synthesis of oleic acid-coated iron oxide nanoparticles

Magnetic iron oxide nanoparticles were synthesized using a slightly modified method of that previously reported.[19] $Fe(acac)_3$ (2.14 g, 8.4 mmol) and benzyl alcohol (45 mL, 0.43 mol) were charged to a 250-mL, three-neck, round-bottom flask equipped with a water condenser and nitrogen inlet and placed in a Belmont metal bath with an overhead stirrer with thermostatic (± 1ºC) control. The solution was held at 110°C for 1 h under N_2, then the temperature was raised to 205ºC and maintained for 40 h. The reaction was cooled to room temperature and the particles were collected by centrifugation (4000 rpm, 30 min). The iron oxide nanoparticles were washed 3X with acetone (100 mL each), then were dispersed in chloroform (20 mL) containing oleic acid (0.3 g). The solvent was removed under vacuum at room temperature, and the oleic acid-coated iron oxide nanoparticles were washed 3X with acetone (100 mL each) to remove excess oleic acid. The nanoparticles were dried under vacuum for 24 h at 25˚C.

3.3.3 Synthesis of Nile Red acrylate

3.3.3.1 *(5-Diethylamino)-2-nitrosophenol hydrochloride*

3-Diethylaminophenol (16.5 g, 0.1 mol) was dissolved in a mixture of 35 mL of concentrated HCl and 20 mL of water, and was cooled to 0°C. A solution of sodium nitrite (6.9 g, 0.1 mol) in 50 mL of water was added dropwise over 2 h and the temperature of the reaction was maintained at 0-5°C. The resulting brown slurry was stirred for 3.5 h. Following filtration and washing with 30 mL of 4 M aqueous HCl, the product was dried, then recrystallized from 150 mL of ethanol to yield a yellow powder (16.4 g, 72%). ^{1}H NMR in DMSO-d_6: δ = 7.36 (1H, d), 6.90 (1H, d), 5.74 (1H, s), 3.60 (4H, m), 1.20 (6H, t).

3.3.3.2 *9-Diethylamino-2-hydroxy-5H-benzo[α]phenoxazin-5-one (NR-OH)*

2-Hydroxy substituted-Nile Red (NR-OH) was synthesized by a known procedure according to Briggs et al.[31] 5-Diethylamino-2-nitrosophenol hydrochloride (1.28 g, 5.5 mmol) and 1,6-dihydroxynaphthalene (0.90 g, 5.6 mmol) were dissolved in 250 mL of dry DMF and heated under reflux for 5 h. The solvent was removed under reduced pressure to yield a dark blue-green solid. Subsequent purification by silica gel column chromatography (ethyl acetate: isopropanol, 4:1) yielded 0.52 g (28%) of a dark green solid. ^{1}H NMR in DMSO-d_6: δ = 10.38 (1H, s), 7.94 (1H, d), 7.86 (1H, d), 7.56 (1H, d), 7.07 (1H, dd), 6.78 (1H, d), 6.62 (1H, d), 6.13 (1H, s), 3.48 (4H, q), 1.17 (6H, t).

3.3.3.3 *Acrylate monomer containing Nile Red (NR-acrylate)*

A Nile Red acrylate monomer was prepared in a two-step procedure that included treatment of NR-OH with thallium ethoxide in a solvent to form the thallium salt (NR-OTl), then NR-OTl was reacted with acryloyl chloride to yield the NR-acrylate monomer. Thallium ethoxide (0.15 mL,

2.12 mmol) was added to a solution of NR-OH (0.42 g, 1.26 mmol) in 30 mL of dry DMF and the mixture was stirred at room temperature for 2 h. Then 0.34 mL of acryloyl chloride (4.20 mmol) was added into the reaction mixture and stirred overnight. To remove the thallium salt formed in the reaction, the mixture was passed through a small silica gel column and then the column was washed with ethyl acetate. Evaporation of the solvents in the eluent yielded 0.48 g (1.24 mmol, 98% yield) of a NR-acrylate monomer. ^{1}H NMR in DMSO-d_6: δ = 8.26 (1H, s), 8.17 (1H, d), 7.61 (1H, d), 7.51 (1H, d), 6.84 (1H, d), 6.67 (1H, s), 6.61 (1H, d), 6.46 (1H, dd), 6.28 (1H, s), 6.21 (1H, d), 3.48 (4H, q), 1.17 (6H, t).

3.3.4 Synthesis of ammonium bis(phosphonate)-functional PNIPAM and bis(phosphonate)-functional poly(NIPAM-*co*-Nile Red acrylate)

Bis(phosphonate)-PNIPAM and bis(phosphonate)-PNIPAM-*co*-Nile Red acrylate were synthesized by a procedure adapted from our previous work.[24] A bis(phosphonate)-functional ATRP initiator was prepared and utilized with CuCl/Me_6TREN as a catalyst system for the polymerizations. The initiator (0.32 g, 6.48 x 10^{-4} mol), NIPAM (4.6 g, 4.07 x 10^{-2} mol), CuCl (65 mg, 6.48 x 10^{-4} mol), Me_6TREN (190 μL, 6.48 x 10^{-2} mol), and a DMF:H_2O mixture (v:v 3:1, 8 mL) were added to a 25-mL Schlenk flask. After it was degassed by three freeze-pump-thaw cycles, the flask was kept under a slight pressure of N_2. The reaction mixture was immersed in an oil bath at 25ºC for polymerization. After 60 min, the mixture was diluted with THF (20 mL) and passed through an alumina column to remove the copper catalyst. The polymer was isolated by precipitation in *n*-hexane twice, collected by filtration, and dried under vacuum at room temperature for 24 h. The number-average molecular weight (M_n) determined by SEC was ~ 11,000 g mol^{-1} with a PDI of 1.07. ^{1}H NMR revealed that there were approximately 65 NIPAM repeat units per initiator moiety. To remove the ethoxy groups from the (bis)phosphonate

endgroup, bis(phosphonate)-PNIPAM (1.10 g, 1.53 x 10^{-4} mol) was dissolved in anhydrous dichloromethane (30 mL). Trimethylsilyl bromide (0.190 g, 1.22 x 10^{-3} mol) was added dropwise to the mixture under a dry N_2 atmosphere. The solution was stirred at room temperature for 24 h, then most of the solvent and by-products were removed under vacuum at room temperature. Anhydrous methanol (5 mL) was added to the resultant polymer and stirred for 4 h. Bis(phosphonic acid)-PNIPAM was recovered by precipitation into hexane and dried under vacuum. Bis(phosphonate)-PNIPAM-*co*-Nile Red acrylate was synthesized in a similar procedure using a 50:1 molar ratio of NIPAM to the Nile Red acrylate. To remove any unreacted free monomer, the polymer (1 g) was dissolved in methanol (5 mL) and dialyzed twice against methanol (2 L) through a cellulose acetate membrane (MWCO 3,500 g mol^{-1}). The copolymer was recovered by precipitation into hexane, then dried under vacuum at room temperature.

3.3.5 Coating of iron oxide nanoparticles with PNIPAM and PNIPAM-*co*-Nile Red acrylate

A representative method for preparing PNIPAM-coated iron oxide nanoparticles with a targeted composition of 33 wt% iron oxide is provided. Oleic acid-coated iron oxide nanoparticles (33.0 mg) were dispersed in chloroform (10 mL) and charged into a 50-mL round-bottom flask. A polymer blend of ammonium bis(phosphonate)-functional PNIPAM and PNIPAM-*co*-Nile Red acrylate (50:50 wt%, 67.0 mg) was dissolved in DMF (10 mL) and added to the dispersion. The reaction mixture was sonicated in a VWR 75T sonicator for 4 h under N_2, then stirred at room temperature for 24 h. The nanoparticles were precipitated in hexanes (300 mL). A permanent magnet was utilized to collect the iron oxide nanoparticles and free oleic acid was decanted with the supernatant. The particles were dried under vacuum at room temperature overnight, then dispersed in de-ionized water (20 mL) with sonication for 30-60 s. The complex was dialyzed

against de-ionized water (1 L) for 24 h using a 25,000 g mol^{-1} MWCO dialysis bag, then freeze-dried to obtain a 'purple-brown' solid product.

3.3.6 Characterization

^{1}H NMR spectra of the polymers were acquired at 400 MHz (Varian Unity or Varian INOVA). Size exclusion chromatography (SEC) was performed on a liquid chromatograph equipped with a Waters 1515 isocratic HPLC pump, Waters Autosampler, Waters 2414 refractive index detector and Viscotek 270 RALLS/viscometric dual detector. The mobile phase was N-methylpyrrolidone containing 0.05 M LiBr. A Waters Styragel HR-1 + HR-3 + HR-4 column set maintained at 60ºC because of the viscous nature of NMP was used. Both the solvent and the sample solution were filtered before introduction into the SEC system. Absolute molecular weights were determined with a Universal Calibration that was based on polystyrene standards.

Inductively coupled plasma atomic emission spectroscopy (ICP-AES) was performed on a SPECTRO ARCOS 165 ICP spectrometer (SPECTRO Analytical Instruments, Germany) to measure the concentration of iron in the magnetite-polymer complexes. The particles (10 mg) were dispersed in de-ionized water (5 mL). The dispersion (1 mL) was mixed with 4 mL of concentrated nitric acid to digest iron oxide and release free iron. The mixture was reacted for 5 days at room temperature and diluted with de-ionized water to a concentration of 0.02 mg mL^{-1} prior to measurement. The reported results are the mean of three measurements.

Dynamic light scattering (DLS) measurements were performed using a Zetasizer NanoZS particle analyzer (Malvern Instruments Ltd., Malvern, U. K.) equipped with a 4 mW solid-state He-Ne laser (λ = 633 nm) at a scattering angle of 173°. The average translational diffusion coefficient (D_t) was extracted from a single exponential (cumulants) fit of the correlation curve and the intensity-average hydrodynamic diameter (D_I) was determined through the Stokes-Einstein

equation: $D_I = k_B T/(3\pi\eta D_t)$, where k_B is the Boltzmann constant, T is the absolute temperature and η, the solvent viscosity. Samples dispersed in de-ionized water to appropriate concentrations were passed through a 100-nm syringe filter (Whatman Anotop) before measurements. The reported intensity-weighted hydrodynamic diameters were averaged from three measurements.

Fluorescence measurements were performed on a Synergy Mx multimode microplate reader (BioTek Instruments, Winooski, VT) at an excitation wavelength of 570 nm. Samples were equilibrated at 25 and 35°C for 15 min and the fluorescence emission was recorded from 600 to 850 nm.

Transmission electron microscopy was performed on a Philips EM-420 field emission gun TEM operating at an acceleration voltage of 100 kV. Samples were prepared by casting a drop of a dilute aqueous solution of PNIPAM-coated iron oxide nanoparticles onto an amorphous carbon-coated copper grid. Images were acquired at a magnification of 96,000X, corresponding to a resolution of 3.88 pixels nm^{-1}. The sizes of over 2000 particles from different regions of the grid were measured using Reindeer Graphics' Fovea Pro 4 plug-in for Adobe Photoshop 7.0®. The sample magnetization (M) as a function of applied field (H) (M-H curve) was measured at 300 K using a superconducting quantum interference device (SQuID) magnetometer (MPMS XL, Quantum Design) in the range of ±7 T. In addition a zero field cooled/field cooled (ZFC/FC) test was conducted using the SQuID magnetometer to confirm that the sample was superparamagnetic at room temperature and to determine the maximum blocking temperature.[16]

Magnetic resonance relaxometry was performed with a mq-60 NMR Analyzer (Bruker Minispec) operating at a magnetic field of 1.4 T. This field strength corresponds to a proton Larmor frequency of 60 MHz. Proton transverse relaxation times (T_2) were obtained from fitting a monoexponential decay curve to signal data generated by a Carr-Purcell-Meiboom-Gill (CPMG) spin-echo pulse

sequence with an echo spacing of 1 ms and a repetition time of 5 s. Longitudinal relaxation times (T_1) were obtained from fitting a monoexponential recovery curve to signal data generated with an inversion recovery (IR) pulse sequence using 10 logarithmically spaced inversion times between 50 and 10,000 ms. Each sample (500 μL) was transferred into a 7.5-mm NMR tube and equilibrated at each temperature for 15 min. prior to measurements.

3.4 Results and Discussion

3.4.1 Synthesis of well-defined PNIPAM-coated iron oxide nanoparticles

The polymers for these complexes were synthesized by controlled radical polymerizations wherein the ligands for adsorption onto the magnetite surfaces were incorporated in the initiators (Figure 3.2). Thus, they were designed to adsorb onto the particles from one end only to provide well-defined brushes comprised of terminally-attached chains. This was done to minimize any aggregation of the particles due to multiple adsorption sites on the polymers during the coating process. The ATRP polymerization of bis(phosphonate)-functional PNIPAM and PNIPAM-*co*-Nile Red acrylate followed by their adsorption onto discrete magnetite nanoparticles from organic media afforded magnetite-PNIPAM complexes. The final composition of the complexes was determined by ICP-AES analysis to be 65.1 ± 0.26 wt% polymer, which was in good agreement with the targeted composition of 67 wt%. This result was also consistent with previous findings in our group that phosphonate-functional polymers can be adsorbed onto magnetite in high concentrations.[30,32]

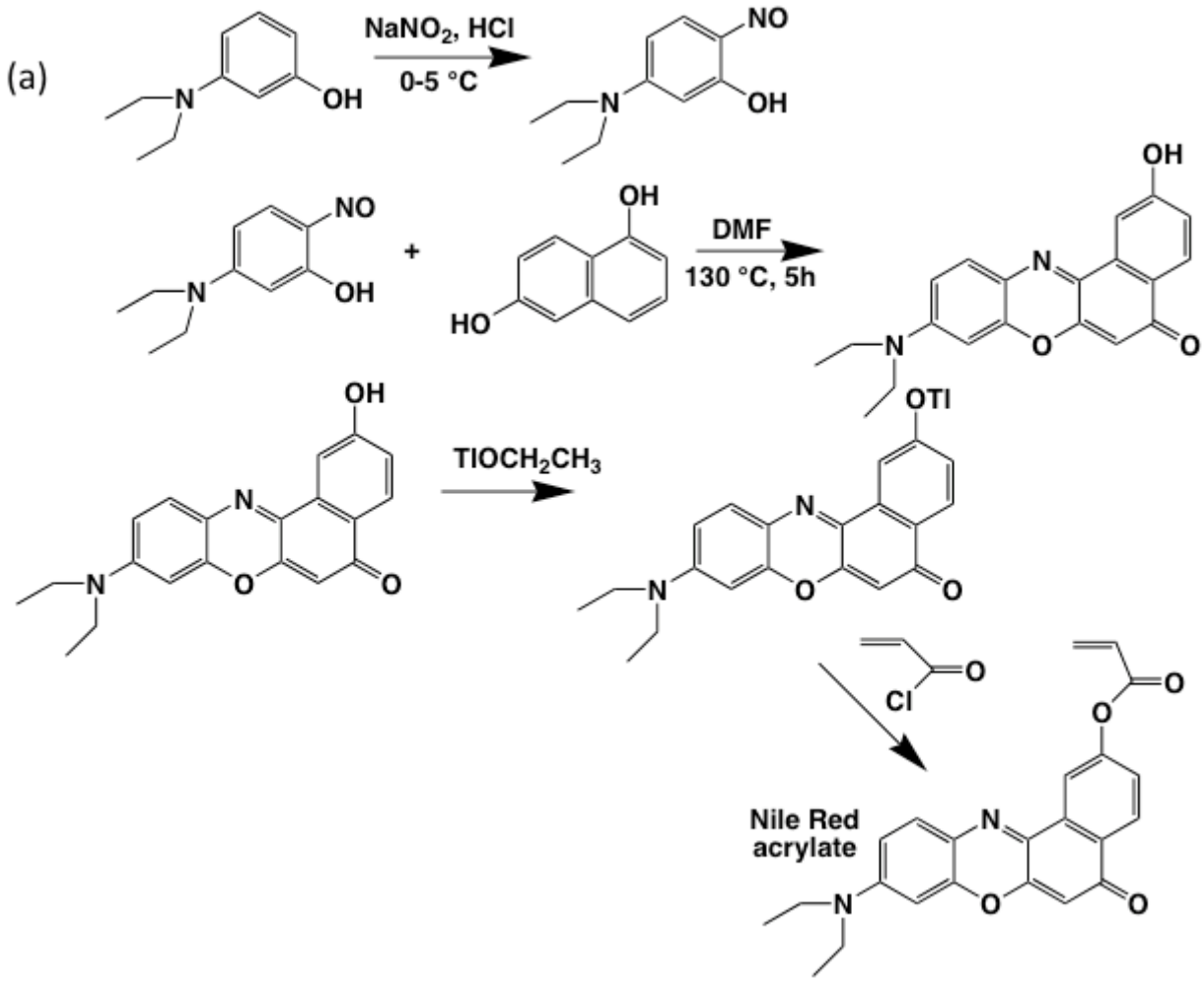
(a)
NaNO2, HCl
0-5 °C
NO
OH
N
OH
NO
OH
N
OH
+
OH
HO
DMF
130 °C, 5h
OH
N
O
O
N
OH
N
O
O
TlOCH2CH3
OTl
N
O
O
N
Cl
O
O
O
Nile Red
acrylate
N
O
O
N

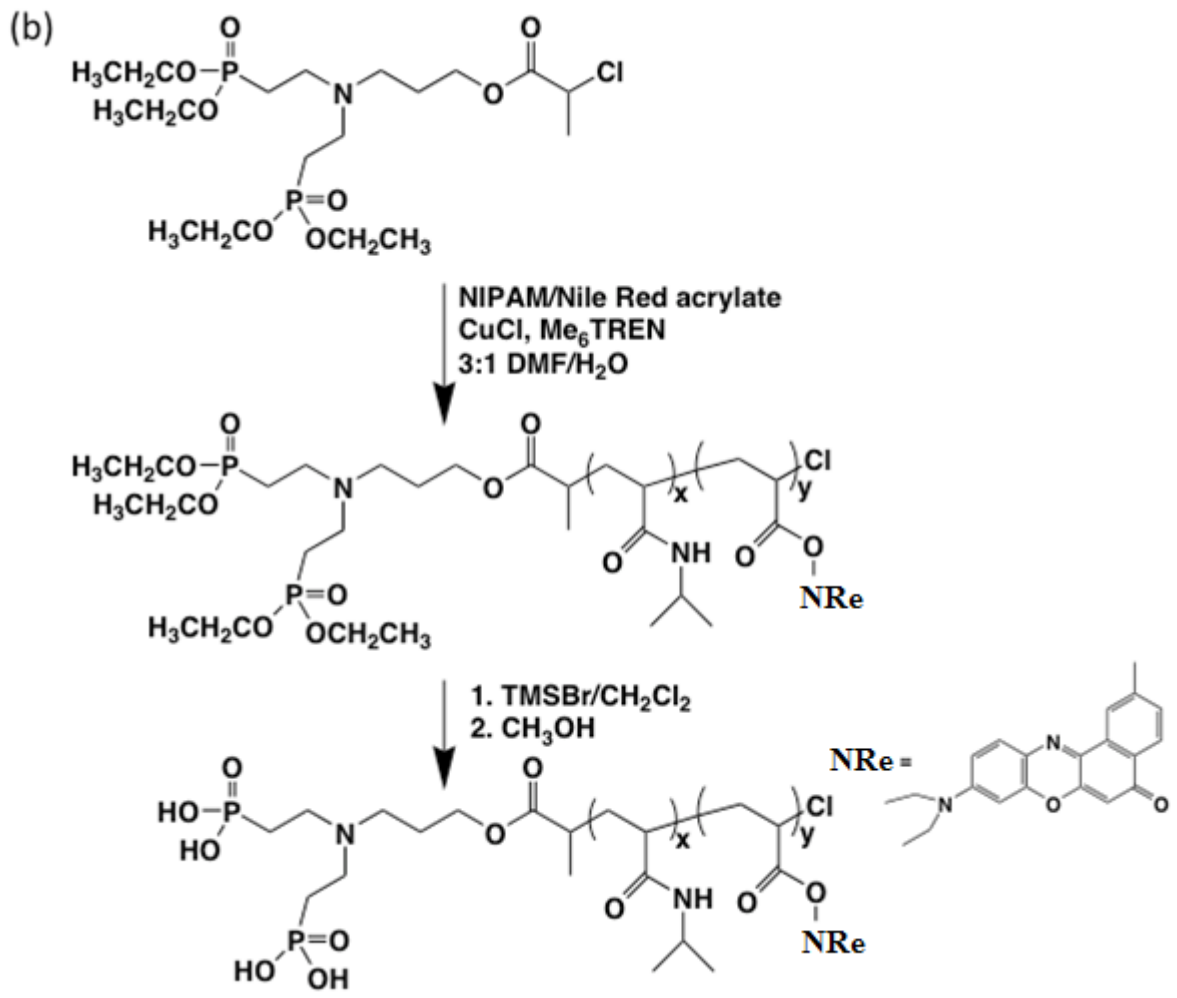

Figure 3.2 Synthesis of a Nile Red-containing acrylate monomer (a), and synthesis of bis(phosphonate) functional PNIPAM-*co*-Nile Red acrylate (b).

3.4.2 Size analysis of PNIPAM-coated iron oxide nanoparticles

Figure 3.3a shows a representative TEM image of the PNIPAM-coated magnetite nanoparticles. Only the magnetite cores are distinguishable because of their relatively high electron density. The sizes of approximately 2400 particles were measured and the data were fitted by the lognormal distribution function:

$$P(r) = \frac{1}{\sqrt{2\pi}\sigma r} e^{\frac{-[\ln\left(\frac{r}{r_m}\right)]^2}{2\sigma^2}} \tag{3.1}$$

where $P(r)$ is the probability density of the distribution, r is the core radius, and r_m and σ^2 are the median radius and variance, respectively. The median radius of the magnetite nanoparticles was 4.14 nm and the standard deviation was 1.52 nm.

(a) (b)

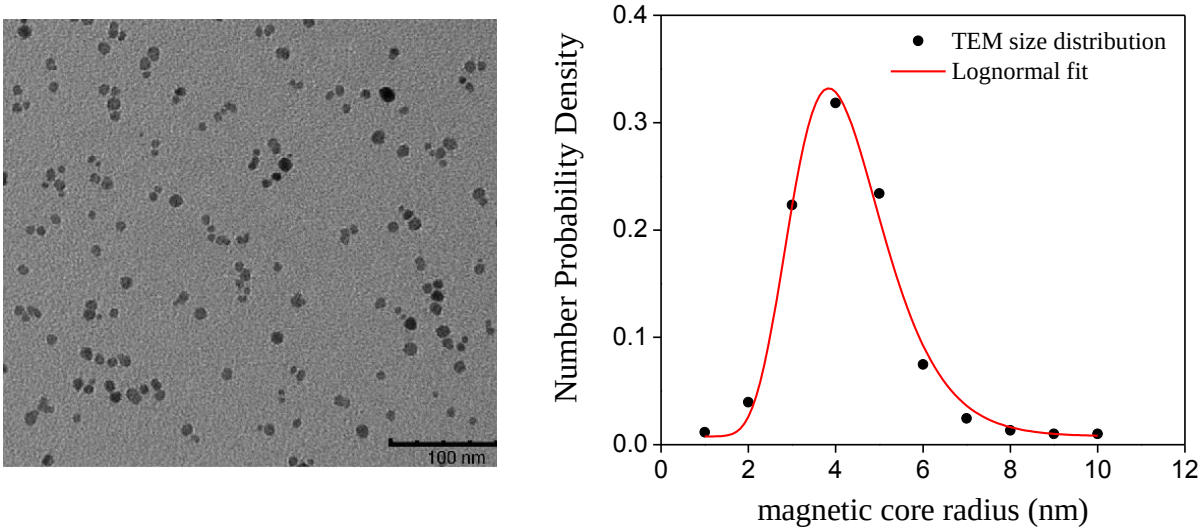

Figure 3.3 Representative TEM image of PNIPAM-coated magnetic iron oxide nanoparticles (a). The measured TEM particle sizes were described by a lognormal distribution function (continuous red line) to yield an average radius of 4.14 ± 1.52 nm (b).

3.4.2.1 *Modeling to predict hydrodynamic sizes*

The hydrodynamic sizes of the PNIPAM-coated iron oxide nanoparticles were estimated using the Vagberg density distribution model, based on a model originally developed for star polymers by Daoud and Cotton.[33,34] This model, modified by Mefford et al. for magnetic nanoparticle-polymer core-shell complexes, has been used to predict the sizes of polyether- and PDMS-coated iron oxide nanoparticles, in water and chloroform respectively, to within 8% without any adjustable

parameters.[35-37] As depicted in Figure 3.4, this model consists of concentric shells of polymer chains emanating from the central magnetic core with a constant number of blobs per shell. The blob diameter, ξ(r), is a continuous function of distance from the surface of the core.

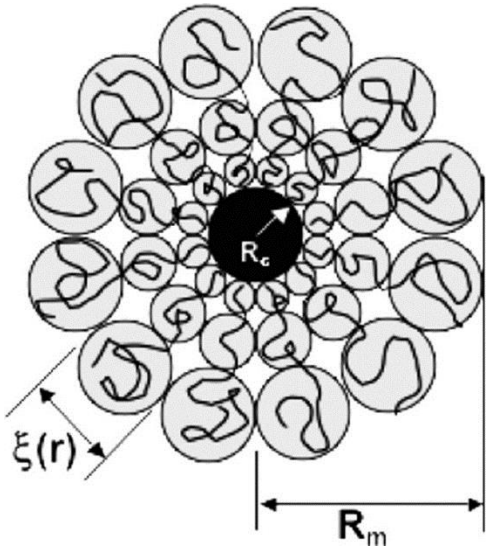

Figure 3.4 Representation of the iron oxide nanoparticle (of radius R_c) coated with a terminally-anchored polymer, based on the Vagberg density distribution model. Reproduced from reference [36], Copyright 2008, with permission from American Chemical Society. Mefford, O. T.; Vadala, M. L.; Goff, J. D.; Carroll, M. R. J.; Mejia-Ariza, R.; Caba, B. L.; St Pierre, T. G.; Woodward, R. C.; Davis, R. M.; Riffle, J. S.: Stability of polydimethylsiloxane-magnetite nanoparticle dispersions against flocculation: Interparticle interactions of polydisperse materials. *Langmuir* **2008**, *24*, 5060-5069. Used with permission from American Chemical Society 2013.

The TEM image analysis data were fitted with a lognormal probability distribution function to calculate the average specific surface area of the iron oxide nanoparticles. The TGA-derived loadings of polymer and iron oxide, combined with the specific surface area lead to the average chain density, α, given as:

$$\alpha = \frac{(1 - w_{IO})N_{av}\rho_{IO}}{3M_n w_{IO}} \int_0^\infty P(r)\, dr \qquad (3.2)$$

where w_{IO}: weight fraction of iron oxide in the iron oxide-PNIPAM complex (0.35)

M_n: number-average molecular weight of PNIPAM (11,000 g/mol)

ρ_{IO}: density of iron oxide (magnetite, 5.18 g/cm^3)

N_{av}: Avogadro's number

$P(r)$: Probability density of the iron oxide core radius

r: radius of the magnetic core

The average number of chains per particle: $f = 4\pi r^2 \alpha$ (3.3)

The complex radius (magnetic core + PNIPAM shell), R_m, is then calculated as follows:

$$R_m(r) = \left\{ \frac{N_k {l_k}^{1/\upsilon}\, 8 f^{(1-\upsilon)/2\upsilon}}{3\upsilon 4^{1/\upsilon}} + r^{1/\upsilon} \right\}^{\upsilon} \quad (3.4)$$

where υ is the Flory exponent for PNIPAM in water at 25°C (= 0.518), and N_k and l_k are the number of statistical segments per PNIPAM chain and the Kuhn segment length given by:

$$N_k = \frac{n}{C_\infty} \quad (3.5)$$

$$l_k = C_\infty l_0 \quad (3.6)$$

In eq. 3.5-3.6, C_∞ is the characteristic ratio of PNIPAM (= 10.6), l_0 is the average length of a backbone bond (= 0.126 nm), and is the number of backbone bonds in a PNIPAM chain (2 × degree of polymerization).[38,39] Assuming the particles were in the Rayleigh scattering regime, the intensity-average diameter, D_{I}, was calculated as:

$$D_{\mathrm{I}} = 2 \frac{\int_0^\infty R_m(r)^6 \; P(r)\, dr}{\int_0^\infty R_m(r)^5 \; P(r)\, dr} \quad (3.7)$$

Using equations 3.2-3.7, the estimated intensity-weighted diameter of the PNIPAM-coated iron oxide complexes was 36 nm, whereas the experimentally measured diameter from DLS was 38 nm. The excellent agreement between the predicted and measured hydrodynamic sizes indicates that the complexes consisted mostly of individually dispersed nanoparticles. This result is especially promising when investigating aggregation-related changes in suspensions of well-defined polymer-coated magnetic nanoparticles. The relatively narrow size distribution of the complexes was also evident from the low polydispersity indices (< 0.15) obtained from DLS.

3.4.3 Magnetic properties

The zero-field-cooled/field-cooled (ZFC/FC) curves for the iron oxide-PNIPAM complexes shown in Figure 3.5a show that the sample is superparamagnetic at 300 K with a maximum blocking temperature of 140 K. The magnetization (M) versus applied field (H) curve for the complexes at 300 K is depicted in Figure 3.5b. The complex has a saturation magnetization (M_S) of 17.5 Am^2/kg at an applied field of 2 T. Since the complex consists of 35 wt% iron oxide, this corresponds to an M_S at room temperature of ~50 Am^2/kg for the iron oxide nanoparticle core. The decrease in saturation magnetization compared to the value of bulk magnetite can be attributed to spin canting caused by reduced coordination and broken exchange at the particle surface and/or broken symmetry associated with crystalline disorder.[40-43]

(a)

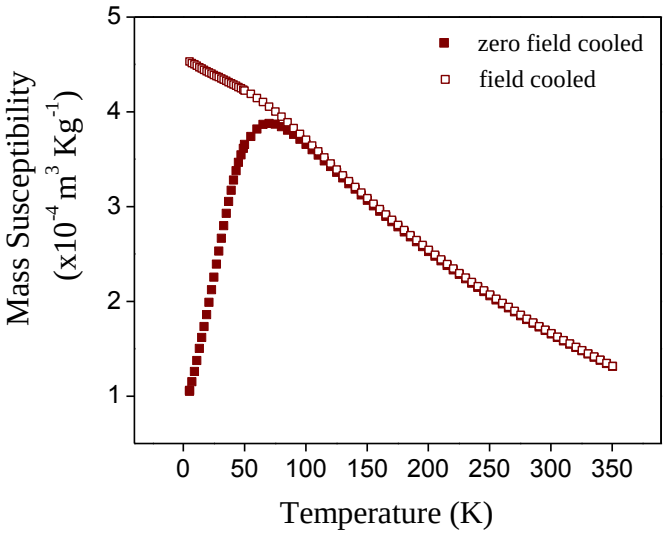

(b)

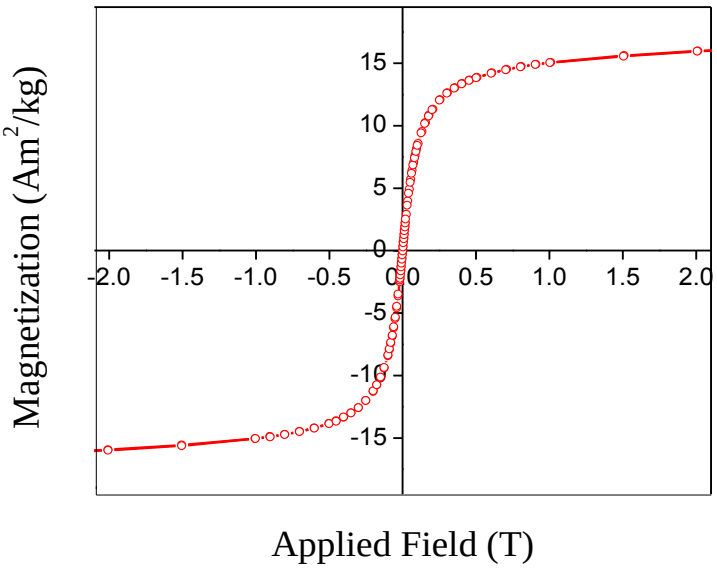

Figure 3.5 (a) The zero-field-cooled/field-cooled (ZFC/FC) curves for the iron oxide-PNIPAM complexes show that the sample is superparamagnetic at 300 K with a maximum blocking temperature of 140 K. (b) The magnetization (*M*) versus applied field (*H*) curve for the complexes at 300 K.

3.4.4 LCST-induced aggregation of PNIPAM-coated iron oxide nanoparticles

3.4.4.1 *Dynamic light scattering*

Thermally-induced aggregation of the nanoparticle complexes in water was characterized by dynamic light scattering. Figure 3.6 shows the evolution of hydrodynamic size of the nanoparticles in water (0.1 mg mL^{-1}) as a function of temperature. The intensity-weighted diameter was recorded at each temperature because of its sensitivity to aggregation arising from the sixth power dependence of the scattering intensity on radius.[44] At 25°C, the complexes exhibited a constant diameter D_I = 38 nm. As the temperature was increased above ~33.5°C, the hydrodynamic size increased, signaling the onset of aggregation induced by passing through the LCST. Below the LCST, the PNIPAM chains are hydrated random coils extending into solution. The highly expanded and mutually repulsive chains are effective in providing steric stabilization to the nanoparticle dispersions and preventing aggregation due to attractive van der Waals forces and magnetic dipolar interactions. When heated above the transition temperature, a thermodynamically-driven phase separation occurs which is characterized by increased contact between the polymer segments accompanied by loss of hydration.[45,46] At the transition temperature, the interaction between the polymer chains changes from net repulsion to net attraction. This results in aggregate formation in the dispersion in the absence of steric stabilization, which is evident as a continuous increase in the hydrodynamic size.

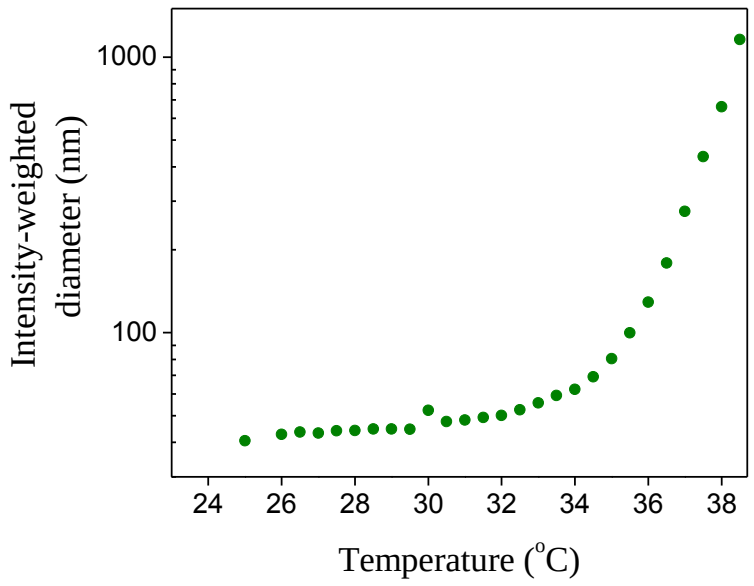

Figure 3.6 Thermally-induced aggregation of the nanoparticle complexes in water was characterized by dynamic light scattering.

3.4.4.2 *Fluorescence spectroscopy*

Aggregation of the complexes above the LCST of the polymer was probed by steady-state fluorescence spectroscopy of the magnetite-PNIPAM nanoparticles containing the Nile Red-acrylate comonomer in the brush layers. An acrylate derivative of the highly fluorescent laser dye, Nile Red, was copolymerized with NIPAM to form a bis(phosphonate)-functional PNIPAM-*co*-Nile Red copolymer, then this copolymer was adsorbed onto the magnetite nanoparticles through the bis(phosphonate) endgroup to form a brush layer. The fluorescence of PNIPAM-*co*-Nile Red-coated nanoparticles in aqueous solution was markedly red-shifted with respect to emission in relatively non-polar solvents with a maximum emission intensity at λ = 665 nm. The solvatochromic behavior of Nile Red has been well studied and the dye has been used by many researchers as a hydrophobic probe owing to its remarkable sensitivity to the polarity of the microenvironment.[47-51] At 25°C in water, there was no difference in fluorescence emission

wavelengths between a PNIPAM-*co*-Nile Red copolymer solution and the magnetite-PNIPAM-*co*-Nile Red nanoparticles. At 35°C, which is above the LCST transition of PNIPAM-*co*-Nile Red, we observed a remarkable quenching of the fluorescence of the magnetite-polymer complex. Such fluorescence quenching is characteristic of aggregated, planar conjugated chromophores like Nile Red.[52,53] In aqueous solution, the fluorescence of Nile Red is normally quenched because it aggregates due to its hydrophobic nature. Covalently incorporating the Nile Red comonomer in the hydrophilic PNIPAM chain prevents the dye from aggregating below the LCST and that this results in the observed fluorescence from the magnetite-PNIPAM-*co*-Nile Red complexes in water at 25°C (Figure 3.7a). It is reasoned that flocculation of the magnetite-PNIPAM-*co*-Nile Red nanoparticles above the LCST of the polymer led to concomitant dye aggregation and fluorescence quenching (Figure 3.7b).

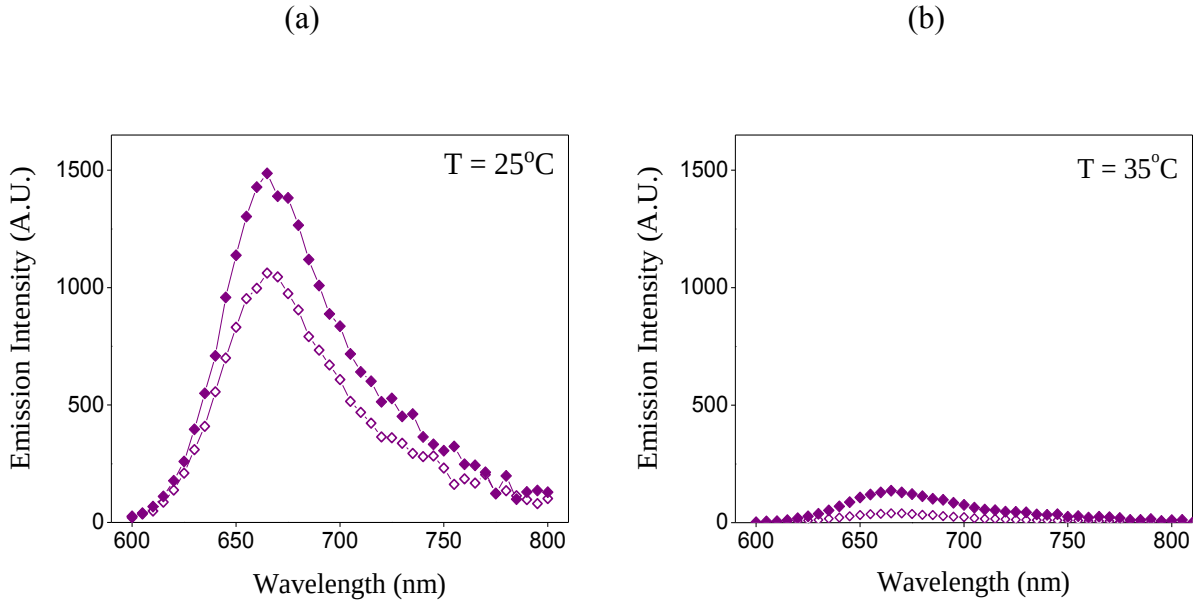

Figure 3.7 Fluorescence of iron oxide-PNIPAM-*co*-Nile Red nanoparticles below LCST (a). Fluorescence quenching due to aggregation of nanoparticles above the LCST (b). Data are shown for concentrations of 0.1 mg mL^{-1} (closed diamonds) and 0.05 mg mL^{-1} (open diamonds).

3.4.4.3 *Magnetic resonance relaxometry*

NMR relaxometry performed on dispersions of the magnetite-PNIPAM complexes as a function of temperature also revealed dramatic shortening of T_2 relaxation times above the LCST transition temperature of PNIPAM. Figure 3.8a shows the results for complexes at concentrations of 0.05 and 0.1 mg mL^{-1}. For relatively small particles, the transverse relaxation time of suspensions of these particles can be represented by the motional averaging regime described by eq. 3.8, where f is the volume fraction occupied by the magnetic particles in suspension, $\Delta\omega$ is the spread of Larmor frequencies at the surface of the particle, r is the particle radius and D is the self-diffusion coefficient of water:[12]

$$\frac{1}{T_2} = \frac{16f(\Delta\omega)^2 r^2}{45D} \tag{3.8}$$

Below the LCST of PNIPAM, where the complexes are individually dispersed nanoparticles, the trend is governed by the temperature dependence of the self-diffusion coefficient of water. The gradual increase in D with temperature causes a concomitant increase in T_2, according to eq. 3.8. However, the T_2 was observed to peak at ~35°C, and this was followed by a sharp and continuous decrease with temperature. This was attributed to the LCST-induced aggregation of complexes causing significant relaxation rate ($1/T_2$) enhancement. The agglomerated nanoparticles, owing to their larger size, have longer correlation times ($=r^2/D$) and shorter T_2 relaxation times. A control experiment was performed with poly(ethylene oxide)-coated iron oxide nanoparticles under the same experimental conditions. These complexes were similar to the PNIPAM-coated iron oxide described in this paper – the polymer loading was 67% and the polymer was anchored to the magnetite using terminal phosphonate moieties. The detailed synthesis and characterization of the magnetite-PEO complexes is described elsewhere.[30,32] As shown in Figure 3.8b, the variation of

T_2 of the PEO-coated iron oxide, unlike the case of PNIPAM-coated nanoparticles, was entirely linear in the range of temperatures studied, reflecting only changes in the self-diffusion coefficient of the water. This confirms that the LCST-induced aggregation of primary PNIPAM-coated nanoparticles was indeed responsible for the observed reduction of T_2 relaxation times.

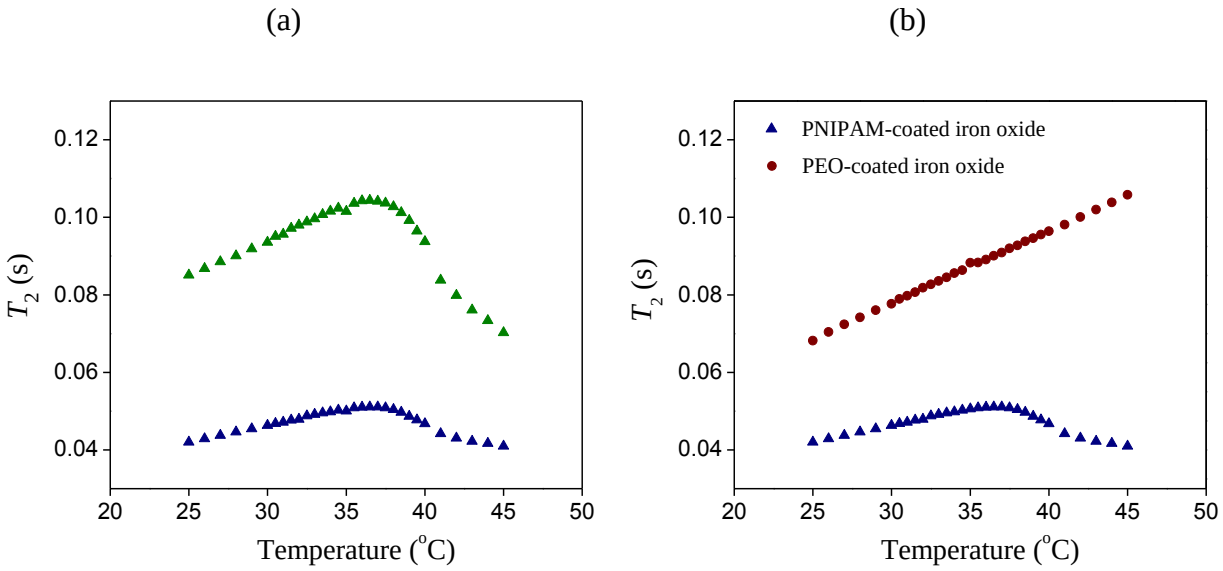

Figure 3.8 LCST-induced aggregation of PNIPAM-coated iron oxide nanoparticles leads to reduction of the T_2 relaxation times (a). Data shown is for 0.05 mg mL^{-1} (green triangles) and 0.1 mg mL^{-1} (blue triangles) of complexes in de-ionized water. Comparison of T_2 relaxation times of PNIPAM-coated iron oxide (blue triangles) and PEO-coated iron oxide nanoparticles (brown circles) at a concentration of 0.1 mg mL^{-1} (b).

According to Roch et al., the formation of aggregates leads to reduction in the exchange of fast-relaxing water protons within the aggregate with the slow-relaxing protons in the bulk water outside the aggregate, thus increasing T_1.[12] Any enhanced hydrophobicity of the polymer above the LCST may also inhibit direct access of water protons to the magnetic particles, which could also increase T_1 relaxation times. This behavior was observed with the iron oxide-PNIPAM

complex above the LCST (Figure 3.9). As in the case for T_2 relaxation, the control iron oxide-PEO complex did not show any noticeable change in the T_1 relaxation times over the range of 25-45°C.

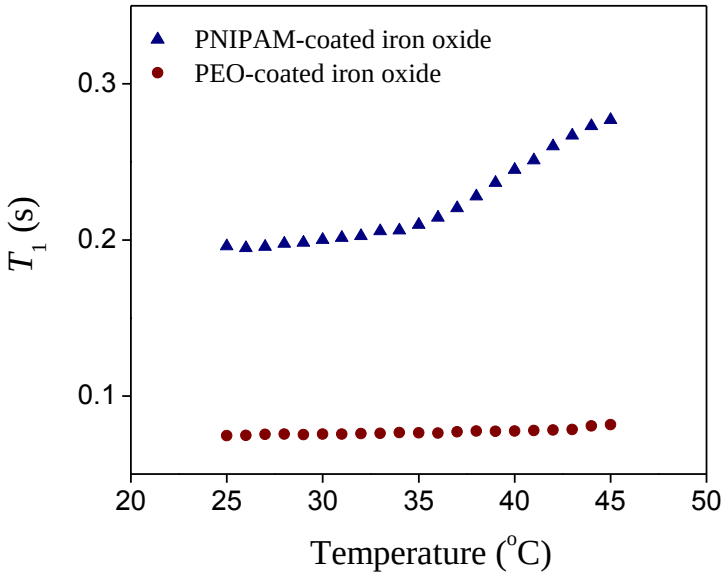

Figure 3.9 Effect of aggregation of PNIPAM-coated iron oxide nanoparticles (blue triangles) on the T_1 relaxation time.

3.4.5 Temperature-magnetic field dual responsivity

Figure 3.10 illustrates the temperature/magnetic field dual responsivity of the magnetite-PNIPAM nanoparticles. At 25°C (< LCST), the particles were highly dispersible in water and exhibited good colloidal stability at concentrations as high as 20 mg mL^{-1}. No sedimentation was observed when a vial containing the dispersion was placed atop a NdFeB permanent magnet. By contrast, at 40°C (> LSCT), there was a sharp increase in turbidity and the particles could be collected with the permanent magnet. The ability to collect the particles with a magnet is due to an increase in the magnetophoretic mobility as the particles aggregate above the LSCT. For the same field and field gradient conditions the magnetophoretic mobility increases with the square of the radius. The dispersibility of the complexes could be fully restored by cooling the dispersions down to room

temperature and sonicating. This experiment provided further confirmatory evidence that the thermoresponsive nature of the PNIPAM shell triggered aggregation of the nanoparticles.

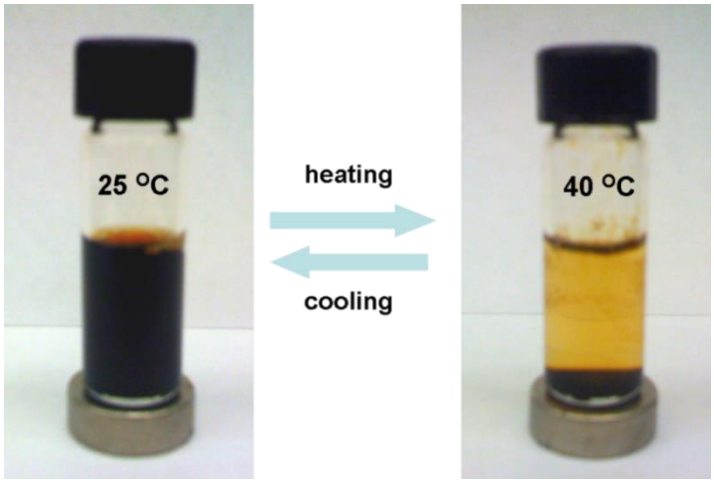

Figure 3.10 Dispersion-flocculation behavior of magnetite-PNIPAM nanoparticles as a function of temperature and magnetic field (c = 20 mg mL^{-1}).

We envisage that both temperature and magnetic field sensitivity offer potential for the design of 'smart' multifunctional magnetic nanocarriers for biomedical applications such as drug delivery combined with the capability to monitor biodistribution through MRI. We believe that the ability to conjugate Nile Red in the brush layers, as demonstrated in this work, lends the thermoresponsive magnetite-PNIPAM-*co*-Nile Red nanoparticles to investigations of localized heating effects under the influence of an external AC magnetic field by monitoring changes in fluorescence. Localized temperature increase in the brush, caused by orientational relaxation processes in the superparamagnetic nanoparticle cores, can be harnessed to potentially release biologically active molecules held in the brush through non-covalent forces.[54,55] Current efforts in our group also include detailed investigations on the thermally-induced aggregation behavior of these nanoparticles with an aim to fabricate controlled magnetic nanoclusters for enhanced performance as T_2 contrast agents.

3.5 Conclusions

We have reported on the thermoresponsive properties of magnetite core-PNIPAM-*co*-Nile Red shell nanoparticles. Well-defined, water-dispersible nanostructures were synthesized via atom transfer radical polymerization of bis(phosphonate)-terminated PNIPAM-*co*-Nile Red acrylate followed by adsorption of the polymer onto discrete magnetite nanoparticles. The temperature-dependent aggregation of nanoparticles induced by the LCST of the PNIPAM-*co*-Nile Red shell was observed by DLS, fluorescence spectroscopy and NMR relaxometry. Aggregation was accompanied by drastic shortening of the transverse relaxation times. In addition, the fluorescence emission derived from the Nile Red acrylate comonomer being dispersed in water below the LCST was quenched dramatically upon aggregation of the copolymer above the LCST. Combining a thermosensitive polymeric shell with a magnetic core paves the way for multistimuli-responsive nanoparticles, such as 'smart' T_2 contrast agents for magnetic resonance imaging or materials for inducing biological response due to changes in brush structure around the magnetic core.

3.6 References

(1) Latorre, M.; Rinaldi, C.: Applications of magnetic nanoparticles in medicine: magnetic fluid hyperthermia. *P R Health Sci J* **2009**, *28*, 227-238.

(2) Krishnan, K. M.: Biomedical nanomagnetics: A spin through possibilities in imaging, diagnostics, and therapy. *IEEE Trans. Magn.* **2010**, *46*, 2523-2558.

(3) Purushotham, S.; Ramanujan, R. V.: Modeling the performance of magnetic nanoparticles in multimodal cancer therapy. *J. Appl. Phys.* **2010**, *107*.

(4) Jain, T. K.; Morales, M. A.; Sahoo, S. K.; Leslie-Pelecky, D. L.; Labhasetwar, V.: Iron oxide nanoparticles for sustained delivery of anticancer agents. *Mol. Pharm.* **2005**, *2*, 194-205.

(5) Wilson, K. S.; Goff, J. D.; Riffle, J. S.; Harris, L. A.; St Pierre, T. G.: Polydimethylsiloxane-magnetite nanoparticle complexes and dispersions in polysiloxane carrier fluids. *Polym. Adv. Technol.* **2005**, *16*, 200-211.

(6) Mefford, O. T.; Woodward, R. C.; Goff, J. D.; Vadala, T. P.; St Pierre, T. G.; Dailey, J. P.; Riffle, J. S.: Field-induced motion of ferrofluids through immiscible viscous media: Testbed for restorative treatment of retinal detachment. *J. Magn. Magn. Mater.* **2007**, *311*, 347-353.

(7) Bulte, J. W. M.; Kraitchman, D. L.: Iron oxide MR contrast agents for molecular and cellular imaging. *NMR Biomed.* **2004**, *17*, 484-499.

(8) Lee, H.; Lee, E.; Kim, D. K.; Jang, N. K.; Jeong, Y. Y.; Jon, S.: Antibiofouling polymer-coated superparamagnetic iron oxide nanoparticles as potential magnetic resonance contrast agents for in vivo cancer imaging. *J. Am. Chem. Soc.* **2006**, *128*, 7383-7389.
(9) Regmi, R.; Bhattarai, S. R.; Sudakar, C.; Wani, A. S.; Cunningham, R.; Vaishnava, P. P.; Naik, R.; Oupicky, D.; Lawes, G.: Hyperthermia controlled rapid drug release from thermosensitive magnetic microgels. *J. Mater. Chem.* **2010**, *20*, 6158-6163.
(10) Weissleder, R.; Bogdanov, A.; Neuwelt, E. A.; Papisov, M.: Long-circulating iron-oxides for MR-imaging. *Adv. Drug Deliv. Rev.* **1995**, *16*, 321-334.
(11) Matsumoto, Y.; Jasanoff, A.: T-2 relaxation induced by clusters of superparamagnetic nanoparticles: Monte Carlo simulations. *Magn. Reson. Imaging* **2008**, *26*, 994-998.
(12) Roch, A.; Gossuin, Y.; Muller, R. N.; Gillis, P.: Superparamagnetic colloid suspensions: Water magnetic relaxation and clustering. *J. Magn. Magn. Mater.* **2005**, *293*, 532-539.
(13) Carroll, M. R. J.; Woodward, R. C.; House, M. J.; Teoh, W. Y.; Amal, R.; Hanley, T. L.; St Pierre, T. G.: Experimental validation of proton transverse relaxivity models for superparamagnetic nanoparticle MRI contrast agents. *Nanotechnology* **2010**, *21*.
(14) Gillis, P.; Moiny, F.; Brooks, R. A.: On T-2-shortening by strongly magnetized spheres: A partial refocusing model. *Magn. Reson. Med.* **2002**, *47*, 257-263.
(15) Yablonskiy, D. A.; Haacke, E. M.: Theory of NMR signal behavior in magnetically inhomogeneous tissues - The static dephasing regime. *Magn. Reson. Med.* **1994**, *32*, 749-763.
(16) Bedanta, S.; Kleemann, W.: Supermagnetism. *J. Phys. D-Appl. Phys.* **2009**, *42*.
(17) Berret, J. F.; Schonbeck, N.; Gazeau, F.; El Kharrat, D.; Sandre, O.; Vacher, A.; Airiau, M.: Controlled clustering of superparamagnetic nanoparticles using block copolymers: Design of new contrast agents for magnetic resonance imaging. *J. Am. Chem. Soc.* **2006**, *128*, 1755-1761.
(18) Ai, H.; Flask, C.; Weinberg, B.; Shuai, X.; Pagel, M. D.; Farrell, D.; Duerk, J.; Gao, J. M.: Magnetite-loaded polymeric micelles as ultrasensitive magnetic-resonance probes. *Adv. Mater.* **2005**, *17*, 1949-1952.
(19) Carroll, M. R. J.; Huffstetler, P. P.; Miles, W. C.; Goff, J. D.; Davis, R. M.; Riffle, J. S.; House, M. J.; Woodward, R. C.; St Pierre, T. G.: The effect of polymer coatings on proton transverse relaxivities of aqueous suspensions of magnetic nanoparticles. *Nanotechnology* **2011**, *22*.
(20) Osborne, E. A.; Jarrett, B. R.; Tu, C. Q.; Louie, A. Y.: Modulation of T2 relaxation time by light-induced, reversible aggregation of magnetic nanoparticles. *J. Am. Chem. Soc.* **2010**, *132*, 5934-5935.
(21) Perez, J. M.; Josephson, L.; O'Loughlin, T.; Hogemann, D.; Weissleder, R.: Magnetic relaxation switches capable of sensing molecular interactions. *Nat. Biotechnol.* **2002**, *20*, 816-820.
(22) Schellenberger, E.; Rudloff, F.; Warmuth, C.; Taupitz, M.; Hamm, B.; Schnorr, J.: Protease-specific nanosensors for magnetic resonance imaging. *Bioconjugate Chem.* **2008**, *19*, 2440-2445.
(23) M. Heskins; Guillet, J. E.: Solution properties of poly(N-isopropylacrylamide). *J. Macromol. Sci. A: Pure & Appl. Chem.* **1968**, *2*, 1441-1455.
(24) Pothayee, N.; Balasubramaniam, S.; Davis, R. M.; Riffle, J. S.; Carroll, M. R. J.; Woodward, R. C.; Pierre, T. G. S.: Synthesis of 'ready-to-adsorb' polymeric nanoshells for magnetic iron oxide nanoparticles via atom transfer radical polymerization. *Polymer* **2011**, *52*, 1356-1366.
(25) Rubio-Retama, J.; Zafeiropoulos, N. E.; Serafinelli, C.; Rojas-Reyna, R.; Voit, B.; Cabarcos, E. L.; Stamm, M.: Synthesis and characterization of thermosensitive PNIPAM

microgels covered with superparamagnetic gamma-Fe2O3 nanoparticles. *Langmuir* **2007**, *23*, 10280-10285.
(26) Herrera, A. P.; Barrera, C.; Zayas, Y.; Rinaldi, C.: Monitoring colloidal stability of polymer-coated magnetic nanoparticles using AC susceptibility measurements. *J. Coll. Interf. Sci.* **2010**, *342*, 540-549.
(27) Herrera, A. P.; Rodriguez, M.; Torres-Lugo, M.; Rinaldi, C.: Multifunctional magnetite nanoparticles coated with fluorescent thermo-responsive polymeric shells. *J. Mater. Chem.* **2008**, *18*, 855-858.
(28) Xia, J. H.; Gaynor, S. G.; Matyjaszewski, K.: Controlled/"living" radical polymerization. Atom transfer radical polymerization of acrylates at ambient temperature. *Macromolecules* **1998**, *31*, 5958-5959.
(29) Pinna, N.; Grancharov, S.; Beato, P.; Bonville, P.; Antonietti, M.; Niederberger, M.: Magnetite nanocrystals: Nonaqueous synthesis, characterization, and solubility. *Chem. Mater.* **2005**, *17*, 3044-3049.
(30) Goff, J. D.; Huffstetler, P. P.; Miles, W. C.; Pothayee, N.; Reinholz, C. M.; Ball, S.; Davis, R. M.; Riffle, J. S.: Novel phosphonate-functional poly(ethylene oxide)-magnetite nanoparticles form stable colloidal dispersions in phosphate-buffered saline. *Chem. Mater.* **2009**, *21*, 4784-4795.
(31) S. J. Briggs, M.; Bruce, I.; N. Miller, J.; J. Moody, C.; C. Simmonds, A.; Swann, E.: Synthesis of functionalised fluorescent dyes and their coupling to amines and amino acids. *J. Chem. Soc., Perkin Trans. 1* **1997**, 1051-1058.
(32) Miles, W. C.; Goff, J. D.; Huffstetler, P. P.; Reinholz, C. M.; Pothayee, N.; Caba, B. L.; Boyd, J. S.; Davis, R. A.; Riffle, J. S.: Synthesis and colloidal properties of polyether-magnetite complexes in water and phosphate-buffered saline. *Langmuir* **2009**, *25*, 803-813.
(33) Vagberg, L. J. M.; Cogan, K. A.; Gast, A. P.: Light-scattering study of starlike polymeric micelles. *Macromolecules* **1991**, *24*, 1670-1677.
(34) Daoud, M.; Cotton, J. P.: Star-shaped polymers: a model for the conformation and its concentration dependence. *J. Phys.* **1982**, *43*, 531-538.
(35) Mefford, O. T.; Carroll, M. R. J.; Vadala, M. L.; Goff, J. D.; Mejia-Ariza, R.; Saunders, M.; Woodward, R. C.; St Pierre, T. G.; Davis, R. M.; Riffle, J. S.: Size analysis of PDMS-magnetite nanoparticle complexes: Experiment and theory. *Chem. Mater.* **2008**, *20*, 2184-2191.
(36) Mefford, O. T.; Vadala, M. L.; Goff, J. D.; Carroll, M. R. J.; Mejia-Ariza, R.; Caba, B. L.; St Pierre, T. G.; Woodward, R. C.; Davis, R. M.; Riffle, J. S.: Stability of polydimethylsiloxane-magnetite nanoparticle dispersions against flocculation: Interparticle interactions of polydisperse materials. *Langmuir* **2008**, *24*, 5060-5069.
(37) Miles, W. C.; Goff, J. D.; Huffstetler, P. P.; Mefford, O. T.; Riffle, J. S.; Davis, R. M.: The design of well-defined PDMS-magnetite complexes. *Polymer* **2010**, *51*, 482-491.
(38) Fang, Z.; Zhen, T.; Sato, T. Molecular chain properties of poly(N-isopropyl acrylamide). *Sci. China, Ser. B: Chem*. **1999**, *42*, 290–297.
(39) Hirotsu, S. Softening of bulk modulus and negative Poisson's ratio near the volume phase transition of polymer gels. *J. Chem. Phys*. **1991**, *94*, 3949-3957.
(40) Li, D.; Teoh, W. Y.; Woodward, R. C.; Cashion, J. D.; Selomulya, C.; Amal, R.: Evolution of morphology and magnetic properties in silica/maghemite nanocomposites. *J. Phys. Chem. C* **2009**, *113*, 12040-12047.
(41) Morup, S.: Spin-canting and transverse relaxation at surfaces and in the interior of ferrimagnetic particles. *J. Magn. Magn. Mater.* **2003**, *266*, 110-118.

(42) Kodama, R. H.; Berkowitz, A. E.; McNiff, E. J.; Foner, S.: Surface spin disorder in NiFe2O4 nanoparticles. *Phys. Rev. Lett.* **1996**, *77*, 394-397.
(43) Morales, M. P.; Veintemillas-Verdaguer, S.; Montero, M. I.; Serna, C. J.; Roig, A.; Casas, L.; Martínez, B.; Sandiumenge, F.: Surface and internal spin canting in γ-Fe2O3 nanoparticles. *Chem. Mater.* **1999**, *11*, 3058-3064.
(44) Berne, B. J.; Pecora, R.: Dynamic light scattering: with applications to chemistry, biology, and physics; Wiley: New York, **1976**.
(45) Schild, H. G.: Poly(N-isopropylacrylamide) – Experiment, theory and application. *Prog. Polym. Sci.* **1992**, *17*, 163-249.
(46) Pelton, R.: Poly(N-isopropylacrylamide) (PNIPAM) is never hydrophobic. *J. Coll. Interf. Sci.* **2010**, *348*, 673-674.
(47) Greenspan, P.; Fowler, S. D.: Spectrofluorometric studies of the lipid probe, nile red. *J. Lipid Res.* **1985**, *26*, 781-789.
(48) Dutta, A. K.; Kamada, K.; Ohta, K.: Spectroscopic studies of nile red in organic solvents and polymers. *J. Photochem. Photobiol. A-Chem.* **1996**, *93*, 57-64.
(49) Tajalli, H.; Gilani, A. G.; Zakerhamidi, M. S.; Tajalli, P.: The photophysical properties of nile red and nile blue in ordered anisotropic media. *Dyes and Pigments* **2008**, *78*, 15-24.
(50) Vauthey, E.: Picosecond transient grating study of the reorientation dynamics of nile red in different classes of solvent. *Chem. Phys. Lett.* **1993**, *216*, 530-536.
(51) Daban, J. R.; Samso, M.; Bartolome, S.: Use of nile red as a fluorescent-probe for the study of the hydrophobic properties of protein sodium dodecyl-sulfate complexes in solution. *Anal. Biochem.* **1991**, *199*, 162-168.
(52) Levitsky, I.; Krivoshlykov, S. G.; Grate, J. W.: Rational design of a nile Red/polymer composite film for fluorescence sensing of organophosphonate vapors using hydrogen bond acidic polymers. *Anal. Chem.* **2001**, *73*, 3441-3448.
(53) deSilva, A. P.; Gunaratne, H. Q. N.; Gunnlaugsson, T.; Huxley, A. J. M.; McCoy, C. P.; Rademacher, J. T.; Rice, T. E.: Signaling recognition events with fluorescent sensors and switches. *Chem. Rev.* **1997**, *97*, 1515-1566.
(54) Rahimi, M.; Wadajkar, A.; Subramanian, K.; Yousef, M.; Cui, W.; Hsieh, J.-T.; Nguyen, K. T.: In vitro evaluation of novel polymer-coated magnetic nanoparticles for controlled drug delivery. *Nanomedicine: Nanotechnol., Biol. Med.* **2010**, *6*, 672-680.
(55) Hoare, T.; Santamaria, J.; Goya, G. F.; Irusta, S.; Lin, D.; Lau, S.; Padera, R.; Langer, R.; Kohane, D. S.: A magnetically triggered composite membrane for on-demand drug delivery. *Nano Lett.* **2009**, *9*, 3651-3657.

4 Towards Design of Magnetic Nanoparticle Clusters Stabilized by Biocompatible Diblock Copolymers for T_2-Weighted MRI Contrast

Sharavanan Balasubramaniam,[†] *Sanem Kayandan,*[†] *Yin-Nian Lin*,[†] *Deborah F. Kelly*,[§] *Michael J. House,*[‡] *Robert C. Woodward,*[‡] *Timothy G. St. Pierre,*[‡] *Judy S. Riffle*[†] *and Richey M. Davis*[†]

[†]Macromolecules and Interfaces Institute, Virginia Tech, Blacksburg, VA 24061, U. S. A.
[§]Virginia Tech Carilion Research Institute, Roanoke, VA 24016, U. S. A.
[‡]School of Physics, The University of Western Australia, Crawley, Western Australia 6009, Australia.

Reproduced with permission from *Langmuir* **2014**, DOI: 10.1021/la403591z.

4.1 Abstract

This chapter describes the fabrication of magnetic particles comprised of clusters of iron oxide nanoparticles (7.4 nm mean diameter) stabilized by a biocompatible, amphiphilic diblock copolymer, poly(ethylene oxide-*b*-D,L-lactide). Particles with quantitative incorporation of up to 40 wt% iron oxide and hydrodynamic sizes in the range of 80-170 nm were prepared. The particles consist of hydrophobically-modified iron oxide nanoparticles within the core-forming polylactide block with the poly(ethylene oxide) forming a corona to afford aqueous dispersibility. The transverse relaxivities (r_2) increased with average particle size and exceeded 200 s^{-1} mM Fe^{-1} at 1.4 T and 37°C for iron oxide loadings above 30 wt%. These experimental relaxivities typically agreed to within 15% with the values predicted using analytical models of transverse relaxivity and cluster (particle core) size distributions derived from cryo-TEM measurements. Our results show that the theoretical models can be used for the rational design of biocompatible MRI contrast agents with

tailored compositions and size distributions. Furthermore, we note that particles with hydrophilic microenvironments have considerably higher experimental relaxivities than the hydrophobic-core particles at similar primary nanoparticle and overall particle sizes and iron oxide loadings. These results indicate that the internal particle structure is an important determinant of the observed transverse relaxivities.

4.2 Introduction

Over the last decade, there has been considerable interest in integrating imaging agents and therapeutics into one system by their co-encapsulation within macromolecular carriers to enable 'theranostic' nanoparticles for delivering drugs and simultaneously monitoring their biodistribution *in vivo*.[1-3] Magnetic iron oxide nanoparticles are known to shorten the transverse relaxation times (T_2) of water and have been approved by the United States Food and Drug Administration (FDA) as negative contrast agents for magnetic resonance imaging (MRI).[4,5] Magnetite (Fe_3O_4) and maghemite (γ-Fe_2O_3) nanoparticles (size < 20 nm) have been studied as T_2 contrast agents for bioimaging owing to their good magnetic properties and biocompatibility. Upon exposure to an external magnetic field, nanoparticulate iron oxides with high magnetic susceptibility induce strong local field inhomogeneities leading to an increase in the NMR transverse relaxation rate (R_2) of the water protons. The sensitivity of the contrast agent is expressed in terms of the transverse relaxivity (r_2) that is the proton relaxation rate enhancement per millimolar iron and is a function of particle size, magnetization and aggregation.[6-8] Higher transverse relaxivities translate into better image contrast in T_2-weighted MRI.

It has been found in our previous studies and elsewhere that controlled aggregation of magnetic nanoparticles can produce a greater R_2 increase than the primary nanoparticles and are therefore more effective as MRI contrast agents.[7-12] This effect can be attributed to either an increase in

average size, via clustering, that within the motional averaging regime leads to higher r_2 values, or due to a larger fraction of the cluster size distribution being within the static dephasing regime, where r_2 reaches its maximum value. Recently, an appreciable amount of research has been focused on designing stable clusters of magnetic nanoparticles in various geometries where high transverse relaxivities (300-600 s^{-1} mM Fe^{-1}) have been achieved.[13-18] However, adequate control over particle sizes and magnetic nanoparticle loadings has not been demonstrated so far.

The objective of this work is to elucidate the structure-property relationships governing the transverse relaxivity of polymer particles containing iron oxide nanoparticles within the framework of the analytical models of transverse relaxivity. Many particle systems designed for MRI contrast enhancement are comprised of broad size distributions which can only be described using a combination of models for the motional averaging, static dephasing and echo-limited regimes.[12] Therefore, reliable characterization of the particle size distributions and their incorporation in the r_2 modeling is important to achieve quantitative correlations of transverse relaxivities with the analytical models.[12] Carroll et al. showed that the analytical models satisfactorily predicted the r_2 relaxivities of predominantly single maghemite nanoparticles when the relaxation rates given by the analytical models for the three relaxation regimes were integrated over size distributions derived from small angle X-ray scattering.[12] However, the accurate prediction of transverse relaxivities of hybrid magnetic nanostructures such as iron oxide-block copolymer clusters with appreciable size polydispersities has remained a challenge.[15,19] This issue is especially important when designing theranostic particles that combine an MRI imaging contrast function with a drug delivery capability. In one study, a comparison between experimental r_2 and analytical model predictions was made for nanoparticles comprised of polymethacrylate-based microgels that contained iron oxide.[18] The predictions were based on the average particle sizes

measured by dynamic light scattering (DLS) rather than by integrating over the entire size distribution and semi-quantitative agreement was found. This and other studies point to the need to quantitatively account for the particle size distribution in order to accurately predict relaxivities.

The preparation of colloidally-stable biocompatible nanoparticles is of prime importance from an *in vivo* standpoint. The most common strategy for stabilizing magnetic nanoparticle clusters is to encapsulate them within diblock copolymers where one block provides complexation with the active ingredients and the other block, often poly(ethylene oxide), imparts aqueous dispersibility and reduces uptake by the reticuloendothelial system (RES).[20] In this regard, core-shell structures formed of biocompatible, amphiphilic diblock copolymers are noteworthy, where hydrophobic cores formed from biodegradable polymers such as poly(D,L-lactide), poly(D,L-lactide-*co*-glycolide) or poly(ε-caprolactone) can be used to encapsulate hydrophobically-modified magnetic nanoparticles into clusters.[16,21,22] High transverse relaxivities have been achieved with these clusters compared to individually-dispersed nanoparticles. The fabrication route towards controlled magnetic nanoparticle-copolymer clusters has mostly relied on emulsion or solvent evaporation methods which can suffer from several disadvantages such as low loading efficiencies and inadequate control over particle sizes and loadings. Prud'homme and co-workers have reported extensively on a scalable rapid precipitation technique using a multi-inlet vortex mixer to produce stable nanoparticles containing drugs, imaging agents, peptides and targeting ligands.[23-27] In this method, an organic stream containing the imaging agents and/or drugs and a block copolymer stabilizer is rapidly combined with a miscible non-solvent (water) under high supersaturations to yield kinetically-trapped nanoparticles with controlled compositions and sizes.[28]

Herein, we report biocompatible magnetic particles consisting of iron oxide nanoparticles clustered within the amphiphilic diblock copolymer, 5k-poly(ethylene oxide)-*b*-10k-poly(D,L-lactide) fabricated by rapid precipitation in a multi-inlet vortex mixer. The particles were characterized using dynamic light scattering, thermogravimetric analysis, cryo-transmission electron microscopy, SQuID magnetometry and NMR relaxometry. Biocompatible magnetic particles with a range of sizes and iron oxide loadings enable investigations of structure-relaxivity relationships within the framework of the analytical models of transverse relaxivity. We compare the experimental r_2 values with those predicted from analytical models, accounting for the effects of cluster size distribution. Finally, we compare the transverse and longitudinal relaxivities of hydrophobic- and hydrophilic-core particles, providing new insights into the effect of the internal particle structure on the observed relaxivities.

4.3 Experimental Section

4.3.1 Materials

Iron (III) acetylacetonate, tin (II) 2-ethylhexanoate (stannous octoate), benzyl alcohol (> 98%), oleic acid (OA, 90%, technical grade) and tetrahydrofuran (THF, anhydrous) were purchased from Aldrich and used as received. Diethyl ether (anhydrous) and ethyl acetate (HPLC grade) were purchased from Fisher Scientific and used as received. Toluene (Fischer Scientific) was stirred over calcium hydride and distilled. D,L-lactide was obtained from Purac and recrystallized from ethyl acetate twice. Poly(ethylene oxide) methyl ether (mPEG) macroinitiator with a molar mass of ~5000 g mol^{-1} was obtained from Aldrich and vacuum-dried at room temperature for 18 h before use. Uranyl formate was purchased from Electron Microscopy Sciences (Hatfield, PA, U. S. A.) and diluted to 1% in Milli-Q water for use.

4.3.2 Synthesis of oleic acid-coated iron oxide nanoparticles

Magnetic iron oxide nanoparticles were synthesized using a method adapted from Pinna et al.[29,30] Iron (III) acetylacetonate (2.14 g, 8.4 mmol) and benzyl alcohol (45 mL, 0.43 mol) were charged into a 250-mL, three-neck, round bottom flask equipped with an overhead stirrer and placed in a Belmont metal bath with thermostatic control (± 1°C). The solution was heated at 115°C for 1 h under N_2. The reaction temperature was subsequently increased to 205°C over 4 h and maintained for 40 h. The reaction mixture was cooled to room temperature and the nanoparticles were collected by centrifugation (4000 rpm, 30 min) and washed three times with acetone. The nanoparticles were dried at room temperature under N_2 for 30 min and dispersed in chloroform (20 mL) containing oleic acid (0.3 mL). The solvent was removed by rotary evaporation and the oleic acid-coated iron oxide nanoparticles were washed three times with acetone to remove excess oleic acid. The nanoparticles were dried under vacuum for 24 h at 25°C.

4.3.3 Synthesis of poly(ethylene oxide-*b*-D,L-lactide)

A 5k-mPEG-*b*-10k-PDLLA M_n block copolymer was synthesized by ring-opening polymerization of D,L-lactide initiated by mPEG using stannous octoate as the catalyst.[31] D,L-lactide (4.44 g, 0.03 mol), mPEO (2.22 g, 4.44 x 10^{-4} mol) and 17 mL toluene were charged to a 250-mL, flame-dried, round bottom flask equipped with a magnetic stir bar. The flask was placed in an oil bath at 80°C to dissolve the monomer and initiator. A stock solution of stannous octoate in toluene was prepared with a concentration of 0.012 g mL^{-1}. The catalyst solution (0.98 mL) was added to the flask and the temperature of the oil bath was raised to 105°C. The polymerization was allowed to proceed for 48 h. The polymer was isolated by precipitation into cold diethyl ether and collected by vacuum filtration. The product was vacuum dried at 40°C for 40 h, with yield 5.68 g.

4.3.4 Fabrication of iron oxide-block copolymer particles

A representative procedure for preparing copolymer-stabilized oleic acid-coated magnetic nanoparticle clusters containing 30 wt% iron oxide (sample C3) is as follows. Oleic acid-coated iron oxide (OA-IO, 64 mg) was added to tetrahydrofuran (THF) (3.5 mL) containing mPEG-*b*-PDLLA (115.5 mg). A four-jet multi-inlet vortex mixer design based on one previously reported was used to form the particles.[25] The THF solution was fed into the multi-inlet vortex mixer at 11.6 mL min^{-1} using a computer-controlled syringe pump (New Era Pump Systems, Farmingdale, New York) along with three streams of de-ionized water at 38.5 mL min^{-1}, controlled by a PHD 4000 programmable syringe pump (Harvard Apparatus, Holliston, Massachusetts), yielding a final liquid phase composition of 1:10 (v/v) THF/water. These flow rates corresponded to a mixing Reynolds number of approximately 12,540. After the suspension was formed in the mixer, it was dialyzed to remove THF against de-ionized water (4000 mL) for 24 h using a Spectra/Por dialysis bag (25,000 MWCO, Spectrum Laboratories, Inc.) with four changes of dialysate. The dialyzed suspension was freeze-dried for 72 h (0.021 mBar, -52°C) and stored as a solid until it was needed for suspension experiments.

4.3.5 Characterization

The iron oxide content of the oleic acid-coated primary nanoparticles and the copolymer stabilized particles were determined by thermogravimetric analysis (Q5000 TGA, TA Instruments). Samples (10-15 mg) were heated in a nitrogen atmosphere up to 700°C at a rate of 10°C min^{-1}. The mass remaining (%) at 700°C was reported as the weight fraction of iron oxide in the particles. The magnetization of the samples was measured by superconducting quantum interference device

(SQuID) magnetometry (7T MPMS, Quantum Design). The magnetization versus applied field (*M-H*) curve was measured for dry samples at 300 K between -4 to +4 T.

4.3.5.1 *Size Analysis*

The size of the oleic acid-coated iron oxide nanoparticles was determined by transmission electron microscopy using a Philips Model EM420 TEM. A drop of the nanoparticle suspension in hexane ($c = 0.1$ mg mL^{-1}) was cast on an amorphous carbon-coated copper grid. Images were acquired at a magnification of 96,000×. The sizes of over 1000 nanoparticles were measured using image analysis software (Reindeer Graphics' Fovea Pro 4 plug-in for Adobe Photoshop) and fitted using a lognormal distribution function to determine the mean diameter. The size distributions of the iron oxide-block copolymer particles were measured by dynamic light scattering (DLS) and by nanoparticle tracking analysis (NTA). DLS was performed at 25°C on a Zetasizer Nano-ZS particle analyzer (Malvern Instruments Ltd., Worcestershire, U. K.) equipped with a 4 mW He-Ne laser ($\lambda = 633$ nm) and backscatter detection (scattering angle = 173°). The average translational diffusion coefficient was extracted from a cumulants fit of the scattered intensity correlation curve and the intensity-weighted hydrodynamic diameter (D_I) was determined through the Stokes-Einstein equation using the Zetasizer Nano 6.2 software. Lyophilized samples were dispersed in de-ionized water at a concentration of 0.1 mg mL^{-1} and sonicated in a water bath sonicator (Model 8890, Cole Parmer) for 10 min prior to analysis. The reported intensity-weighted diameter for each sample was averaged from five measurements. Number-weighted size distributions were measured by nanoparticle tracking analysis on a NanoSight NS500 (NanoSight Ltd., Amesbury, U. K.). The sample preparation and concentration were the same as for DLS.

The size distributions of the particle cores (denoted as 'clusters') were characterized by cryo-TEM. For this method, 2 μL aliquots of each sample (2.5 mg mL^{-1}) were applied to glow-discharged C-flat holey carbon EM grids (Protochips, Inc.) having 2-micron holes and 1-micron of carbon spacer between the holes. Following a 1-minute incubation step at room temperature, each grid was blotted for 7-9 seconds and plunge-frozen into liquid ethane using a Cryoplunge 3 device with GentleBlot technology (Gatan, Inc., Pleasanton, CA). Frozen-hydrated specimens were transferred to a 626 Gatan cryo-holder under liquid nitrogen and remained at a temperature of -180°C until entering the TEM. The frozen-hydrated specimens were imaged using a FEI Spirit BioTwin TEM (FEI Company, Hillsboro, OR) equipped with a LaB_6 filament operating at 120 kV under low-dose conditions (~ 3 electrons / $Å^2$). Images of clusters located in the holes were recorded on a FEI Eagle 2k HS CCD camera having a pixel size of 30 μm at a nominal magnification of 50,000× with a final sampling of 6 Å per pixel. We used a defocus value of −1.0 μm and collected 6 images of sample C1, 26 images of C2, 47 images of C3 and 42 images of C4. We selected and windowed out individual clusters from the images that were intact and sufficiently distanced from other particles using the SPIDER software package.[32] Selected clusters used for size analysis totaled 491 for C1, 711 for C2, 478 for C3, and 649 for C4. We used the distance measure function in SPIDER to accurately determine the diameter along the longest axis of each cluster and the measured values were tabulated into a text file and used for further analysis. In addition to cryo-TEM, TEM images were obtained for dried specimens stained with 1% uranyl formate to visualize the polymer shell which made it possible to investigate samples consisting of a mixture of iron oxide-block copolymer particles along with empty polymeric particles.

4.3.5.2 *Relaxivity Measurements*

Proton transverse (r_2) and longitudinal (r_1) relaxivities of the particles were measured in de-ionized water at 37.5°C using a mq-60 NMR Analyzer (Bruker Minispec) at a magnetic field strength of 1.41 T (ω_0 = 60 MHz). T_2 relaxation times were obtained from fitting a monoexponential decay curve to signal data generated by a Carr-Purcell-Meiboom-Gill (CPMG) spin-echo pulse sequence with an inter-echo time = 1 ms and repetition time = 6 s. T_1 relaxation times were obtained from fitting a monoexponential recovery curve to signal data generated with an inversion recovery (IR) pulse sequence using ten inversion times between 50 and 10000 ms. Samples were diluted in water in the concentration range of 0.01-0.1 mg mL^{-1} and 500 μL of each concentration was transferred into a 7.5 mm NMR tube and equilibrated for 15 min. prior to measurements. The relaxivities r_1 and r_2 were determined from the slopes of the straight lines on a graph of the respective relaxation rate (s^{-1}) versus iron concentration (mM Fe). Fe concentrations were determined by inductively coupled plasma - atomic emission spectroscopy (Spectro Arcos, Spectro Analytical Instruments, Germany; detection limit: 4 $\mu g\ L^{-1}$) following digestion with concentrated HNO_3 at a concentration of 0.02 mg mL^{-1} for five days at 25°C.

4.4 Results and Discussion

4.4.1 Particle fabrication and characterization

The primary iron oxide nanoparticles had a mean diameter of 7.4 nm as determined from a lognormal fit of the sizes measured from TEM (Figure 4.1a). The oleic acid content of the nanoparticles was 15.8 wt% as determined by TGA (Figure 4.1b).

(a)

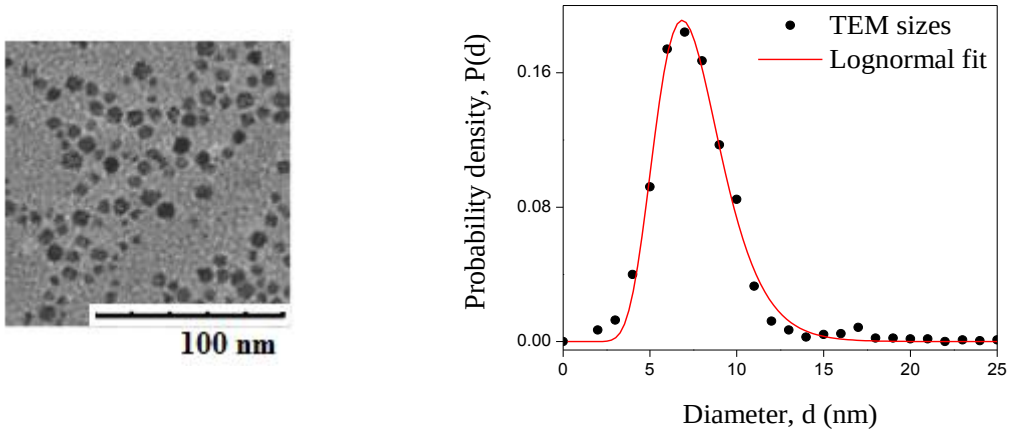

(b)

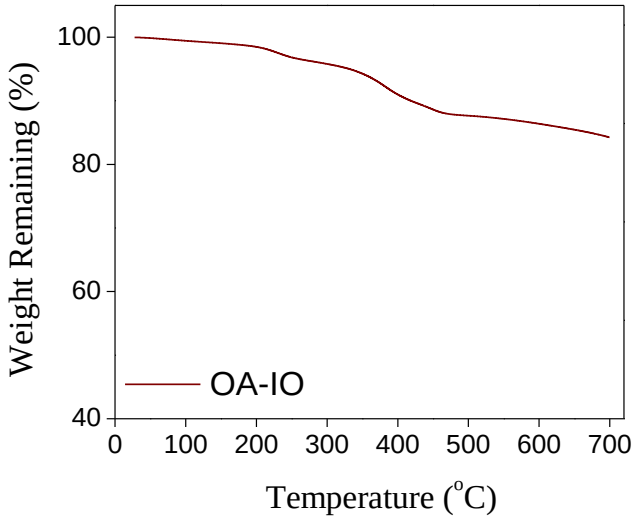

Figure 4.1 (a) The primary iron oxide nanoparticles had a mean diameter of 7.4 nm as determined from a lognormal fit of the sizes measured from TEM. (b) The oleic acid content of the nanoparticles was 15.8 wt% as determined by TGA.

Quantitative incorporation of iron oxide in the particles was achieved by controlling only the loading of oleic acid-coated iron oxide nanoparticles during the fabrication process. Figure 4.2 depicts the thermogravimetric curves of the iron oxide-copolymer particles with targeted loadings of 10, 20, 30, and 40 wt% iron oxide (C1-C4). The measured iron oxide loadings were 12, 21, 32,

and 42 wt% indicating quantitative control of nanoparticle incorporation. The mPEG-*b*-PDLLA diblock was completely burned out around 600°C.

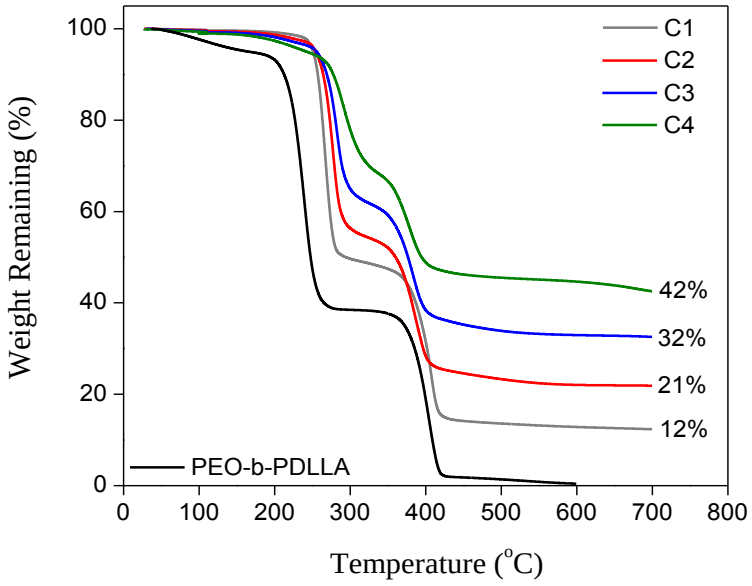

Figure 4.2 Quantitative incorporation of iron oxide in the particles was achieved by controlling only the loading of oleic acid-coated iron oxide nanoparticles during the fabrication process.

The lyophilized samples were easily redispersed in de-ionized water with mild sonication indicating that the surface coverage of the hydrophilic PEO chains was sufficient to provide aqueous dispersibility. This is noteworthy in view of the well-documented aggregation that many nanoparticles, including those stabilized with PEO, exhibit upon freeze-drying unless a cryo-protectant is used.[33] In the present study, no cryo-protectants were used. In this study, a copolymer concentration ~10 times higher than the critical aggregation concentration was chosen for the clusters fabrication which aided in efficient encapsulation of the hydrophobic iron oxide nanoparticles. The critical aggregation concentration of the copolymer in the 1:10 (v/v) THF-water mixture was determined as 0.3 mg mL^{-1} by measuring the scattering intensities of a range of

copolymer concentrations (0.005-10 mg mL^{-1}) by dynamic light scattering at 25°C. The average particle size and polydispersity by dynamic light scattering are shown in Table 4.1. The intensity-weighted diameter increased from 89 to 163 nm as the iron oxide loading increased from 12 to 42 wt%.

Table 4.1 Hydrodynamic size and polydispersity index of OA-IO/mPEG-*b*-PDLLA particles by dynamic light scattering

	Iron oxide content (wt %)	Intensity-weighted diameter by dynamic light scattering (nm)	Polydispersity index by dynamic light scattering
C1	12	89	0.16
C2	21	117	0.12
C3	32	147	0.15
C4	42	163	0.17

The hydrodynamic sizes by dynamic light scattering monitored as a function of time at 37°C did not change after 24 h. Figure 4.3 shows the intensity-weighted hydrodynamic diameter of C1 and C3 particles as a function of time. Additionally, the number-weighted size distributions were characterized using nanoparticle tracking analysis (NTA), which captures a video of the nanoparticles diffusing under Brownian motion and tracks them individually to measure the diffusion coefficient and size. The number-average diameters and standard deviations [D_N, σ] of the particles (C1-C4) as determined by a lognormal fit of the NTA sizes were [85, 0.36], [108, 0.31], [134, 0.35] and [117, 0.40], respectively.

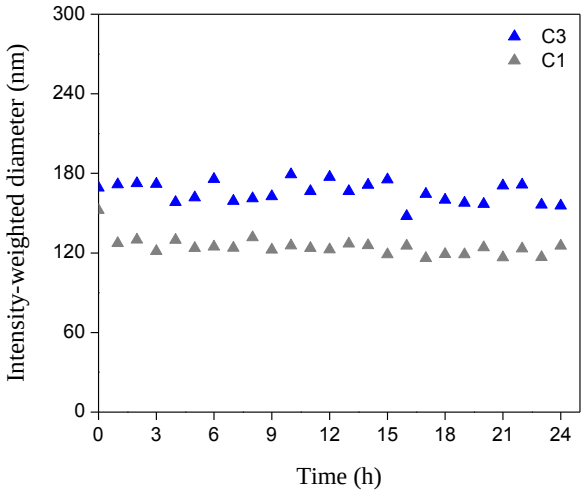

Figure 4.3 The hydrodynamic sizes by dynamic light scattering monitored as a function of time at 37°C did not change after 24 h.

Figure 4.4 shows representative cryo-TEM images for clusters C1-C4. The number-weighted size distributions for the four clusters as measured by cryo-TEM were converted to the volume-weighted probability distribution of the cluster core sizes, $P_v(d_c)$, using the following equation:

$$P_v(d_c) = \frac{N(d_c){d_c}^3}{\sum\left(N(d_c){d_c}^3\right)} \tag{4.1}$$

where d_c is the cluster diameter and $N(d_c)$ is the number of the clusters with diameter d_c. The volume-weighted size distributions, shown in Figure 4.5, were used for the prediction of transverse relaxivities.

The averaging volume probability distribution functions - $P_v(d_c)$- shown in Figure 4.5 represent averages over orientations for nonspherical clusters. By consistently measuring each cluster in cryo-TEM projection images, only systematic errors are introduced that do not greatly impact the averaged results. For the frozen-hydrated clusters in Figure 4.4, the variability in 3D orientation

of the clusters contributed to the diameter measurements but, given that around 600 clusters were analyzed for each sample, the averaging over the orientation yields approximate spherical diameters which are still much more accurate than any indirect method such as DLS or NTA. The theories for the transverse relaxivity were derived assuming spherical particles and thus applying the cryo-TEM size analysis to these models necessarily involves having to make several assumptions.

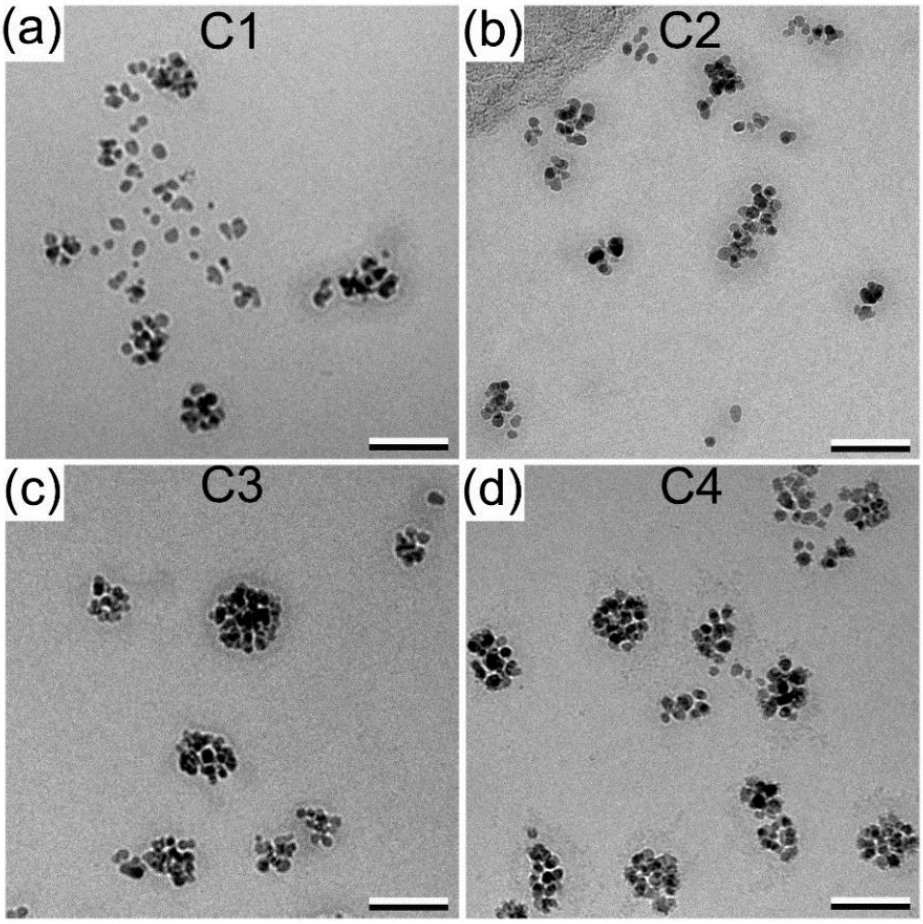

Figure 4.4 Representative cryo-TEM images of OA-IO/mPEG-*b*-PDLLA clusters C1 (a), C2 (b), C3 (c), and C4 (d). Scale bar in each panel is 50 nm.

The cluster size distributions are not monomodal but rather reflect the discrete nature of the distribution captured by cryo-TEM. Moreover, the cryo-TEM analyses capture the size of particle cores (iron oxide nanoparticles and hydrophobic components) rather than the hydrodynamic size distribution that is measured by both DLS and NTA. For example, for sample C4, the number average core size measured by cryo-TEM was 32 nm, whereas the corresponding hydrodynamic diameters from DLS and NTA were 86 and 117 nm, respectively. Similar comparisons were found for samples C1-C3. It is critically important to use the correct cluster size distributions for modeling of transverse relaxivities as will be discussed in a later section.

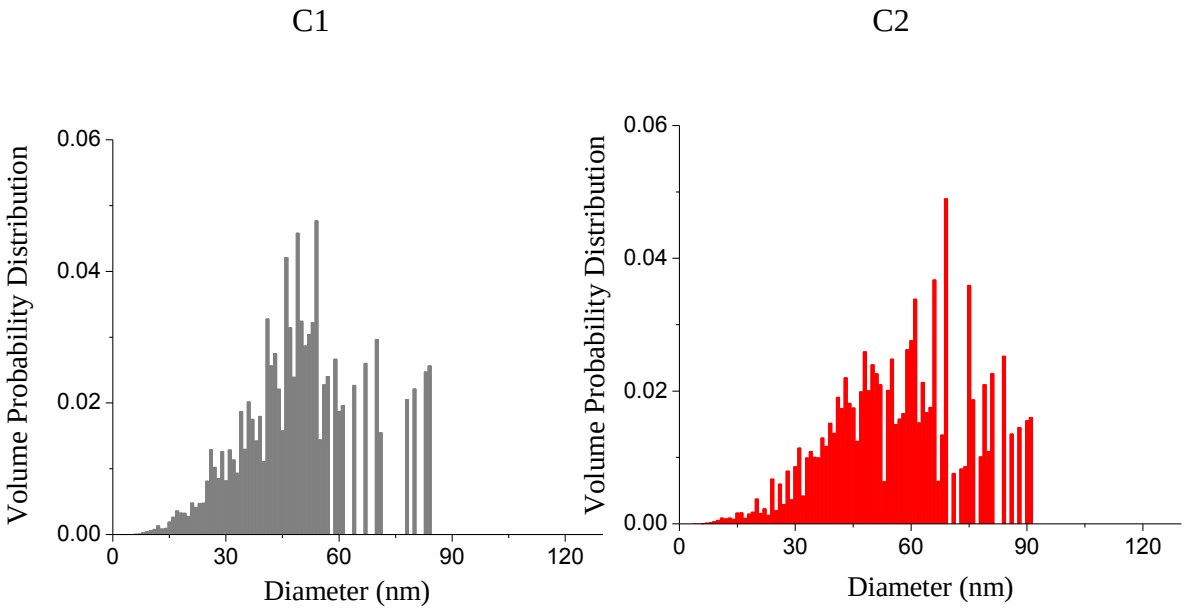

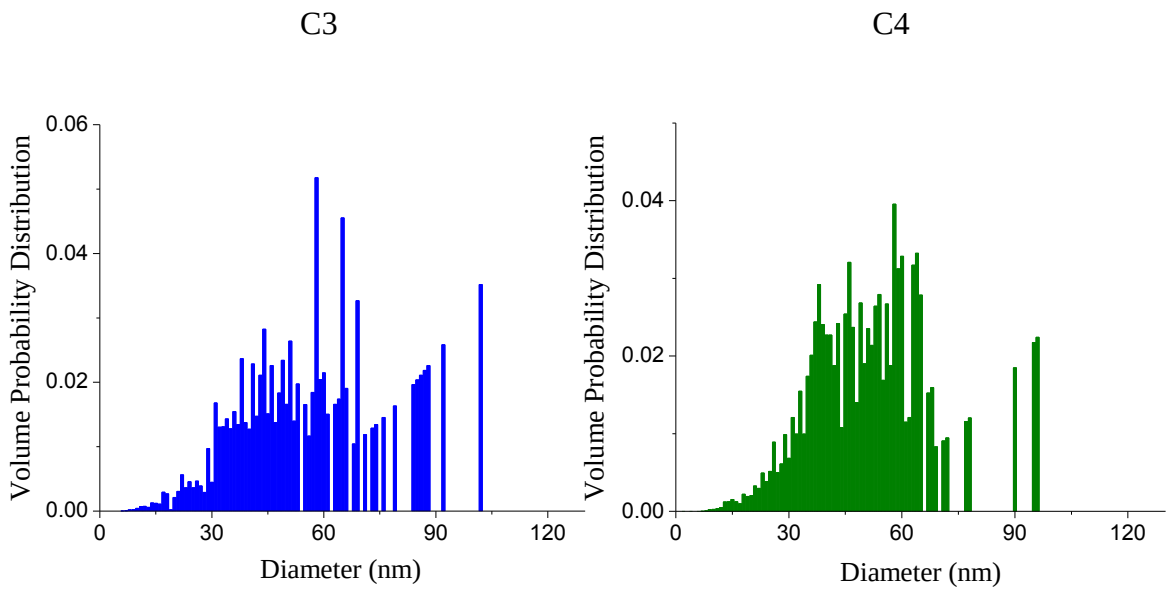

Figure 4.5 Size distributions of OA-IO/mPEG-*b*-PDLLA clusters derived from cryo-transmission electron microscopy.

The *M-H* curves of primary iron oxide nanoparticles and iron oxide-block copolymer particles measured by SQuID magnetometry are shown in Figure 4.6 and revealed no signs of hysteresis at 300 K. The mass magnetizations of the iron oxide and the oleic acid coated-iron oxide nanoparticles at an applied field of 4 T were 66 and 56 Am^2/kg, respectively. The lower magnetization of the latter corresponds to the 16 wt% oleic acid coating around the primary nanoparticles. Recently, the mass magnetization of 7.5 nm Fe_3O_4 nanoparticles at 5 T was reported to be 70 Am^2/kg.[34] For comparison, the magnetization of 8-nm maghemite nanoparticles is ~ 54.8 Am^2/kg at 5 T.[35] Our magnetization value of 66 Am^2/kg at 4 T for 7.4 nm nanoparticles suggests that the phase of iron oxide is predominantly magnetite. This is consistent with the findings of Pinna et al who developed the iron oxide synthesis method used in this work and who found, using Raman and Mossbauer spectroscopies, that iron oxides made by the thermal decomposition of iron (III) acetylacetonate consisted of ~95 wt% Fe_3O_4 and ~5% α-Fe_2O_3.[30] A sample of the copolymer-

stabilized particles containing 25 wt% iron oxide had a saturation magnetization of 16 Am^2/kg owing to the large fraction of organics.

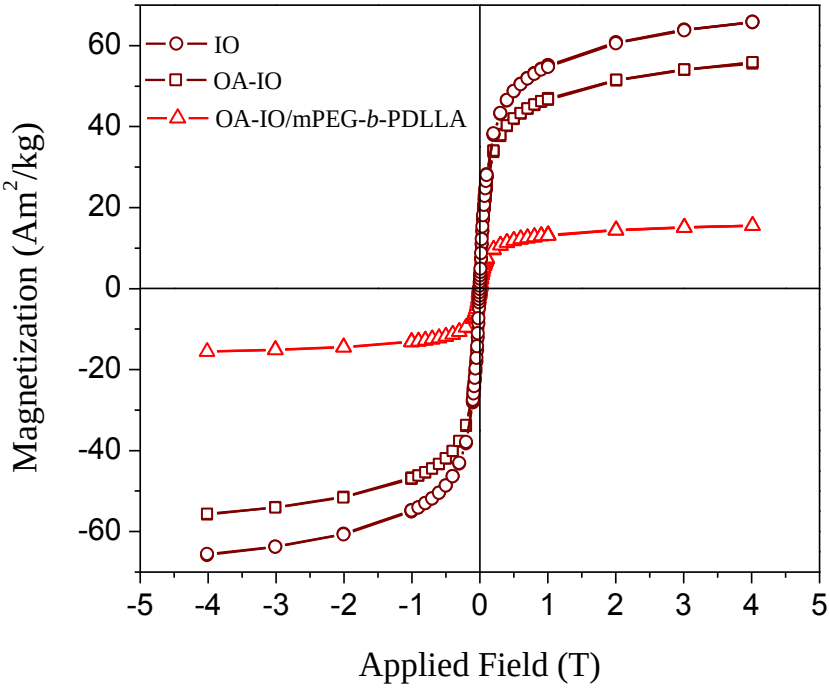

Figure 4.6 Magnetization as a function of applied field for iron oxide nanoparticles, oleic acid coated-iron oxide nanoparticles and OA-IO/mPEG-*b*-PDLLA particles at 300 K.

4.4.2 Relaxivities

The proton transverse (r_2) relaxivities of the OA-IO/mPEG-*b*-PDLLA particles increased with increasing iron oxide loadings/average particle sizes as shown in Figure 4.7a. Particles containing relatively higher loadings of iron oxide (> 30 wt %) had r_2 relaxivities greater than 200 s^{-1} mM Fe^{-1} which compares favorably with the r_2 reported for Feridex (41 s^{-1} mM Fe^{-1} at 1.5 T, 37°C),[36] a commercial T_2 contrast agent. The r_1 relaxivities of all the particles were low [2-3 s^{-1} mM Fe^{-1}], consistent with the hydrophobic nature of the particle cores (Figure 4.7b). According to Roch et al., the formation of aggregates leads to a reduction in the exchange of fast-relaxing water protons

within the aggregate with the slow-relaxing protons in the bulk water outside the aggregate, leading to a decrease in longitudinal relaxivities.[37] The hydrophobic organic coating also prevents direct access of water to the nanoparticles, thus increasing the T_1 relaxation time.

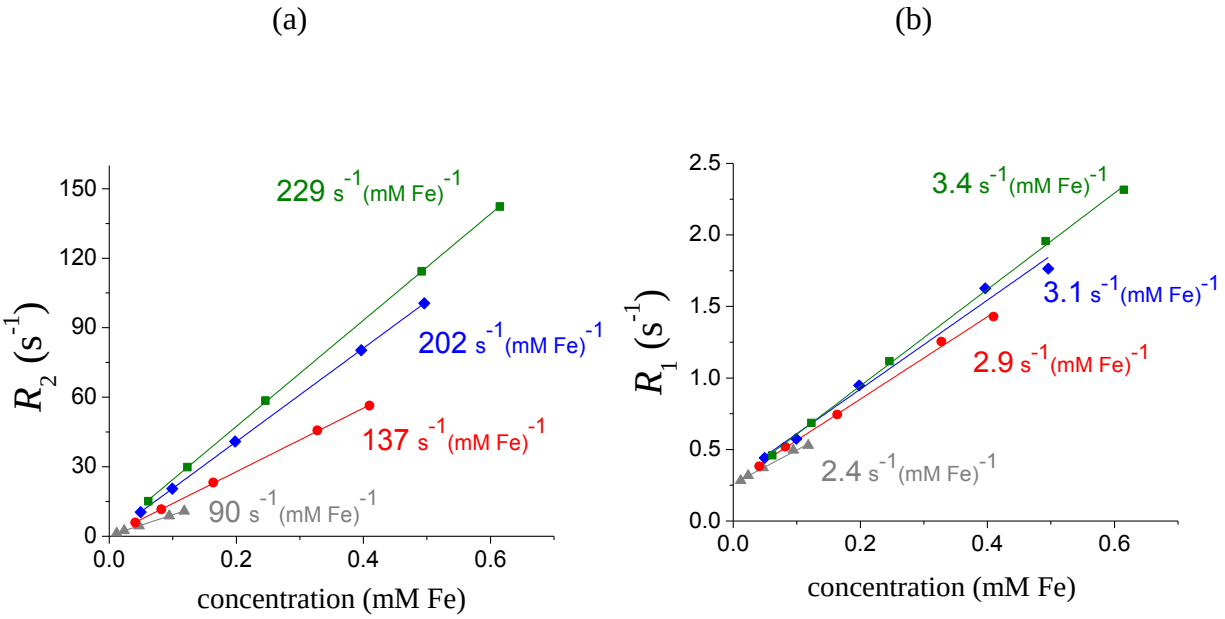

Figure 4.7 Proton transverse r_2 (a) and longitudinal r_1 (b) relaxivities of OA-IO/mPEG-*b*-PDLLA particles at 1.4 T and 37.5°C.

4.4.2.1 *Prediction of transverse relaxivities using cryo-TEM size distributions*

Dephasing of proton magnetic moments in the presence of magnetic nanoparticles is generally described by the motional averaging regime (MAR), static dephasing regime (SDR) and echo-limited regime (ELR), depending on the particle characteristics including size and magnetization, and experimental parameters such as the inter-echo time of the pulse sequence.[11,38-40] The motional averaging regime is given by the condition $\Delta\omega.\tau_D < 1$, where $\Delta\omega$, given by eq. 4.2, is the precession frequency variation near the particle or cluster surface, and τ_D, given by eq. 4.3, is the time taken by the proton to diffuse a distance on the order of the particle diameter:

$$\Delta\omega = \frac{\mu_o \gamma M_v}{3} \tag{4.2}$$

$$\tau_D = \frac{d^2}{4D} \tag{4.3}$$

The parameters μ_o, γ, M_v, d and D are the vacuum magnetic permeability (= $4\pi \times 10^{-7}$ T-m/A), gyromagnetic ratio of the proton (= 2.67×10^8 rad/s-T), volumetric magnetization of the particle, diameter of the particle and diffusion coefficient of water (= 3×10^{-9} m^2/s at 37.5°C), respectively. In the MAR, the protons experience a wide range of precession frequencies due to diffusion in the inhomogeneous fields around the magnetic particles which are effectively time-averaged, and the transverse relaxation rate has a quadratic dependence on the particle diameter according to eq. 4.4:[12]

$$(R_2)_{ma} = \frac{4f(\Delta\omega)^2 d^2}{45D} \tag{4.4}$$

where f is the volume fraction of the particles. The relaxation rate is given by the static dephasing regime ($\Delta\omega.\tau_D > \pi\sqrt{3}/2$) when the NMR signal decay due to spin dephasing occurs faster than diffusion processes average out the phases of the proton spins.[38] The SDR consists of a relaxation rate plateau where R_2 has its maximum value and is independent of size eq. 4.5:

$$(R_2)_{sd} = \frac{2\pi f(\Delta\omega)}{\sqrt{27}} \tag{4.5}$$

In the MAR and SDR, the relaxation rate is independent of the echo time, $2\tau_{CP}$ (time between two successive 180° pulses in the Carr-Purcell-Meiboom-Gill spin multi-echo pulse sequence), and R_2 and R_2^* are equivalent. A critical particle size is reached at $\tau_D \sim 2\tau_{CP}$, when the echo pulses become

efficient in refocusing the proton spins and the transverse relaxation rate decreases with particle/cluster size. This is the echo-limited regime, where the relaxation rate has an echo time as well as size dependence, according to eq. 4.6:[40]

$$(R_2)_{el} = \frac{7.2fDx^{\frac{1}{3}}(1.52 + fx)^{\frac{5}{3}}}{d^2} \quad (4.6)$$

where $x = \Delta\omega.\tau_{CP}$. It is clear from eq. 4.4-4.6 why most synthetic efforts towards efficient magnetic particle contrast agents are focused on controlled clustering of primary nanoparticles as high relaxivities can be easily achieved by increasing the overall cluster size. Furthermore, r_2 can be maximized when the size distribution is tailored to be narrow and located entirely within the static dephasing regime.

In this work, we modeled the transverse relaxivities of the clusters C1-C4 using the approach of Carroll et al. which involves integrating equations 4.4-4.6 over the size distributions.[12] In that work, theoretical values of r_2 of predominantly single maghemite nanoparticles in the size range of 6-13 nm were calculated by integration over a lognormal distribution of nanoparticle sizes derived from transmission electron microscopy and small-angle X-ray scattering. Good agreement was observed between the experimental and predicted r_2s based on SAXS data that included aggregates in suspension. In the present work, we used (i) the cluster (oleic acid-coated iron oxide + PDLLA) size distributions measured using cryo-transmission electron microscopy (Figure 4.5), (ii) magnetization of the primary iron oxide nanoparticles at 1.4 T assuming magnetite (Fe_3O_4, ρ = 5,180 kg/m^3), and (iii) the volume fraction of iron oxide in the clusters derived from TGA. The volume fraction of iron oxide in the clusters, φ, was calculated from the TGA weight fractions of

iron oxide, using the densities 5.18, 0.895, and 1.2 g/cm^3 for magnetite, oleic acid, and PDLLA, respectively:

$$\varphi = \frac{\frac{w_{IO}}{\rho_{IO}}}{\frac{w_{IO}}{\rho_{IO}} + \frac{w_{OA}}{\rho_{OA}} + \frac{w_{PDLLA}}{\rho_{PDLLA}}} \tag{4.7}$$

The calculated φ was used for estimating the magnetization (M_v), $\Delta\omega$, volume fraction of clusters in a 1 mM Fe suspension (f), and the respective relaxation rates ($(R_2)_{ma}, (R_2)_{sd}, (R_2)_{el}$). Table 4.2 shows the calculated volume fraction of iron oxide in the clusters (φ).

Table 4.2 Weight fractions of particle components from thermogravimetric analysis and calculated volume fraction of iron oxide in the clusters (φ)

	w_{IO}	w_{OA}	w_{PDLLA}	w_{PEO}	Volume fraction of iron oxide in OA-IO/mPEG-*b*-PDLLA particles, φ_{IO}	Volume fraction of iron oxide in the clusters, φ
C1	0.12	0.02	0.56	0.29	0.03	**0.04**
C2	0.21	0.04	0.49	0.26	0.06	**0.08**
C3	0.32	0.06	0.41	0.21	0.09	**0.13**
C4	0.42	0.08	0.33	0.17	0.14	**0.18**

The magnetization of the clusters was calculated using the magnetization of the primary iron oxide nanoparticles at the relaxometry field of 1.4 T (M_{IO} = 57 Am^2/kg), derived from the *M*-*H* curve in Figure 4.6, and the volume fraction of iron oxide in the clusters according to eq. 4.8:

$$M_v = M_{IO} \times \rho_{IO} \times \varphi \tag{4.8}$$

In order to calculate the transverse relaxation rates per mM Fe, the volume fraction of the clusters in a suspension containing 1 mM Fe (f) was calculated as follows:

Volume fraction of iron oxide (Fe_3O_4) in a 1 mM Fe suspension (f'):

$$1\ mM\ Fe = 1 \times 10^{-3}\ M\ Fe = \frac{1 \times 10^{-3}\ moles\ Fe}{10^3\ g\ H_2O} = \frac{1 \times 10^{-4}\ moles\ Fe}{100\ g\ H_2O}$$

$$= \frac{1 \times 10^{-4}\ \times 55.948\ g\ Fe}{100\ g\ H_2O} = \frac{1 \times 10^{-4}\ \times 55.948 \times 1.3813\ g\ Fe_3O_4}{100\ g\ H_2O}$$

$$= \frac{77.281 \times 10^{-4}\ g\ Fe_3O_4}{100\ g\ H_2O} = \frac{77.281 \times 10^{-4}\ cm^3\ Fe_3O_4}{5.18 \times 100\ cm^3\ H_2O}$$

$$= \frac{1.49 \times 10^{-5}\ cm^3\ Fe_3O_4}{100\ cm^3\ H_2O}$$

$$f' = \frac{V_{Fe_3O_4}}{V_{cluster} + V_{PEO} + V_{H_2O}} = 1.49 \times 10^{-5} \tag{4.9}$$

Volume fraction of clusters: $$f = \frac{V_{cluster}}{V_{cluster} + V_{PEO} + V_{H_2O}} \tag{4.10}$$

From eq. 4.9 and eq. 4.10, $$\frac{f}{V_{cluster}} = \frac{f'}{V_{Fe_3O_4}} \tag{4.11}$$

Since $$\varphi = \frac{V_{Fe_3O_4}}{V_{cluster}} \tag{4.12}$$

$$f = \frac{f'}{\varphi} = \frac{1.49 \times 10^{-5}}{\varphi} \tag{4.13}$$

The threshold diameters for the onset of the static dephasing (eq. 4.14) and echo-limited regimes (eq. 4.15) were calculated according to Roch et al:[37]

$$d_{sd} = \sqrt{\frac{5\pi D\sqrt{3}}{2\Delta\omega}} \tag{4.14}$$

$$d_{el} = 2\sqrt{\frac{1.49Dx^{1/3}(1.52 + fx)^{5/3}}{\Delta\omega}} \tag{4.15}$$

Table 4.3 Calculated magnetization (M_v), volume fraction of cluster in a 1 mM Fe suspension (f), threshold diameters for static dephasing (d_{sd}) and echo-limited regimes (d_{el})

	M_v (A/m)	f (× 10^{-4})	d_{sd} (nm)	d_{el} (nm)
C1	13181	3.33	166	532
C2	24111	1.82	123	435
C3	38893	1.13	97	371
C4	53920	0.82	82	332

Finally, the transverse relaxivity for each cluster was calculated by integration over the cryo-TEM derived cluster size distributions, and using the values of $\Delta\omega$ and f, as calculated above:

$$r_{2,\text{predicted}} = \frac{4f(\Delta\omega)^2}{45D}\sum_{d=1}^{d_{sd}} {d_c}^2.P_v(d_c) + \frac{2\pi f(\Delta\omega)}{\sqrt{27}}\sum_{d=d_{sd}}^{d_{el}} P_v(d_c) + 7.2fDx^{\frac{1}{3}}(1.52 + fx)^{\frac{5}{3}}.\sum_{d=d_{el}}^{\infty} {d_c}^{-2}.P_v(d_c)\,\mathrm{d}d_c \tag{4.16}$$

Table 4.4 Predicted transverse relaxivities of OA-IO/mPEG-*b*-PDLLA particles and contributions from the motional averaging, static dephasing and echo-limited regimes

	Measured r_2 (s^{-1} mM Fe^{-1})	Predicted r_2 (s^{-1} mM Fe^{-1})	Contribution to Predicted r_2 from MAR	Contribution to Predicted r_2 from SDR	Contribution to Predicted r_2 from ELR
C1	90	**59**	59	0	0
C2	137	**141**	141	0	0
C3	202	**232**	211	21	0
C4	229	**254**	217	37	0

As shown in Table 4.4, the predicted relaxivities for samples C2-C4 are typically within 15% of the measured r_2s. The increase in r_2 with average cluster size occurs due to an increase in cluster size within the MAR, and due to a larger fraction of clusters experiencing static dephasing conditions. In the case of C1, for which the difference is 34%, we observed a significant number of iron oxide-free particles in the TEM images on stained specimens. In TEM images of negatively stained samples that were air-dried, approximately 40% of the particles in C1 did not contain iron oxide nanoparticles whereas nearly all of the particles in samples C2-C4 contained iron oxide (Figure 4.8). Images of negatively stained specimens were not used for modeling the relaxivities as flattening artifacts introduced during the air-drying step commonly result in inaccurate measurements of TEM samples. The high incidence of iron oxide-free particles in sample C1 is consistent with it having the lowest targeted loading of iron oxide (10 wt %) and with the nucleation and growth process by which the particles form in the multi-inlet vortex mixer. If we accounted only for the particles that contained iron oxide nanoparticles, the estimated relaxivity for C1 would have been higher owing to the higher relative volume fraction of iron oxide and hence better agreement with the measured r_2 would have resulted. For C1 and C2, the calculated

relaxivities were attributed entirely to the motional averaging regime, whereas for C3 and C4, there was a 9% and 15% contribution to the calculated relaxivity from the static dephasing regime. None of the samples had clusters large enough to be in the echo-limited regime. It should be noted that some maghemite is always present with magnetite owing to the oxidation of the latter. Thus, the r_2 predictions were also done based on maghemite (ρ = 4,900 kg m^{-3}) instead of magnetite (ρ = 5,180 kg m^{-3}). However, the differences in the predicted relaxivities were only about 10%, i.e. the r_2 values based on maghemite were 53 (C1), 127 (C2), 209 (C3) and 229 (C4). These calculations show that only marginal differences in the predicted relaxivities occur for variations in the chemical composition of the iron oxide. Our results show that the analytical models of transverse relaxivity can be used as a predictive tool for the design of theranostic magnetic nanocarriers based on amphiphilic block copolymers.

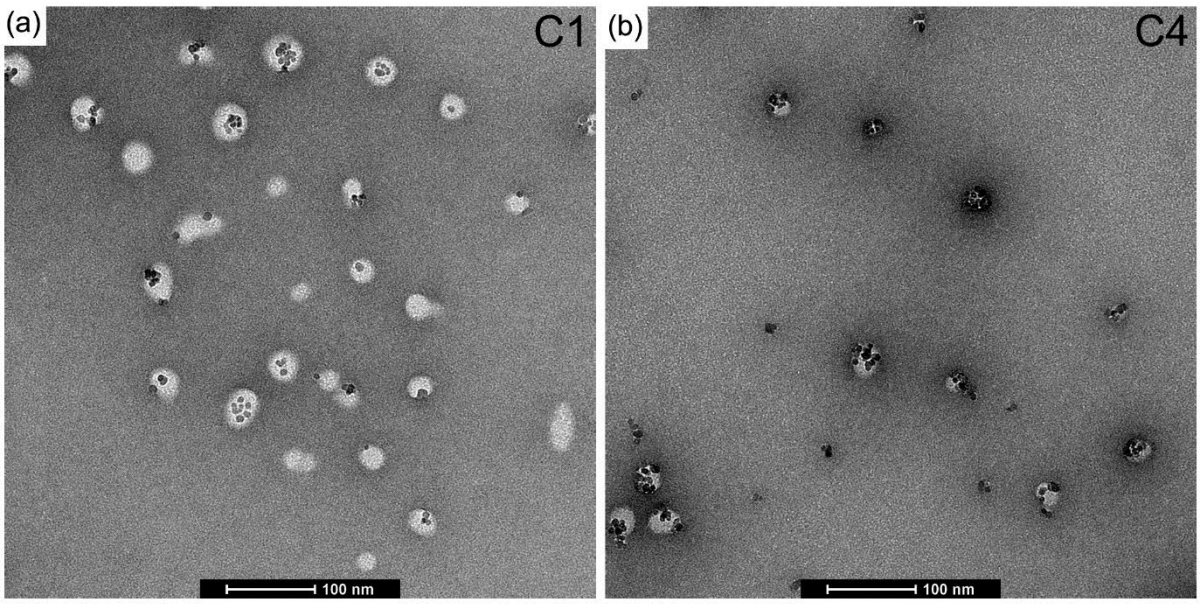

Figure 4.8 TEM images of C1 (a) and C4 (b) specimens stained with 1% uranyl formate. A significant number of iron oxide-free polymer particles are seen in C1.

4.4.2.2 *Prediction of transverse relaxivities using DLS and NTA size distributions*

To compare with the results obtained using cryo-TEM, the cluster size distributions derived from dynamic light scattering and nanoparticle tracking analysis, which measure particle sizes including the PEO corona, were also used. The PEO brush thickness was estimated for each particle based on the NTA-derived number-average diameter using the modified density distribution model.[41,42] The mass of PDLLA in the particle core was first estimated, followed by calculation of the volume and radius of the core, as follows:

Mass of PDLLA:
$$m_{PDLLA} = \frac{N_{agg} M_n}{N_{av}} \tag{4.17}$$

where N_{agg}: number of PDLLA chains in the core

M_n: number-average molecular weight of PDLLA (9,650 g/mol)

N_{av}: Avogadro's number

Volume of particle core:
$$V_{core} = \frac{m_{IO}}{\rho_{IO}} + \frac{m_{OA}}{\rho_{OA}} + \frac{m_{PDLLA}}{\rho_{PDLLA}} \tag{4.18}$$

Radius of particle core:
$$R_{core} = \left(\frac{3V_{core}}{4\pi}\right)^{1/3} \tag{4.19}$$

Radius of particle:
$$R = \left\{ \frac{N_k {l_k}^{1/\upsilon}\, 8 {N_{agg}}^{(1-\upsilon)/2\upsilon}}{3\upsilon 4^{1/\upsilon}} + {R_{core}}^{1/\upsilon} \right\}^{\upsilon} \tag{4.20}$$

where N_k: Number of Kuhn segments (83)

l_k: Kuhn segment length (0.61)[42]

υ: Flory exponent for PEO in water at 25°C (0.583)[43]

Brush thickness:
$$t = R - R_{core} \tag{4.21}$$

In the above calculations, the value of N_{agg} was adjusted for each particle to get calculated R values equal to the measured number-weighted mean radius from NTA. For each particle, the sizes in the number-weighted distribution derived from both DLA and NTA were subtracted by $2t$ to approximate the particle core diameters, and the resulting size distribution was used for integration to predict r_2. The brush thickness was is the range of 15-18 nm for all the clusters. Figure 4.9 shows the DLS and NTA cluster size distributions after applying the brush thickness correction.

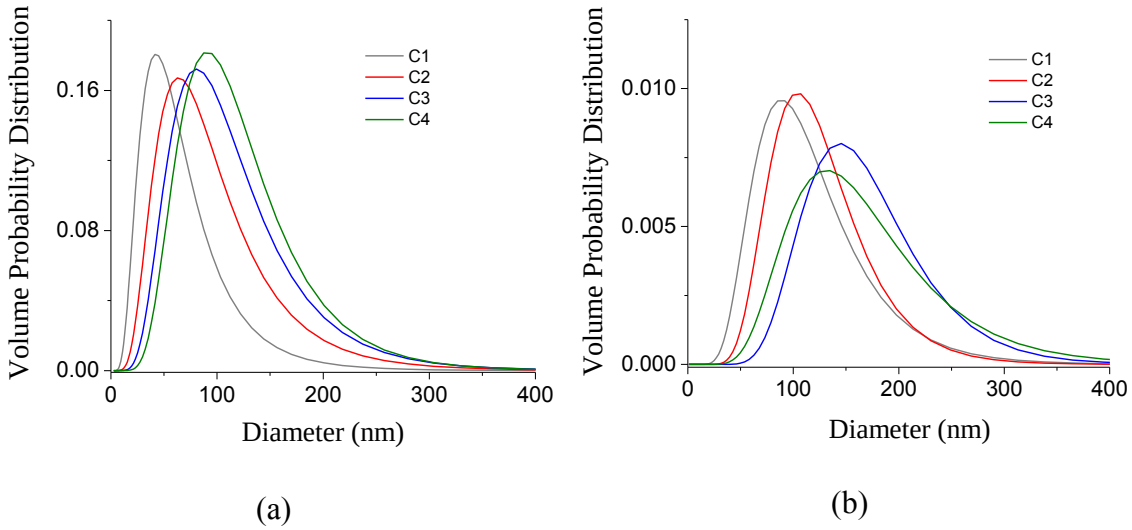

Figure 4.9 Size distributions of OA-IO/mPEG-*b*-PDLLA particle cores derived from (a) dynamic light scattering, and (b) nanoparticle tracking analysis.

Table 4.5 shows the estimated PEO brush thickness and predicted relaxivity for each particle. The predicted r_2s were factors of 2.5-3 higher than the measured relaxivities. As a limiting case, the calculations were done assuming that all the PEO was buried in the particle core (and hence no distinct brush). However, the discrepancies were considerable still. In this case, the NTA-predicted r_2s were 249, 464, 583 and 587 s^{-1} mM Fe^{-1} for clusters C1, C2, C3 and C4, respectively. The corresponding DLS-predicted r_2s were 66, 232, 421 and 532, respectively. It is believed that these

large discrepancies occur because DLS and NTA did not accurately capture the smaller particles in the distributions. This was confirmed by the presence of significant numbers of individual nanoparticles and small clusters in the cryo-TEM images. Thus, a direct measurement of the cluster size distributions as afforded by cryo-TEM is necessary for quantitative analysis of the relaxivities of iron oxide-amphiphilic block copolymer particles.

Table 4.5 Transverse relaxivity predictions based on DLS and NTA size distributions (assuming distinct PEO brush around the cluster)

	Estimated PEO brush thickness (nm)	Measured r_2 (s^{-1} mM Fe^{-1})	Predicted r_2 - NTA (s^{-1} mM Fe^{-1})	Predicted r_2 -DLS (s^{-1} mM Fe^{-1})
C1	15	90	282	73
C2	17	137	456	245
C3	18	202	576	398
C4	16	229	582	493

4.4.3 Magnetic field stability of the particles

To investigate the effect of magnetic field-induced aggregations, the R_2 relaxation rates of the clusters were measured, suspended at a concentration of 0.1 mg mL^{-1} in de-ionized water as well as agarose gel and placed in the relaxometer field (1.4 T) as a function of time. Agarose was dissolved in boiling water at a concentration of 0.5 wt% and mixed with an aqueous suspension of the clusters to yield a final cluster concentration of 0.1 mg mL^{-1}. Each sample (500 μL) was transferred into the NMR tube and allowed to gel at room temperature prior to measurements. The results are presented in Figure 4.10 below.

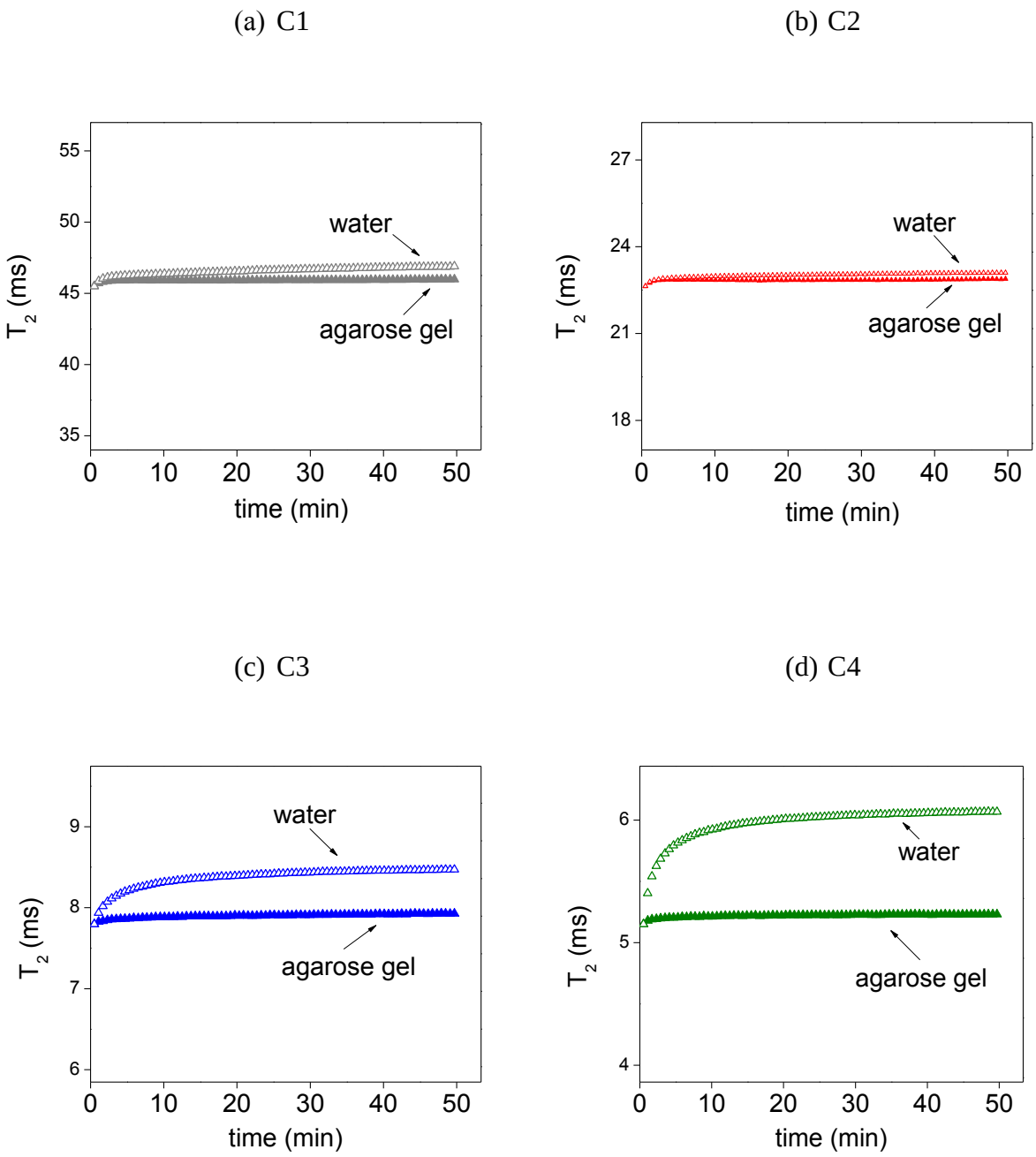

Figure 4.10 Time dependence of the proton transverse relaxation time of aqueous suspensions of OA-IO/mPEG-*b*-PDLLA particles in the magnetic field (1.4 T).

Only very small decreases in R_2 with time were noted for clusters C1 and C2 (3% and 2%, respectively). For the larger clusters C3 and C4 with higher loadings of iron oxide, the R_2 decrease

was 8% and 15%, respectively, indicating cluster-chain formation at these sizes and magnetizations. However, these field-induced aggregations were noted only over a period of tens of minutes. On the timescale of the r_2 experiments (< 30 s) presented in Figure 4.7a, the T_2 relaxation times of the suspensions with or without aggregation (in water or agarose gel) are comparable.

4.4.4 Hydrophobic- versus hydrophilic-core particles

We have found that the inner structure of the particles has a pronounced effect on the transverse relaxivities. Hydrophilic-core particles (illustrated in Figure 4.11b) synthesized from ~ 7-nm iron oxide nanoparticles (similar to the primary iron oxide used in the case of OA-IO/mPEG-*b*-PDLLA particles) have been found to have very high r_2s, approaching 600 s^{-1} mM Fe^{-1} at 1.4 T (Table 4.6). These magnetic-block ionomer particles were synthesized by crosslinking the amine termini on the outer corona of iron oxide-poly(ethylene oxide-*b*-acrylate) complexes with hydrophilic, oligomeric poly(ethylene oxide) diacrylate.[44]

Figure 4.11 Hydrophobic (C1-C4) versus hydrophilic-core particles.

The average hydrodynamic sizes of the hydrophilic particles were controlled by varying the concentration of the crosslinking reaction and were in the range 50-180 nm. The transverse

relaxivities of these particles increased with average size as in the case of the OA-IO/mPEG-*b*-PDLLA (Figure 4.11a) but were considerably higher at similar particle sizes and iron oxide loadings. For example, hydrophilic-core particles with an intensity-average diameter of 143 nm and comprised of 32 wt% iron oxide had an r_2 of 410 s^{-1} mM Fe^{-1}, whereas the C3 hydrophobic-core particles (32 wt% iron oxide, D_I = 147 nm) had r_2 = 202 s^{-1} mM Fe^{-1}, about 50% lower.

Table 4.6 Transverse and longitudinal relaxivities of hydrophilic-core particles at 1.4 T

Intensity-weighted hydrodynamic diameter, (nm)	r_2 (s^{-1} mM Fe^{-1})	r_1 (s^{-1} mM Fe^{-1})
55	68	18
50	93	14
119	194	30
105	255	40
143	410	34
139	444	69
181	604	43
174	534	75

It is believed that the high field gradients experienced by the water protons by diffusion within the core of the clusters result in the markedly higher relaxivities for the hydrophilic particles. Interestingly, the longitudinal relaxivities of the hydrophilic particles were also high, owing perhaps to the rapid exchange of fast relaxing protons within the cluster and the slow relaxing protons in bulk water. These results indicate that the relaxivities are influenced not only by the well-known structural parameters such as size, magnetization and volume fraction of magnetic nanoparticles, but also by the internal microstructure. Further investigations on the hydrophilic-

core particles are required to elucidate the effects of inter-nanoparticle spacing and particle size distribution on the transverse relaxivities.

The results in Table 4.6 were rationalized using an empirical equation based on the classical motional averaging model to predict the transverse relaxivities of hybrid magnetic nanoparticles such as controlled clusters. Vuong et al. showed that the normalized r_2s of magnetic particles over a range of sizes, morphologies and magnetizations followed a universal scaling law varying with the square of the particle hydrodynamic diameter.[19] We used the volume fractions of iron oxide (φ) in all of the dried particles (from TGA) in the hydrodynamic size range of 50–180 nm and the magnetizations (M_v at 1.4 T) to normalize the observed r_2s to $[(r_2.\varphi)/ M_v{}^2]$ and plotted them versus (Diameter)^2 (Figure 4.12). The iron oxide volume fraction within the cluster is based on the TGA analyses and does not account for water included in the clusters. At present, we have no ready method for measuring the iron oxide volume fraction in the hydrated clusters. The plot of $[(r_2.\varphi)/ M_v{}^2]$ versus the square of the hydrodynamic diameters was a straight line with a slope of 2.2×10^{-12}, a factor of 5 smaller than the prefactor in Vuong et al. (from Figure 1 in that reference). The difference in the prefactor could be attributed, in part, to effects of hydration in the clusters. Other variables may also affect r_2 such as the diffusion coefficient of water in the cluster and the spacing between the iron oxide particles in the cluster. These effects can be captured in part by recent Monte Carlo computer simulations for r_2 of hydrophilic clusters.[11,45-47]

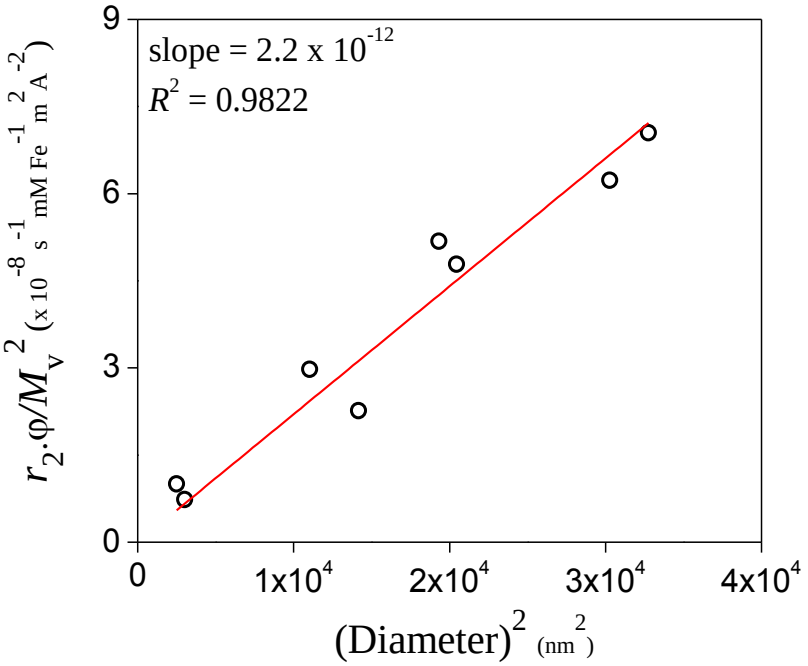

Figure 4.12 Relationship between transverse relaxivities of hydrophilic-core particles normalized by the volume fractions of iron oxide (in dried samples) and the hydrodynamic diameters.

4.5 Conclusions

We have described water-dispersible magnetic particles stabilized with amphiphilic poly(ethylene oxide-*b*-D,L-lactide) copolymer wherein hydrophobically-modified iron oxide nanoparticles were clustered within the polylactide core of the copolymer. Quantitative control over iron oxide loading, up to 40 wt%, holds promise for the design of MRI contrast agents and theranostic nanocarriers. Transverse relaxivities correlated with average particle sizes and iron oxide loadings, and exceeded 200 s^{-1} mM Fe^{-1} for particles containing > 30 wt% iron oxide. The transverse relaxivities predicted using the analytical models agree to within 15% with the measured relaxivities for iron oxide loadings greater than 20 wt%. For samples that contain a mixture of clusters and iron oxide-free polymer particles (i.e. "dead" micelles), the agreement was understandably not as good. We believe that the analytical models of transverse relaxivity can be

used a predictive tool to rationally design magnetic nanocarriers for theranostic applications. Preliminary data suggest that a hydrophobic drug (ritonavir) can be co-encapsulated within iron oxide-poly(ethylene oxide-*b*-D,L-lactide) nanocarriers with high transverse relaxivities. These data are presented in the Appendix section (A.4).

4.6 References

(1) Nasongkla, N.; Bey, E.; Ren, J. M.; Ai, H.; Khemtong, C.; Guthi, J. S.; Chin, S. F.; Sherry, A. D.; Boothman, D. A.; Gao, J. M.: Multifunctional polymeric micelles as cancer-targeted, MRI-ultrasensitive drug delivery systems. *Nano Lett.* **2006**, *6*, 2427-2430.

(2) Yang, J.; Lee, C. H.; Ko, H. J.; Suh, J. S.; Yoon, H. G.; Lee, K.; Huh, Y. M.; Haam, S.: Multifunctional magneto-polymeric nanohybrids for targeted detection and synergistic therapeutic effects on breast cancer. *Angew. Chem. Int. Ed.* **2007**, *46*, 8836-8839.

(3) Pothayee, N.; Pothayee, N.; Jain, N.; Hu, N.; Balasubramaniam, S.; Johnson, L. M.; Davis, R. M.; Sriranganathan, N.; Riffle, J. S.: Magnetic block ionomer complexes for potential dual imaging and therapeutic agents. *Chem. Mater.* **2012**, *24*, 2056-2063.

(4) Ohgushi, M.; Nagayama, K.; Wada, A.: Dextran-magnetite: a new relaxation reagent and its application to T2 measurements in gel systems. *J. Magn. Reson.* **1978**, *29*, 599-601.

(5) Geraldes, C.; Laurent, S.: Classification and basic properties of contrast agents for magnetic resonance imaging. *Contrast Media Mol. Imaging* **2009**, *4*, 1-23.

(6) Jun, Y. W.; Huh, Y. M.; Choi, J. S.; Lee, J. H.; Song, H. T.; Kim, S.; Yoon, S.; Kim, K. S.; Shin, J. S.; Suh, J. S.; Cheon, J.: Nanoscale size effect of magnetic nanocrystals and their utilization for cancer diagnosis via magnetic resonance imaging. *J. Am. Chem. Soc.* **2005**, *127*, 5732-5733.

(7) Carroll, M. R. J.; Huffstetler, P. P.; Miles, W. C.; Goff, J. D.; Davis, R. M.; Riffle, J. S.; House, M. J.; Woodward, R. C.; St Pierre, T. G.: The effect of polymer coatings on proton transverse relaxivities of aqueous suspensions of magnetic nanoparticles. *Nanotechnology* **2011**, *22*.

(8) Balasubramaniam, S.; Pothayee, N.; Lin, Y. N.; House, M.; Woodward, R. C.; St Pierre, T. G.; Davis, R. M.; Riffle, J. S.: Poly(N-isopropylacrylamide)-coated superparamagnetic iron oxide nanoparticles: Relaxometric and fluorescence behavior correlate to temperature-dependent aggregation. *Chem. Mater.* **2011**, *23*, 3348-3356.

(9) Berret, J. F.; Schonbeck, N.; Gazeau, F.; El Kharrat, D.; Sandre, O.; Vacher, A.; Airiau, M.: Controlled clustering of superparamagnetic nanoparticles using block copolymers: Design of new contrast agents for magnetic resonance imaging. *J. Am. Chem. Soc.* **2006**, *128*, 1755-1761.

(10) Ai, H.; Flask, C.; Weinberg, B.; Shuai, X.; Pagel, M. D.; Farrell, D.; Duerk, J.; Gao, J. M.: Magnetite-loaded polymeric micelles as ultrasensitive magnetic-resonance probes. *Adv. Mater.* **2005**, *17*, 1949-1952.

(11) Matsumoto, Y.; Jasanoff, A.: T-2 relaxation induced by clusters of superparamagnetic nanoparticles: Monte Carlo simulations. *Magn. Reson. Imaging* **2008**, *26*, 994-998.

(12) Carroll, M. R. J.; Woodward, R. C.; House, M. J.; Teoh, W. Y.; Amal, R.; Hanley, T. L.; St Pierre, T. G.: Experimental validation of proton transverse relaxivity models for superparamagnetic nanoparticle MRI contrast agents. *Nanotechnology* **2010**, *21*.
(13) Xu, F.; Cheng, C.; Chen, D.-X.; Gu, H.: Magnetite nanocrystal clusters with ultra-high sensitivity in magnetic resonance imaging. *ChemPhysChem* **2012**, *13*, 336-341.
(14) Yoon, T.-J.; Lee, H.; Shao, H.; Hilderbrand, S. A.; Weissleder, R.: Multicore assemblies potentiate magnetic properties of biomagnetic nanoparticles. *Adv. Mater.* **2011**, *23*, 4793-4797.
(15) Poeselt, E.; Kloust, H.; Tromsdorf, U.; Janschel, M.; Hahn, C.; Masslo, C.; Weller, H.: Relaxivity optimization of a PEGylated iron-oxide-based negative magnetic resonance contrast agent for T-2-weighted spin-echo imaging. *ACS Nano* **2012**, *6*, 1619-1624.
(16) Ai, H.; Flask, C.; Weinberg, B.; Shuai, X. T.; Pagel, M. D.; Farrell, D.; Duerk, J.; Gao, J.: Magnetite-loaded polymeric micelles as ultrasensitive magnetic-resonance probes. *Adv. Mater.* **2005**, *17*, 1949-1952.
(17) Pothayee, N.; Balasubramaniam, S.; Pothayee, N.; Jain, N.; Hu, N.; Lin, Y.; Davis, R. M.; Sriranganathan, N.; Koretsky, A. P.; Riffle, J. S.: Magnetic nanoclusters with hydrophilic spacing for dual drug delivery and sensitive magnetic resonance imaging. *J. Mater. Chem. B* **2013**.
(18) Lee, E. S. M.; Shuter, B.; Chan, J.; Chong, M. S. K.; Ding, J.; Teoh, S.-H.; Beuf, O.; Briguet, A.; Tam, K. C.; Choolani, M.; Wang, S.-C.: The use of microgel iron oxide nanoparticles in studies of magnetic resonance relaxation and endothelial progenitor cell labelling. *Biomaterials* **2010**, *31*, 3296-3306.
(19) Vuong, Q. L.; Berret, J.-F.; Fresnais, J.; Gossuin, Y.; Sandre, O.: A universal scaling law to predict the efficiency of magnetic nanoparticles as MRI T2-Contrast Agents. *Adv. Healthcare Mater.* **2012**, *1*, 502-512.
(20) Jokerst, J. V.; Lobovkina, T.; Zare, R. N.; Gambhir, S. S.: Nanoparticle PEGylation for imaging and therapy. *Nanomedicine* **2011**, *6*, 715-728.
(21) Wang, Y.; Ng, Y. W.; Chen, Y.; Shuter, B.; Yi, J.; Ding, J.; Wang, S. C.; Feng, S. S.: Formulation of superparamagnetic iron oxides by nanoparticles of biodegradable polymers for magnetic resonance imaging. *Adv. Func. Mater.* **2008**, *18*, 308-318.
(22) Yang, J.; Lee, C.-H.; Park, J.; Seo, S.; Lim, E.-K.; Song, Y. J.; Suh, J.-S.; Yoon, H.-G.; Huh, Y.-M.; Haam, S.: Antibody conjugated magnetic PLGA nanoparticles for diagnosis and treatment of breast cancer. *J. Mater. Chem.* **2007**, *17*, 2695-2699.
(23) Johnson, B. K.; Prud'homme, R. K.: Flash nanoprecipitation of organic actives and block copolymers using a confined impinging jets mixer. *Aust. J. Chem.* **2003**, *56*, 1021-1024.
(24) Johnson, B. K.; Prud'homme, R. K.: Mechanism for rapid self-assembly of block copolymer nanoparticles. *Phys. Rev. Lett.* **2003**, *91*, 118302/1-118302/4.
(25) Liu, Y.; Cheng, C.; Liu, Y.; Prud'homme, R. K.; Fox, R. O.: Mixing in a multi-inlet vortex mixer (MIVM) for flash nanoprecipitation. *Chem. Eng. Sci.* **2008**, *63*, 2829-2842.
(26) D'Addio, S. M.; Prud'homme, R. K.: Controlling drug nanoparticle formation by rapid precipitation. *Adv. Drug Deliv. Rev.* **2011**, *63*, 417-426.
(27) Ungun, B.; Prud'homme, R. K.; Budijono, S. J.; Shan, J.; Lim, S. F.; Ju, Y.; Austin, R.: Nanofabricated upconversion nanoparticles for photodynamic therapy. *Opt. Express* **2009**, *17*, 80-86.
(28) Gindy, M. E.; Panagiotopoulos, A. Z.; Prud'homme, R. K.: Composite block copolymer stabilized nanoparticles: Simultaneous encapsulation of organic actives and inorganic nanostructures. *Langmuir* **2008**, *24*, 83-90.

(29) Goff, J. D.; Huffstetler, P. P.; Miles, W. C.; Pothayee, N.; Reinholz, C. M.; Ball, S.; Davis, R. M.; Riffle, J. S.: Novel phosphonate-functional poly(ethylene oxide)-magnetite nanoparticles form stable colloidal dispersions in phosphate-buffered saline. *Chem. Mater.* **2009**, *21*, 4784-4795.
(30) Pinna, N.; Grancharov, S.; Beato, P.; Bonville, P.; Antonietti, M.; Niederberger, M.: Magnetite nanocrystals: Nonaqueous synthesis, characterization, and solubility. *Chem. Mater.* **2005**, *17*, 3044-3049.
(31) Zhang, X.; Li, Y.; Chen, X.; Wang, X.; Xu, X.; Liang, Q.; Hu, J.; Jing, X.: Synthesis and characterization of the paclitaxel/MPEG-PLA block copolymer conjugate. *Biomaterials* **2005**, *26*, 2121-2128.
(32) Frank, J.; Radermacher, M.; Penczek, P.; Zhu, J.; Li, Y.; Ladjadj, M.; Leith, A.: SPIDER and WEB: processing and visualization of images in 3D electron microscopy and related fields. *J Struct Biol* **1996**, *116*, 190-199.
(33) D'Addio, S. M.; Kafka, C.; Akbulut, M.; Beattie, P.; Saad, W.; Herrera, M.; Kennedy, M. T.; Prud'homme, R. K.: Novel method for concentrating and drying polymeric nanoparticles: hydrogen bonding coacervate precipitation. *Mol. Pharm.* **2010**, *7*, 557-564.
(34) Kucheryavy, P.; He, J.; John, V. T.; Maharjan, P.; Spinu, L.; Goloverda, G. Z.; Kolesnichenko, V. L.: Superparamagnetic iron oxide nanoparticles with variable size and an iron oxidation state as prospective imaging agents. *Langmuir* **2013**, *29*, 710-716.
(35) Morales, M. P.; Veintemillas-Verdaguer, S.; Montero, M. I.; Serna, C. J.; Roig, A.; Casas, L.; Martinez, B.; Sandiumenge, F.: Surface and internal spin canting in γ-Fe2O3 nanoparticles. *Chem. Mater.* **1999**, *11*, 3058-3064.
(36) Rohrer, M.; Bauer, H.; Mintorovitch, J.; Requardt, M.; Weinmann, H. J.: Comparison of magnetic properties of MRI contrast media solutions at different magnetic field strengths. *Invest. Rad.* **2005**, *40*, 715-724.
(37) Roch, A.; Gossuin, Y.; Muller, R. N.; Gillis, P.: Superparamagnetic colloid suspensions: Water magnetic relaxation and clustering. *J. Magn. Magn. Mater.* **2005**, *293*, 532-539.
(38) Yablonskiy, D. A.; Haacke, E. M.: Theory of NMR signal behavior in magnetically inhomogeneous tissues - The static dephasing regime. *Magn. Reson. Med.* **1994**, *32*, 749-763.
(39) Koenig, S. H.; Kellar, K. E.: Theory of 1/T1 and 1/T2 NMRD profiles of solutions of magnetic nanoparticles. *Magn. Reson. Med.* **1995**, *34*, 227-233.
(40) Gillis, P.; Moiny, F.; Brooks, R. A.: On T-2-shortening by strongly magnetized spheres: A partial refocusing model. *Magn. Reson. Med.* **2002**, *47*, 257-263.
(41) Vagberg, L. J. M.; Cogan, K. A.; Gast, A. P.: Light-scattering study of starlike polymeric micelles. *Macromolecules* **1991**, *24*, 1670-1677.
(42) Miles, W. C.; Goff, J. D.; Huffstetler, P. P.; Reinholz, C. M.; Pothayee, N.; Caba, B. L.; Boyd, J. S.; Davis, R. A.; Riffle, J. S.: Synthesis and colloidal properties of polyether-magnetite complexes in water and phosphate-buffered saline. *Langmuir* **2009**, *25*, 803-813.
(43) Nolan, S. L.; Phillips, R. J.; Cotts, P. M.; Dungan, S. R.: Light scattering study on the effect of polymer composition on the structural properties of PEO–PPO–PEO Micelles. *J. Coll. Interf. Sci.* **1997**, *191*, 291-302.
(44) Pothayee, N.; Balasubramaniam, S.; Pothayee, N.; Jain, N.; Hu, N.; Lin, Y.; Davis, R. M.; Sriranganathan, N.; Koretsky, A. P.; Riffle, J. S.: Magnetic nanoclusters with hydrophilic spacing for dual drug delivery and sensitive magnetic resonance imaging. *J. Mater. Chem. B* **2013**, *1*, 1142-1149.
(45) Bennett, K. M.; Shapiro, E. M.; Sotak, C. H.; Koretsky, A. P.: Controlled aggregation of ferritin to modulate MRI relaxivity. *Biophys. J.* **2008**, *95*, 342-351.

(46) Paquet, C.; de Haan, H. W.; Leek, D. M.; Lin, H. Y.; Xiang, B.; Tian, G. H.; Kell, A.; Simard, B.: Clusters of superparamagnetic iron oxide nanoparticles encapsulated in a hydrogel: A particle architecture generating a synergistic enhancement of the T-2 Relaxation. *ACS Nano* **2011**, *5*, 3104-3112.
(47) Vuong, Q. L.; Gillis, P.; Gossuin, Y.: Monte Carlo simulation and theory of proton NMR transverse relaxation induced by aggregation of magnetic particles used as MRI contrast agents. *J. Magn. Reson.* **2011**, *212*, 139-148.

5 Well-defined Nanoparticles of Ritonavir Stabilized by Amphiphilic Block Copolymers

Sharavanan Balasubramaniam,[†] *Sanem Kayandan,*[§] *Jue Liang*,[§] *Yanchun Liu,*[§] *Bruce Orler,*[§] *Robert B. Moore,*[†,§,] *S. Richard Turner,*[†,§] *Judy S. Riffle,*[†,§] *and Richey M. Davis* [†,*]

[†]Macromolecules and Interfaces Institute, [§]Department of Chemistry, and [*]Department of Chemical Engineering, Virginia Tech, Blacksburg, VA 24061, U. S. A.

5.1 Abstract

There is a need for well-defined nanoparticles of antiretroviral drugs for the treatment of human immunodeficiency virus type one (HIV-1) with potential for drug targeting to the brain. Herein, we report nanoparticles of the antiretroviral drug, ritonavir, stabilized by amphiphilic block copolymers comprised of poly(ethylene oxide-*b*-D,L-lactide) and poly(ethylene oxide-*b*-butylene oxide). Monomodal size distributions and control over particle sizes (85-130 nm) were achieved by incorporation of hydrophobic homopolymer additives (11k-poly(L-lactide) or 2k-poly(butylene oxide)) during the nanoparticle preparation process. Drug loadings above 20 wt% and encapsulation efficiencies in the range of 70-80% were achieved. Differential scanning calorimetry and powder X-ray diffraction experiments revealed that ritonavir was trapped in the amorphous form in the nanoparticles. The nanoparticles were colloidally stable over 24 hours under simulated physiological conditions (PBS containing 1% BSA, T = 37°C).

5.2 Introduction

The desire for site-specific delivery of drugs in order to maximize therapeutic efficacy and minimize side effects has led to the emergence of nanomedicine. Polymeric materials are recognized for their potential as drug delivery vehicles owing to their biocompatibility, high drug loading capacities, controlled or triggered release of drugs, tunability of physicochemical properties, and potential for active targeting.[1] In this regard, block copolymers are an important class of materials that hold a lot of promise as carriers of therapeutics and imaging agents. The design of block copolymer nanoparticles encapsulating high payloads of drugs for delivery to specific sites *in vivo* has been a heavily researched area.

Amphiphilic block copolymers comprised of hydrophobic and hydrophilic blocks are noted for their ability to self-assemble into micelles in solvents selective for one of the blocks. These core-shell structures, in the size range of 10-100 nm, have been utilized as carriers for hydrophobic drugs which are localized in the hydrophobic cores. The hydrophilic block is often comprised of poly(ethylene glycol) (PEG), a biocompatible, non-ionic polymer that forms the outer corona providing steric stabilization to the nanoparticles. In addition, PEG reduces non-specific uptake by the reticuloendothelial system (RES) and extends the blood circulation times.[2] Block copolymers of PEG and biocompatible, hydrophobic polymers such as poly(propylene oxide), poly(D,L-lactide), and poly(ε-caprolactone) have been extensively used as carriers of anti-cancer hydrophobic drugs such as paclitaxel and doxorubicin.[3-7] However, reports of well-defined block copolymer nanoparticles for antiretroviral therapy for the treatment of human immunodeficiency virus type one (HIV-1) are limited.

The central nervous system represents one of the major anatomical reservoirs for HIV-1, and the replication of the virus in the brain leads to a range of neurological disorders. Currently, over

twenty antiretroviral drugs have been approved in the United States and are classified as nucleoside reverse transcriptase inhibitors (NRTIs), non-nucleoside reverse transcriptase inhibitors (NNRTIs), protease inhibitors (PIs), fusion inhibitors (FIs), and integrase strand transfer inhibitors (ISTIs).[8] Although highly active antiretroviral drugs are known to reduce disease severity, there is still a lack of effective treatment for HIV-associated neurocognitive disorders. This problem has been attributed, to a large extent, to the poor permeability of antiretroviral drugs across the blood-brain barrier, which owing to its physical structure, presence of efflux pumps, and higher expression of metabolizing enzymes, acts as a major physiological barrier against drug entry.[9] Based on several basic and preclinical studies, it has been posited that nanoparticle-based drug delivery systems have tremendous potential for targeting antiretroviral drugs to the brain.[10]

There are several reports of the formulation and therapeutic efficacy of antiretroviral drug nanoparticles. These systems were comprised of various classes of antiretroviral drugs encapsulated as solid lipid nanoparticles or loaded in polymers such as poly(butylcyanoacrylate), poly(lactic-*co*-glycolic acid), and poly(lactic acid)-poly(ethylene oxide).[11-15] However, most of these works relied on the emulsion/solvent evaporation technique for the preparation of drug-loaded nanoparticles which has limitations including inadequate control over particle sizes, low drug entrapment efficiencies, and several purification steps. One recent study described nanoformulations of various antiretroviral drugs using the wet-milling technique leading to particle sizes greater than 250 nm and with considerable polydispersities.[16] There is a need for well-defined antiretroviral drug nanoparticles with good control over particle sizes and compositions, and relatively narrow size polydispersities. Prud'homme and co-workers have reported extensively on a scalable rapid precipitation technique using a multi-inlet vortex mixer to produce stable block copolymer nanoparticles containing drugs, imaging agents, peptides and targeting ligands.[17-21] In

this method, an organic stream containing the drugs and a block copolymer stabilizer is rapidly combined with a miscible non-solvent (water) under high supersaturations to yield kinetically-trapped nanoparticles with controlled compositions and sizes.

In this paper, we describe the synthesis and characterization of well-defined ritonavir nanoparticles stabilized by amphiphilic block copolymers comprised of poly(ethylene oxide-*b*-D,L-lactide) and poly(ethylene oxide-*b*-butylene oxide), made by rapid precipitation in a multi-inlet vortex mixer. Ritonavir (RTV) (Figure 5.1), a protease inhibitor with extremely low aqueous solubility (1.3 μg mL^{-1} at pH 6.8 and 37°C),[22] was chosen as a model antiretroviral drug. PIs are an important class of antiretroviral drugs that prevent viral replication by selectively binding HIV-1 proteases and blocking proteolytic cleavage of protein precursors that are necessary for the production of infectious viral particles. We demonstrate the use of homopolymers of the respective hydrophobic block (poly(L-lactide) and poly(butylene oxide)) as hydrophobic additives during the nanoparticle fabrication process to give monomodal size distributions.

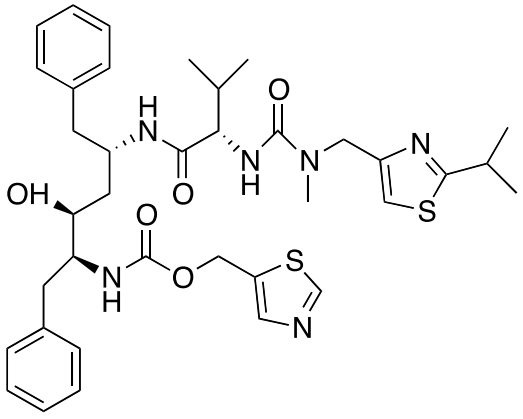

Figure 5.1 Molecular structure of ritonavir.

5.3 Experimental Section

5.3.1 Materials

Tin (II) 2-ethylhexanoate (stannous octoate), dibutyltin (IV) oxide, benzyl alcohol (> 98%) and tetrahydrofuran (THF, anhydrous) were purchased from Aldrich and used as received. Diethyl ether (anhydrous) and ethyl acetate (HPLC grade) were purchased from Fisher Scientific and used as received. Toluene (Fischer Scientific) was stirred over calcium hydride and distilled. D,L-lactide was obtained from Purac and recrystallized from ethyl acetate twice. Poly(ethylene oxide) methyl ether (mPEG) macroinitiator with a molar mass of ~5000 g mol^{-1} was obtained from Aldrich and vacuum-dried at room temperature for 18 h before use. Dimethyl-1,4-cyclohexane dicarboxylate (DMCD) and 2,2,4,4-tetramethyl-1,3-cyclobutanediol (CBDO) were gifts from Eastman Chemical Company. Phosphate buffered saline (PBS, 1×) was purchased from Cell Gro with the following composition: 1 mM KH_2PO_4, 154 mM NaCl, 6 mM Na_2HPO_4. Bovine serum albumin was purchased from American Bioanalytical.

5.3.2 Synthesis of poly(ethylene oxide-*b*-D,L-lactide)

A mPEG(5k)-PDLLA(10k) block copolymer was synthesized by ring-opening polymerization of D,L-lactide initiated by mPEG using stannous octoate as the catalyst.[23] D,L-lactide (4.44 g, 0.03 mol), mPEG (2.22 g, 4.44 x 10^{-4} mol) and 17 mL toluene were charged to a 250-mL, flame-dried, round bottom flask equipped with a magnetic stir bar. The flask was placed in an oil bath at 80°C to dissolve the monomer and initiator. A stock solution of stannous octoate in toluene was prepared with a concentration of 0.012 g mL^{-1}. The catalyst solution (0.98 mL) was added to the flask and the temperature of the oil bath was raised to 105°C. The polymerization was allowed to proceed

for 48 h. The polymer was isolated by precipitation into cold diethyl ether and collected by vacuum filtration. The product was vacuum dried at 40°C for 40 h, with yield 5.68 g.

5.3.3 Synthesis of poly(L-lactide) homopolymer

A PLLA homopolymer (M_n: 11,000 g mol^{-1}) was prepared with benzyl alcohol as the initiator.[24] L-lactide (2.05 g, 0.01 mol) and 6.5 mL toluene were charged into a 100 mL round-bottom flask equipped with a stir bar and condenser. Benzyl alcohol (0.36 mL of a 0.51 M solution in toluene, 0.18 mmol) was added to the stirring reaction via syringe. Stannous octoate catalyst solution (0.31 mL, 0.012 g mL^{-1}) in toluene was added to the flask. The polymerization was conducted at toluene reflux for 48 h. The polymer was isolated by precipitation into cold diethyl ether and collected by vacuum filtration. The product was vacuum dried at 40°C for 40 h and 1.65 g of polymer was obtained.

5.3.4 Synthesis of poly(ethylene oxide-*b*-butylene oxide)

An exemplary procedure for the synthesis of mPEG(5k)-PBO(9k) is provided. A 5,000 M_n mPEG (5.0 g, 1.0 mmol) was added to a 60-mL pressure tube equipped with a stir bar and dried under vacuum at 70°C for 12 h, then cooled to RT. 18-Crown-6 ether (0.26 g, 1.0 mmol) was added and dried under vacuum at RT for 0.5 h. Potassium hydride/mineral oil suspension (80 mg, 30 wt%, 0.6 mmol) was added and dried under vacuum at RT for 0.5 h. The mixture was heated to 70°C with slow nitrogen purge for 12 h followed by applying vacuum to remove any residual hydrogen. 1,2-BO (12 mL, 10 g) was syringed into the pressure tube and the mixture was stirred at 70°C for 12 h. The reaction was cooled to RT and diluted with dichloromethane (100 mL). Acetic acid (0.06 g, 1.0 mmol) was added to neutralize the alkoxide. The organic phase was washed with DI water

(3 × 100 mL). The obtained organic solution was dried under vacuum at 70 °C yielding a waxy solid (13.8 g, 92%).

5.3.5 Synthesis of poly(butylene oxide) homopolymer

A benzyl-PBO (M_n: 2,000 g mol^{-1}) was synthesized via anionic ring-opening polymerization of 1,2-BO. A potassium naphthalide solution was prepared by charging naphthalene (14.1 g, 0.11 mol) into a 250-mL, flame-dried, round-bottom flask equipped with a glass stir bar. Dry THF (100 mL) was syringed into the flask to dissolve the naphthalene. Potassium metal (3.96 g, 0.10 mol) was added to the solution followed by a N_2 purge for 30 min. The solution was stirred overnight and titrated with 1 N HCl to determine the molarity of the potassium naphthalide solution (0.95 M). 18-Crown-6 ether (2.6 g, 10 mmol) was added to a 60-mL pressure tube equipped with a stir bar and dried under vacuum at RT for 0.5 h. Benzyl alcohol (1.08 g, 10 mmol) was added and dried under vacuum at RT for 0.5 h followed by addition of potassium naphthalide solution (10 mL, 9.5 mmol). 1,2-BO (24 mL, 20 g) was syringed into the pressure tube and the mixture was stirred at 70 °C for 12 h. The reaction was cooled to RT and diluted with dichloromethane (150 mL). Acetic acid (0.60 mL, 10 mmol) was added to neutralize the alkoxide. The organic phase was washed with DI water (3 × 100 mL). The obtained organic solution was dried under vacuum at 70°C yielding a liquid (19.4 g, 99%).

5.3.6 Synthesis of block copolymer-stabilized ritonavir nanoparticles

Polylactide and polyether nanoparticles with targeted loadings of 10, 20 and 30 wt% RTV were prepared. A representative procedure for preparing RTV-polylactide nanoparticles containing 20

wt% RTV is as follows. Ritonavir (38.5 mg) was dissolved in THF (3.5 mL) containing mPEG(5k)-PDLLA(10k) (115.5 mg) and PLLA(11k) (38.5 mg). A four-jet multi-inlet vortex mixer design based on one previously reported was used to form the nanoparticles.[18] The THF solution was filtered with a 0.2 μm Nylon syringe filter, and fed into the multi-inlet vortex mixer at 9.99 mL min^{-1} using a computer-controlled syringe pump (New Era Pump Systems, Farmingdale, New York) along with three streams of de-ionized water at 33.3 mL min^{-1}, controlled by a PHD 4000 programmable syringe pump (Harvard Apparatus, Holliston, Massachusetts), yielding a final liquid phase composition of 1:10 (v/v) THF/water. After the nanoparticle suspension was formed in the mixer, it was dialyzed to remove THF against de-ionized water (4000 mL) for 24 h using a Spectra/Por dialysis bag (1,000 MWCO, Spectrum Laboratories, Inc.) with four changes of dialysate. The dialyzed suspension was freeze-dried for 72 h (0.021 mBar, -52°C) and stored as a solid product.

5.3.7 Size analysis of nanoparticles

Dynamic light scattering (DLS) measurements were performed using a Zetasizer NanoZS particle analyzer (Malvern Instruments Ltd., Malvern, U. K.) equipped with a 4 mW solid-state He-Ne laser (λ = 633 nm) at a scattering angle of 173°. The average translational diffusion coefficient (D_t) was extracted from a single exponential (cumulants) fit of the correlation curve and the intensity-average hydrodynamic diameter (D_I) was determined through the Stokes-Einstein equation: $D_I = k_B T/(3\pi\eta D_t)$, where k_B is the Boltzmann constant, T is the absolute temperature and η, the solvent viscosity. The reported intensity-weighted hydrodynamic diameters were averaged from five measurements. The critical aggregation concentrations (*cac*) of the copolymers in a 1:10 (v/v) THF-water mixture were determined by measured the scattering intensities of a range of

copolymer concentrations (0.001 – 10 mg mL^{-1}) by dynamic light scattering at 25°C. The inflection point on a graph of the mean count rate (kilocounts per second) as a function of copolymer concentration was taken as the *cac*.

5.3.8 Determination of drug content

The drug loadings of the nanoparticles were determined by reversed-phase high performance liquid chromatography using an Agilent 1200 HPLC system consisting of a quaternary pump, online degasser, autosampler, and Agilent Chemstation LC 3D software. The chromatographic separation was performed with a ZORBAX Eclipse XDB-C18 column (4.5 × 150 mm, 5.0 μm pore size) maintained at 30°C. Ritonavir was detected by UV detection at a wavelength of 240 nm. The mobile phase consisted of 40/60 acetonitrile/potassium phosphate buffer (0.05 M, pH 5.65) at a flow rate of 1.5 mL min^{-1}. The total run time and the sample injection volume were 20 min. and 5 μL, respectively. The retention time for RTV was 10.6 min. To measure the drug content, lyophilized samples were suspended in acetonitrile at a concentration of 1 mg mL^{-1} and sonicated for 15 min. The solutions were filtered with a 0.2 μm Nylon filter, and analyzed by HPLC in triplicate. The drug concentrations were determined by comparison to a standard curve for RTV (see Appendix section, A.3). The drug loading and encapsulation efficiency were calculated as follows:

$$Drug\ loading\ (wt\%) = \frac{mass\ of\ RTV\ encapsulated}{total\ mass\ of\ nanoparticles} \times 100 \tag{5.1}$$

$$Encapsulation\ efficiency\ (\%) = \frac{experimental\ RTV\ loading}{targeted\ RTV\ loading} \times 100 \tag{5.2}$$

5.3.9 Crystallinity analysis

Differential scanning calorimetry (DSC) and powder X-ray diffraction (PXRD) analyses were performed to evaluate the crystallinity of the ritonavir nanoparticles. Thermal transitions were measured using a TA Q2000 DSC (TA Instruments, New Castle, DE) equipped with an RCA90 refrigerated cooling accessory and calibrated with indium. About 3-5 mg of each sample was weighed in a TZero aluminium pan (TA Instruments) for the analyses. Dry N_2 was used as the purge gas at 50 mL min^{-1} and samples were heated at a rate of 10°C min^{-1}. Melting point and enthalpy of fusion were determined from the first heat scan. The thermal transitions were analyzed using the Universal Analysis 2000 software. PXRD spectra were recorded using a Bruker AXS D8 Discover X-ray diffractometer equipped with a $Cu_{K\alpha}$ source (λ = 1.5406 Å) and operating at an accelerating potential of 60 kV. Experiments were conducted at a scan range was 10 - 40° 2θ with a step size of 0.01°. The scanning speed was 4° min^{-1}.

5.3.10 Viscosity of copolymer solutions

The shear viscosities of the block copolymer solutions in THF were measured at 25°C using an AR-G2 rheometer (TA Instruments, New Castle, U. S. A.). The shear rate range was 0.01-100 s^{-1}. The copolymer concentrations were 33 mg mL^{-1} and 11 mg mL^{-1} for mPEG(5k)-PDLLA(10k) and mPEG(5k)-PBO(9k), respectively.

5.4 Results and Discussion

5.4.1 Nanoparticle synthesis

Nanoparticles of ritonavir were formulated using mPEG(5k)-PDLLA(10k) and mPEG(5k)-PBO(9k) diblock copolymer stabilizers. The critical aggregation concentrations of the copolymers

in the mixed solvent (25°C, 9 vol % THF) determined by dynamic light scattering were ~0.3 mg mL^{-1} and ~0.1 mg mL^{-1} for mPEG(5k)-PDLLA(10k) and mPEG(5k)-PBO(9k), respectively (Figure 5.2). The lower *cac* for the latter is consistent with the higher hydrophobicity of PBO relative to PDLLA.

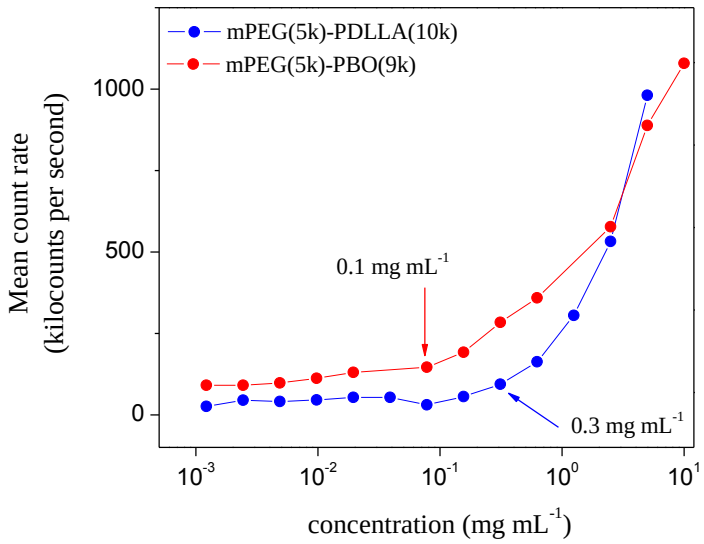

Figure 5.2 Aggregation of mPEG(5k)-PDLLA(10k) and mPEG(5k)-PBO(9k) diblock copolymers in 1:10 THF-water (v/v) at 25°C.

Control diblock copolymer nanoparticles (without incorporation of drug) prepared at ten-fold higher concentrations relative to the *cac* showed bimodal particle size distributions. The incorporation of drug under these conditions led to ill-defined aggregates with broad size distributions. The addition of homopolymers of the respective hydrophobic blocks during the nanoparticle formulation process was found to significantly improve the polydispersities, leading to monomodal size distributions. Semi-crystalline poly(L-lactide) (PLLA(11k)) and amorphous poly(butylene oxide) (PBO(2k)) were dissolved with the respective block copolymer in THF at a

homopolymer:copolymer weight ratio of 1:3, and subsequently rapidly mixed with water in the multi-inlet vortex mixer to precipitate nanoparticles. Figure 5.3 shows the intensity-weighted size distributions of the drug-free copolymer nanoparticles with and without the addition of the homopolymers. The nanoparticle suspensions exiting the mixer were diluted in de-ionized water to a concentration of 0.1 mg mL^{-1}, sonicated in a water-bath for 10 min. and analyzed by dynamic light scattering. The mean intensity-weighted diameters were 132 nm and 98 nm for PLLA(11k)/ mPEG(5k)-PDLLA(10k) and PBO(2k)/mPEG(5k)-PBO(9k) nanoparticles, respectively, with a polydispersity index of 0.18 for both. It was reasoned that the homopolymer provides a substrate for copolymer assembly, thus serving as a nucleating agent for nanoparticle formation. The use of a hydrophobic macromolecule to induce heterogeneous nucleation was previously demonstrated by Saad who added poly(caprolactone) homopolymer of various molecular weights to control particle sizes of paclitaxel-loaded mPEG-PCL nanoparticles.[25]

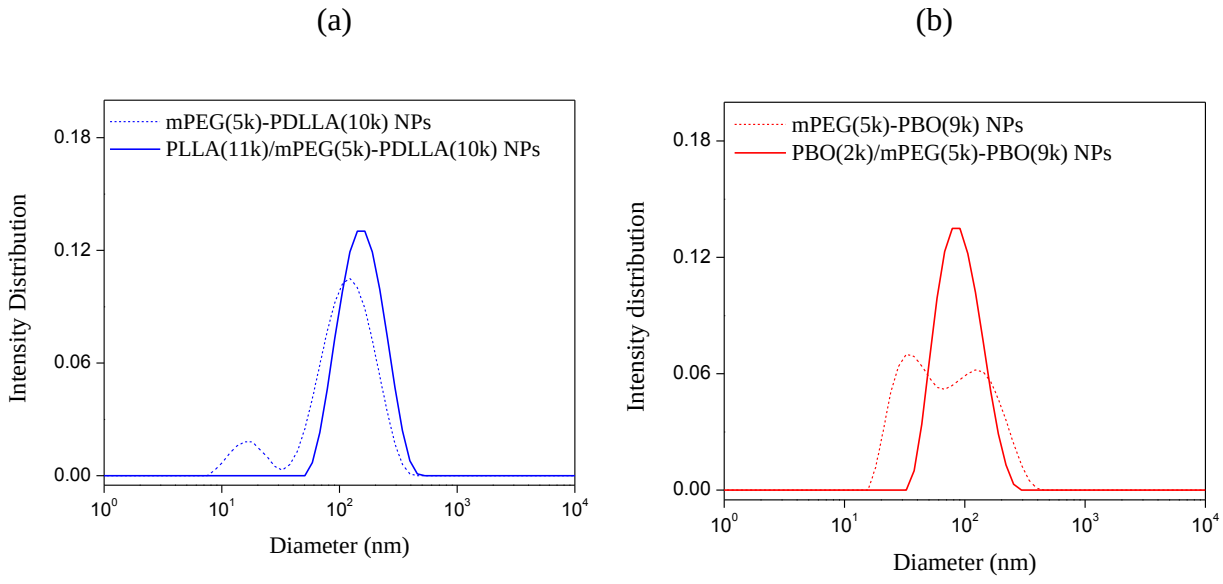

Figure 5.3 Size distributions of block copolymer nanoparticles with and without incorporation of hydrophobic homopolymers in the nanoparticle cores.

The rapid precipitation process affords kinetic control over nanoparticle characteristics and overcomes the limitations of techniques which rely on thermodynamic equilibrium yielding low drug loadings and broad particle size distributions. A high Reynolds number homogeneous mixing in the multi-inlet vortex mixer is essential for the simultaneous aggregation of the solute (ritonavir in this work) and assembly of the stabilizing copolymer producing well-defined, block copolymer stabilized drug nanoparticles. The Reynolds number for mixing was calculated from the viscosities and velocities of the four inlet streams comprised of one organic stream and three water streams, and the diameter of the mixer chamber (D = 6.1 × 10^{-3} m), as shown below:

$$R_e = \sum_{i}^{N} \frac{V_i . D}{\nu_i} \tag{5.3}$$

where V_i and ν_i are the velocity (m s^{-1}) and kinematic viscosity (m^2 s^{-1}) of i^{th} the inlet stream, and N = 4. The measured shear viscosities of the mPEG(5k)-PDLLA(10k) and mPEG(5k)-PBO(9k) copolymer solutions, 9.65 × 10^{-4} and 7.21 × 10^{-4} kg m^{-1} s^{-1} respectively, were used to compute the Reynolds numbers. The calculated R_es were 12,540 and 12,860 for the two systems, respectively (see Appendix section, A.1). It has been shown in previous studies that R_e > 2000-3000, the turbulent flow in the mixer leads to homogeneous mixing leading to nanoparticles with low polydispersities and sizes. Thus, the high Reynolds numbers in this work are high enough to produce well-defined ritonavir nanoparticles.

5.4.2 Size and drug loading analyses

Nanoparticles containing targeted ritonavir loadings of 10, 20, and 30 wt% were formulated by varying the initial drug concentrations in the THF solution containing the homopolymer and the diblock copolymer. The copolymer concentration (10× higher than the equilibrium concentration

or *cac*) and the homopolymer:copolymer ratio (1:3, w/w) were kept constant at each drug loading for a given polymer system. The drug solubility and supersaturation values are tabulated in the Appendix (A.6). Figure 5.4 shows the drug loadings of the RTV nanoparticles determined by HPLC. Interestingly, near constant encapsulation efficiencies in the range of 75-80% were achieved irrespective of the targeted drug loading and the composition of the hydrophobic block.

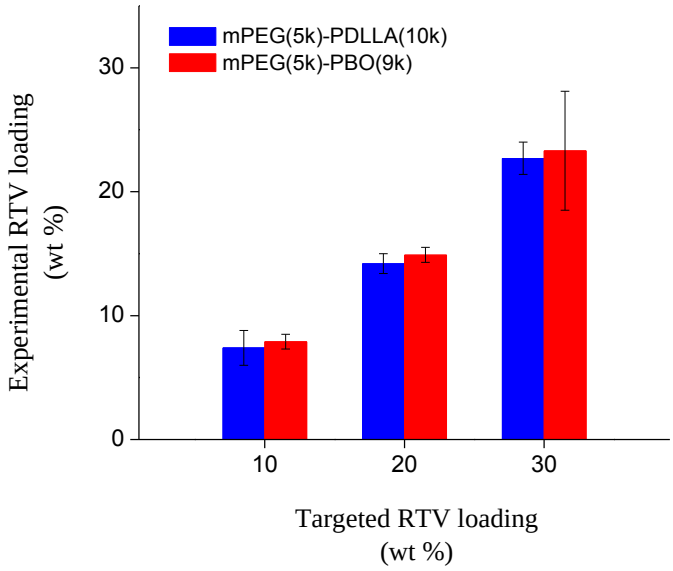

Figure 5.4 Drug loading of block copolymer-stabilized ritonavir nanoparticles at various targeted RTV loadings in the range of 10-30 wt% (Error bars represent standard deviations from three measurements).

Ritonavir nanoparticles stabilized with mPEG(5k)-PDLLA(10k) with targeted compositions of 10, 20, and 30 wt% drug are abbreviated as **PLA7**, **PLA14**, and **PLA23**, respectively, indicating the amount of encapsulated drug. The respective compositions within the mPEG(5k)-PBO(9k) series are called **PBO8**, **PBO15**, and **PBO23**, respectively. Table 5.1 shows the intensity-weighted diameters, polydispersity indices, and the experimentally determined drug loadings for the nanoparticles stabilized with the polylactide and polyether copolymers. The DLS data presented are for nanoparticles immediately after formation by rapid precipitation. The error bars for sizes

represent the standard deviation from five measurements. Monomodal size distributions with relatively low polydispersities (< 0.2) were obtained with both polymer systems and all targeted ritonavir loadings. The PLA nanoparticles were roughly 40 nm larger than the analogous PBO nanoparticles. It was reasoned that the mPEG(5k)-PBO(9k) molecule nucleates more rapidly owing to the higher hydrophobicity of PBO relative to PDLLA, resulting in smaller particle sizes.

Table 5.1 Hydrodynamic diameters and polydispersities of ritonavir nanoparticles

	mPEG(5k)-PDLLA(10k)				mPEG(5k)-PBO(9k)		
	RTV loading	D_I (nm)	PDI		RTV loading	D_I (nm)	PDI
PLA7	7 wt%	133 ± 4	0.15	**PBO8**	8 wt%	88 ± 4	0.15
PLA14	14 wt%	128 ± 5	0.19	**PBO15**	15 wt%	86 ± 3	0.18
PLA23	23 wt%	120 ± 4	0.18	**PBO23**	23 wt%	88 ± 6	0.19

While the PLA nanoparticles could be readily redispersed in de-ionized water after dialysis and lyophilization with mild sonication in a water bath sonicator, the PBO-based nanoparticles showed aggregation, and redispersion in water was afforded using probe-tip sonication (Tekmar Sonic Disruptor) for 2 min. This is likely because of inter-particle bridging due to the fluid PBO core of the nanoparticles. It is noteworthy that monomodal size distributions and PDIs in the range 0.10-0.15 were obtained for the all the PBO nanoparticles after dispersion using probe-tip sonication.

5.4.3 Crystallinity analysis

DSC thermograms revealed endothermic melting peaks for ritonavir, mPEG(5k), **PLA14** and **PBO15** NPs containing ~15 wt% RTV (Figure 5.5a). The peak at 62°C for mPEG(5k) with an

enthalpy of 191 J g^{-1} represents its melting transition. The peak melting temperatures and melting enthalpies of the diblock copolymers and the RTV-loaded nanoparticles are shown in Table 5.2. The melting transitions in the range of 45-53°C in the copolymers and the nanoparticles indicate a separated PEG phase. Furthermore, the presence of RTV did not significantly change the PEG melting temperatures indicating that the drug is localized in the hydrophobic PDLLA or PBO core. Thus, it is reasonable to envision the nanoparticles as comprised of a core formed by the drug and the hydrophobic polymers and a distinct PEG corona. The lower melting temperatures relative to pristine mPEG(5k) are indicative of a lower degree of crystallinity in the copolymer and nanoparticle form. The reduced melting enthalpies of 58 and 27 J g^{-1} in the diblock copolymers and the nanoparticles are consistent with a lower proportion of mPEG in these matrices. Significantly, no endothermic transitions corresponding to ritonavir were observed in the nanoparticles suggesting that the drug was trapped in the amorphous state in the particles.

Table 5.2 Peak melting temperatures and melting enthalpies of RTV-block copolymer nanoparticles

	Peak Melting Temperature (°C)	Melting Enthalpy (J g^{-1})
RTV	126	92
mPEG(5k)	62	191
mPEG(5k)-PDLLA(10k)	49	58
mPEG(5k)-PBO(9k)	53	58
PLA14 NPs	49	27
PBO15 NPs	45	26

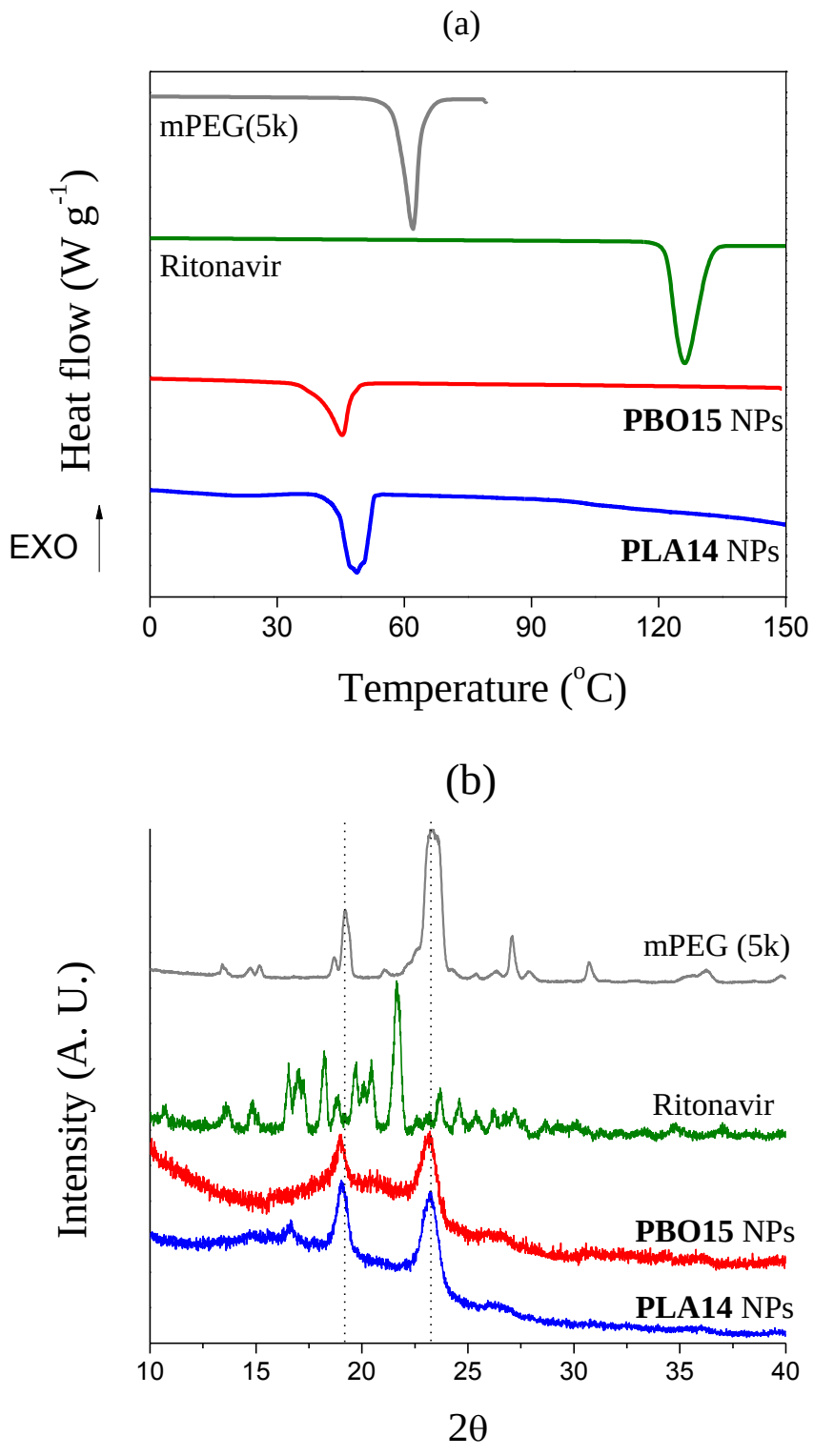

Figure 5.5 (a) DSC thermograms (first heat scans) and (b) PXRD patterns of ritonavir nanoparticles stabilized with mPEG(5k)-PBO(9k) and mPEG(5k)-PDLLA(10k) copolymers.

The X-ray diffraction patterns of ritonavir, mPEG(5k), **PBO15** and **PLA14** nanoparticles containing ~15 wt% RTV are shown in Figure 5.5b. Ritonavir showed an intense diffraction peak at 2θ = 21.6° and numerous lower intensity peaks between 13-20° and 22-30°. The nanoparticles showed two diffraction peaks at 18.9° and 23.2° attributed to PEG.[26] These peaks indicate PEG phase separation in the nanoparticles and drug localization in the PDLLA core. The low intensity peak at 2θ = 16.6° in the **PLA14** nanoparticles was attributed to the crystallization of PLLA.[27] The ritonavir peaks were absent in both the **PBO15** and **PLA14** spectra providing further confirmatory evidence that the drug was in the amorphous form in the nanoparticles. The phase of the drug in nanoparticle form strongly influences the observed bioavailability. In general, higher *in vitro* solution supersaturations and higher *in vivo* bioavailabilities can be achieved with amorphous drug nanoparticles relative to their crystalline counterparts owing to the higher chemical potential of the amorphous form.[28,29]

5.4.4 Colloidal stability in physiological media

The colloidal stability of the ritonavir nanoparticles in physiological media was evaluated by dynamic light scattering. The **PLA14** and **PBO15** nanoparticles were dispersed in phosphate buffered saline (PBS, pH 7.4) and the hydrodynamic diameter was monitored every 30 min. over 24 h. As shown in Figure 5.6a, the hydrodynamic sizes for both the systems remained constant at a measurement temperature of 25°C. In order to simulate physiological conditions, the nanoparticles were also dispersed in PBS containing 1 wt% bovine serum albumin (BSA), and the sizes were measured at 37°C over 24 h. The intensity-weighted size distributions (Figure 5.6b, inset) revealed two distinct peaks attributable to the BSA (~ 8 nm) and the nanoparticles. There

was no evidence of aggregation after 24 h, indicating that the PEO coverage of the nanoparticles was sufficient to prevent undesired protein adsorption and/or aggregation.

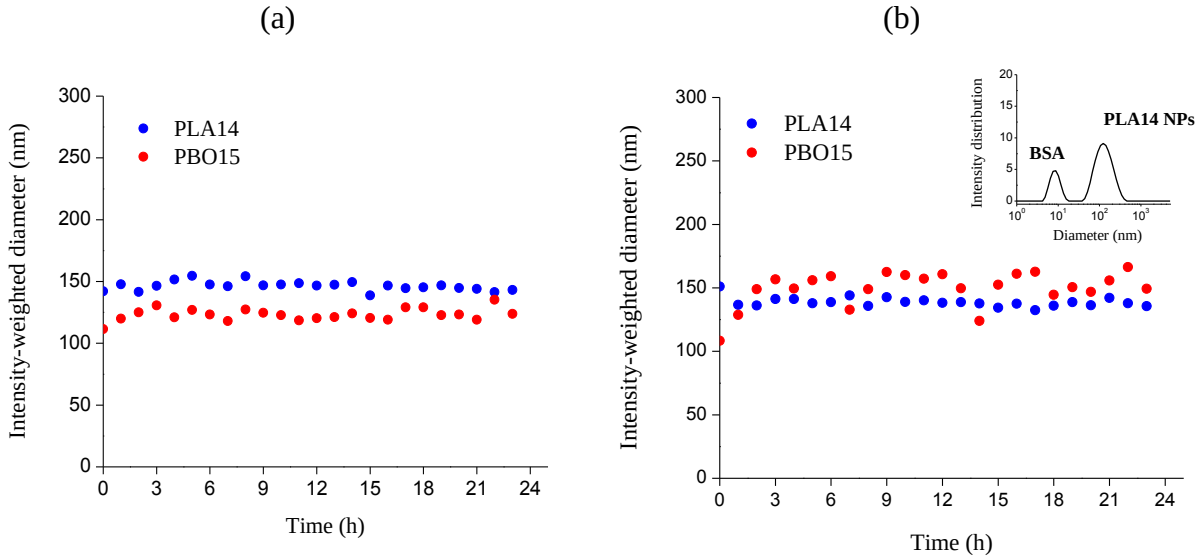

Figure 5.6 Stability of block copolymer stabilized-ritonavir nanoparticles in PBS at 25°C (a) and in PBS containing 1 wt% BSA at 37°C (b).

5.4.5 Ritonavir nanoparticles with potential for tailored drug release kinetics

The synthesis of well-defined nanoparticles containing clinically useful drug loadings and sustained release of the encapsulated drug is highly desirable. With this goal in mind, polyester and polyether nanoparticles were prepared with some variation in the polymer chemistries. Block copolymer nanoparticles composed of mPEG(5k)-PDLLA(10k) as the stabilizer and encapsulating ritonavir were prepared using a highly hydrophobic and high T_g polyester homopolymer additive. This homopolymer was used instead during nanoparticle fabrication instead of the 11k-poly(L-lactide) described earlier. We hypothesized that the combination of high T_g and hydrophobicity of the nanoparticle core could potentially result in sustained release of the drug. The amorphous copolyester, poly(oxy-2,2,4,4-tetramethyl-1,3-cyclobutanediyloxy-1,4-cyclohexanedicarbonyl) [Poly(TMCBD-CHDC)], was synthesized by melt polycondensation from the cycloaliphatic ester,

dimethyl-1,4-cyclohexane dicarboxylate (DMCD), and the cycloaliphatic diol, 2,2,4,4-tetramethyl-1,3-cyclobutanediol (CBDO), with dibutyltin oxide as the catalyst as shown the reaction scheme (Figure 5.7) below. The number-average molecular weight of this polymer was 2,500 g mol^{-1}, as determined by size exclusion chromatography. The polymer had a T_g of 65°C as determined by differential scanning calorimetry.

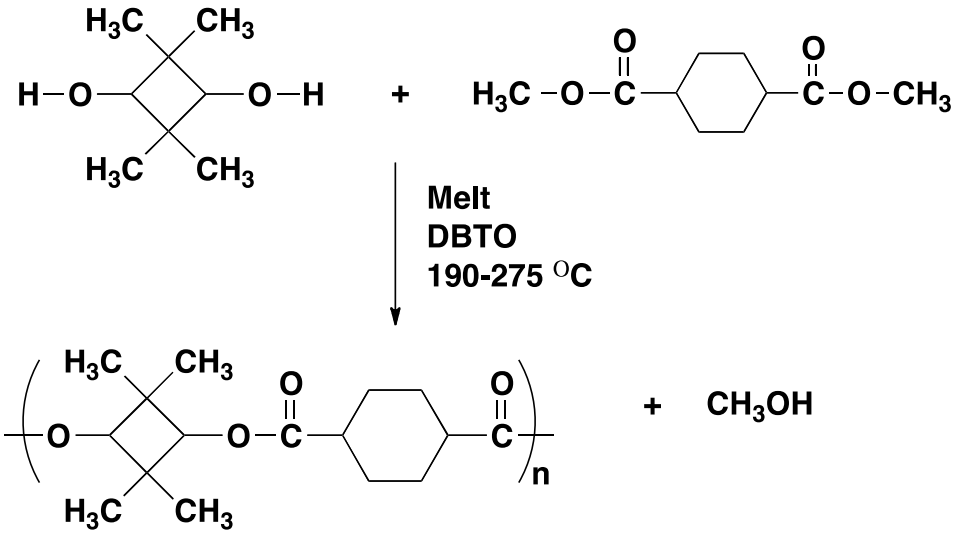

Figure 5.7 Synthetic scheme for Poly(TMCBD-CHDC).

In the case of the polyether block copolymer, a mPEG(5k)-PEVGE(0.76k)-PBO(9k) triblock copolymer with crosslinkable vinyl end groups in the middle block was synthesized (Figure 5.8a). In this case, it was surmised that fabricating triblock copolymer nanoparticles loaded with ritonavir, and subsequently crosslinking the vinyl groups on the outside of the core would provide a 'fence' leading to slow and sustained release of the drug. The triblock copolymer, a waxy solid, was synthesized from mPEG (M_n: 5,000 g mol^{-1}) with sequential addition of ethoxy vinyl glycidyl ether and 1,2-butylene oxide. The critical aggregation concentration of this copolymer in a 1:10 (v/v) THF:water solvent mixture was ~0.08 mg mL^{-1} as determined by dynamic light scattering (Figure 5.8b).

(a) (b)

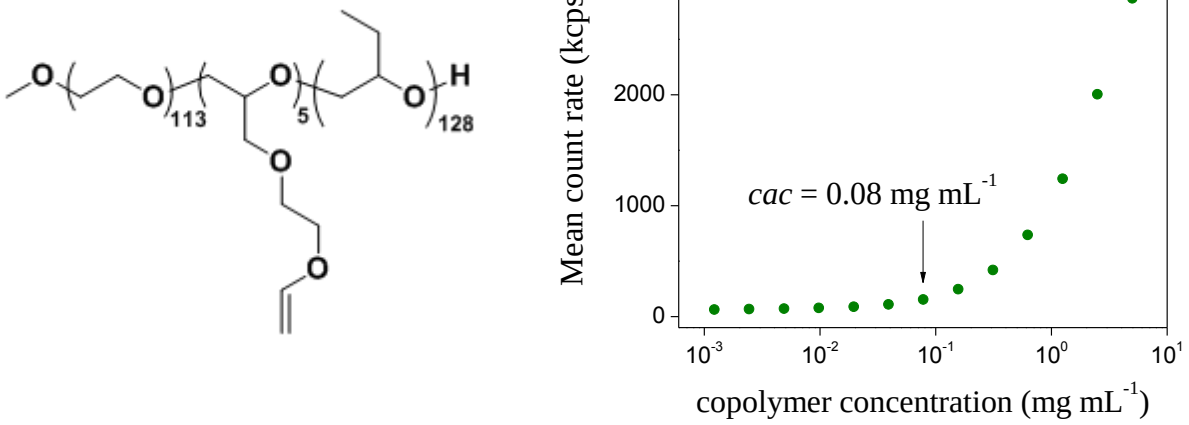

Figure 5.8 (a) Chemical structure of the mPEG(5k)-*b*-PEVGE(0.76k)-*b*-PBO(9k) triblock copolymer. (b) Critical aggregation concentration of the triblock copolymer in THF-water (1:10, v/v).

The nanoparticle fabrication method was similar to that described earlier in section 5.3.6. Ritonavir nanoparticles stabilized mPEG(5k)-*b*-PEVGE(0.76k)-*b*-PBO(9k) and mPEG(5k)-PDLLA(10k) were fabricated using the multi-inlet vortex mixer at a THF:water volume ratio of 1:10. The targeted loadings of drug were 10 wt% and 20 wt%, respectively. With the polyether triblock copolymer, no homopolymer additive was required to obtain monomodal size distributions. Notably, the control triblock copolymer nanoparticles had a very low distribution of sizes (PDI = 0.07) and an intensity-weighted average diameter of 94 nm by dynamic light scattering. In the case of the polylactide, ritonavir and poly(TMCBD-CHDC) homopolymer were co-encapsulated in the nanoparticles at 20 wt% each. The nanoparticles in either case were dialyzed against de-ionized water for 24 h and lyophilized to obtain a solid product which was readily redispersed in water. Figure 5.9 shows representative DLS size distribution curves for both systems after lyophilization

and redispersion in water. The drug loadings, hydrodynamic diameters and polydispersity indices are summarized in Table 5.3.

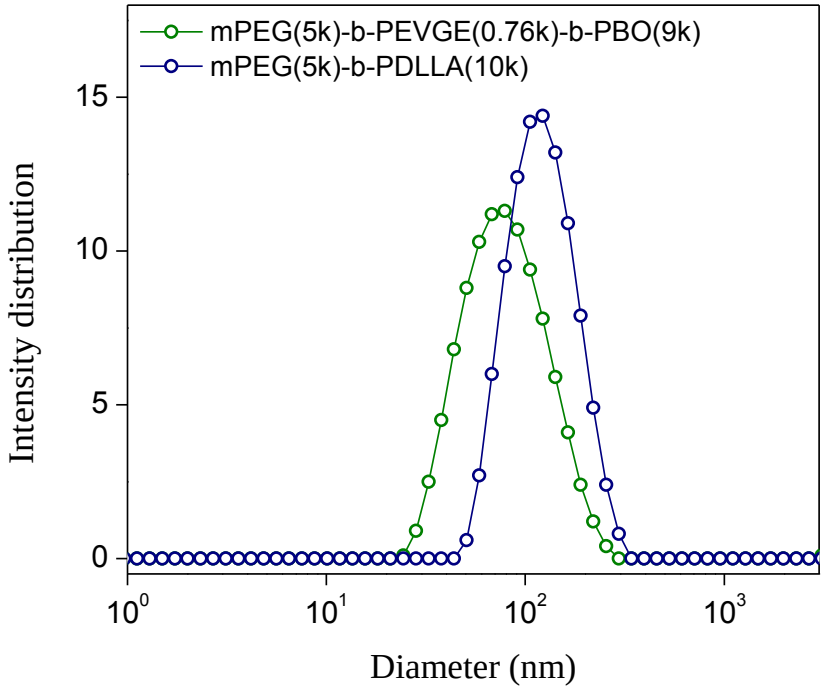

Figure 5.9 Representative DLS size distributions of ritonavir nanoparticles stabilized with (a) mPEG(5k)-*b*-PEVGE(0.76k)-*b*-PBO(9k), and (b) mPEG(5k)-PDLLA(10k) and co-encapsulating poly(TMCBD-CHDC).

Table 5.3 Size and drug loading of ritonavir nanoparticles stabilized with mPEG(5k)-*b*-PEVGE(0.76k)-*b*-PBO(9k) and mPEG(5k)-PDLLA(10k)

Copolymer stabilizer	Homopolymer	Targeted RTV loading	Measured RTV loading	D_I (nm)[c]	PDI[c]
mPEG-PEVGE-PBO	---	10 wt%	8.7 wt%[a]	83 ± 4	0.20
mPEG-PDLLA[d]	poly(TMCBD-CHDC)[e]	20 wt%	16 wt%[b]	132 ± 5	0.14

[a]Determined by HPLC
[b]Determined by NMR
[c]Average of 5 measurements
[d]Copolymer concentration in mixer = 3.0 mg mL^{-1}
[e]Homopolymer:copolymer = 1:3 (w/w)

5.5 Conclusions

In this study, well-defined and colloidally-stable ritonavir nanoparticles were prepared using amphiphilic block copolymer stabilizers comprised of poly(ethylene oxide-*b*-D,L-lactide) and poly(ethylene oxide-*b*-butylene oxide). Monomodal size distributions were achieved by incorporation of homopolymers of the respective hydrophobic block (11k-poly(L-lactide) or 2k-poly(butylene oxide)) as additives during the nanoparticle preparation process. Encapsulation efficiencies in the range of 70-80% were achieved with both systems at targeted drug loadings of 10, 20, and 30 wt%. The encapsulated ritonavir was in its amorphous form as indicated by differential scanning calorimetry and powder X-ray diffraction experiments. These are promising results for nanoparticle-based antiretroviral therapy. Ritonavir nanoparticles (1) co-encapsulating a highly hydrophobic and high T_g homopolymer additive, and (2) stabilized by a novel polyether triblock copolymer with a crosslinkable center block were also successfully prepared. It is believed that increasing the T_g of the nanoparticle core or introducing a crosslinked 'fence' around the core with variable crosslinking densities are potential ways to achieve sustained and tunable release rates.

5.6 References

(1) Kamaly, N.; Xiao, Z.; Valencia, P. M.; Radovic-Moreno, A. F.; Farokhzad, O. C.: Targeted polymeric therapeutic nanoparticles: design, development and clinical translation. *Chem. Soc. Rev.* **2012**, *41*, 2971-3010.
(2) Jokerst, J. V.; Lobovkina, T.; Zare, R. N.; Gambhir, S. S.: Nanoparticle PEGylation for imaging and therapy. *Nanomedicine* **2011**, *6*, 715-728.
(3) Kwon, G. S.; Kataoka, K.: Block copolymer micelles as long-circulating drug vehicles. *Adv. Drug Deliv. Rev.* **1995**, *16*, 295-309.

(4) Yokoyama, M.; Satoh, A.; Sakurai, Y.; Okano, T.; Matsumura, Y.; Kakizoe, T.; Kataoka, K.: Incorporation of water-insoluble anticancer drug into polymeric micelles and control of their particle size. *J. Control. Rel.* **1998**, *55*, 219-229.
(5) Burt, H. M.; Zhang, X.; Toleikis, P.; Embree, L.; Hunter, W. L.: Development of copolymers of poly(d,l-lactide) and methoxypolyethylene glycol as micellar carriers of paclitaxel. *Coll. Surf. B: Biointerfaces* **1999**, *16*, 161-171.
(6) Zhang, X.; Jackson, J. K.; Burt, H. M.: Development of amphiphilic diblock copolymers as micellar carriers of taxol. *Int. J. Pharm.* **1996**, *132*, 195-206.
(7) Tyrrell, Z. L.; Shen, Y.; Radosz, M.: Fabrication of micellar nanoparticles for drug delivery through the self-assembly of block copolymers. *Prog. Polym. Sci.* **2010**, *35*, 1128-1143.
(8) Vyas, T. K.; Shahiwala, A.; Amiji, M. M.: Improved oral bioavailability and brain transport of saquinavir upon administration in novel nanoemulsion formulations. *Int. J. Pharm.* **2008**, *347*, 93-101.
(9) Nowacek, A.; Gendelman, H. E.: NanoART, neuroAIDS and CNS drug delivery. *Nanomedicine* **2009**, *4*, 557-574.
(10) Silva, G. A.: Nanotechnology approaches for drug and small molecule delivery across the blood brain barrier. *Surg. Neurol.* **2007**, *67*, 113-116.
(11) Mainardes, R. M.; Gremiao, M. P. D.; Brunetti, I. L.; Da, F. L. M.; Khalil, N. M.: Zidovudine-loaded PLA and PLA-PEG blend nanoparticles: influence of polymer type on phagocytic uptake by polymorphonuclear cells. *J. Pharm. Sci.* **2009**, *98*, 257-267.
(12) Destache, C. J.; Belgum, T.; Christensen, K.; Shibata, A.; Sharma, A.; Dash, A.: Combination antiretroviral drugs in PLGA nanoparticle for HIV-1. *BMC Infect Dis* **2009**, *9*, 198.
(13) Kuo, Y.-C.; Su, F.-L.: Transport of stavudine, delavirdine, and saquinavir across the blood-brain barrier by polybutylcyanoacrylate, methylmethacrylate-sulfopropylmethacrylate, and solid lipid nanoparticles. *Int. J. Pharm.* **2007**, *340*, 143-152.
(14) Rao, K. S.; Reddy, M. K.; Horning, J. L.; Labhasetwar, V.: TAT-conjugated nanoparticles for the CNS delivery of anti-HIV drugs. *Biomaterials* **2008**, *29*, 4429-4438.
(15) Chattopadhyay, N.; Zastre, J.; Wong, H.-L.; Wu, X. Y.; Bendayan, R.: Solid lipid nanoparticles enhance the delivery of the HIV protease inhibitor, atazanavir, by a human brain endothelial cell line. *Pharm. Res.* **2008**, *25*, 2262-2271.
(16) Nowacek, A. S.; Balkundi, S.; McMillan, J.; Roy, U.; Martinez-Skinner, A.; Mosley, R. L.; Kanmogne, G.; Kabanov, A. V.; Bronich, T.; Gendelman, H. E.: Analyses of nanoformulated antiretroviral drug charge, size, shape and content for uptake, drug release and antiviral activities in human monocyte-derived macrophages. *J. Control. Rel.* **2011**, *150*, 204-211.
(17) Johnson, B. K.; Prud'homme, R. K.: Flash nanoprecipitation of organic actives and block copolymers using a confined impinging jets mixer. *Aust. J. Chem.* **2003**, *56*, 1021-1024.
(18) Liu, Y.; Cheng, C. Y.; Prud'homme, R. K.; Fox, R. O.: Mixing in a multi-inlet vortex mixer (MIVM) for flash nano-precipitation. *Chem. Engg. Sci.* **2008**, *63*, 2829-2842.
(19) Ungun, B.; Prud'homme, R. K.; Budijono, S. J.; Shan, J.; Lim, S. F.; Ju, Y.; Austin, R.: Nanofabricated upconversion nanoparticles for photodynamic therapy. *Opt. Express* **2009**, *17*, 80-86.
(20) Gindy, M. E.; Panagiotopoulos, A. Z.; Prud'homme, R. K.: Composite block copolymer stabilized nanoparticles: simultaneous encapsulation of organic actives and inorganic nanostructures. *Langmuir* **2008**, *24*, 83-90.
(21) D'Addio, S. M.; Prud'homme, R. K.: Controlling drug nanoparticle formation by rapid precipitation. *Adv. Drug Deliv. Rev* **2011**, *63*, 417-426.

(22) Ilevbare, G. A.; Liu, H.; Edgar, K. J.; Taylor, L. S.: Understanding polymer properties important for crystal growth inhibition—impact of chemically diverse polymers on solution crystal growth of ritonavir. *Cryst. Growth Des.* **2012**, *12*, 3133-3143.
(23) Zhang, X.; Li, Y.; Chen, X.; Wang, X.; Xu, X.; Liang, Q.; Hu, J.; Jing, X.: Synthesis and characterization of the paclitaxel/MPEG-PLA block copolymer conjugate. *Biomaterials* **2005**, *26*, 2121-2128.
(24) Kim, S. H.; Han, Y.-K.; Kim, Y. H.; Hong, S. I.: Multifunctional initiation of lactide polymerization by stannous octoate/pentaerythritol. *Die Makromolekulare Chemie* **1992**, *193*, 1623-1631.
(25) Saad, W. S.: Drug nanoparticle formation via flash nanoprecipitation: conjugation to encapsulate and control the release of paclitaxel. PhD Thesis, Princeton University, **2007**.
(26) Li, S.; Vert, M.: Synthesis, characterization, and stereocomplex-induced gelation of block copolymers prepared by ring-opening polymerization of l(d)-Lactide in the presence of poly(ethylene glycol). *Macromolecules* **2003**, *36*, 8008-8014.
(27) Liu, R.; He, B.; Li, D.; Lai, Y.; Tang, J. Z.; Gu, Z.: Synthesis and characterization of poly(ethylene glycol)-b-poly(l-histidine)-b-poly(l-lactide) with pH-sensitivity. *Polymer* **2012**, *53*, 1473-1482.
(28) Yang, W.; Johnston, K. P.; Williams, R. O.: Comparison of bioavailability of amorphous versus crystalline itraconazole nanoparticles via pulmonary administration in rats. *Eur. J. Pharm. Biopharm.* **2010**, *75*, 33-41.
(29) Fukuoka, E.; Makita, M.; Yamamura, S.: Glassy state of pharmaceuticals. II. Bioinequivalence of glassy and crystalline indomethacin. *Chem. Pharm. Bull.* **1987**, *35*, 2943-2948.

6 Biocompatible Fluorescent Nanoparticles for Intracellular Nanomedicine Tracking

6.1 Abstract

The intracellular trafficking of nanoparticle drug delivery systems is not well understood. Understanding the subcellular dynamics and transport of polymeric carriers is vital for improving the therapeutic outcome of nanomedicine. In this chapter, biocompatible, fluorescent nanoparticles of poly(ethylene oxide-*b*-D,L-lactide) encapsulating organic and inorganic fluorophores were prepared by the rapid precipitation technique. 5(6)-Carboxyfluorescein and CdSe-ZnS core-shell quantum dots were utilized as model fluorophores.

6.2 Introduction

In the recent years, significant advances have been made in the design of polymeric drug delivery systems. Biodegradable polymeric nanoparticles have attracted considerable attention as carriers of imaging and therapeutic agents. Most therapeutic molecules have poor aqueous solubility and low bioavailability. The use of polymeric nanoparticles enables higher bioavailability and simultaneous biodistribution tracking through co-encapsulation of a variety of organic and inorganic imaging agents such as magnetic nanoparticles, fluorescent dyes, quantum dots and gold nanospheres. Although various cellular internalization pathways have been discovered, the intracellular fate and trafficking of polymeric carriers is not well understood.[1,2] As a result, achieving therapeutic concentrations at specific target sites within cells is a major problem.[3] Thus, characterizing the intracellular trafficking of polymeric nanoparticles is fundamental to understanding biodistribution and transport of nanomedicine *in vivo*.

Biodegradable polymer nanoparticles encapsulating fluorescent dyes can be used for the real-time monitoring of nanomedicine transport, intracellular uptake and delivery using fluorescence microscopy.[4] Towards this goal, fluorescently-labeled nanoparticles comprised of the biocompatible and biodegradable copolymer, poly(ethylene oxide-*b*-D,L-lactide) were prepared by rapid precipitation in a multi-inlet vortex mixer. An organic dye, 5(6)-carboxyfluorescein, and CdSe-ZnS quantum dots were chosen as model fluorophores in this study. 5(6)-carboxyfluorescein (CF) is an inexpensive, water-soluble fluorophore with green fluorescence that has the structure of fluorescein with an extra carboxyl group located at the 5- or 6-position (Figure 6.1). It has a pKa of 6.5 and bears 2-3 negative charges in aqueous solution at neutral pH.[5] CF has been used as an intracellular pH reporter owing to its highly pH-dependent absorption spectrum.[6] It has been shown that viable cells uptake the neutral, colorless molecule fluorescein diacetate, which permeates the membrane and is converted into the fluorescent carboxyfluorescein by intracellular enzymes and remains trapped inside the cell due to its polar nature.[7]

(a)

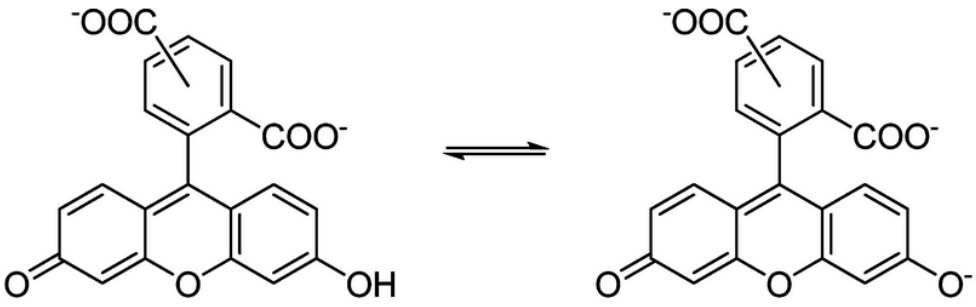

(b)

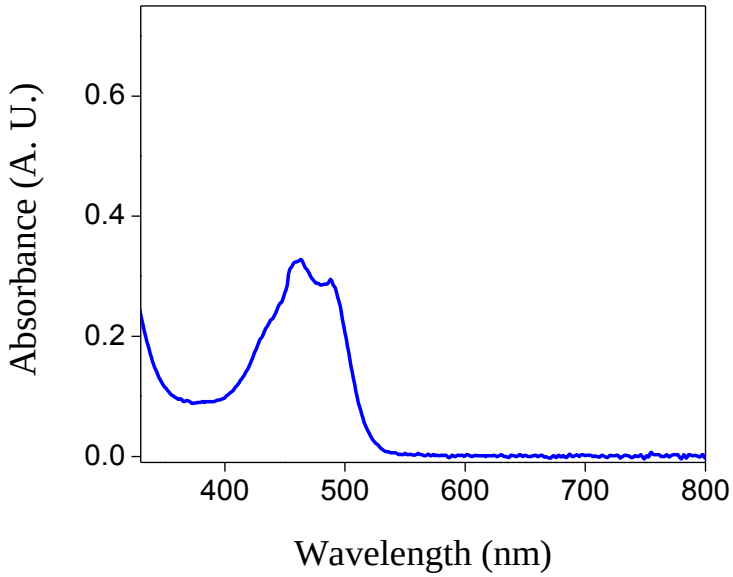

Figure 6.1 (a) Molecular structure of 5(6)-carboxyfluorescein (CF). (b) Electronic absorption spectrum of CF in methanol (c = 0.2 mg mL^{-1}).

Semiconductor quantum dot nanoparticles exhibit intensely bright fluorescence and possess high photostability relative to many organic fluorophores making them suitable for visualizing single particles for longer time periods. Furthermore, their emission characteristics can be easily tuned according to the size of the nanoparticles. The desirable optical properties combined with sufficient electron density and size diversity make quantum dots suitable for correlative light/electron microscopy.[8] Cadmium selenide-zinc sulfide (CdSe-ZnS) core-shell nanoparticles are among the most well-characterized quantum dots.[9] Their size dependent photoluminescence spans almost the entire visible range of the electromagnetic spectrum, and has been exploited in a range of applications including lasers, light emitting diodes, *in vitro* and *in vivo* imaging.[10] The CdSe-ZnS QDs used in this study were hydrophobically modified and dispersible in tetrahydrofuran (Figure 6.2).

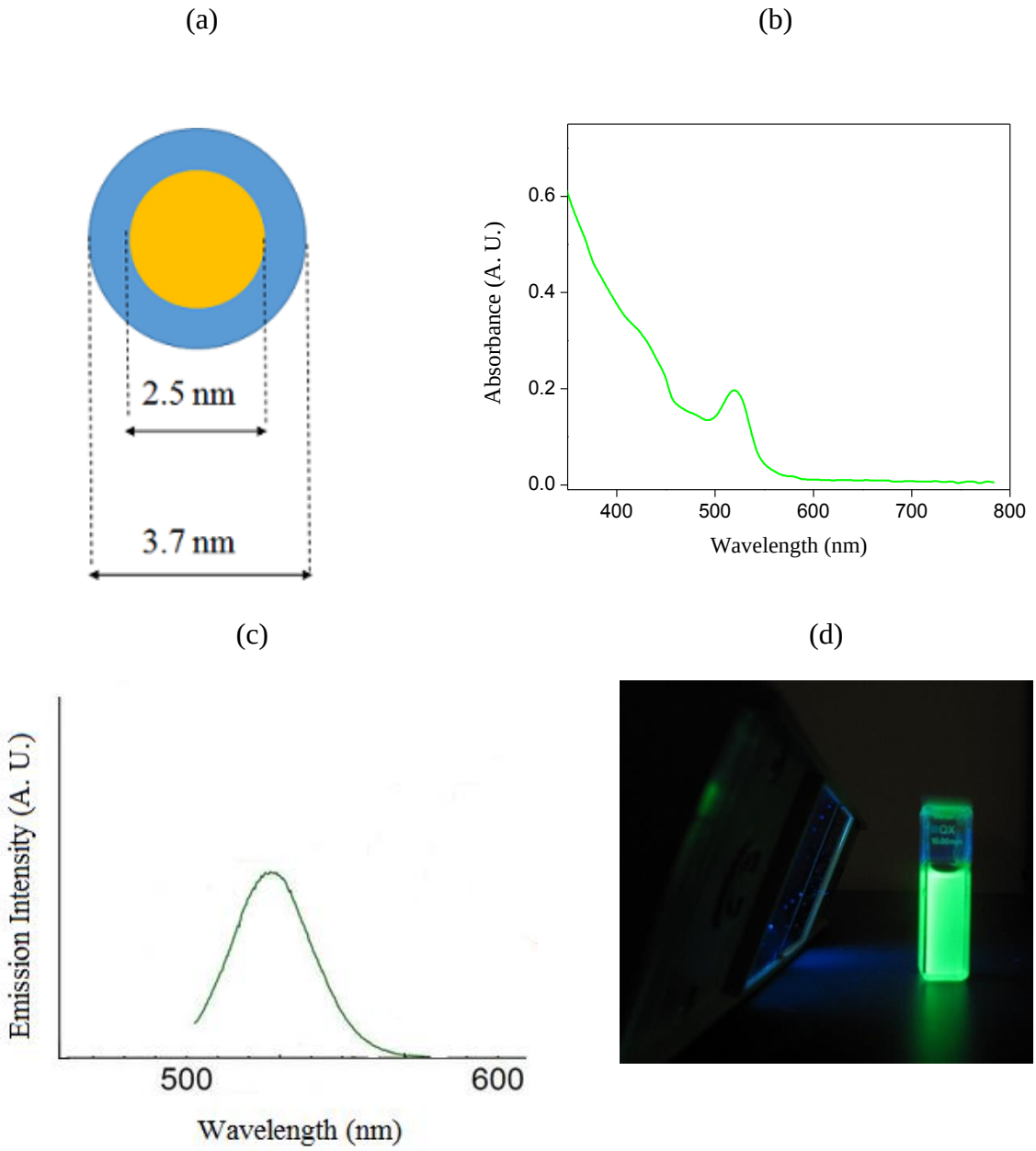

Figure 6.2 (a) Illustration of the CdSe-ZnS core-shell QD used in this study. (b) Absorption spectrum of the CdSe-ZnS QD suspension in THF (c = 0.33 mg mL^{-1}). (c) Fluorescence spectrum of CdSe-ZnS QD suspension shows emission maximum at 530 nm (λ_{exc} = 485 nm).[11] (d) Bright green photoluminescence from the quantum dot suspension (b) under UV illumination.

6.3 Experimental Section

6.3.1 Materials

Tin (II) 2-ethylhexanoate (stannous octoate) and tetrahydrofuran (THF, anhydrous) were purchased from Aldrich and used as received. Diethyl ether (anhydrous) and ethyl acetate (HPLC grade) were purchased from Fisher Scientific and used as received. Toluene (Fischer Scientific) was stirred over calcium hydride and distilled. D,L-lactide was obtained from Purac and recrystallized from ethyl acetate twice. Poly(ethylene oxide) methyl ether (mPEG) macroinitiator with a molar mass of ~5000 g mol^{-1} was obtained from Aldrich and vacuum-dried at room temperature for 18 h before use. Hydrophobic CdSe-ZnS core-shell quantum dots (Plasmachem GmbH) and 5(6)-carboxyfluorescein (Aldrich) were used as the fluorescent dyes.

6.3.2 Fabrication of fluorescent nanoparticles

6.3.2.1 *Carboxyfluorescein/poly(ethylene oxide-b-D,L-lactide) nanoparticles* (CF/mPEG-PDLLA)

A 5k-mPEG-*b*-10k-PDLLA M_n block copolymer was synthesized by ring-opening polymerization of D,L-lactide initiated by mPEO using stannous octoate as the catalyst.[12] The synthesis of the copolymer is described in detail in Chapter 4 (4.3.3). Fluorescent nanoparticles with a targeted composition of 10 wt% carboxyfluorescein were prepared. The 5k-mPEG-*b*-10k-PDLLA copolymer (99 mg) and 5(6)-carboxyfluorescein (11 mg) were dissolved in THF (3 mL). The THF solution was passed through a 1 μm PTFE filter prior to nanoparticle preparation. A four-jet multi-inlet vortex mixer design based on one previously reported was used to form the nanoparticles.[13] The THF solution was fed into the multi-inlet vortex mixer at 9.99 mL min^{-1} using a computer-controlled syringe pump (New Era Pump Systems, Farmingdale, New York) along with three

streams of de-ionized water at 33.3 mL min^{-1}, controlled by a PHD 4000 programmable syringe pump (Harvard Apparatus, Holliston, Massachusetts), yielding a final liquid phase composition of 1:10 (v/v) THF/water. After the suspension was formed in the mixer, it was dialyzed to remove THF against de-ionized water (2 L) for 24 h using a Spectra/Por dialysis bag (25,000 MWCO, Spectrum Laboratories, Inc.) with four changes of dialysate. The dialyzed suspension was freeze-dried for 72 h (0.030 mBar, -48°C) and stored as a solid product in the dark.

6.3.2.2 *CdSe-ZnS QD/poly(ethylene oxide-b-D,L-lactide) nanoparticles (*QD/mPEG-PDLLA*)*

Fluorescent nanoparticles with a targeted composition of 2.6 wt% CdSe-ZnS quantum dots were prepared. The 5k-mPEG-*b*-10k-PDLLA copolymer (66 mg) and CdSe-ZnS (1.8 mg) were dissolved in THF (2 mL). The THF solution was passed through a 0.2 μm Nylon filter prior to nanoparticle preparation. The THF solution was fed into the multi-inlet vortex mixer at 9.99 mL min^{-1} using a computer-controlled syringe pump (New Era Pump Systems, Farmingdale, New York) along with three streams of de-ionized water at 33.3 mL min^{-1}, controlled by a PHD 4000 programmable syringe pump (Harvard Apparatus, Holliston, Massachusetts), yielding a final liquid phase composition of 1:10 (v/v) THF/water. After the suspension was formed in the mixer, it was dialyzed to remove THF against de-ionized water (4 L) for 24 h using a Spectra/Por dialysis bag (1,000 MWCO, Spectrum Laboratories, Inc.) with four changes of dialysate. The dialyzed suspension was freeze-dried for 72 h (0.040 mBar, -48°C) and stored as a solid product in the dark.

6.3.3 Characterization

The nanoparticle size distributions were measured by dynamic light scattering (DLS). DLS was performed at 25°C on a Zetasizer Nano-ZS particle analyzer (Malvern Instruments Ltd., Worcestershire, U. K.) equipped with a 4 mW He-Ne laser (λ = 633 nm) and backscatter detection

(scattering angle = 173°). The reported intensity-weighted diameter for each sample was averaged from five measurements. Electronic absorption spectra of the fluorophores and fluorescently-labeled nanoparticles were recorded on an Evolution 300 UV-Vis spectrophotometer (Thermo Scientific, Waltham, MA) using a quartz cuvette with an optical path length of 10 mm. Fluorescence emission spectra of nanoparticle suspensions in de-ionized water were recorded on a Synergy Mx multimode microplate reader (BioTek Instruments, Winooski, VT).

6.4 Results

Figure 6.3 depicts the size distributions for the CF/mPEG-PDLLA nanoparticles immediately after the rapid precipitation process and after processing, i.e. dialysis and lyophilization. The nanoparticles exiting the mixer had a monomodal size distribution with D_I = 71 ± 2 nm (N = 5) and PDI = 0.14. The lyophilized sample was readily resuspended in de-ionized water (c = 0.14 mg mL^{-1}) under mild sonication, and yielded D_I = 95 ± 2 nm and PDI = 0.13. These results indicate that well-defined nanoparticles were formed.

(a)

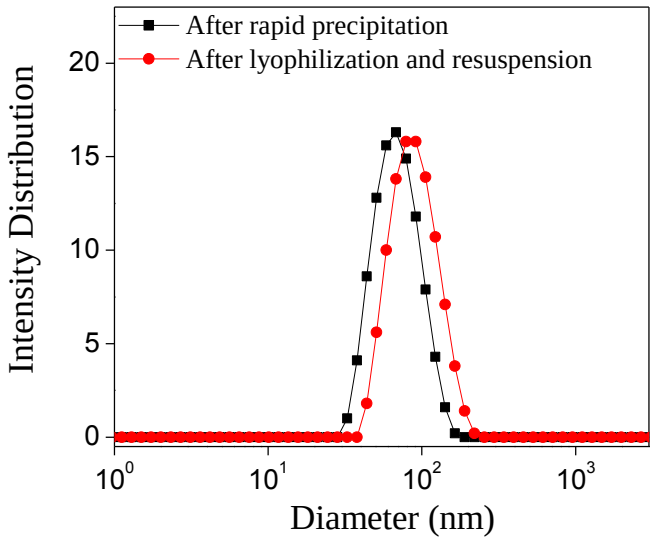

(b)

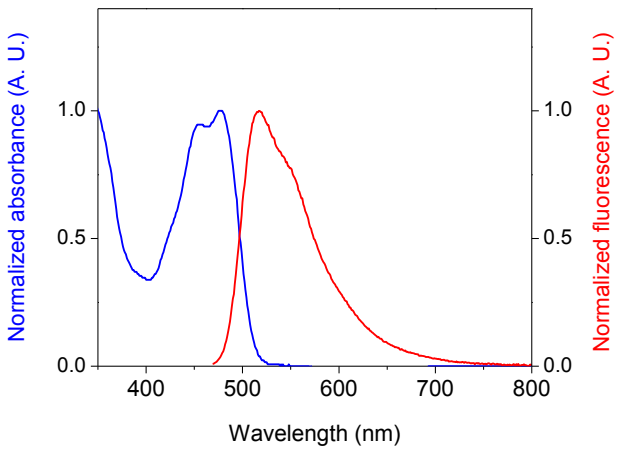

(c)

Figure 6.3 (a) Representative DLS size distributions of CF/mPEG-PDLLA nanoparticles after preparation by rapid precipitation (black) and after dialysis and lyophilization (red). (b) UV/Vis absorption and fluorescence spectra of CF/mPEG-PDLLA nanoparticles dispersed in de-ionized water. (c) Bright green photoluminescence from CF/mPEG-PDLLA nanoparticle suspension under UV illumination.

It is noteworthy that no homopolymer additive was necessary to obtain monomodal size distributions and low PDIs as in the case of the hydrophobic drug ritonavir, which is considerably more insoluble. Thus, it seems apparent that factors other than the hydrophobicity of the active

compound effect particle nucleation in the rapid precipitation process. In the present example of CF, it is possible that specific interactions between the fluorophore and the polylactide block aid nucleation and growth of nanoparticles. We measured the glass transition temperatures of a 10k-poly(D,L-lactide) homopolymer which forms the core of the nanoparticle and a blend of CF and PDLLA to see if the fluorophore influenced the T_g of the polymer because of specific interactions. Nanoparticles of PDLLA(10k) and CF/PDLLA (1:6, w/w) were prepared in the multi-inlet vortex mixer for DSC analyses. As shown in Figure 6.4, the fluorophore had no observable effect on the T_g of the PDLLA (~ 48°C) at the weight ratio in which it was present in the fluorescent nanoparticles.

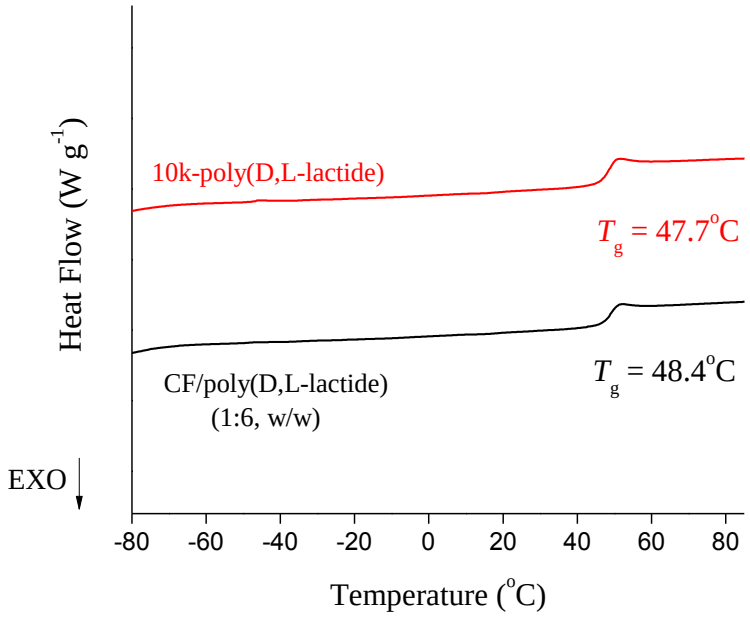

Figure 6.4 DSC thermograms of PDLLA and CF/PDLLA nanoparticles show no observable change in T_g due to incorporation of the fluorophore.

The experimental fluorophore loading in the CF/mPEG-PDLLA nanoparticles was quantified using UV-Vis spectroscopy. Lyophilized nanoparticles were suspended in methanol (HPLC grade) at a concentration of 1 mg mL^{-1} and sonicated for 15 min. in a water-bath sonicator to disintegrate

the nanoparticles and release the dye. Subsequently, the solution was filtered with a 0.2 μm Nylon filter and the UV-Vis spectrum of the filtrate was recorded. The weight fraction of fluorophore in the complex was determined by comparison to a standard calibration curve for carboxyfluorescein. The standard curve (Figure 6.5) was constructed with known concentrations of CF in methanol in the range of 0.05 - 1 mg mL^{-1}, and absorbance values at λ_{max} = 463 nm. The measured fluorophore loading was 8.6 wt%, compared to the targeted loading of 10 wt%, indicating high encapsulation efficiency.

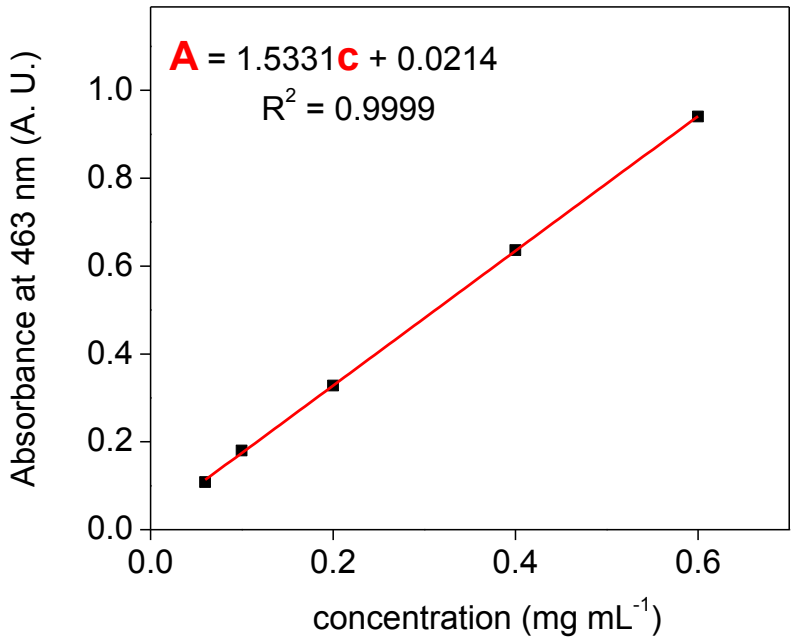

Figure 6.5 Standard curve for 5(6)-carboxyfluorescein dissolved in methanol.

The representative size distributions of the QD/mPEG-PDLLA nanoparticles are shown in Figure 6.6. The nanoparticles exiting the mixer had D_I = 79 ± 8 nm (N = 5) and PDI = 0.29. When compared with unloaded mPEG-PDLLA nanoparticles made in the mixer which yield bimodal size distributions, nanoparticles containing ~ 2.6 wt% QD have lower size distributions. This

indicates that hydrophobic QDs serve to effectively nucleate nanoparticles, analogous to hydrophobically-modified magnetite and hydrophobic homopolymer additives described in the previous chapters.

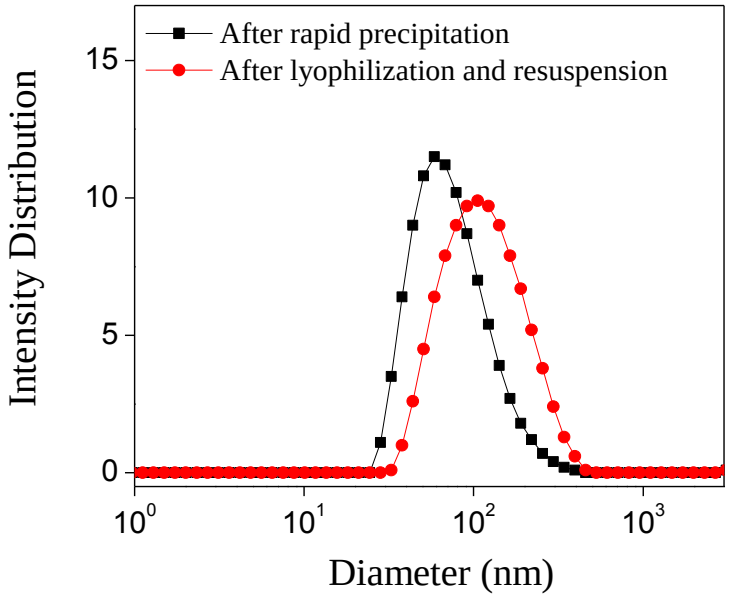

Figure 6.6 Representative DLS size distributions of QD/mPEG-PDLLA nanoparticles after preparation by rapid precipitation (black) and after dialysis and lyophilization (red).

6.5 Summary

Investigations of intracellular trafficking of amphiphilic block copolymer nanoparticles are crucial for the rational design of nanomedicines with improved therapeutic efficacies. For an increasing number of pharmaceuticals, the therapeutic targets are intracellular. Macrophage cell targeting using polymeric nanoparticles has been shown to be important for antiviral therapy (macrophagic cells are known to be a reservoir for virus particles) and antimicrobial therapy (e.g. treatment of intracellular pathogens such as Salmonella).[14,15] In this regard, several important questions need to be elucidated, such as the effect of nanoparticle size/chemistry on the intracellular dynamics

and drug release, the time frame of drug release, the velocity of nanoparticle movement inside cells, and the interaction between the nanoparticle and various subcellular components.

Fluorescence microscopy has evolved as the preferred tool for monitoring intracellular dynamics. Polymeric nanoparticles encapsulating fluorescent dyes represent model systems for such investigations where the release of the dye (similar to a drug molecule in size) enclosed in the nanoparticles can be tracked with fluorescence microscopy. For example, the nanoparticle trajectory and release of the dye (indicated by decrease in the fluorescence intensity) can be observed. Tools such as confocal imaging reveal the intracellular localization of nanoparticles. However, these static images do not reflect the dynamics involved in the nanoparticle movement and potential heterogeneity in the intracellular trajectories of these materials. Single particle tracking with wide-field laser-induced fluorescence microscopy is suitable for studying the dynamics of intracellular trafficking.[16] In this method, time-lapse images of nanoparticles moving inside cells can be recorded, and the trajectory of each nanoparticle can be mapped by finding centroids of the particles in each frame using mathematical fitting of the fluorescent images. The data will help answer several fundamental questions leading to the design and optimization of nanomedicines with better therapeutic efficacies.

6.6 References

(1) Hillaireau, H.; Couvreur, P.: Nanocarriers' entry into the cell: relevance to drug delivery. *Cell. Mol. Life Sci.* **2009**, *66*, 2873-2896.
(2) Ruenraroengsak, P.; Cook, J. M.; Florence, A. T.: Nanosystem drug targeting: facing up to complex realities. *J. Control. Rel.* **2010**, *141*, 265-276.
(3) Kristl, J.; Plajnsek, K. T.; Kreft, M. E.; Jankovic, B.; Kocbek, P.: Intracellular trafficking of solid lipid nanoparticles and their distribution between cells through tunneling nanotubes. *Eur. J. Pharm. Sci.* **2013**, *50*, 139-148.
(4) Torchilin, V. P.: Fluorescence microscopy to follow the targeting of liposomes and micelles to cells and their intracellular fate. *Adv. Drug Deliv. Rev.* **2004**, *57*, 95-109.

(5) Bonizzoni, M.; Long, S. R.; Rainwater, C.; Anslyn, E. V.: PAMAM dendrimer-induced aggregation of 5(6)-carboxyfluorescein. *J. Org. Chem.* **2012**, *77*, 1258-1266.
(6) Thomas, J. A.; Buchsbaum, R. N.; Zimniak, A.; Racker, E.: Intracellular pH measurements in ehrlich ascites tumor cells utilizing spectroscopic probes generated in situ. *Biochemistry* **1979**, *18*, 2210-2218.
(7) Graber, M. L.; DiLillo, D. C.; Friedman, B. L.; Pastoriza-Munoz, E.: Characteristics of fluoroprobes for measuring intracellular pH. *Anal. Biochem.* **1986**, *156*, 202-212.
(8) Loukanov, A. R.; Emin, S.: Quantum dots for detection, identification and tracking of single biomolecules in tissue and cells. Scrivener Publishing, **2012**, 649-677.
(9) Dabbousi, B. O.; Rodriguez-Viejo, J.; Mikulec, F. V.; Heine, J. R.; Mattoussi, H.; Ober, R.; Jensen, K. F.; Bawendi, M. G.: (CdSe)ZnS core−shell quantum dots: synthesis and characterization of a size series of highly luminescent nanocrystallites. *J. Phys. Chem. B* **1997**, *101*, 9463-9475.
(10) Biju, V.; Itoh, T.; Anas, A.; Sujith, A.; Ishikawa, M.: Semiconductor quantum dots and metal nanoparticles: syntheses, optical properties, and biological applications. *Anal. Bioanal. Chem.* **2008**, *391*, 2469-2495.
(11) Chizhik, A. I.; Gregor, I.; Enderlein, J.: Quantum yield measurement in a multicolor chromophore solution using a nanocavity. *Nano Lett.* **2013**, *13*, 1348-1351.
(12) Zhang, X.; Li, Y.; Chen, X.; Wang, X.; Xu, X.; Liang, Q.; Hu, J.; Jing, X.: Synthesis and characterization of the paclitaxel/MPEG-PLA block copolymer conjugate. *Biomaterials* **2005**, *26*, 2121-2128.
(13) Liu, Y.; Cheng, C. Y.; Prud'homme, R. K.; Fox, R. O.: Mixing in a multi-inlet vortex mixer (MIVM) for flash nano-precipitation. *Chem. Engg. Sci.* **2008**, *63*, 2829-2842.
(14) Bender, A. R.; von, B. H.; Kreuter, J.; Duncan, I. B.; Ruebsamen-Waigmann, H.: Efficiency of nanoparticles as a carrier system for antiviral agents in human immunodeficiency virus-infected human monocytes/macrophages in vitro. *Antimicrob. Agents Chemother.* **1996**, *40*, 1467-1471.
(15) Ranjan, A.; Pothayee, N.; Seleem, M. N.; Boyle, S. M.; Kasimanickam, R.; Riffle, J. S.; Sriranganathan, N.: Nanomedicine for intracellular therapy. *FEMS Microbiol. Lett.* **2012**, *332*, 1-9.
(16) Wang, J.; Lu, C.: Single molecule λ-DNA stretching studied by microfluidics and single particle tracking. *J. Appl. Phys.* **2007**, *102*, 074703/1-074703/6.

7 Synthesis of Iron Oxide Nanoparticle Clusters with Potential for Alternating Magnetic Field-Induced Biological Responses

7.1 Abstract

In this chapter, iron oxide nanoparticles with an average diameter of 25 nm and low size dispersity were synthesized by the thermal decomposition of iron (III) oleate complex. The oleic acid-coated nanoparticles were assembled into clusters stabilized by the diblock copolymer, 5k-mPEG-*b*-10k-PDLLA and comprised of ~20 wt% oleic acid-coated iron oxide. Post-lyophilization, the particles were readily redispersed in de-ionized water with mild sonication. The overall hydrodynamic size of the particles was 175 nm as determined by dynamic light scattering.

7.2 Introduction

Upon exposure to alternating magnetic fields (AMFs), superparamagnetic iron oxide nanoparticles dissipate energy in the form of heat through the Néel and Brownian relaxation mechanisms.[1] At nanoparticle sizes above the superparamagnetic regime (*ca*. 18 nm for Fe_3O_4), heat dissipation can be enhanced by hysteretic losses. This characteristic of magnetic nanoparticles has been utilized in magnetic fluid hyperthermia to kill tumor cells, and for AMF-actuated remote release of drugs.[2-5] Rinaldi and co-workers found that iron oxide nanoparticles conjugated with epidermal growth factor (EGF), in an AMF, result in 99.9% reduction in viability of cancer cells overexpressing the epidermal growth factor receptor, without significantly heating the medium.[6] The amount of heat dissipated by the magnetic nanoparticle under the influence of the AMF is quantified as the specific absorption rate (SAR) which depends on the amplitude and frequency of the AMF as well as the

properties of the nanoparticle (size, composition, saturation magnetization, magnetic susceptibility):[1,7]

$$SAR = \frac{\pi^3 {\mu_0}^2 {M_s}^2 d^3 {H_0}^2 f^2 \tau}{3\rho k_B T(1 + 2\pi f\tau)^2} \tag{7.1}$$

where μ_0 is the permeability of free space (T-m/A), M_s, d, and ρ are the saturation magnetization, diameter, and mass density of the magnetic nanoparticle, respectively, H_0 and f are the field strength and frequency of the AMF, respectively, and τ is the effective relaxation time of the nanoparticle given by eq. 7.2:

$$\frac{1}{\tau} = \frac{1}{\tau_B} + \frac{1}{\tau_N} \tag{7.2}$$

where τ_B and τ_N are the Brownian and Néel relaxation times, respectively. In the Brownian mode of relaxation, the magnetic moment is blocked within the crystal structure and as a result, the realignment of the magnetic moment along the external field involves rotation of the entire particle.

$$\tau_B = \frac{3\eta V_H}{k_B T} \tag{7.3}$$

In eq. 7.3, η is the viscosity of the medium in which the magnetic nanoparticle is suspended, and V_H is the hydrodynamic volume including the coating around the nanoparticle providing dispersibility, k_B is the Boltzmann constant and T is the absolute temperature. In Néel relaxation, the magnetic moment flips by overcoming the magnetocrystalline anisotropy barrier.

$$\tau_N = \tau_0 e^{\frac{K_a V}{k_B T}} \tag{7.4}$$

In eq. 7.4, K_a is the magnetocrystalline anisotropy constant (= 13,500 J m^{-3} for Fe_3O_4),[8] V is the volume of the magnetic nanoparticle, and τ_0 is a characteristic time (assumed to be a constant with a value of 10^{-9} s) and indicates the strength of interparticle interactions. Smaller values of τ_0 indicate the presence of interparticle interactions.[9]

The local confinement of magnetic nanoparticles, through controlled aggregation, is desirable for achieving higher heating rates. Béalle et al. found that the aggregation of ~7 nm and ~9 nm maghemite nanoparticles in liposomes (~200 nm) at high volume fractions (~30%) led to higher SAR values relative to the individually dispersed nanoparticles.[10] Lartigue et al. also showed that multicore maghemite nanoparticle clusters possessed up to 10 times higher SAR values than the corresponding individual nanoparticles.[11] In the above examples, an important factor determining the observed SAR is the inter-nanoparticle magnetic interactions within the cluster. Recently, Rinaldi et al. have elucidated the effect of inter-nanoparticle distance within the cluster on the observed SAR values.[9] They fabricated magnetomicelles comprised of oleic acid-coated iron oxide nanoparticles and poly(ethylene oxide)-*b*-poly(caprolactone) block copolymer with various PCL molecular weights (2k, 5k, and 20k g mol^{-1}). Significantly, they noted a decrease in inter-nanoparticle interactions and SAR values with increasing PCL molecular weight.

In this study, ~25 nm iron oxide nanoparticles coated with oleic acid, with low size polydispersity, were synthesized and assembled into biocompatible, water-dispersible clusters. It is hypothesized that clusters with large iron oxide nanoparticle cores and potentially tunable inter-nanoparticle spacings will lead to substantial, tailored heating rates upon exposure to an alternating magnetic field.

7.3 Experimental

7.3.1 Materials

Sodium oleate (95%) was purchased from TCI America. Oleic acid (90%, technical grade), iron (III) chloride hexahydrate ($FeCl_3.6H_2O$, 98%), tetrahydrofuran (anhydrous) and hexanes (HPLC grade) were purchased from Aldrich. Ethanol (200 proof) was purchased from Decon Labs. De-ionized water (18.2 MΩ cm) produced with a Milli-Q water purification system (Millipore) was used for all syntheses.

7.3.2 Synthesis of 25 nm iron oxide nanoparticles

7.3.2.1 *Synthesis of iron (III) oleate precursor*

The iron-oleate complex was synthesized by reacting sodium oleate and iron (III) chloride.[12] Briefly, 10.8 g of iron chloride (40 mmol) and 36.5 g of sodium oleate (120 mmol) were dissolved in a solvent mixture comprised of 60 mL de-ionized water, 80 mL ethanol and 140 mL hexane. The solution was sparged with N_2 for 15 min. and heated at 70°C for 4 h. After the reaction was completed, the upper organic layer containing the iron oleate product was separated using a separatory funnel and washed three times with 50 mL water. After washing, hexane removed by rotary evaporation and the viscous product was dried overnight under N_2 purge.

7.3.2.2 *Synthesis of iron oxide nanoparticles*

Iron oxide nanoparticles functionalized with oleic acid were synthesized using iron (III) oleate as the precursor.[12,13] Iron oleate (3.6 g, 4 mmol) and oleic acid (0.57 g, 2 mmol) were dissolved in 20 mL of 1-eicosene with sonication. This solution was transferred into a 250 mL three-neck flask equipped with an overhead stirrer and placed in a Belmont metal bath with thermostatic control.

The solution was heated at 115°C for 30 min. under N_2. The reaction temperature was subsequently increased to 330°C at the rate of 3°C min^{-1} under a N_2 blanket and held at that temperature for 30 min. The reaction mixture was cooled to room temperature followed by addition of a 1:1 mixture of ethanol and hexane and centrifuged (6000 rpm, 10 min.) to collect the nanoparticles. The pelleted nanoparticles were redispersed in 10 mL hexane, flocculated with 5 mL ethanol, and centrifuged at 6,000 rpm for 10 min. three times. The nanoparticles were suspended in hexane.

7.3.3 Fabrication of iron oxide-block copolymer particles

A 5k-mPEO-*b*-10k-PDLLA M_n block copolymer was synthesized by ring-opening polymerization of D,L-lactide initiated by mPEG using stannous octoate as the catalyst.[14] The synthesis of the copolymer is described in detail in Chapter 4 (4.3.3). Oleic acid-coated iron oxide nanoparticles (33 mg) and mPEG-PDLLA (132 mg) were added to tetrahydrofuran (4 mL) and sonicated for 20 min. followed by filtration with a 1.0 μm PTFE filter. A four-jet multi-inlet vortex mixer design based on one previously reported was used to form the clusters.[15] The THF solution was fed into the multi-inlet vortex mixer at 9.99 mL min^{-1} using a computer-controlled syringe pump (New Era Pump Systems, Farmingdale, New York) along with three streams of de-ionized water at 33.3 mL min^{-1}, controlled by a PHD 4000 programmable syringe pump (Harvard Apparatus, Holliston, Massachusetts), yielding a final liquid phase composition of 1:10 (v/v) THF/water. These flow rates corresponded to a mixing Reynolds number of approximately 12,500. After the suspension was formed in the mixer, it was dialyzed to remove THF against de-ionized water (4000 mL) for 24 h using a Spectra/Por dialysis bag (1,000 MWCO, Spectrum Laboratories, Inc.) with four changes of dialysate. The dialyzed suspension was freeze-dried for 72 h (0.018 mBar, -52°C).

7.3.4 Characterization

Particle size distributions were measured by dynamic light scattering at 25°C on a Zetasizer NanoZS (Malvern Instruments, Worcestershire, U. K.). Lyophilized iron oxide-block copolymer particles were diluted in de-ionized water to a concentration of 0.1 mg mL^{-1} for the analysis. The intensity-weighted diameter and polydispersity index were averaged from five measurements. The size of the primary oleic acid-coated iron oxide nanoparticles was determined by transmission electron microscopy using a Philips Model EM420 TEM. A drop of the nanoparticle suspension in hexane (c = 0.1 mg mL^{-1}) was cast on an amorphous carbon-coated copper grid. Images were acquired at a magnification of 96,000×. The sizes of 700 nanoparticles were measured using image analysis software (Reindeer Graphics' Fovea Pro 4 plug-in for Adobe Photoshop) and fitted using a lognormal distribution function to determine the mean diameter:

$$P(d) = \frac{1}{\sqrt{2\pi}\sigma d} e^{\frac{-[\ln\left(\frac{d}{d_m}\right)]^2}{2\sigma^2}} \tag{7.5}$$

where $P(d)$ is the number probability density, d_m is the mean diameter, and σ is the standard deviation.

7.4 Results and Discussion

The iron oxide nanoparticles had an average diameter of 24.9 nm (σ = 0.1) as determined by a lognormal fit to the size histogram obtained from image analysis of transmission electron micrographs. A representative TEM micrograph of the iron oxide cores and the size distribution are shown in Figure 7.1 and Figure 7.2, respectively.

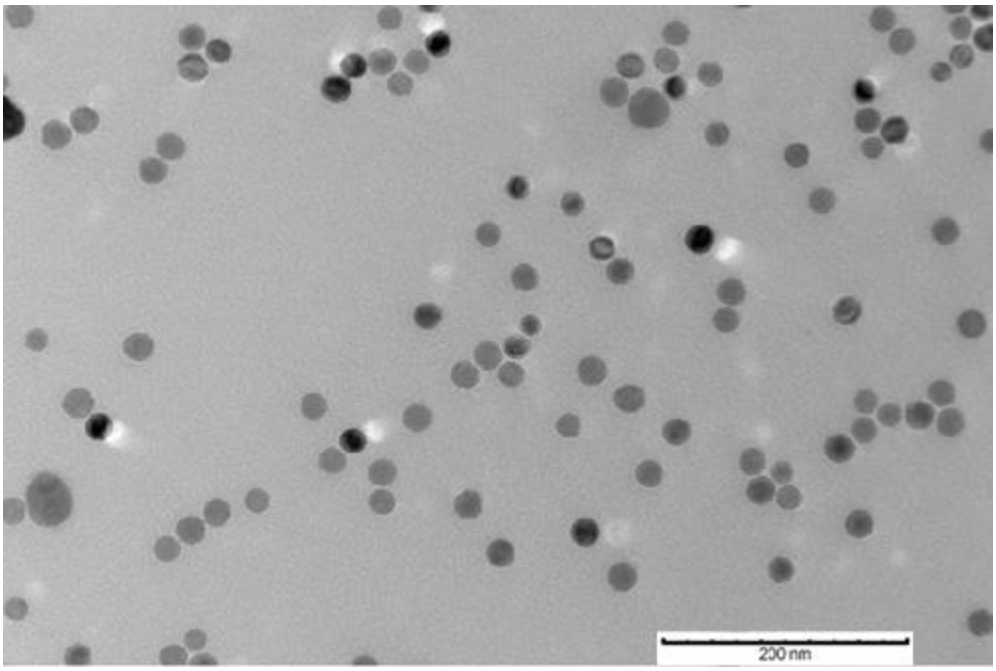

Figure 7.1 Representative TEM micrograph of iron oxide nanoparticles.

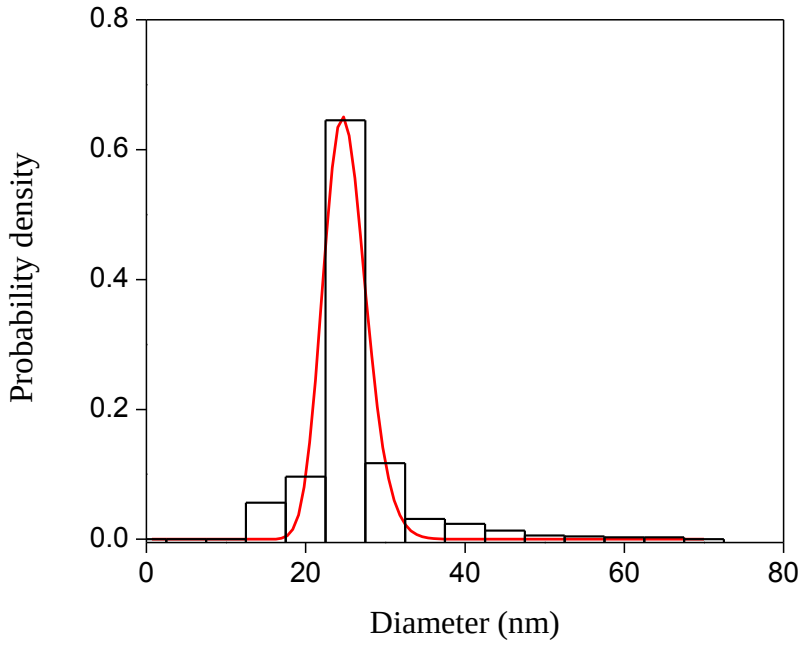

Figure 7.2 A lognormal fit of the nanoparticle diameters measured from TEM images yielded a mean diameter of 24.9 nm with a standard deviation $\sigma = 0.1$.

Block copolymer-stabilized particles with a targeted loading of 20 wt% oleic acid-coated iron oxide, wherein the iron oxide cores were clustered within the hydrophobic polylactide block, were fabricated by rapid precipitation in the multi-inlet vortex mixer. Since the weight fraction of oleic acid is presently unknown, the iron oxide loading in the particles was based on oleic acid-coated iron oxide rather than uncoated iron oxide such as described in Chapter 4 (4.4.1). The lyophilized particles were easily dispersed in de-ionized water with water-bath sonication and had an intensity-weighted diameter of 176 ± 13 nm (n = 5) and a PDI of 0.21 (Figure 7.3).

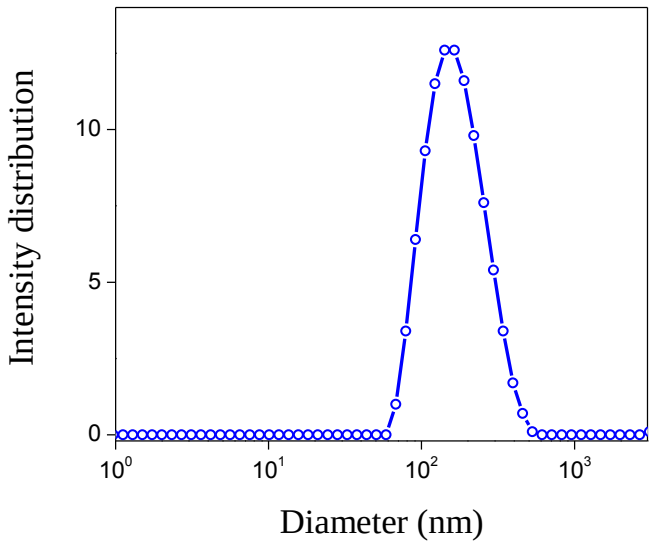

Figure 7.3 Representative DLS size distribution of iron oxide-block copolymer particles comprised of 25 nm iron oxide nanoparticles coated with oleic acid.

The alternating magnetic field-induced heating of the iron oxide clusters can be potentially studied by the co-encapsulation of a hydrophobic fluorescent molecule such as Nile red in the particles to mimic a poorly water-soluble drug. If sufficient heating rates are produced, a physical change in the polymer carrier such as the glass transition of the poly(D,L-lactide) may be effected, resulting in the release of the fluorophore and a concomitant increase in the fluorescence intensity.

Besides AMF-induced heat dissipation, larger iron oxide nanoparticles are also more efficient for T_2 contrast in MRI.[16] Cluster sizes and iron oxide loadings can be tailored to mostly fall into the static dephasing regime so as to achieve high transverse relaxation rates. The measurement of the *M-H* hysteresis curve of the 25 nm nanoparticles would enable the estimation of the threshold diameter of the cluster for static dephasing conditions at a given loading of iron oxide. Table 7.1 shows the estimated threshold diameters for static dephasing and echo-limited regimes for 7.4 nm and 25 nm nanoparticles at a loading of 20 wt% iron oxide and using the mPEG(5k)-*b*-PDLLA(10k) copolymer stabilizer. The equations of Roch et al. described in Chapter 4 (eq. 4.14-4.15) were used for these calculations. The measured magnetization of the 7.4 nm nanoparticles at 1.4 T (= 57 Am^2/kg) was used. Since the corresponding value for the larger nanoparticles is yet to be determined, the value of bulk magnetite (= 82 Am^2/kg)[17] was used.

Table 7.1 Estimated threshold diameters for static dephasing and echo-limited regimes for iron oxide-mPEG-*b*-PDLLA clusters at a loading of 20 wt% iron oxide

Diameter of primary iron oxide nanoparticle (nm)	Threshold diameter for SDR (nm)	Threshold diameter for ELR (nm)
7.4	126	443
25	105	412

At similar iron oxide loadings, static dephasing conditions can be achieved at smaller cluster (particle core) sizes when primary nanoparticles with higher size and magnetization are used.

7.5 Conclusions

Biocompatible block copolymer particles comprised of clustered iron oxide nanoparticles with relatively large nanoparticle diameters have potential applications in sensitive magnetic resonance

imaging and alternating magnetic field-induced release of hydrophobic drugs co-encapsulated within the core-forming polylactide block. As a first step toward this goal, 25 nm iron oxide nanoparticles were synthesized and assembled into clusters stabilized by the biodegradable amphiphilic block copolymer, mPEG-*b*-PDLLA, by the rapid precipitation technique. It is hypothesized that substantial heating rates can be produced that can be potentially tuned by varying the nanoparticle loadings to control the inter-nanoparticle spacings and magnetic interactions.

7.6 References

(1) Rosensweig, R. E.: Heating magnetic fluid with alternating magnetic field. *J. Magn. Magn. Mater.* **2002**, *252*, 370-374.

(2) Laurent, S.; Dutz, S.; Haefeli, U. O.; Mahmoudi, M.: Magnetic fluid hyperthermia: Focus on superparamagnetic iron oxide nanoparticles. *Adv. Coll. Interf. Sci.* **2011**, *166*, 8-23.

(3) Kumar, C. S. S. R.; Mohammad, F.: Magnetic nanomaterials for hyperthermia-based therapy and controlled drug delivery. *Adv. Drug Deliv. Rev.* **2011**, *63*, 789-808.

(4) Dobson, J.: Remote control of cellular behaviour with magnetic nanoparticles. *Nat. Nanotechnol.* **2008**, *3*, 139-143.

(5) Purushotham, S.; Chang, P. E. J.; Rumpel, H.; Kee, I. H. C.; Ng, R. T. H.; Chow, P. K. H.; Tan, C. K.; Ramanujan, R. V.: Thermoresponsive core-shell magnetic nanoparticles for combined modalities of cancer therapy. *Nanotechnology* **2009**, *20*, 305101/1-305101/11.

(6) Creixell, M.; Bohórquez, A. C.; Torres-Lugo, M.; Rinaldi, C.: EGFR-targeted magnetic nanoparticle heaters kill cancer cells without a perceptible temperature rise. *ACS Nano* **2011**, *5*, 7124-7129.

(7) Liu, X. L.; Choo, E. S. G.; Ahmed, A. S.; Zhao, L. Y.; Yang, Y.; Ramanujan, R. V.; Xue, J. M.; Fan, D. D.; Fan, H. M.; Ding, J.: Magnetic nanoparticle-loaded polymer nanospheres as magnetic hyperthermia agents. *J. Mater. Chem. B* **2014**, *2*, 120-128.

(8) Gossuin, Y.; Gillis, P.; Hocq, A.; Vuong, Q. L.; Roch, A.: Magnetic resonance relaxation properties of superparamagnetic particles. *Wiley Interdiscip. Rev.: Nanomed. Nanobiotechnol.* **2009**, *1*, 299-310.

(9) Olayo-Valles, R.; Rinaldi, C.: Modulation of interparticle interactions and specific absorption rate in magnetomicelles through changes in the molecular weight of the hydrophobic polymer block. *Part. Part. Syst. Charact.* **2013**, *30*, 964-971.

(10) Béalle, G.; Di Corato, R.; Kolosnjaj-Tabi, J.; Dupuis, V.; Clément, O.; Gazeau, F.; Wilhelm, C.; Ménager, C.: Ultra magnetic liposomes for MR imaging, targeting, and hyperthermia. *Langmuir* **2012**, *28*, 11834-11842.

(11) Lartigue, L.; Hugounenq, P.; Alloyeau, D.; Clarke, S. P.; Lévy, M.; Bacri, J.-C.; Bazzi, R.; Brougham, D. F.; Wilhelm, C.; Gazeau, F.: Cooperative organization in iron oxide multi-core nanoparticles potentiates their efficiency as heating mediators and MRI contrast agents. *ACS Nano* **2012**, *6*, 10935-10949.

(12) Park, J.; An, K.; Hwang, Y.; Park, J.-G.; Noh, H.-J.; Kim, J.-Y.; Park, J.-H.; Hwang, N.-M.; Hyeon, T.: Ultra-large-scale syntheses of monodisperse nanocrystals. *Nat. Mater.* **2004**, *3*, 891-895.
(13) Chen, R.; Christiansen, M. G.; Anikeeva, P.: Maximizing hysteretic losses in magnetic ferrite nanoparticles via model-driven synthesis and materials optimization. *ACS Nano* **2013**, *7*, 8990-9000.
(14) Zhang, X.; Li, Y.; Chen, X.; Wang, X.; Xu, X.; Liang, Q.; Hu, J.; Jing, X.: Synthesis and characterization of the paclitaxel/MPEG-PLA block copolymer conjugate. *Biomaterials* **2005**, *26*, 2121-2128.
(15) Liu, Y.; Cheng, C. Y.; Prud'homme, R. K.; Fox, R. O.: Mixing in a multi-inlet vortex mixer (MIVM) for flash nano-precipitation. *Chem. Eng. Sci.* **2008**, *63*, 2829-2842.
(16) Ai, H.; Flask, C.; Weinberg, B.; Shuai, X. T.; Pagel, M. D.; Farrell, D.; Duerk, J.; Gao, J.: Magnetite-loaded polymeric micelles as ultrasensitive magnetic-resonance probes. *Adv. Mater.* **2005**, *17*, 1949-1952.
(17) Roca, A. G.; Morales, M. P.; O'Grady, K.; Serma, C. J.: Structural and magnetic properties of uniform magnetite nanoparticles prepared by high temperature decomposition of organic precursors. *Nanotechnology* **2006**, *17*, 2783-2788.

8 Conclusions and Future Work

This research has been focused on laying the foundation for developing novel therapeutic materials that can be delivered into distant malignant sites and other target tissues, non-invasively monitored by magnetic resonance imaging, and remotely actuated by external alternating magnetic fields to elicit therapeutic responses. To this end, the main aim of this dissertation was the fabrication and structure-property relationships of polymer particles containing magnetic iron oxide nanoparticles and poorly water-soluble antiretroviral therapeutics. A key requirement for structure-property investigations is the synthesis of well-defined particles.

In order to elucidate the effects of aggregation on the NMR relaxation times of magnetic nanoparticle suspensions and hence the MRI contrast efficiencies, a well-defined particle complex comprised of an 8 nm superparamagnetic iron oxide core stabilized by a poly(*N*-isopropylacrylamide) corona was utilized. The hydrodynamic diameter of the core-shell complex was predicted using the modified Vagberg density distribution model, and found to agree with the measured intensity-weighted hydrodynamic diameter to within 5%. Conformational changes in the PNIPAM corona driven by its lower critical solution temperature (LCST) were used to systematically induce aggregation of the complexes. Aggregation was accompanied by a drastic reduction in the transverse relaxation times and an increase in the longitudinal relaxation times. Establishing aggregation-relaxation relationships can provide a sensitive means for using MRI to characterize regulated small clusters in complex biological systems.

One of the major objectives of this work was the facile fabrication and quantitative analysis of controlled clusters of iron oxide nanoparticles stabilized with biocompatible polymers with high

loading capacities for sensitive MRI. With this goal in mind, clusters of 7.4 nm iron oxide nanoparticles encapsulated within the biodegradable amphiphilic block copolymer, mPEG-*b*-PDLLA, with variable size distributions and iron oxide loadings were fabricated by a scalable rapid precipitation technique using a multi-inlet vortex mixer. Quantitative incorporation of the iron oxide, up to 40 wt%, in the block copolymer particles was demonstrated. By accounting for the cluster size distributions measured using cryo-TEM which was especially sensitive to measuring the sizes of the iron oxide-containing polymer cores, the transverse relaxivities of the particles were successfully predicted to typically within 15%, using the analytical relaxivity models. This study enables the rational design of hydrophobic-core theranostic particles that can co-encapsulate hydrophobic drugs such as ritonavir. Using this methodology, the MRI contrast efficiencies can be significantly enhanced by tailoring particle compositions and sizes to fall mostly within the static dephasing regime, where the transverse relaxation rate has its maximum value.

The transverse and longitudinal relaxivities of hydrophilic-core particles, similar to the hydrophobic-core particles in the primary nanoparticle characteristics (size, magnetization), were also studied. Particles with hydrophilic interiors were synthesized in Professor Riffle's group by chemically crosslinking individual iron oxide-poly(ethylene oxide-*b*-acrylate) complexes bearing amine termini with PEG diacrylate. The hydrophilic particles were found to exhibit remarkably higher transverse and longitudinal relaxivities than the hydrophobic-core particles at similar iron oxide loadings, with the r_2 relaxivities close to the theoretical limit for ~ 8 nm Fe_3O_4. It is believed that the access by diffusion of water molecules to high field gradients within the core of the particles leads to the enhanced relaxation characteristics. Future work with the hydrophilic particles could include varying the molecular weight of the PEG diacrylate crosslinker to further

investigate the effect of inter-nanoparticle distance on the relaxivities. In addition to the nanoparticle size, magnetization and volume fraction within the cluster, the number of nanoparticle cores, the inter-nanoparticle distance and the cluster size distributions need to be characterized in order to accurately model particles with this morphology.

Besides enhanced MRI contrast, controlled iron oxide clusters also have potential applications in alternating magnetic field-induced remote drug release. The dissipation of heat through orientational relaxation processes in the magnetic nanoparticles can be exploited to effect physical changes in the surrounding polymer chains triggering release of drug molecules held through non-covalent interactions. The rapid precipitation technique used for most of the particle fabrication work described in this dissertation can be readily employed for the assembly of clusters of relatively larger nanoparticles (~25 nm diameter) coated with oleic acid. Furthermore, it is hypothesized AMF-induced heating rates can be controlled by manipulating the iron oxide nanoparticle spacings and strength of magnetic interactions within the cluster. The AMF-induced heating can possibly be studied by co-encapsulating a hydrophobic fluorescent molecule in the particles to mimic a poorly water-soluble drug and observing changes in fluorescence upon release of the fluorophore.

Another objective of this work was to design well-defined nanoparticles of antiretroviral drugs for the treatment of human immunodeficiency virus type one. Two amphiphilic block copolymer stabilizers were employed in this study, comprised of poly(D,L-lactide) and poly(butylene oxide) as the hydrophobic blocks for complexation of the drug. Homopolymers of the respective hydrophobic block (11k-poly(L-lactide) or 2k-poly(butylene oxide)) were synthesized and incorporated as additives during the nanoparticle preparation process in order to obtain monomodal size distributions. Encapsulation efficiencies in the range of 70-80 % were achieved

with both systems at targeted drug loadings in the range of 10-30 wt%. The encapsulated ritonavir was in its amorphous form as indicated by differential scanning calorimetry and powder X-ray diffraction experiments. Preliminary release data suggest that ritonavir is rapidly released from the polylactide nanoparticles (within 1-2 hours) under simulated physiological conditions, whereas release is sustained in the case of the more hydrophobic poly(butylene oxide). Future experiments could utilize the high T_g poly(TMCBD-CHDC) hydrophobic homopolymer instead of poly(L-lactide) for sustained drug release in the case of the mPEG-*b*-PDLLA stabilized nanoparticles. Since polymer hydrophobicity likely correlates with drug release rates, the solubility parameter of the hydrophobic block may be used to guide the choice of amphiphilic copolymer carrier for a given drug. The experimental drug loadings, release rates and size distributions for a given polymer system may be incorporated into, or used to verify, existing drug release models to quantitatively analyze how these properties affect release.

Appendix

A.1 Exemplary calculation of Reynolds number (R_e) for nanoparticle fabrication in the multi-inlet vortex mixer

Diameter of the mixer chamber ($D_{chamber}$)	6.12×10^{-3}	m
Diameter of the inlet stream (D_{is})	1.11×10^{-3}	m
Density of water, 25°C (ρ_{water})	997.1	kg m^{-3}
Density of THF, 25°C (ρ_{THF})	882	kg m^{-3}
Shear viscosity of water (η_{water})	8.94×10^{-4}	kg m^{-1} s^{-1}
Shear viscosity of THF solution (η_{THF}) (containing 33 mg mL^{-1} of mPEG(5k)-*b*-PDLLA(10k))	9.65×10^{-4}	kg m^{-1} s^{-1}
Kinematic viscosity of water ($\upsilon_{water} = \eta_{water}/\rho_{water}$)	8.96×10^{-7}	m^2 s^{-1}
Kinematic viscosity of THF solution ($\upsilon_{THF} = \eta_{THF}/\rho_{THF}$)	1.09×10^{-6}	m^2 s^{-1}
Volumetric flow rate of water stream	33.3	mL min^{-1}
Volumetric flow rate of THF stream	9.99	mL min^{-1}
Water stream injection velocity (u_{water})	56.58×10^{-2}	m s^{-1}
THF stream injection velocity (u_{THF})	16.97×10^{-2}	m s^{-1}

Mixing Reynolds number: $$R_e = D_{chamber} \cdot \left(\frac{u_{THF}}{\nu_{THF}} + 3\frac{u_{water}}{\nu_{water}}\right) \quad \text{(A.1)}$$

$$R_e = 12{,}541$$

A.2 Fluorescence image showing bright green emission from the QD/mPEG-PDLLA nanoparticles internalized in HeLa cells after incubation for 1.5 h at 37°C

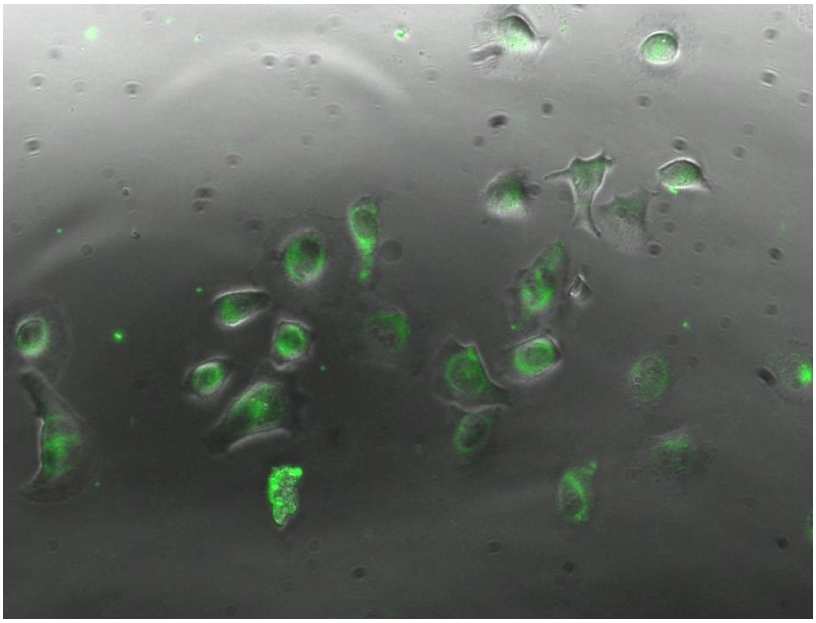

A.3 HPLC calibration curve for antiretroviral drugs – ritonavir and atazanavir (UV detection at 240 nm)

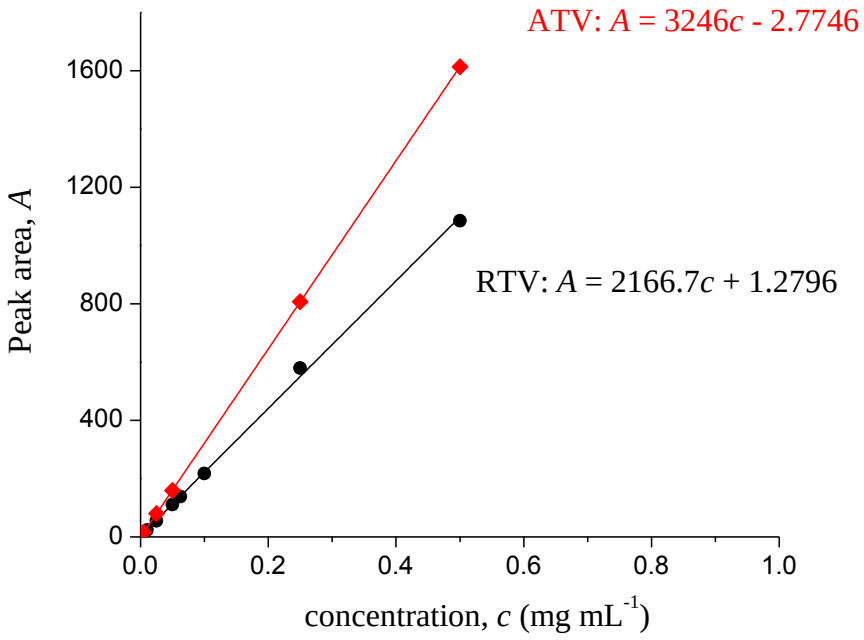

A.4 Block copolymer nanoparticles encapsulating both iron oxide and ritonavir

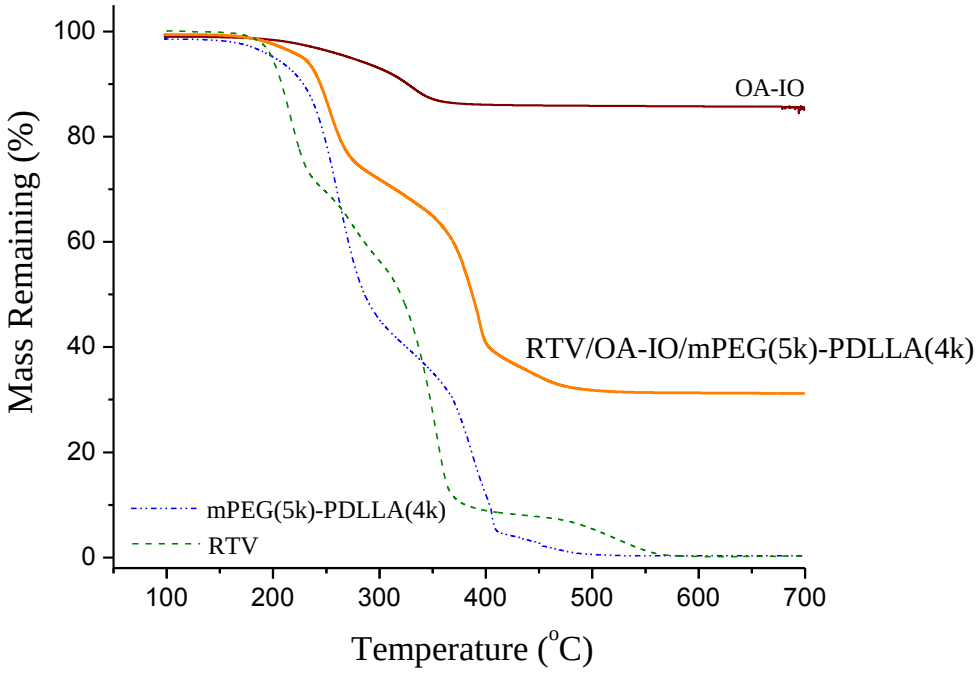

Figure A.4.1 Thermogravimetric curves of ritonavir (RTV), oleic acid coated-iron oxide (OA-IO), mPEG(5k)-PDLLA(4k) diblock copolymer, and copolymer-stabilized particles encapsulating RTV and OA-IO. The iron oxide loading in the OA-IO nanoparticles and in the composite particles is 85.5 wt% and 30.7 wt%, respectively.

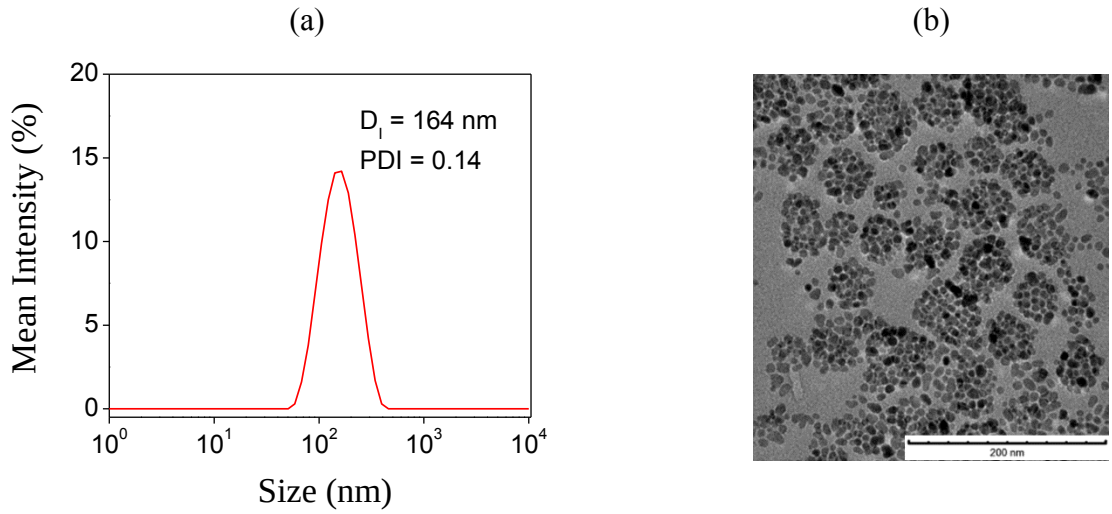

Figure A.4.2 (a) DLS intensity-weighted size distribution of mPEG(5k)-PDLLA(4k) particles co-encapsulating ritonavir and oleic acid-coated iron oxide. (b) Representative TEM micrograph of RTV/OA-IO/mPEG(5k)-PDLLA(4k) particles (scale bar: 200 nm).

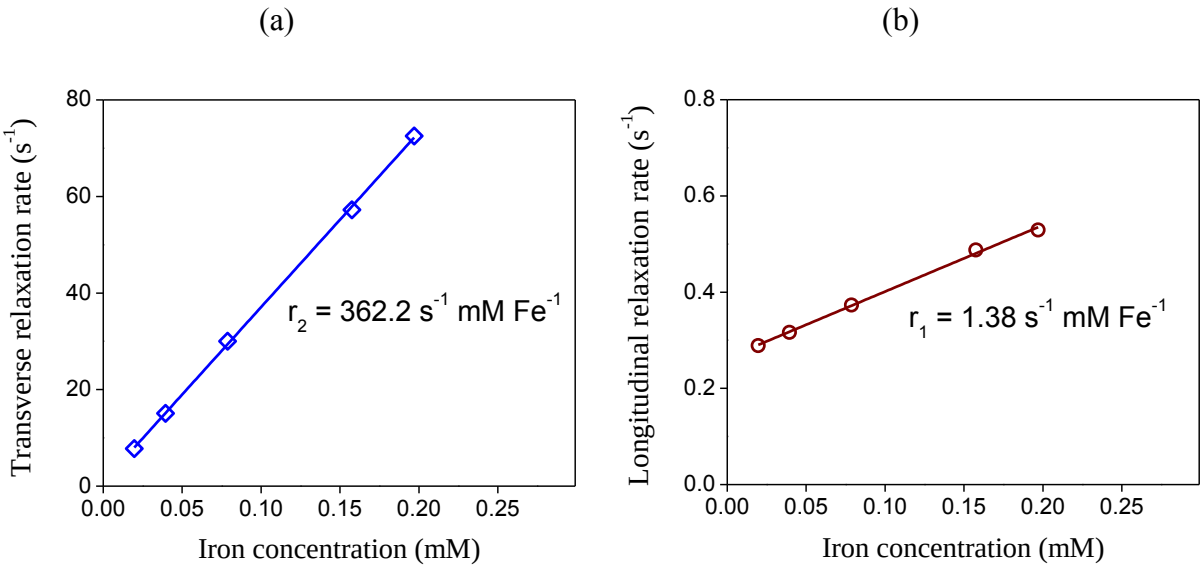

Figure A.4.3 Transverse (a) and longitudinal (b) relaxivities of RTV/OA-IO/mPEG(5k)-PDLLA(4k) particles at 1.4 T and 37.5°C.

A.5 Comparison of drug loading efficiencies of various antiretroviral drug-copolymer nanoparticles

Block copolymer stabilizer: mPEG(5k)-PDLLA(10k)
Homopolymer additive: PLLA(11k) (homopolymer:copolymer = 1:3, w/w)
Targeted loading of drug: 33 wt%

Table A.5.1 Drug loading efficiencies of block copolymer nanoparticles encapsulating various antiretroviral drugs

Antiretroviral drug	Drug loading*
Ritonavir	19 wt%
Efavirenz	27 wt%
Atazanavir	1 wt%

*Measured by HPLC

A.6 Ritonavir solubility and supersaturation values in the preparation of ritonavir-block copolymer nanoparticles

To measure the solubility of ritonavir in the mixed solvent, RTV (55 mg) was added to 55 mL of the solvent (5 mL THF + 50 mL H_2O), and stirred at 300 rpm for 72 h at 25°C. This mixture was filtered with a 0.1 μm Anotop® syringe filter, and the filtrate was analyzed by HPLC.

Measured solubility of RTV in THF/water = 9.01 μg mL^{-1}

Table A.6.1 Drug solubility and supersaturation values in the preparation of polylactide and polybutylene oxide nanoparticles encapsulating ritonavir

Sample	C_{RTV} (mg mL^{-1})	RTV Supersaturation ratio	Sample	C_{RTV} (mg mL^{-1})	RTV Supersaturation ratio
PLA7	0.44	49	**PBO8**	0.15	16
PLA14	1.00	111	**PBO15**	0.33	37
PLA23	1.71	190	**PBO23**	0.57	63